

JOHANN ANDRADE FERRARETO

Human comfort in tall buildings subjected to wind-induced motion

“Conforto em edifícios altos sob ação do vento”

São Paulo

(2017)

JOHANN ANDRADE FERRARETO

Human comfort in Tall Building's subjected to wind-induced motion

“Conforto em edifícios altos sob ação do vento”

Thesis presented to the *Escola Politécnica da Universidade de São Paulo* to obtain the title of Doctor of Science.

Field of studies: Structural Engineering

Supervisor: Prof. Carlos Eduardo Nigro Mazzilli.

São Paulo

(2017)

Este exemplar foi revisado e corrigido em relação à versão original, sob responsabilidade única do autor e com a anuência de seu orientador.

São Paulo, _____ de _____ de _____

Assinatura do autor: _____

Assinatura do orientador: _____

Catálogo-na-publicação

Ferrareto, Johann Andrade

Human comfort in tall buildings subjected to wind-induced motion / J. A. Ferrareto -- versão corr. -- São Paulo, 2017.
285 p.

Tese (Doutorado) - Escola Politécnica da Universidade de São Paulo.
Departamento de Engenharia de Estruturas e Geotécnica.

1.Tall buildings 2.Structural analysis 3.Dynamic analysis 4.Comfort Assessment 5.Wind tunnel I.Universidade de São Paulo. Escola Politécnica. Departamento de Engenharia de Estruturas e Geotécnica II.t.

DEDICATORY

This work is dedicated to my family and friends, as a whole and individually.

First, I dedicate it to my father, for setting me up on the engineering path, then to my mother and sister, for helping me stay on it. I would also like to dedicate it to my grandparents, role models in my academic life.

And to all of them, including many others not cited here, for understanding my absence while I was writing this thesis.

ACKNOWLEDGEMENTS

I would like to thank many professionals who contributed to this work and without whom the results achieved here would not be possible.

First, I would like to thank my supervisor, Prof. Mazzilli, for his management, guidance and wisdom throughout these years of hard work, but mostly for his patience.

Then, I would like to thank Prof. França, for his substantial contribution, both in early and late stages of this work, helping me gather data for the case studies and for the initial publications.

I would also like to show gratitude to Prof. Acir, for introducing me to wind engineering and for allowing me to acquire further knowledge in areas beyond structural engineering. Also, Prof. Irwin, who helped me extend this knowledge to the probabilistic field of studies.

Finally, I would like to show gratitude to Professors João Cyro André and Mario Franco for their readiness to contribute to this work and for their valuable contributions in the fields of structural engineering and wind engineering as well.

A special thanks to the following companies and universities, without which the results obtained in this thesis wouldn't be possible: *Escola Politécnica da Universidade de São Paulo, Universidade Federal do Rio Grande do Sul, Alan G. Davenport Wind Engineering Group, França & Associados Projetos Estruturais, Rowan Williams Davies and Irwin Inc.*

“Structural Engineering is the art and science of molding Materials we do not fully understand; into Shapes we cannot precisely analyze; to resist Forces we cannot accurately predict; all in such a way that society at large is given no reason to suspect the extent of our ignorance.”

(James Amrhein)

Structural Engineering International – January 1996.

RESUMO

O estudo das oscilações de edifícios altos sob ação do vento é uma área multidisciplinar que envolve conhecimentos de diferentes campos de estudo: engenharia estrutural, engenharia de vento, confiabilidade e até fisiologia humana, para citar apenas alguns. Em paralelo, a criação de novos materiais de construção de alta resistência, aliados às últimas tendências na construção de edifícios altos, permite sistemas estruturais cada vez mais esbeltos aplicados a edifícios cada vez mais altos. Este contexto leva a uma situação em que estes sistemas estruturais são sensíveis aos efeitos dinâmicos das cargas de vento e onde o conforto humano é frequentemente o critério preponderante para o projeto estrutural. Esta área multidisciplinar, com seus sistemas estruturais esbeltos, aliada aos aspectos econômicos e ambientais da construção de edifícios altos, exige uma melhor integração entre os campos acima referidos para se alcançar conforto humano em edifícios sustentáveis (tanto do ponto de vista ambiental quanto do econômico). Esta tese tem como eixo de investigação os "elos fracos" da corrente de cargas de vento de Davenport e discute os critérios de cada campo envolvido na avaliação das oscilações de um edifício alto: análise dinâmica, modelagem de elementos finitos, modelagem probabilística de vento e avaliação de conforto. O eixo de investigação proposto visa a trazer precisão ao procedimento, criando um conjunto de critérios confiáveis para a avaliação da resposta dinâmica a partir de ensaios em túnel de vento de edifícios altos. Esta tese também visa a conectar estes campos de estudo, trazendo a compreensão de cada um deles para todos os outros e para validar as interações multidisciplinares na corrente de Davenport. Finalmente, uma grande dispersão de resultados é obtida para dois edifícios altos em São Paulo. Esta dispersão serve para corroborar a deficiência da integração entre estes campos de estudo e para apresentar um conjunto de critérios que traga precisão ao procedimento, permitindo, concomitantemente, projetos mais econômicos e sustentáveis.

Palavras-chave: Edifícios altos. Análise estrutural. Análise dinâmica. Análise de conforto. Critérios de projeto. Cargas de vento. Túnel de vento.

ABSTRACT

Assessing tall building oscillation is a multidisciplinary area involving knowledge from different fields of study: structural engineering, wind engineering, reliability, and even human physiology, to name a few. With the modern high strength structural materials and the latest tendencies in tall buildings construction, new structural systems have become slender and new buildings have reached greater heights as time passes. This context leads to a situation where these slender structures are sensitive to dynamic effects from wind loads and where human comfort is often the prevailing criterion for the structural design. This multidisciplinary area with slender structural systems allied to economic and environmental aspects from building construction demands a better integration between the abovementioned fields in order to achieve both human comfort and sustainable buildings (from environmental and economic points of view). This thesis aims at connecting the “weak links” of the Davenport’s chain of wind loading, discussing criteria from each field involved in the oscillation assessment of a tall building: dynamic analysis, finite element modelling, wind climate modelling and comfort assessment. The axis of investigation intends to bring precision to the procedure, whilst creating a reliable set of criteria to perform a dynamic response assessment from the wind tunnel testing of tall buildings. This thesis also aims at connecting these fields of study by bringing understanding from each one of them to all the others, and at validating multidisciplinary interactions in the Davenport’s chain. Finally, a wide dispersion of results is obtained for two different tall buildings in São Paulo. This dispersion serves to corroborate the deficient integration between these fields of study and to present a set of criteria that brings precision to the procedure, whilst allowing more economic and sustainable designs.

Keywords: Tall buildings. Structural analysis. Dynamic analysis. Comfort Assessment. Design criteria. Wind loads. Wind tunnel.

CONTENTS

List of figures	xxiii
List of tables	xxix
List of abbreviations	xxxi
List of symbols.....	xxxiii
1 Introduction	39
1.1 Context and motivations.....	39
1.1.1 General context	39
1.1.2 Technical and environmental context (São Paulo, Brazil).....	40
1.1.3 Normative context.....	42
1.1.4 Motivations	45
1.1.4.1 Specifics about the objects of study	46
1.2 Introduction to wind loads on tall buildings	48
1.2.1 Planetary boundary layer, wind profile and turbulence	48
1.2.2 Dynamic wind loads.....	51
1.2.2.1 Along-wind, cross-wind and torsional loads	51
1.2.2.2 Power spectral density (PSD), structural admittance, and duration of wind events.....	54
1.3 Introduction to structural data of tall buildings	56
1.3.1 Natural frequencies – general case	57
1.3.1.1 Tall buildings’ natural frequencies	57
1.3.2 Mode shapes – general case.....	60
1.3.2.1 Tall building’s mode shapes and lumped-mass matrix.....	61
1.3.3 Damping – ξ	64
1.4 Introduction to WTT of tall buildings	67
1.4.1 Simulation of the atmospheric boundary layer	67

1.4.2	Types of WTT.....	69
1.4.2.1	HFFB	70
1.4.2.2	Aeroelastic models	70
1.4.2.3	HFPI	71
1.5	Introduction to comfort assessment.....	73
1.5.1	Current approach to human comfort assessment	75
1.6	Objectives.....	79
1.6.1	Specific objectives – structural engineering	79
1.6.2	Specific objectives – wind engineering.....	80
1.6.3	Specific objectives – comfort criteria	80
1.6.4	Final statements about this thesis objectives	81
2	Dynamic analysis.....	83
2.1	Introduction.....	83
2.2	Equations of motion and mode displacements superposition	83
2.3	Solution in the frequency domain.....	85
2.3.1	Acceleration and forces over the building’s height	87
2.3.2	Peak acceleration assessment.....	88
2.4	Solution in the time domain	89
2.5	Differences between time-domain and frequency-domain responses	90
3	FE modelling criteria.....	93
3.1	Introduction.....	93
3.2	Beam-end-offsets	93
3.3	Modelling floor slabs	94
3.3.1	Validity of the rigid diaphragm hypothesis	94
3.3.2	Floor slab flexural stiffness.....	95
3.3.3	In-plane floor slab flexibility	97

3.4	Modelling non-structural elements.....	98
3.5	Use of the probable Young's modulus.....	99
3.5.1	Stiffness for cracked sections	100
3.6	Synthesis about structural criteria	102
4	Wind modelling criteria	103
4.1	Introduction	103
4.2	Worst-case method and NBR6123-1988.....	105
4.3	Sector-by-sector methods	108
4.4	Up-crossing method	111
4.5	Wind speed in open terrain vs. wind speed on site	114
4.6	Wind modelling in Brazilian wind climate.....	115
5	Comfort criteria.....	117
5.1	Introduction	117
5.2	Kinematic properties of the motion.....	117
5.2.1	Amplitude of motion	117
5.2.2	Velocity	118
5.2.2.1	Linear velocity	118
5.2.2.2	Angular velocity.....	118
5.2.3	Acceleration.....	118
5.2.3.1	Linear acceleration.....	118
5.2.3.2	Angular acceleration (Yaw)	120
5.2.4	Derivative of acceleration (Jerk)	121
5.2.5	Frequency.....	121
5.3	Structural, psychological and statistical properties of motion	127
5.3.1	Psychological and physiological factors.....	127
5.3.1.1	Visual cues.....	128

5.3.2	Return period	128
5.3.3	Duration.....	130
5.3.3.1	Duration of the windstorm.....	130
5.3.4	Peak, rms and waveform.....	131
5.3.5	Probabilistic evaluation of human comfort.....	134
5.4	Discussion	136
5.4.1	Psychological and statistical significance for user's comfort	136
5.4.1.1	Peak and rms accelerations	136
5.4.1.2	Assessing complex motion	137
5.4.2	Frequency biodynamic amplification	140
5.4.3	Alternative approach to human comfort assessment of motion.....	142
5.4.3.1	Alternative assessment of human comfort.....	144
5.4.3.2	Probabilistic method application and future research	146
5.5	Chapter synthesis	146
6	Methodology	149
6.1	FE modelling.....	149
6.1.1	Beam-end-offsets.....	149
6.1.2	Use of probable Young's modulus	150
6.1.3	Floor slab modelling	150
6.1.4	Structural dynamic data	152
6.2	Dynamic analyses.....	152
6.2.1	Modal loads.....	155
6.2.2	Frequency-domain analysis	159
6.2.3	Time-domain analysis	161
6.3	Wind load modelling	163
6.3.1	Worst case method	163

6.3.2	Up-crossing method.....	164
6.4	Comfort evaluation of assessed accelerations	166
6.4.1	Deterministic comfort assessment	166
6.4.2	Probabilistic comfort assessment	166
6.5	Modulus of elasticity for comfort analysis	167
7	Case study	171
7.1	Building A	171
7.1.1	General information	171
7.1.2	Building's dynamic and mechanical properties	173
7.2	Results for building A	174
7.2.1	Structural modelling criteria	174
7.2.1.1	Natural frequencies	174
7.2.1.2	Mode shapes.....	177
7.2.1.3	Modal results (frequency domain)	182
7.2.1.4	Final acceleration results for each structural model	186
7.2.2	Dynamic analysis criteria	187
7.2.2.1	Validation of results.....	187
7.2.2.2	Peak factors and joint action factors	191
7.2.2.3	Higher modal contribution	196
7.2.2.4	PSD of the time-domain results.....	202
7.2.2.5	Location of the user.....	202
7.2.2.6	Summary of structural modelling criteria and dynamic analysis	206
7.2.3	Wind modelling criteria	208
7.2.3.1	Up-crossing method results (non-directional wind climate)	208
7.2.3.2	Up-crossing method results (directional wind climate)	209
7.2.4	Comfort and SLS criteria	212
7.2.4.1	Peak and rms acceleration analysis (deterministic)	212

7.2.4.2	Peak angular velocity analysis (deterministic) and lateral drift.....	215
7.2.4.3	Probabilistic comfort assessment	217
7.2.5	Stiffness validation	219
7.2.5.1	Modal normalized loads.....	219
7.2.5.2	Stiffness validation for shear walls.....	222
7.2.5.3	Stiffness validation for beams and floor slabs.....	225
7.2.6	Summary of criteria for building A	228
7.3	Building B presentation.....	233
7.3.1	General information.....	233
7.3.2	Building's dynamics and mechanical properties.....	234
7.4	Results for building B.....	235
7.4.1	Structural modelling criteria.....	235
7.4.2	Analysis validation with BLWT results.....	237
7.4.3	Dynamic analysis criteria.....	239
7.4.4	Wind, comfort and complete criteria for building B.....	244
7.5	Synthesis of Case studies (buildings A and B)	248
8	Conclusions	251
	Bibliography	255
	Appendix 1 – “Building A” mechanical properties	267
	Appendix 2 – Buildings A1, A2 and A3 mode shapes view.....	271
	Appendix 3 – “Building A” studied shear walls	273
	Appendix 4 – “Building B” mechanical properties	277
	Appendix 5 – Proposal for revision of the NBR6123 standard: comfort chapter (Portuguese).....	281
	Introdução	281
	Critérios de análise dinâmica	282

Critérios de análise estrutural	283
Critérios de modelagem para a velocidade de vento	283
Critérios de conforto	283

LIST OF FIGURES

Figure 1.1 – Practical height limits of structural systems.	41
Figure 1.2 – Example of structure with central concrete core.	42
Figure 1.3 – Model of the surroundings of a Tall Building (Shanghai Tower).	43
Figure 1.4 – Building height vs. natural period (Steel-Buildings).	44
Figure 1.5 – The Alan G. Davenport chain of wind loading.	45
Figure 1.6 – Wind profile, turbulent shear stress and featuring altitudes.	49
Figure 1.7 – Wind Profile and wind turbulence: elevation of the building.	50
Figure 1.8 – Van der Hoven Power Spectrum.	51
Figure 1.9 – Wind profile, pressure distribution, and base forces on the building.	52
Figure 1.10 – Wind forces and eccentricities acting on the building’s façade.	53
Figure 1.11 – Normalized response spectrum of base moment.	55
Figure 1.12 – Lumped mass model.	61
Figure 1.13 – Reference-axis location.	62
Figure 1.14 – Mode shapes of a 50-story tall building.	63
Figure 1.15 – Spires, barriers and roughness elements.	67
Figure 1.16 – Features of the wind speed profile simulated in the wind tunnel.	69
Figure 1.17 – Aeroelastic model testing.	71
Figure 1.18 – Pressure study model.	72
Figure 1.19 – Pressure taps eccentricities/heights/tributary areas.	73
Figure 1.20 – Acceleration assessment overview.	74
Figure 1.21 – Comfort criteria benchmark (1-year return period).	76
Figure 1.22 – Comfort criteria benchmark (10-year return period).	77
Figure 1.23 – 1-year return period along-wind and crosswind peak accelerations of actual tall buildings in Japan.	78
Figure 1.24 – Davenport’s possible weak link for structural criteria.	80

Figure 3.1 – Structures with refined slabs.....	95
Figure 3.2 – Deformed shape of building structures under lateral loads.	96
Figure 3.3 – Natural periods and lateral displacements for 20-storey structures.	96
Figure 3.4 – Rigid Diaphragm and Semi Rigid Diaphragm behaviours.	97
Figure 3.5 – Example of building structures.....	98
Figure 3.6 – Joint frame in-fill under horizontal loads.	99
Figure 3.7 – ELS-F cracking formation.	100
Figure 3.8 – Shear wall modelling with cracked and uncracked regions.....	101
Figure 4.1 – Acceleration results for scenario 3.....	104
Figure 4.2 – Isocurves for V_0 , in m/s.	106
Figure 4.3 – Example probability exceedance for wind speed above the value for 50-year return period.	107
Figure 4.4 – Comparison between non-directional and conditional wind speed per sector in Düsseldorf.	108
Figure 4.5 – Acceleration results for scenario 4.....	110
Figure 4.6 – Acceleration results for scenario 5.....	110
Figure 4.7 – Response boundary.....	111
Figure 4.8 – Up-crossing method overview.....	112
Figure 4.9 – Topographic model to transfer anemometer data.	114
Figure 5.1 – RMS acceleration levels.	119
Figure 5.2 – Summary of the human response to yaw vibration, “r” factors.....	121
Figure 5.3 – Human comfort acceleration assessment (peak).....	122
Figure 5.4 – Human perception acceleration assessment (rms).....	123
Figure 5.5 – Displacement results under sinusoidal vibration.	125
Figure 5.6 – Acceleration results.	126
Figure 5.7 – Magnification factors for the head.....	127
Figure 5.8 – Davenport’s benchmark criteria.	129

Figure 5.9 – Types of vibration and corresponding peak factors.....	131
Figure 5.10 – Motion shapes (a); time histories of sinusoidal (b) and random (c) motions of the test room (low-frequency set).....	132
Figure 5.11 – Examples of sinusoidal acceleration responses of test rooms.	133
Figure 5.12 – Comparison of random and sinusoidal motion perception.....	134
Figure 5.13 – Schematic flow of the probabilistic comfort evaluation method.	135
Figure 5.14 – Crosswind responses for 1% damping ratio.	139
Figure 5.15 – Magnified accelerations from ISO6897 and ISO10137 standards.....	141
Figure 5.16 – Alternative acceleration assessment curve.	145
Figure 5.17 – Comparison between motion sickness and perception thresholds. ...	145
Figure 6.1 – Concrete strength for each building: A (left) and B (right).	150
Figure 6.2 – Structural elements of the typical floor of the studied building.....	151
Figure 6.3 – Dynamic analysis workflow (frequency domain).....	153
Figure 6.4 – Dynamic analysis workflow (time domain).....	154
Figure 6.5 – Pressure taps layout (building A).....	156
Figure 6.6 – Tributary areas and pressures on the building’s façade (building A). ...	157
Figure 6.7 – PSD of the modal accelerations Q_i for 10° azimuth (Building A).	160
Figure 6.8 – Locations for resultant acceleration assessment.....	162
Figure 6.9 – λ_p and ζ_p calibration using AIJ-GEH-2004 perception curves.	167
Figure 7.1 – Studied Building (nearly finished, on the right).	171
Figure 7.2 – Building’s structure: a) blueprint; b) construction photo; c) 3D model..	172
Figure 7.3 – Building’s structural modelling: a), b), c), and d) STRAP; e) Robot.	172
Figure 7.4 – Structural model of the building using TQS software.....	173
Figure 7.5 – Outrigger system.	175
Figure 7.6 – Structural behaviour of an outrigger system under lateral loads.	176
Figure 7.7 – Translational mode shapes for building A3 (x and y components).	178

Figure 7.8 – Translational mode shapes for building A3 (rearranged).	179
Figure 7.9 – Structural system of building A.	180
Figure 7.10 – Structural system of building A.	181
Figure 7.11 – Modal accelerations (rms) for buildings A1, A2 and A3.	183
Figure 7.12 – Resultant accelerations for buildings A1, A2, and A3.	186
Figure 7.13 – Modal acceleration (rms): time vs. frequency domain (Building A3).	188
Figure 7.14 – Reduction factor comparison.	189
Figure 7.15 – Peak modal accelerations: time vs. frequency domain (Building A3).	190
Figure 7.16 – Modal accelerations: 5 th mode, 300°, time domain (Building A3).	191
Figure 7.17 – Peak factors (Building A3, all azimuths).	192
Figure 7.18 – Transient behaviour (Building A3, 340°).	193
Figure 7.19 – Peak factors (Building A3, all azimuths).	194
Figure 7.20 – Final acceleration results (Building A3, all azimuths).	195
Figure 7.21 – Peak and joint action factors (Building A3, all azimuths).	196
Figure 7.22 – rms and peak accelerations (Building A3, all azimuths).	197
Figure 7.23 – Higher modal contribution (components of acceleration).	198
Figure 7.24 – Higher modal contribution (overall and comparison).	199
Figure 7.25 – Higher modal contribution (Y axis component of acceleration, 300°).	201
Figure 7.26 – Modal accelerations PSD (300° sector).	202
Figure 7.27 – Peak and rms responses in different floor locations (300° sector).	203
Figure 7.28 – Higher modal contribution: level 60.70m (peak acceleration).	205
Figure 7.29 – Higher modal contribution: level 60.70m (acceleration components).	206
Figure 7.30 – Worst case method resultant peak accelerations vs. return period... ..	207
Figure 7.31 – Worst case method vs. Up-crossing method (non-directional).	208
Figure 7.32 – Up-crossing method validation with BLWT results.	209
Figure 7.33 – Up-crossing method results (Building A).	210

Figure 7.34 – Critical directions: wind climate and building’s responses.	211
Figure 7.35 – Peak acceleration analysis (Building A).	213
Figure 7.36 – rms acceleration analysis (Building A).....	214
Figure 7.37 – Angular velocity analysis (Building A).....	215
Figure 7.38 – Top displacement at the building’s façade (1-year return period).....	216
Figure 7.39 – Top displacement of the building’s façade (50-year return period)....	217
Figure 7.40 – Deterministic comfort/perception evaluation (1-year return period)...	218
Figure 7.41 – Modal shear forces and torsional moments vs. building heights.	220
Figure 7.42 – View of the 2 nd mode of vibration deflection shape.	221
Figure 7.43 – View of the 3 rd mode of vibration deflection shape.	222
Figure 7.44 – Peak tensile stress for each structural member (shear walls).	224
Figure 7.45 – Peak tensile stress for P24.....	224
Figure 7.46 – Peak tensile stress for each structural member (beams).	226
Figure 7.47 – Peak tensile stress for the floor slabs.....	226
Figure 7.48 – Peak tensile stresses for beams V1, V2, V4 (up-crossing method)...	227
Figure 7.49 – Wind climate results comparison.....	230
Figure 7.50 – Studied Building (renderization).	233
Figure 7.51 – Structural model of the building using TQS software.....	234
Figure 7.52 – Building B floor plan.	236
Figure 7.53 – Resultant accelerations for buildings B1 and B3.	237
Figure 7.54 – Up-crossing method validation with BLWT results for building B1.....	238
Figure 7.55 – Resultant accelerations (peak) for time and frequency domains (Building B3).....	239
Figure 7.56 – Modal accelerations PSD (260° sector).....	240
Figure 7.57 – Peak factors “g” (Building B3, time domain).	241
Figure 7.58 – Transient behaviour (Building B3, 350°).....	241

Figure 7.59 – Higher modal contribution, peak acceleration (Building B3, time domain).....	242
Figure 7.60 – Higher modal contribution, peak angular velocity (Building B3, time domain).....	243
Figure 7.61 – Peak acceleration analysis (Building B3).....	244
Figure 7.62 – Angular velocity analysis (Building B3, time domain).....	247
Figure A1.1 – Mode shapes for A1 structural model (X axis components).	268
Figure A1.2 – Mode shapes for A1 structural model (Y axis components).	269
Figure A1.3 – Mode shapes for A1 structural model (torsional components).....	270
Figure A2.1 – Mode shapes for A1, A2 and A3 buildings (1 st , 2 nd , and 3 rd modes). 271	
Figure A2.2 – Mode shapes for A1, A2 and A3 buildings (4 th , 5 th , and 6 th modes)..	272
Figure A3.1 – Shear walls “P21” (left) and “P24” (right).....	273
Figure A3.2 – Shear wall “P25”.....	274
Figure A3.3 – Shear wall “P32”.....	275
Figure A3.4 – Shear wall “P3”.....	275
Figure A4.1 – Building B mode deflection shapes.	278
Figure A4.2 – Building B mode deflection shapes (modes 1 to 6).	279
Figura A5.1 – Critérios de conforto para a revisão da NBR6123-1988.....	284

LIST OF TABLES

Table 1.1 – Natural frequencies for tall buildings.....	58
Table 1.2 – Comparison: first natural frequencies measured and estimated.....	59
Table 5.1 – Results: accelerations, durations and complaints.....	123
Table 5.2 – Target reliability index β_T	134
Table 5.3 – Comparison of peak accelerations.	138
Table 5.4 – Crosswind responses: accelerations and displacements.	140
Table 5.5 – ISO Standards multiplied by head magnification factors.	141
Table 6.1 – Modulus of elasticity results for “ $t \rightarrow \infty$ ”.....	150
Table 6.2 – $p_i(R; \alpha_i)$ parameters for São Paulo.	165
Table 6.3 – Coefficients λ_p and ζ_p vs. buildings’ first natural frequency.	166
Table 7.1 – Building’s natural frequencies and periods of vibration.....	173
Table 7.2 – Comparison of natural frequencies for the structural models A1, A2, and A3.....	174
Table 7.3 – Natural frequencies comparison rearranged.	179
Table 7.4 – Higher modal contribution (acceleration and displacements).	200
Table 7.5 – Higher modal contribution on acceleration components (Building A3)..	200
Table 7.6 – Probabilistic comfort assessment for different criteria.	218
Table 7.7 – Summary of results of each set of criteria for building A.....	230
Table 7.8 – Building B natural frequencies and periods of vibration.....	234
Table 7.9 – Natural frequencies comparison for B1, B2 and B3 structural models..	236
Table 7.10 – Summary of results of each set of criteria for building B.....	246
Table A1.1 – Building A’s inertial properties.....	267
Table A4.1 – Building B’s inertial properties.....	277

LIST OF ABBREVIATIONS

ABNT-NBR	<i>Associação Brasileira de Normas Técnicas</i>
AIJ	Architectural Institute of Japan
ASCE	American Society of Civil Engineers
BLWT	Boundary Layer Wind Tunnels
CTBUH	Council of Tall Buildings and Urban Habitat
DOF	Degree of freedom
FE	Finite-element
HFFB	High-frequency-force balance
HFPI	High-frequency-pressure integration
ICWE	International Conference on Wind Engineering
ISO	International Organization for Standardisation
NBCC	National Building Code of Canada
NSW	Non-structural walls
PSD	Power spectral density
rms	root-mean-square
SLS	Service Limit State
ULS	Ultimate Limit State
WTT	Wind Tunnel Testing

LIST OF SYMBOLS

$a_{n,j}$	Fourier coefficient
$a_{\text{Peak}}, \vec{a}_{\text{Peak}} $	Modulus of vectorial peak acceleration
$a_T, a_{1-\text{Year}}$	Accelerations for different return periods
$a_x, a_y, a_{\theta R}$	Peak acceleration components
$a_{x,n}, a_{y,n}, a_{\theta,n}$	Cumulative acceleration components for “n” modes of vibration
A	Log-normal distribution parameter, peak acceleration
A_i	Façade tributary area, Weibull distribution parameter
A_z	Section area
b	Concrete beam width
B_j	Coefficient that varies for the required dynamic response
$b_{n,j}$	Fourier coefficient
c, c_x, c_y	Distances from the neutral axes to the section’s point of interest
[C]	Viscous-damping matrix
C_d	Equivalent damping
C_i	Weibull distribution parameter
$C_{\check{p}}$	Pressure coefficient
d	Distance between the reference axis and the floor’s farthest point
$e_{x,\ell}, e_{y,\ell}$	Eccentricities with respect to the reference vertical Z axis
$E_{Ci,28}$	Young’s Modulus of the concrete after 28 days
$E_{Ci,\infty}$	Young’s Modulus of the matured concrete
EI	Flexural stiffness
f, f_j, f_0, f_1	Natural frequencies of vibration
f_{ck}	Concrete’s characteristic compression strength after 28 days
$f_{ct,f}$	Concrete’s tensile strength after 28 days

f_s	Dynamic force acting at the base level of the building
$f_{s\ell}$	Dynamic force acting on a single floor
F	Axial force acting on the structural member
$F_d(t)$	Control force of the active damping system
$F_p(\bar{\omega})$	Fourier transform
$F_Q(Q < R)$	Cumulative probability of the largest yearly wind effect
g, g_x, g_y	Peak factors
h	Resultant horizontal root-mean-square linear accelerations
$h_i, h_\ell, h_{\ell+1}$	Heights
H	Building height
$H(i\bar{\omega})$	Structural admittance
I, I_x, I_y	Section's moments of inertia
$I_{Z\ell}$	Rotational mass moments of inertia about the reference axis Z
j	Day, mode of vibration
k_i	Weibull distribution parameter
K	Stiffness
K_d	Damper stiffness, directionality factor
$[K]$	Stiffness matrix
ℓ	Floor level of the structure
L_u	Macro scale of the longitudinal component of the turbulence
m	Return period, total number of floors
m_ℓ	Mass of the floor concentrated around the centre of mass
$m_x(t)$	Base bending moment (cross-wind)
$m_y(t)$	Base bending moment (along-wind)
$m_z(t)$	Torsional moment at the base

M	Bending moment (internal force)
$[M]$	Structure's mass matrix
M_d	Mass portion of the mass damper
M_j	Bending moment (internal force) due to the j^{th} modal load
$[M]_\ell$	Mass matrix for each floor
$M_{N,j}$	Normalized bending moment (internal force)
$M_x(t), M_y(t)$	Resultant bending moments (internal force)
n	Number of modes, number of degrees-of-freedom, step
$N_{N,j}$	Normalized axial force (internal force)
$N_z(t)$	Resultant normal force (internal force)
\check{p}	Peak suction pressure in the building's façade
$\{p(t)\}$	Dynamic loading applied to the structure by the wind
$p_x(t)$	Base shear force (along-wind)
$p_y(t)$	Base shear force (cross-wind)
P	Random variable for comfort assessment
$P_i(V)$	Probability of exceedance for the wind speed
$P_j(t), P_{j,T}(t)$	Modal loadings
P_m	Cumulative probability
$q(R_{\text{ref}})$	Reference wind pressure
$q(T)$	Wind pressure for a given return period T
r	Factor for equivalency of yaw vibration to translational vibration
R	Radius, return period, rate of up-crossing
s	Coefficient for concrete ageing
$S_p(\bar{\omega})$	Power spectral density function
S_1	Topographic factor

S_2	Height, terrain roughness and building geometry factor
S_3	Statistical factor
t	Concrete age, time
T	Duration of the wind event, return period
T_p	Duration of the dynamic wind loading
$\{\hat{u}\}$	Modal shape of the vibrating system
$\{u(t)\}$	Nodal displacements vector
$\{\dot{u}(t)\}$	Nodal velocities vector
$\{\ddot{u}(t)\}$	Nodal accelerations vector
v_i	Wind speed in the sector i
V	Wind speed
$ \dot{V} $	Empirical parameter for up-crossing method
$V(R)$	Wind speed at the height of reference
V_k	Characteristic wind speed to calculate the wind pressure
$V_{N,j}$	Normalized shear force
$V(z)$	Wind speed over height
V_0	Basic wind speed associated to the response
$V(1/R; \delta\theta_i)$	Sector $\delta\theta_i$ and return period R wind speed
W	Elastic section modulus
x	Variable in the X axis, axis index
$\ddot{x}_{\text{Resultant}}$	Resultant root-mean-square acceleration
x_ℓ	X axis displacement of the centre of mass of each floor
X	Axis name
y	Variable in the Y axis, axis index
y_ℓ	Y axis displacement of the centre of mass of each floor

Y	Axis name
Y_j	Modal amplitude
$Y(t), Y_{n,1}, Y_{j,n}$	Generalized displacement
$\dot{Y}(t), \dot{Y}_{n,1}, \dot{Y}_{j,n}$	Generalized velocity
$\ddot{Y}(t), \ddot{Y}_{n,1}, \ddot{Y}_{j,n}$	Generalized acceleration
z	Variable in the Z axis, axis index, height
z_d	Terrain's constructions height
z_g	Gradient height
z_ℓ	Story " ℓ " height above the ground
z_0	Surface roughness length
Z	Axis name
$ \bar{\alpha} $	Empirical parameter for up-crossing method
β	Reliability index
$\beta_{n,j}$	Ratio between n^{th} harmonic and j^{th} mode angular frequencies
β_T	Comfort design parameter
γ	Euler's constant
$\delta\theta_i$	Wind sector
ζ_P	Log-normal distribution parameter for comfort assessment
λ_L	The linear scale of the wind tunnel simulation
$\ddot{\theta}$	Root-mean-square yaw acceleration
θ_ℓ	Torsion around Z axis of each floor
μ_P	Log-normal distribution parameter for comfort assessment
ξ	Damping ratio of the structure
ξ_a	Aerodynamic damping
ξ_d	Damping originated by damping device

ξ_j	Modal viscous damping ratio
ξ_s	Structural damping
ρ	Air density
$\rho_{ar}\overline{u\overline{w}}$	Atmospheric shear stress over height
σ_a	Standard deviation of the acceleration response
$\sigma_c(t)$	Compression stress due to the axial force $F(t)$
$\sigma_{c,g}$	Stabilizing compression stress due to gravity loads
$\sigma_{t,max}$	Maximum tensile stress
σ_{xy}	Root-mean-square of the resultant acceleration
$\sigma_{\dot{y},j}$	Generalized acceleration's root-mean-square of the j^{th} mode
φ	Joint action factor
$\{\Phi\}_j$	Mode deflection shape vector of the j^{th} mode
$[\Phi]$	Matrix composed by all $\{\Phi\}_j$ vectors
$\Phi_{\ell xj}$	Eigenvector values for the X axis, ℓ^{th} floor and j^{th} mode
$\Phi_{\ell yj}$	Eigenvector values for the Y axis, ℓ^{th} floor and j^{th} mode
$\Phi_{\ell \theta j}$	Eigenvector values for the Z axis (torsion), ℓ^{th} floor and j^{th} mode
$\Phi_{x,j}(h_i)$	Eigenvector values for the X axis, height h_i and j^{th} mode
$\Phi_{y,j}(h_i)$	Eigenvector values for the Y axis, height h_i and j^{th} mode
$\Phi_{\theta,j}(h_i)$	Eigenvector values for the Z axis (torsion), height h_i and j^{th} mode
$\Phi_{x,j}(h_\ell)$	Eigenvector values for the X axis, height h_ℓ and j^{th} mode
$\Phi_{x,j}(h_{\ell+1})$	Eigenvector values for the Y axis, height $h_{\ell+1}$ and j^{th} mode
$\Phi_{(x,y,\theta)}$	j^{th} mode shape at the ℓ^{th} floor in any chosen direction (x, y or θ)
$\omega, \omega_1, \omega_j, \omega_n$	Natural angular frequencies of the building
$\overline{\omega}$	Harmonic angular frequencies of the Fourier transform $F_p(\overline{\omega})$

1 INTRODUCTION

1.1 CONTEXT AND MOTIVATIONS

1.1.1 GENERAL CONTEXT

The present environment situation asks for stronger directives from the whole world to attain long-term sustainability for future generations.

Applying this perception to structural engineering, one might cite the Council of Tall Buildings and Urban Habitat (CTBUH). During CTBUH's conference in 2014 in Shanghai (China), the reduction of the environmental footprint of the big cities was recommended by means of several directives. Among these directives, those which are strongly aligned with this thesis are: (1) the reduction of embodied energy of constructions and (2) the verticalization of dense urban areas. Among all other aspects presented in that conference, these two directives will be the most explored in this thesis.

The verticalization of an urban area is a function of many variables, such as the environment loads acting on its buildings (i.e., wind and seismic loads), the price of the square meter of the land, and the occupation rate defined by the master plan of the city, to name a few.

As an outcome of the two paragraphs above, one can infer that when it is technically feasible, cost-effective, and allowed by the city master plan, tall buildings can solve the problem of high density urban areas in a more sustainable way.

In order to better illustrate this outcome, one can cite the studies performed by Drew et al. (2014). In those studies, the concept of vertical dwellings is explored through an extensive study about the carbon life cycle and embodied energy, not only from the building's structure itself, but also from its operation and from the city infrastructure to serve it (utilities, transport, etc.). The study was made considering a city with the climatic features of Chicago and varied from 2000 residential units to one mega-tall building with 215 floors. The result is that 34 to 58 storey buildings represent the category of structures with maximum efficiency, considering the carbon life cycle and the embodied energy for the hypothesis assumed in those studies. The number of floors may change according to local features such as energy production, local climate, city master plan, public transport, to name a few. However, it remains

the conclusion that tall buildings represent a sustainable solution and that they achieve a point of maxima for this efficiency at a certain height.

This thesis will discuss the technical feasibility and the cost-effectiveness of the verticalization along its axis of investigation, reaching more accurate results in order to achieve an optimal design, allowing the reduction of used material and, therefore, the embodied energy of tall buildings' structures, which may represent nearly 25% of the overall energy use of an efficient tall building (DREW ET AL., 2014).

1.1.2 TECHNICAL AND ENVIRONMENTAL CONTEXT (SÃO PAULO, BRAZIL)

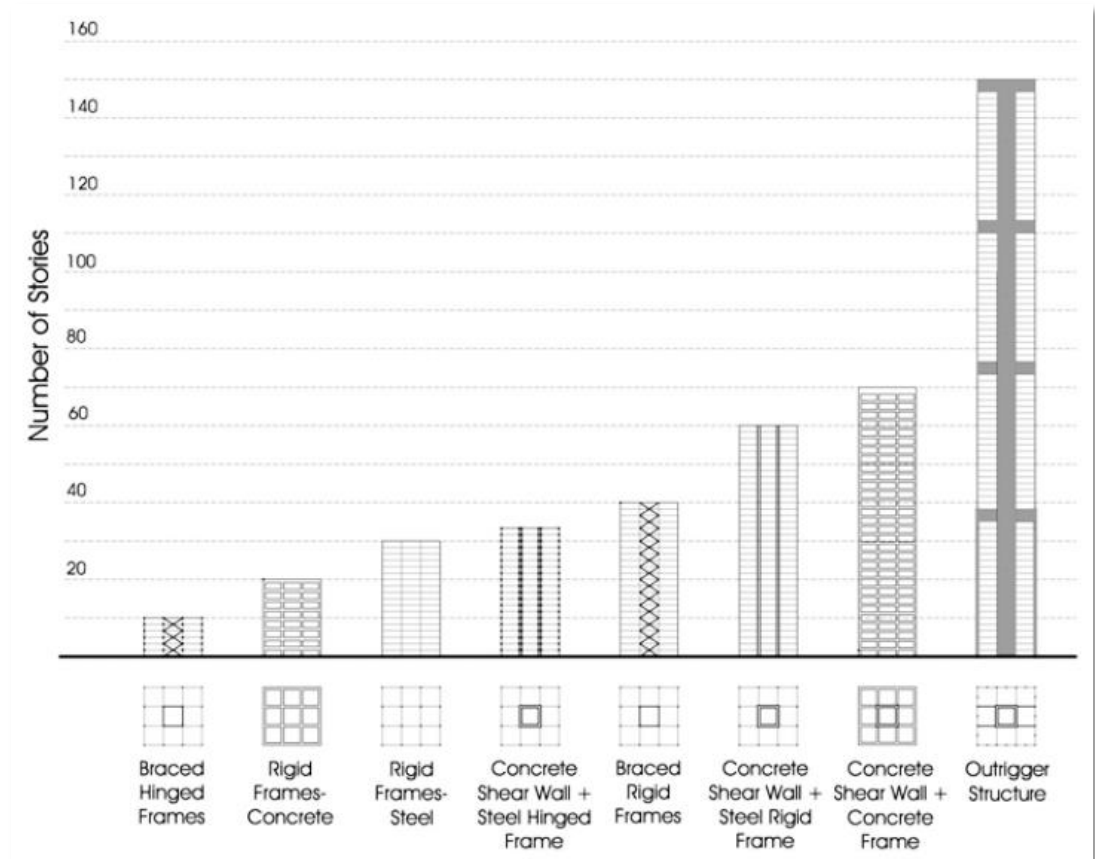
The structural system used in a tall building must fulfil several requirements to be selected as the structural solution to carry the gravity and horizontal loads down to the foundation level. These requirements include comfort (spans, mostly) and cost (most important factor). Needless to say, the structural system must take into consideration site factors such as the foundation soil and the most relevant horizontal loads (seismic loads and/or wind loads) to comply with the safety requirements of the national building codes (SARKISIAN, 2012).

When wind loads govern the structural system design, a different kind of verification takes place in the study: human comfort in tall buildings subjected to wind-induced motion. This kind of study is usually performed with the use of specialized wind tunnel facilities, and the particularities of such experimental analysis, precisely the criteria used to discuss the results, compose an important part of this thesis and are going to be explored later in this chapter.

Wind loads may govern structural design even in seismic areas, where the design often aims at lighter and less stiff structures making them more sensitive to wind-induced excitations. Therefore, serviceability during wind-induced motion may be an issue for tall buildings even in strong seismic areas.

The structural system is highly dependent on the building height/number of stories, since it is also strongly dependent on the lateral forces acting on it. *Figure 1.1* shows the structural systems for several building heights and different structural materials.

Figure 1.1 – Practical height limits of structural systems.



Source: Ali and Moon (2007).

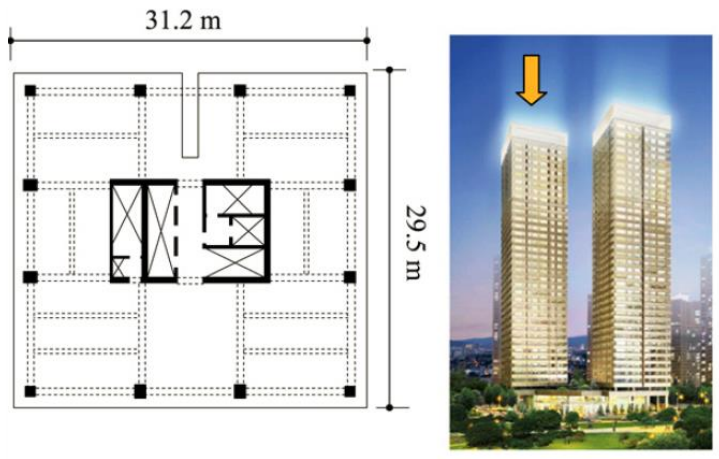
The demand for commercial buildings in the last decades has increased and significantly (ALI and MOON, 2007). This kind of structure requires structural systems with longer spans to provide different office layouts with greater area (comfort) and enough space for service areas (stairs, elevators, restrooms, and shafts).

Allied to these geometrical requirements, the master plan of the City of São Paulo defines a fixed occupation rate of the terrain and together they limit the number of stories to 45-50 in some parts of the urban area. On the other hand, in some regions of the city, due to heavy helicopter traffic, the air space control limits the maximum building height to approximately 130m, which leads to nearly 32-storey buildings (for a storey height of 4.0m).

According to [Figure 1.1](#), these numbers of stories (45-50 and 32) can be successfully supported by a structural system composed by a shear wall with a steel frame (for 32-storey buildings), or a shear wall with a concrete frame (for 50-storey

buildings). Sarkisian (2012) suggests the same structural systems for the same number of stories and proposes the use of shear walls in the central portion of the building around the service areas and steel/concrete columns in the façade of the building. *Figure 1.2* shows a possible layout for this type of structural system.

Figure 1.2 – Example of structure with central concrete core.



Source: Kim et al. (2009).

This thesis studies two tall buildings in the city of São Paulo with 37 and 51 stories. Their structural systems are very similar to those previously described: shear wall with steel gravity columns for the 37-storey building, and shear wall with a concrete frame for the 51-storey building. These buildings will be presented in more details later, in *Chapter 7*.

1.1.3 NORMATIVE CONTEXT

The Brazilian wind code NBR6123-1988 (presently under review) provides the necessary tools to predict wind loads on multi-storey buildings. However, as any normative code, it has its limits of application and cannot address all issues involved in tall-building design due to a number of reasons.

Wind codes around the world specify the wind speed profile for different terrains, topographies and return periods. Nonetheless, no wind code can predict wind interaction with the structures in the proximity and its effects in the studied tall building. NBR6123-1988 is no different and its procedures are not detailed enough when the project requires scale models of the surroundings of the future construction to predict wind interaction with a complex geometry, usually found in dense urban

areas. These models are part of the procedure of Wind Tunnel Testing (WTT) and are illustrated in *Figure 1.3*.

Figure 1.3 – Model of the surroundings of a Tall Building (Shanghai Tower).



Source: Irwin et al. (2013).

Other contributing factor for the shortcomings of national standards is the dynamic nature of the load. *Most of the investigation carried out in this thesis addresses this weak point.* The dynamic analysis of the structure requires the knowledge of a series of specific data:

- Dynamic data of the wind load;
- Natural frequencies and modes of vibration of the building;
- Damping characteristics of the building.

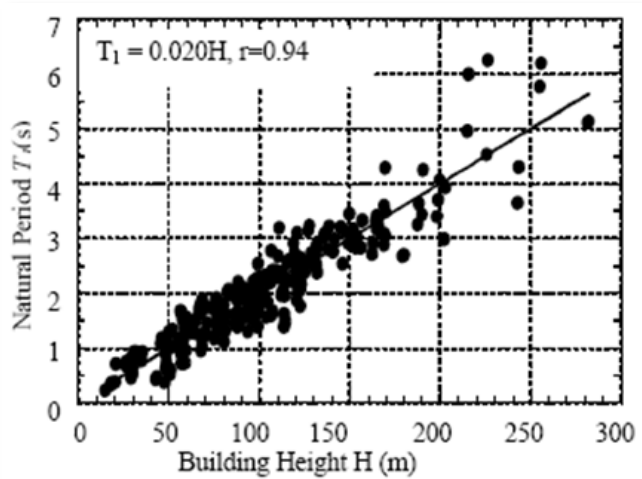
Dynamic data of the wind load is a vague term that covers a wide set of data, to name the most important ones: turbulence profile acting on the building's façade, spatial distribution of loads on the façade, and spectral data of the turbulent wind.

The national standards, derived from intensive studies with research institutions, benchmark with wind tunnel facilities and field data gathering, allow the engineer to access these data in a simplified way, using charts and empiric formulas. Once again, these are only general data, suitable for simpler building shapes and terrain geometry. When the tall building presents complex façade and/or surroundings, the structure is subjected to effects impossible to predict using general

empiric data only. These effects include crosswind loads, torsional effects, vortex-induced vibrations, buffeting, and channelling that can only be assessed with an appropriate WTT.

The prediction of natural frequencies using formulations from national standards is based on regression curves from data gathered on a specific region or country. Each country has its own environmental hazards (hurricanes, strong winds, earthquakes, etc.) and its own economic and cultural issues to deal with. Therefore, each specific region or country will have a set of different structural solutions available, according to its know-how, necessity or purchasing power. Consequently, the structural engineering problem of finding the building's natural frequencies somehow becomes related to the building's construction culture in the studied region. In conclusion, for a given building height, several different structural systems can be used and a wide range of natural frequencies is possible for it. *Figure 1.4* shows the dispersion of data around a regression curve. One might notice in this figure that the lower the building's natural frequency prediction (or, alternatively, the higher the natural period is), the greater the dispersion.

Figure 1.4 – Building height vs. natural period (Steel-Buildings).



Source: Tamura (2007).

In addition, predictions from national building codes of other dynamic features of the structure, such as mode shapes, are restricted to the first mode of vibration, whilst a complete dynamic assessment of a tall building subjected to wind-induced vibrations requires a multimodal approach (ROSA ET AL., 2012). The

complete explanation about mode shapes for tall buildings and multimodal approach will be provided in [section 1.3.2](#) and in [Chapter 2](#), respectively.

However, one of the biggest issues of the dynamic approach is the structural engineers' common practice of using equivalent static loads. Several building codes provide methodologies to assess wind-load effects on tall buildings with equivalent static loads instead of carrying out a dynamic analysis. When it comes to defining the Ultimate Limit State (ULS) of the structure, these equivalent static loads may provide an adequate prediction of the building's response. Nonetheless, when it comes to multimodal analysis for Service Limit State (SLS), such as the building's deflections, angular speed or accelerations, the static approach is not adequate, as it doesn't provide results with enough details to assess these building responses.

The constructions studied in [Chapter 7](#) fall into the “tall building” category of structures, according to CTBUH criteria, due to their height and surroundings. Relatively to local context, their height surpasses the neighbouring constructions and the buildings' surroundings present a fair amount of complexity. Therefore, per CTBUH criteria for WTT of tall buildings, specific studies in wind tunnel facilities are recommended for these projects (IRWIN ET AL., 2013).

1.1.4 MOTIVATIONS

In today's context of big cities, the category of tall building construction is quickly gaining ground due to environmental and economic issues. These new constructions require an extensive multidisciplinary knowledge to make them feasible and current national standards alone are not suitable for this category of structures due to the reasons abovementioned, leaving a great deal of responsibility to a multidisciplinary group of areas of study: structural engineering, wind engineering and comfort assessment. At this point, it is interesting to recall Davenport's chain of wind loading, shown in [Figure 1.5](#).

Figure 1.5 – The Alan G. Davenport chain of wind loading.



Source: Irwin et al. (2013).

Each link of this chain represents a step of the work of the wind engineer in order to assess wind loads on structures. This thesis will discuss these links with a focus on tall buildings.

The “wind climate” link gathers field information from stations (usually located at airports) and associates them with procedures from local wind codes to provide a suitable assessment of the wind speed distribution and directions for design purposes. The next link, “influence of the terrain,” represents the surroundings of the building along with the terrain roughness, followed by a link (“aerodynamic effects”) representing the aerodynamics of the building’s façade and its interferences with nearby structures (IRWIN ET AL., 2013).

Most of the work of this thesis resides in the next two links. The “dynamic effects” link is related to the dynamic evaluation of the wind-induced response. This link requires a deep interaction between the structural engineer and the wind engineer, as this is the link that requires the dynamic approach instead of the equivalent static loading and which gathers the greatest amount of dynamic data from both disciplines (i.e., natural frequencies, mode shapes, dynamic loads on the building’s façade) to be converted into the building’s dynamic response. The subsequent link is related to the criteria used to assess the building’s response and evaluate the comfort/safety level.

In these links, the probability to “break the chain” due to a misinterpretation of data is bigger, since they present a great deal of interface from different disciplines that have a partial or limited understanding of what each other ensures.

This thesis focuses on the understanding of the set of criteria of each discipline, in the use of these data to perform a tall building’s motion assessment, and the impact of each criterion on the final motion assessment. Hopefully, this work will bring a better understanding throughout these areas of study and improve the precision of the design procedure.

1.1.4.1 *Specifics about the objects of study*

Latest advances in structural materials, including 65psi (450MPa) steel, high-strength concrete, and new composite structures allow for a great reduction in the use of material for tall buildings (ROSA ET AL., 2012; SARKISIAN, 2012). These

improvements enable both slender structures and slender structural elements, which lead to an overall reduction of the stiffness of the building.

These new materials are applied to the structural systems discussed in this thesis: concrete core with a steel/concrete frame. And these structural systems are commonly used for tall-building design and often present fundamental modes of vibration with a behaviour very similar to a cantilever beam (WU ET AL., 2007; SARKISIAN, 2012).

Moreover, these structural systems often present important torsional modes of vibration, since the structural elements that resist horizontal loads are mostly concentrated in the concrete core. This concentration leads to a shorter lever arm to resist torsional moment originated from wind loads and/or inertial loads, enabling the presence of torsional modes of vibration with lower natural frequencies.

For these structures, the number of natural frequencies under 1.0Hz tends to be greater, making them more susceptible to dynamic effects from the wind loads (ROSA ET AL., 2012).

These circumstances leverage the importance of SLS studies of tall buildings for comfort assessment *when compared to ULS*, because:

- Lower natural frequencies for higher modes of vibration allow higher modal contribution in the dynamic analysis;
- Higher modal contribution is more effective to increase building accelerations (more related with SLS) than it is to increase displacements (more related to ULS) (ROSA ET AL., 2012);
- Cantilever behaviour, usually presented by shear walls, features higher displacement for tall structures than moment frames and, consequently, higher accelerations;
- Users are highly susceptible to torsional acceleration, since it might exaggerate the feeling of movement for them due to visual cues (ISO10137, 2007);
- Torsional accelerations can increase linear accelerations in the perimeter of the building floor (HANSEN ET AL., 1973; ROSA ET AL., 2012) (see *Figure 1.20*).

It is important, however, to remind that SLS studies only make sense when strength criteria (ULS) are already met (SARKISIAN, 2012). On the assumption that ULS conditions are satisfied for the objects of study, this thesis will address structural modelling, dynamic effects, and comfort criteria (SLS).

The last obstacles in the SLS verification are the *uncertainties of the user's threshold of comfort*. When one executes a verification of strength criteria, the uncertainties of the applied loads, of the structural model used in the analysis, and of the strength of the materials are taken in consideration through a reliability analysis. The practical outcome of this reliability analysis is the set of factors given by each building code to amplify design loads and/or to reduce the strength of structural materials. The conceptual result is: when correctly applied, these factors help to minimize the risk of structural failure to a level considered acceptable by society, allowing semi-probabilistic approaches such as the *allowable stress format* or the *load/strength factor* (SCHNEIDER, 2006).

The human comfort assessment, on the other hand, lacks the same consistency presented by ULS analysis for the strength of structural members. The explanation for this inconsistency is mainly a result of the great number of inexact variables involved in the problem, such as: gender, body posture, expectancy of movement and fear triggered by others, to name a few (TARANATH, 2012). In addition, each individual will have a different set of variables, greatly increasing the dispersion around a given average value. This scenario narrows the object of study for this thesis to "*comfort assessment of multi-storey slender tall buildings*", due to the importance of serviceability verifications for this category of structures.

1.2 INTRODUCTION TO WIND LOADS ON TALL BUILDINGS

1.2.1 PLANETARY BOUNDARY LAYER, WIND PROFILE AND TURBULENCE

The planetary boundary layer is the region of the troposphere directly affected by the presence of the surface of the earth with driving forces including flow modifications due to topography changes, heat transfers and water evaporation. Whilst the driving forces push the wind, the earth's terrain roughness slows the wind at lower heights. The transfer of momentum to the boundary layer occurs through the turbulent shear stress and is better depicted in *Figure 1.6*, along with the wind

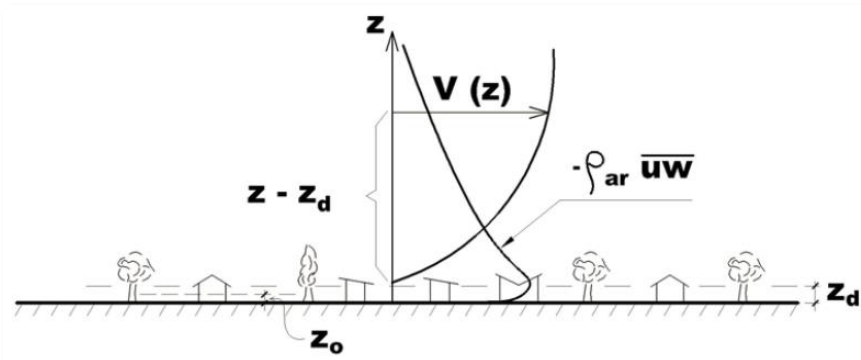
profile and the altitudes that feature the boundary layers (LOREDO-SOUZA ET AL., 2004).

This shear stress defines three distinct regions in the boundary layer (LOREDO-SOUZA ET AL., 2004):

- Superficial layer: it is where the values of the flow and stress " $\rho_{ar}\overline{uW}$ " vary in less than 10% of their average value;
- Interfacial layer: it is a sub-layer within the superficial layer, where the molecular transport prevails over the turbulent one. It is characterized by stagnation zones among the obstacles, which in the big cities are designated by trees and constructions and its height is " z_d " (see [Figure 1.6](#));
- Ekman's layer: it is the layer where the shear stress decreases to zero in the gradient height " z_g ".

The gradient height may vary according to the surface roughness length and the wind speed; synoptic storms with high wind speeds present boundary layer thicknesses between two and three kilometres (LOREDO-SOUZA ET AL., 2004; IRWIN ET AL., 2013).

Figure 1.6 – Wind profile, turbulent shear stress and featuring altitudes.



Source: Loredo-Souza et al. (2004).

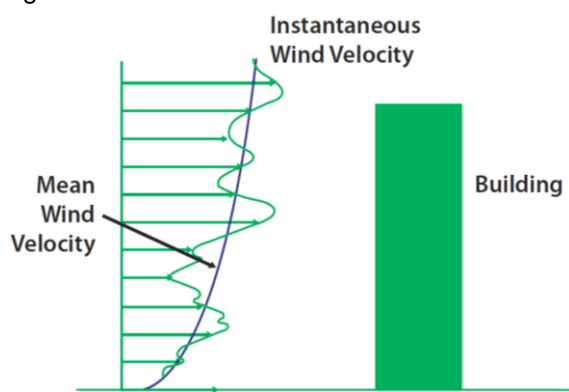
Synoptic winds and synoptic storms are terms used to define the standard boundary layer profiles in the wind-related events, in which there is an increasing wind speed for higher altitudes in the range of the gradient height (see [Figure 1.6](#)). Non-synoptic winds, such as tornadoes and thunderstorms, pose no structural risk for tall buildings, since these phenomena: (a) present a maximum wind speed well

below the height of this kind of structure; (b) present relatively short duration to impose structural dynamic risk (as it will be explained later in this section); or (c) present an spatial extent so small that the probability of a direct hit is also very small and can be neglected when the overall reliability scenario is taken into consideration. As for cladding loads, these non-synoptic winds might still be considered for the lower part of the building, but not for the dynamic wind load assessment (IRWIN ET AL., 2013).

The wind load acting on a tall building's façade has mean and fluctuating components. The mean speed is averaged about an hour, whilst the fluctuating component is due to the turbulence of the wind. This turbulence can be originated by the terrain roughness and surroundings, and also from the own signature of the turbulence of the building itself (IRWIN ET AL., 2013).

The wind turbulence intensity is calculated by dividing the standard deviation of the wind speed fluctuations by the mean wind speed. It usually assumes values in the range of 10 to 30% near the earth's surface (LOREDO-SOUZA ET AL., 2004; IRWIN ET AL., 2013), and it is strong enough to provide a uniform temperature to the wind mixture, suppressing convective effects and allowing an adiabatic approach to wind load studies in WTTs (LOREDO-SOUZA ET AL., 2004; ASCE-2005).

Figure 1.7 – Wind Profile and wind turbulence: elevation of the building.

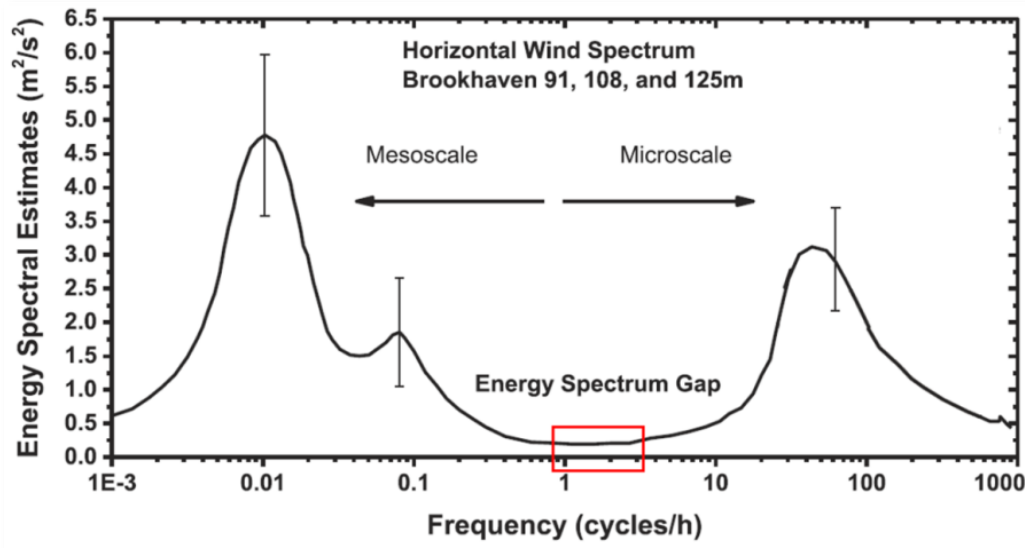


Source: Irwin et al. (2013).

The time scale of the wind turbulence and of the mean wind speed can be better explained using the Van der Hoven power spectrum, clarified in [Figure 1.8](#). In this power spectrum, one can see a spectral “gap” around 1-3 cycles/hour, meaning

that one can expect a steady behaviour for the mean wind speed for time intervals of 20 minutes to one hour (HANSEN ET AL., 1973).

Figure 1.8 – Van der Hoven Power Spectrum.



Source: Adapted from Van Der Hoven (1957).

The turbulent fluctuations exist at the peak indicated in the region of “microscale” climate behaviour. This region shows a considerable amount of energy within a time scale in the order of seconds, which takes place around the natural period of tall buildings, 1s to 10s (CHANG, 1973).

1.2.2 DYNAMIC WIND LOADS

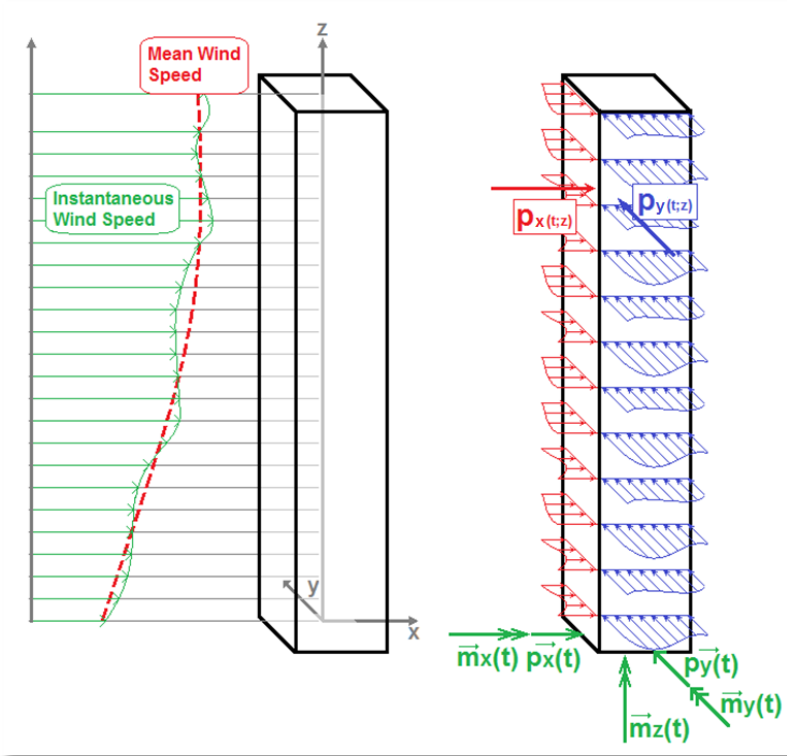
1.2.2.1 Along-wind, cross-wind and torsional loads

Since the natural periods of vibration of tall buildings are quite long, the wind event duration to be considered in design should be at least a few minutes to approximately one hour (IRWIN ET AL., 2013).

These dynamic loads are often expressed through the power spectral density of the loads acting on the building’s façade. These loads present three main directions: along-wind, cross-wind and torsional values.

Figure 1.9 illustrates these wind loads due to the wind flow in the along-wind (x) direction. The wind speed is a function of time “t” and height “z”. The pressure on the building’s façade is a function of space (x, y and z) and time as well.

Figure 1.9 – Wind profile, pressure distribution, and base forces on the building.



Source: Author.

To apply these loads on the structure using a multi-storey tall building approach, the pressure should be integrated on the façade surface corresponding to the floor height. Then, each story “ ℓ ” would present three load components: one force “ $p_{x,\ell}(t)$ ” in the along-wind direction, one force “ $p_{y,\ell}(t)$ ” in the cross-wind direction, and one yaw moment “ $m_{z,\ell}(t)$ ” about the reference axis of the building, commonly referred to as “torsional moment” in the literature.

The torsional component can be interpreted as the displacements around the reference vertical axis of the resulting forces in each direction for each floor. These forces are represented by [Figure 1.10](#) and calculated by eq. (1.1) to (1.5).

$$\sum_{\ell=1}^m p_{x,\ell}(t) = p_x(t) \quad (1.1)$$

$$\sum_{\ell=1}^m p_{y,\ell}(t) = p_y(t) \quad (1.2)$$

$$\sum_{\ell=1}^m z_{\ell} p_{x,\ell}(t) = m_y(t) \quad (1.3)$$

$$\sum_{\ell=1}^m z_{\ell} p_{y,\ell}(t) = -m_x(t) \quad (1.4)$$

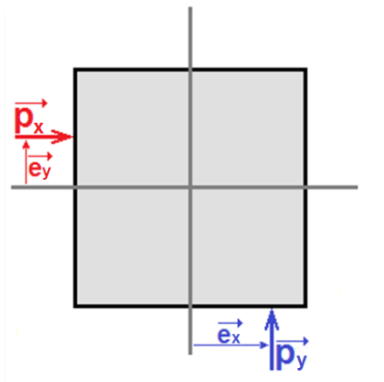
$$\sum_{\ell=1}^m e_{x,\ell} p_{y,\ell}(t) - \sum_{\ell=1}^m e_{y,\ell} p_{x,\ell}(t) = m_z(t) \quad (1.5)$$

where:

- z_{ℓ} stands for the story height above the ground;
- $e_{y,\ell}$ stands for the resultant along-wind force eccentricity on the “ ℓ^{th} ” floor;
- $e_{x,\ell}$ stands for the resultant cross-wind force eccentricity on the “ ℓ^{th} ” floor.

“ $p_x(t)$ ”, “ $p_y(t)$ ”, “ $m_y(t)$ ”, “ $m_x(t)$ ” and “ $m_z(t)$ ” are, respectively: base shear force (along-wind), base shear force (cross-wind), base bending moment (along-wind), base bending moment (cross-wind), and torsional moment at the base. These five measures represent the acting forces on the base and they are essential to perform several verifications for WTT.

Figure 1.10 – Wind forces and eccentricities acting on the building’s façade.



Source: Author.

Cross-wind excitations and torsional loadings can occur in a building for several reasons, such as asymmetric shape, asymmetric wind flow due to the surrounding area of the building, and turbulence effects both from the surroundings (buffeting) and naturally from the atmospheric boundary layer (IRWIN ET AL., 2013).

Normally, the peak along-wind force, cross-wind force, and torsional moment do not happen at the same time. This feature brings to attention one more time the reason of performing WTT, such as high-frequency-pressure-integration or high-frequency-force-balance, to find suitable combinations of these loads (IRWIN ET AL., 2013).

1.2.2.2 Power spectral density (PSD), structural admittance, and duration of wind events

Using Fourier transforms “ $F_p(\bar{\omega})$ ” in the time history of these forces: “ $p_{x,\ell}(t)$ ”, “ $p_{y,\ell}(t)$,” and “ $m_z(t)$,” the PSD functions “ $S_p(\bar{\omega})$ ” can be obtained for each one of them (CLOUGH AND PENZIEN, 2010):

$$S_p(\bar{\omega}) = \frac{F_p(\bar{\omega})}{2\pi} \quad (1.6)$$

where “ $\bar{\omega}$ ” is the set of harmonic angular frequencies of the Fourier transforms and PSD functions.

This approach to calculate the wind loads acting on the building is part of the procedure called *frequency-domain analysis*. This kind of analysis is commonly used after the WTT to assess the building’s dynamic response and will be detailed in *Chapter 2*.

An analysis of the PSD of the wind load or the structure’s response is always useful to achieve a better understanding of the situation regardless of the approach to be used to assess the building dynamic response (frequency or *time-domain analysis*).

In the frequency-domain analysis, the building’s response is obtained by multiplying the PSD functions “ $S_p(\bar{\omega})$ ” by the structural admittance “ $H(\bar{\omega})$ ” squared.

$$H(\bar{\omega}) = \frac{1}{K[1 + 2\xi i(\bar{\omega}/\omega) - (\bar{\omega}/\omega)^2]} \quad (1.7)$$

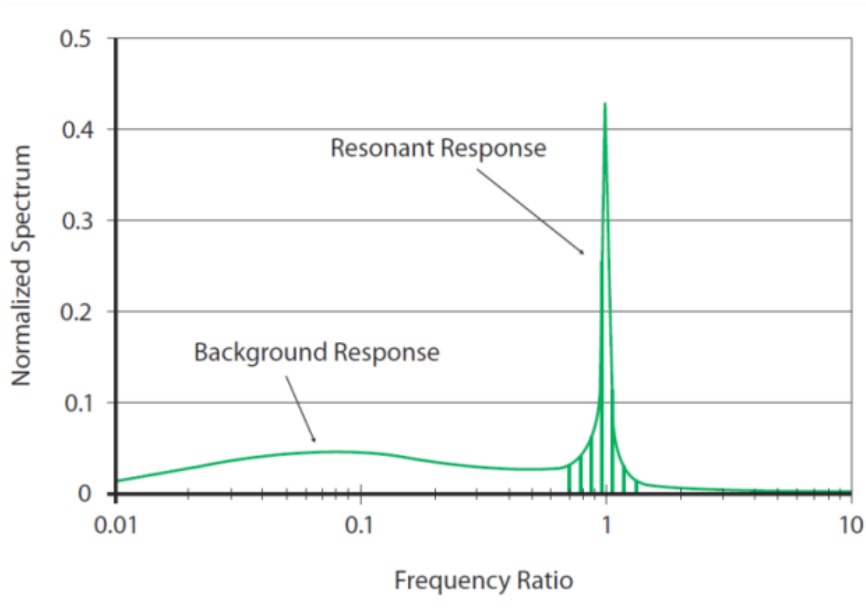
where “ ω ” is the natural frequency of the building, “ K ” stands for the stiffness of the structure, and “ ξ ” is the damping ratio of the structure, usually in the range of 1-3%, depending on type of construction material.

One can observe that when “ $H(\bar{\omega} = \omega)$,” the admittance function assumes the value “ $H(\omega) = 1/(2\xi iK)$ ”. When multiplied by the PSD value “ $S_p(\bar{\omega} = \omega)$ ”, the

result is the static response multiplied by the dynamic amplification of the resonant angular frequency (BLESSMANN, 1988). This method presents concepts that are very close to the current structural engineers approach: *equivalent static loads*, previously discussed.

The final result of the operation between the PSD and the admittance functions is shown in *Figure 1.11*, where two responses can be observed: background response and resonant response. The background response is related to the fluctuating instantaneous wind pressures applied to the building's façade, which present chaotic behaviour over the building height (low correlation) due to the turbulent nature of these fluctuations (IRWIN ET AL., 2013).

Figure 1.11 – Normalized response spectrum of base moment.



Source: Irwin et al. (2013).

The resonant response is caused when these background loads sustain their effect in the buildings surface in frequencies close to the natural frequencies of the building, causing it to move according to its natural modes of vibration. This movement triggers inertial forces of opposite direction to the elastic forces provided by the structure. These forces present a perfect correlation within the building height and are a function of the building's natural frequency, mass distribution, and mode deflection shape. For tall and slender buildings, these forces control the building motion over the background loads (IRWIN ET AL., 2013).

The duration of these background loads must have a minimum value in order to introduce enough energy into the system to trigger the inertial forces of the tall building. This minimum duration is the time span above which the system has already dissipated the introduced energy with structural damping or other energy dissipation device. For the sake of an argument, one can analyse the exponential decay function “ $f(\Delta t)$ ” of the amplitude of movement of each wind load impulse, given in eq. (1.8):

$$f(\xi; \omega; \Delta t) = e^{-\xi\omega\Delta t} \quad (1.8)$$

This is the decay formulation for under-critically damped systems (typical for tall building structures). Considering the typical range of natural periods ($1s < T < 10s$) and damping ratios ($1\% < \xi < 3\%$), the maximum time span for an impulse caused by a wind load to be reduced to 1% of its value is around 733s – one might observe that the amplitude reduction to 1% means a motion energy reduction to 0.01%. It means that the duration of the synoptic wind event must be at least around 12 minutes to validate a non-transient and ergodic system hypothesis, used in frequency-domain analysis. This 12-minute duration can be reduced according to design data, like the natural frequency and the overall damping of the system.

It is not uncommon to find in the literature wind events lasting more than one hour (HANSEN ET AL., 1973; DENOON ET AL., 2000). In these events, the common procedure takes into consideration the hour in which the dynamic loads are most severe, so as to assess the building’s dynamic response. This one-hour time span can be subsequently divided into several smaller fractions of time (still larger than the minimum duration) to perform the dynamic analysis in each one of them.

It is important to note that the steady behaviour of the mean wind speed, ranging from 20 minutes to one hour (from the Van Der Hover power spectrum), is larger than the time span required to consider the hypothesis of the ergodic system.

1.3 INTRODUCTION TO STRUCTURAL DATA OF TALL BUILDINGS

The structural data was informally presented in the last section, making clear the importance of the structural engineering in the assessment of the response of wind-induced motions in tall buildings. These data will be formally presented in this

chapter with a specific approach for structures of multi-storey tall buildings subjected to WTT. These data can be summarized as:

- Natural frequencies;
- Mode shapes or mode deflection shapes;
- Mass matrix;
- Damping of the system.

1.3.1 NATURAL FREQUENCIES – GENERAL CASE

The equations of motion for free vibrations of undamped multi-degree-of-freedom systems are (CLOUGH AND PENZIEN, 2010):

$$[M]\{\ddot{u}(t)\} + [K]\{u(t)\} = \{0\} \quad (1.9)$$

Assuming the response is harmonic (the same behaviour of the single degree of freedom system) and synchronous, the *characteristic-value* problem arises (CLOUGH AND PENZIEN, 2010):

$$([K] - \omega^2[M])\{\hat{u}\} = \{0\} \quad (1.10)$$

where “ $\{\hat{u}\}$ ” corresponds to the modal shape of the vibrating system. The system accepts non-trivial solution only when:

$$|[K] - \omega^2[M]| = 0 \quad (1.11)$$

The eq. (1.11) is called *frequency equation* of the vibrating system and it has “n” real positive roots (“ ω_1 ” to “ ω_n ”), one for each possible mode of vibration (CLOUGH AND PENZIEN, 2010), where “n” is the number of degrees of freedom of the model. The mode of vibration with the lowest value of angular frequency is called the first (or fundamental) mode, the next higher value is the second mode, and so on.

1.3.1.1 Tall buildings’ natural frequencies

Tall buildings have the first natural frequencies varying from about 0,1Hz to 1Hz (CHANG, 1973). Several authors and normative codes have tried to predict the first natural frequency of a tall building (TAMURA, 2007; NBR6123-1988; ASCE-88), mostly based on the building height and the type of material and/or structural system (see [Table 1.1](#)).

$$f_j = \omega_j / 2\pi \quad (1.12)$$

Table 1.1 – Natural frequencies for tall buildings.

Structural System / Material	Source	f_1 (Hz)
Reinforced Concrete – Framed structure	NBR6123-1988	50/H
Reinforced Concrete – Shear Wall	NBR6123-1988	59/H
Steel – Framed structure	NBR6123-1988	$3.45/(\sqrt{H} - 1.38)$
Steel Buildings	TAMURA (2007)	42/H
Reinforced Concrete Buildings	TAMURA (2007)	56/H
Steel Buildings	ASCE-88	$11.8/H^{0.75}$
Reinforced Concrete Buildings	ASCE-88	$16.4/H^{0.75}$

Source: Author.

where:

- f_j stands for the j^{th} natural frequency of the building, in Hz;
- f_1 stands for the first natural frequency of the building, in Hz;
- H stands for the height of the building, in meters.

Sarkisian (2012) presents the first and the second natural frequencies for a set of tall buildings. Using the estimators presented in [Table 1.1](#), a comparison is made in [Table 1.2](#), illustrating that the assessment of the first natural frequency through normative formulas may lead to inaccurate results.

[Table 1.2](#) also shows that some authors' formulations get close enough to the real natural frequencies. This is the case of Tamura's (2007) natural frequency assessment of 0.135Hz and 0.114Hz for the Al Hamra Tower (0.133Hz) and the Jinta Tower (0.122Hz), respectively, whilst ASCE-88 predicted natural frequencies of 0.178Hz and 0.140Hz, respectively.

In other cases, normative codes may provide closer predictions. ASCE-88's natural frequency prediction for the Jinao Tower is 0.197Hz (compared to 0.200Hz), whilst Tamura (2007) and NBR6123-1988 predict 0.238Hz and 0.247Hz, respectively.

Finite-element (FE) models are not always as precise as they might look when it comes to finding out the natural frequencies of a building. Kim et al. (2009) found discrepancies of up to 33% between measured natural frequencies of a tall

building and the respective FE model. Several modelling criteria had to be used to correctly assess the buildings' natural frequencies.

Table 1.2 – Comparison: first natural frequencies measured and estimated.

Building	Type/Material	Height	f_1 (Hz)			
			Measured	NBR6123-1988	TAMURA (2008)	ASCE-88
Jin Mao Tower	Mixed	421	0.175	0.180	0.133	0.127
Burj Khalifa	Reinforced Concrete	828	0.091	0.071	0.068	0.106
Al Hamra Tower	Reinforced Concrete	415	0.133	0.142	0.135	0.178
Goldfield Int'l Garden	Reinforced Concrete	150	0.227	0.393	0.373	0.383
Jinta Tower	Steel	369	0.122	0.194	0.114	0.140
Jinao Tower	Mixed	235	0.200	0.247	0.238	0.197

Source: Author.

It is not the finite element method itself, but the modelling criteria used in the FE model that is responsible for the occasionally poor correlation with measured natural frequencies. These modelling criteria, when properly defined, can greatly improve the precision of the natural frequency estimation and they will be discussed in [Chapter 3](#).

The natural frequency estimation of a tall building has a great influence in the final response calculated by the wind engineer. The structural engineer has all of the tools to properly assess the natural frequencies of the building and does not make so much use of it directly. The wind engineer, on the other hand, must make use of these data and has very little control of the criteria used to evaluate the natural frequencies of the building, regardless of how accurate/inaccurate they might be.

It is not uncommon for WTT to consider fixed ratios to increase the natural frequencies given by the structural engineer to perform their dynamic calculations. Such increase might reach up to 30%, based on field measurements from the wind tunnel facility or from benchmark studies. Sensitivity for decreased natural frequency may also be analysed in WTT.

A significant problem in the interface between the structural and the wind engineers in the Davenport's chain of wind loading lies in this subject, precisely in the link called "Dynamic Effects". The wind tunnel facility doesn't know if the structural

engineer is using suitable modelling criteria and could therefore overestimate the natural frequencies by multiplying them by a fixed ratio. Alternatively, the structural engineer might not be using these criteria in the FE model, and by neglecting the fixed ratio for the natural frequencies the wind engineer might be underestimating them.

1.3.2 MODE SHAPES – GENERAL CASE

Once the natural frequencies are correctly assessed through eq. (1.11), the eq. (1.10) can be rewritten as:

$$[E]^j \{\hat{u}\}_j = \{0\} \quad (1.13)$$

where:

$$[E]^j = [K] - \omega_j^2 [M] \quad (1.14)$$

The eq. (1.13) can generate “n” indeterminate systems of equations, one for each mode and frequency of vibration. Due to their indetermination, it is impossible to know beforehand the amplitude of vibration, since it depends on the initial conditions. The shapes of vibration, however, can be determined by solving each system of equation in terms of any non-null degree-of-freedom (DOF) of the system (CLOUGH AND PENZIEN, 2010).

If the unitary value is given to the first element of displacement, provided it does not correspond to a modal node, each mode shape can be written as:

$$\{\hat{u}\}_j = \{\Phi\}_j = \begin{Bmatrix} 1 \\ \Phi_{2j} \\ \vdots \\ \Phi_{nj} \end{Bmatrix} \quad (1.15)$$

and the expanded form of eq. (1.13) becomes (CLOUGH AND PENZIEN, 2010):

$$\begin{bmatrix} e_{11}^j & e_{12}^j & \cdots & e_{1n}^j \\ e_{21}^j & e_{22}^j & \cdots & e_{2n}^j \\ \vdots & \vdots & \ddots & \vdots \\ e_{n1}^j & e_{n2}^j & \cdots & e_{nn}^j \end{bmatrix} \begin{Bmatrix} 1 \\ \Phi_{2j} \\ \vdots \\ \Phi_{nj} \end{Bmatrix} = \begin{Bmatrix} 0 \\ 0 \\ \vdots \\ 0 \end{Bmatrix} \quad (1.16)$$

Subsequently, each system can be solved:

$$\begin{Bmatrix} \Phi_{2j} \\ \vdots \\ \Phi_{nj} \end{Bmatrix} = \begin{bmatrix} e_{22}^j & \dots & e_{2n}^j \\ \vdots & \ddots & \vdots \\ e_{n2}^j & \dots & e_{nn}^j \end{bmatrix}^{-1} \times \begin{Bmatrix} -e_{21}^j \\ \vdots \\ -e_{n1}^j \end{Bmatrix} \quad (1.17)$$

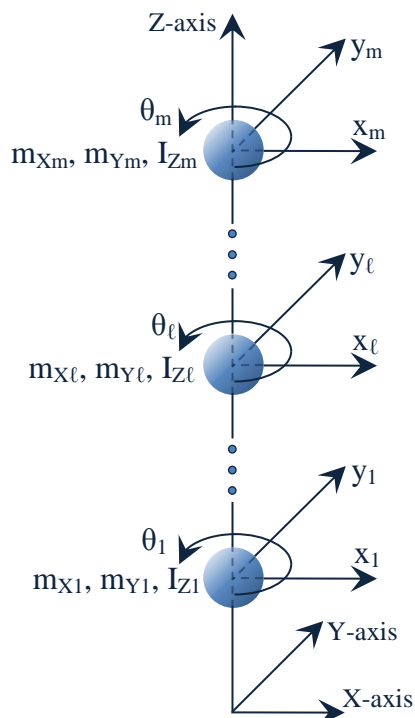
Each vector “ $\{\Phi\}_j$ ” represents a different mode shape and the matrix composed by the “ n ” mode shapes is represented by “[Φ]”:

$$[\Phi] = \begin{bmatrix} \Phi_{11} & \dots & \Phi_{1n} \\ \vdots & \ddots & \vdots \\ \Phi_{n1} & \dots & \Phi_{nn} \end{bmatrix} \quad (1.18)$$

1.3.2.1 Tall building's mode shapes and lumped-mass matrix

Intended for the scope of wind effects on tall buildings, a lumped mass system approach can be used to model the dynamic behaviour of the structure (NBR6123-1988; ROSA ET AL., 2012). This approach, based on the rigid floor diaphragm hypothesis, neglects in-plane floor deformations and restricts the motion of each floor to three DOF: translations on X and Y-axis and rotation about the Z-axis of the building (ROSA ET AL. 2012).

Figure 1.12 – Lumped mass model.



Source: Author.

Figure 1.12 shows a lumped mass model of a building with “m” floors. The lumped-mass matrix of the structure is a diagonal matrix formed by the lumped mass sub-matrix of each floor.

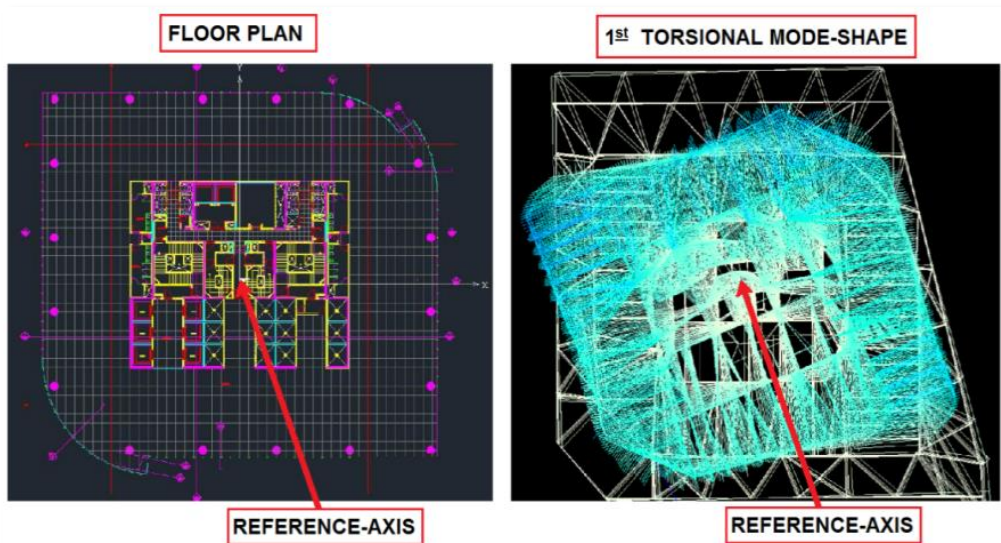
For the ℓ^{th} floor, the lumped mass sub-matrix is (ROSA ET AL. 2012):

$$[M]_{\ell} = \begin{bmatrix} m_{\ell} & 0 & 0 \\ 0 & m_{\ell} & 0 \\ 0 & 0 & I_{z\ell} \end{bmatrix} \quad (1.19)$$

where “ m_{ℓ} ” is the mass of the floor concentrated around the centre of mass, and “ $I_{z\ell}$ ” is the rotational mass moment of inertia about an arbitrary reference axis Z and floor “ ℓ ”. Displacements “ x_{ℓ} ”, “ y_{ℓ} ,” and “ θ_{ℓ} ” refer to the centre of mass of each floor (ROSA ET AL. 2012).

The reference-axis position in-plan is a geometric choice. It should be a convenient position to apply the wind loadings on each floor. In addition, it should be near to a possible “centre of rotation” of the typical floor for the first torsional mode shape. Centre of rotation is a technically unsuitable term to use, since it doesn’t exist for the whole building. It does exist, however, for each floor of the building if one considers a rigid body movement (recall the rigid diaphragm hypothesis). If the stiffness and mass distributions through the building’s floors present a balanced behaviour, the centre of each floor may be aligned along the building’s height. To illustrate the argument, for one of the case studies presented later in [Chapter 7](#) the reference-axis position can be seen on [Figure 1.13](#).

Figure 1.13 – Reference-axis location.



Source: Author.

This location allows the assessment of the mass moment of inertia near the centre of mass of the building. In addition, the applied wind loads on the façades of the building need smaller corrections due to the translation of the applied forces to the reference-axis, since the axis is also close to the geometric centre of the building.

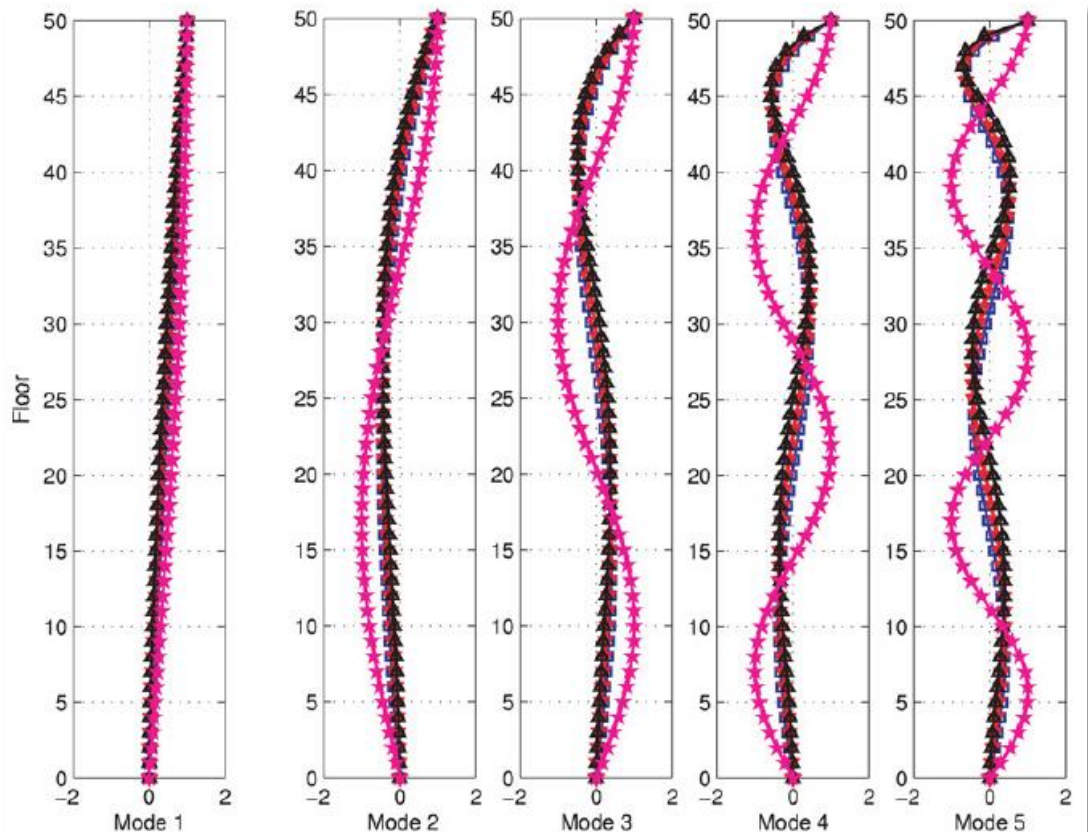
Intended for this method, the mode shapes are condensed in the same way. Only three DOF remain for each floor of the building for each one of the vectors “ $\{\Phi\}_j$ ”.

$$\{\Phi\}_j^T = \{\Phi_{mxj} \quad \Phi_{myj} \quad \Phi_{m\theta j} \quad \dots \quad \Phi_{\ell xj} \quad \Phi_{\ell yj} \quad \Phi_{\ell\theta j} \quad \dots \quad \Phi_{1xj} \quad \Phi_{1yj} \quad \Phi_{1\theta j}\} \quad (1.20)$$

The vector only represents the shape of the vibration and the value of each component is obtained based on the arbitrary amplitude assumed to solve eq. (1.16). Therefore, it can be normalized and, usually, the normalization is made by adjusting the amplitude of displacement to satisfy the following condition (CLOUGH AND PENZIEN, 2010):

$$\{\Phi\}_j^T [M] \{\Phi\}_j = 1 \quad (1.21)$$

Figure 1.14 – Mode shapes of a 50-story tall building.



Source: Huang and Chen (2007).

Figure 1.14 shows the mode shapes of one direction (translation) for a 50-story building. By varying the stiffness of structural elements for each floor, Huang and Chen (2007) were able to find different mode shapes and natural frequencies for the same building. The stiffness variation was assumed to follow a power law over the building's height, with exponents “ β ” equal to 1.00 (blue), 1.25 (red) and 1.50 (black), whilst the pink curve was built using uniform stiffness.

Besides the impact on the natural frequency, it can also bring changes to the lowest mode shapes. The studies conducted in this thesis explore this aspect of the modelling criteria on the mode deflection shapes.

1.3.3 DAMPING – ξ

There are several types of damping that might contribute to a tall building's motion's control. They can be gathered in three main groups: structural damping “ ξ_s ”; damping ratios “ ξ_d ” originated by dampers; and aerodynamic damping “ ξ_a ”. Eq. (1.22) shows the overall damping ratio “ ξ ”.

$$\xi = \xi_s + \xi_d + \xi_a \quad (1.22)$$

Damping ratios are not necessarily structural data because they can be originated either by non-linear effects of structural and non-structural elements of the building (structural damping), or by dampers (TAMURA, 1998). They can also be originated by the building's velocity (aerodynamic damping) and may present significant value for some categories of structures (FERRARO ET AL., 1990; LOREDO-SOUZA, 1998; IRWIN ET AL., 2013).

The structural damping is very hard to calculate and can be assessed through field measurements (WU ET AL., 2007). Building codes usually provide a set of structural damping ratios, one for each structural system type. For example, Brazilian wind code NBR6123-1988 estimates: 1.0% for steel structures, 1.5% for concrete shear walls, and 2.0% for concrete moment frames.

When the overall damping ratio receives contributions from either dampers or aerodynamic damping, the wind engineer's contribution to this parameter becomes clear. This is another case in which an important interaction occurs in the Davenport's chain of wind loading. The structural engineer provides the structural damping whilst the wind engineer completes it with aerodynamic damping. In

collaboration, these two engineers may even implement the design of a damper to mitigate dynamic effects.

Tamura (1998) affirms that there are some advantages in the use of dampers in tall buildings, such as auxiliary damping to improve the structural design and to reduce the uncertainty of the structural damping. He also brings examples of these devices and how they work mathematically. They are:

- Hysteretic dampers: steel dampers, steel joint dampers, lead dampers, friction dampers, and viscous-elastic dampers;
- Viscous dampers: viscous dampers and oil dampers;
- Mass dampers: tuned mass dampers and liquid dampers.

Hysteretic dampers present an amount of stiffness “ K_d ” that must be taken into consideration in the equation of motion for each mode of vibration, along with an equivalent damping “ C_d ” in the control force “ $F_d(t)$ ” assessment (TAMURA, 1998). This solution is composed of several different technologies, including steel dampers, steel joint dampers, lead dampers, friction dampers, and viscoelastic dampers, to name a few. This control force is calculated by:

$$F_d(t) = -[C_d\dot{Y}(t) + K_dY(t)] \quad (1.23a)$$

where “ $Y(t)$ ” and “ $\dot{Y}(t)$ ” are the building’s generalized displacement and generalized velocity, respectively. The generalized displacement, velocity, and acceleration will be explained in [section 2.2](#).

Mass dampers have a mass portion “ M_d ”. Mass dampers might present a viscous damping ratio “ ξ_a ”. Tuned liquid dampers, for example, have the viscous damping originated by friction between the fluids and the container walls, and tuned mass dampers use additional mass inertia effect of an additional mass installed in the building’s structure (TAMURA, 1998). The control force of this kind of damper is given by:

$$F_d(t) = -[M_d\ddot{Y}(t) + C_d\dot{Y}(t)] \quad (1.23b)$$

where “ $\ddot{Y}(t)$ ” is the building’s generalized acceleration.

Finally, viscous dampers and oil dampers use viscous material, where the resisting force is proportional to the building generalized velocity (TAMURA, 1998):

$$F_d(t) = -C_d \dot{Y}(t) \quad (1.23c)$$

The damping devices previously described are categorized as passive damping devices. Active control systems can be used to mitigate or compensate wind forces acting on tall buildings. For that to happen, a precise prediction of the external wind forces “ $p(t)$ ” must occur. Then, active control forces “ $F_d(t)$ ” act by balancing these wind forces according to eq. **(1.23d)** (TAMURA, 1998).

$$F_d(t) = -p(t) \quad (1.23d)$$

The aerodynamic damping “ ξ_a ” plays an important role in some structural motions. Transmission lines might present an aerodynamic damping ratio up to 60% for extreme winds (LOREDO-SOUZA, 1998). For tall buildings, it might represent a reduction of 20% in the final accelerations (FERRARO ET AL., 1990). Aerodynamic damping might also present negative values, creating self-induced movement (such as galloping), or reducing the overall damping ratio (BLESSMANN, 1988). Any reduction in the value of a tall building’s overall damping might cause a noticeable increase to its final acceleration, since the structural damping of this kind of structure is very low (around 1% to 3%).

Structural damping is usually assumed with a constant value in the design stage (WU ET AL., 2007). Several national codes and authors consider an amplitude-dependent damping ratio (AIJ-GEH-2004; WU ET AL., 2007).

Wu et al. (2007) calibrated such amplitude-dependent damping ratios for X and Y axes of movement for the Di Wang Tower. Then, they compared the acceleration results using the amplitude-dependent damping ratio with the acceleration results using constant damping ratios (1%, 2% and 3%) for a wide range of design wind speeds. One of the conclusions was that, for SLS wind loads, a structural damping around 1% showed consistent behaviour with the real scale building motion (with calibrated amplitude-dependent damping ratio).

In the first case study conducted in this thesis (see building A in [Chapter 7](#)), the damping value will be equal to 1.25%. It is the same damping value used by the Boundary Layer Wind Tunnel (BLWT) to perform the dynamic analyses and it is consistent with the results obtained by Wu et al. (2007). For the second case study,

building B, the damping value will be equal to 1.00%, which is the same value used in the WTT, also consistent with the results obtained by Wu et al. (2007).

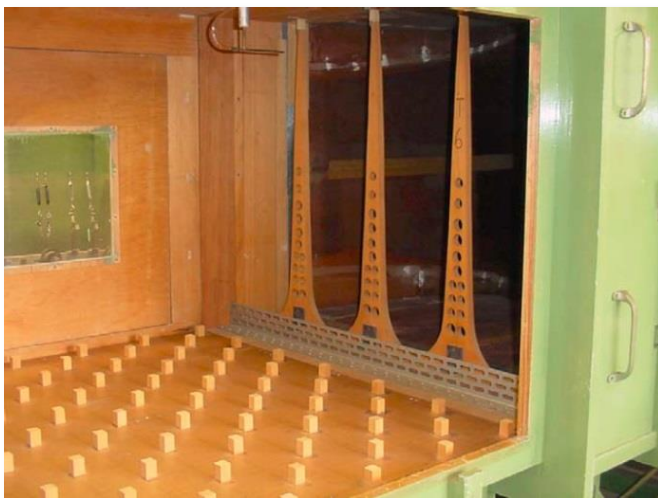
1.4 INTRODUCTION TO WTT OF TALL BUILDINGS

1.4.1 SIMULATION OF THE ATMOSPHERIC BOUNDARY LAYER

The WTT facilities must simulate the main features of natural winds at the studied site in order to provide suitable data on wind-related effects to be applied to the full-scale model of the tall building. The main features were already presented in this thesis and they can be summarized as: vertical distribution of the mean wind speed, intensity of the longitudinal turbulence, and length scale of longitudinal turbulence component (LOREDO-SOUZA ET AL., 2004; ASCE-2005; IRWIN ET AL., 2013).

The simulation of the wind approaching the surrounding model (*Figure 1.3*) is made using long tunnels, usually 2 to 5m wide, with length varying from 15 to 30m. Operating wind speed varies between 10 and 50 m/s in atmospheric pressure (ASCE-2005). There are several techniques to simulate the characteristics of the approaching wind flow, and they usually involve special flow devices at the beginning of the wind tunnel section, followed by elements placed to simulate terrain roughness on the wind tunnel floor (LOREDO-SOUZA ET AL., 2004; ASCE-2005; IRWIN ET AL., 2013).

Figure 1.15 – Spires, barriers and roughness elements.



Source: Loredo-Souza et al. (2004).

The devices in the beginning of the wind tunnel section include spires and barriers and they tend to increase the depth of the boundary layer in the test section, reducing the necessary length of the wind tunnel. The roughness elements on the floor simulate the terrain roughness to the approaching wind (IRWIN ET AL., 2013). *Figure 1.15* illustrates these special flow devices and roughness elements.

The final product of the application of these devices is a wind speed profile for the approaching wind as shown in *Figure 1.7*, with its features adjusted (vertical distribution of the mean wind speed, intensity of the longitudinal turbulence, and the length scale of longitudinal turbulence component, among others). The wind speed profile cannot be simulated over 100% of the wind tunnel's height, i.e., these features do not correspond to a scaled simulation of the atmospheric boundary layer over the entire wind tunnel's height, but they ought to correspond to at least 75% of it (LOREDO-SOUZA ET AL., 2004).

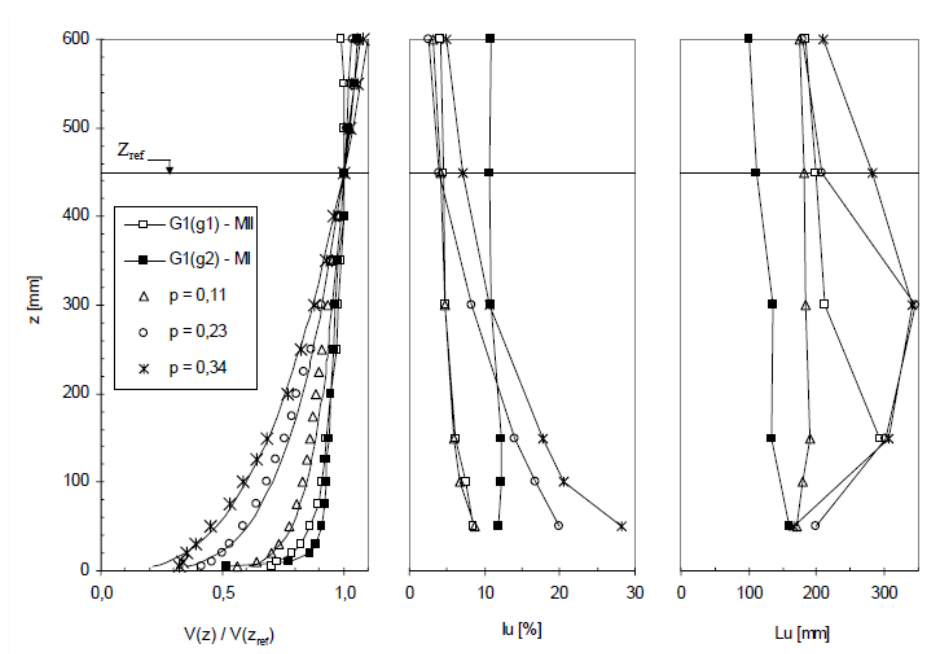
The linear scale of simulation " λ_L " is determined by comparison with real scale data using the only two length components related to wind speed and wind turbulence: macro scale of the longitudinal component of turbulence " L_u " and surface roughness length " z_0 ", previously presented in *Figure 1.6*. Once the linear scale is calibrated with the mean wind speed and with the spectral component of longitudinal turbulence, the other features need only to be checked (LOREDO-SOUZA ET AL., 2004).

Figure 1.16 shows the mean wind speed profile, the longitudinal turbulence intensity and the macro scale of the longitudinal component of the turbulence for five simulated types of wind speed profiles in the *Joaquim Blessmann* wind tunnel, in Porto Alegre-RS, Brazil.

When the approaching wind is properly simulated and calibrated, the remaining wind effects (channelling, buffeting, and shielding) are simulated with surrounding models (see *Figure 1.3*), and the WTT takes place with all the techniques necessary for the study. These techniques are presented in the next section.

This part of the WTT corresponds to the first three links in the Davenport's chain of wind loading (see *Figure 1.5*).

Figure 1.16 – Features of the wind speed profile simulated in the wind tunnel.



Source: Loredo-Souza et al. (2004).

1.4.2 TYPES OF WTT

There are several methods to evaluate wind forces on tall buildings. The three most common are high-frequency-force-balance (HFFB), aero elastic model method, and high-frequency-pressure-integration (HFPI) (IRWIN ET AL., 2013).

There are other studies performed with wind tunnels related to the design of a tall building that are not necessarily related to the evaluation of wind loads, such as pedestrian-level winds, natural ventilation, and cladding loads, to name a few (LOREDO-SOUZA ET AL., 2004; ASCE-2005; IRWIN ET AL., 2013).

Pedestrian-level wind tests are used to measure flow characteristics (speed and direction) at ground level, balconies, and even helipad operations. Results of these tests include the diagnostic of uncomfortable/unsafe zones and mitigation actions, such as wind screens, for example (ASCE-2005; IRWIN ET AL., 2013).

Natural ventilation tests intend to evaluate the wind pressures that drive the ventilation using pressure models (see [Figure 1.18](#)). These pressures serve as boundary conditions for computer fluid dynamics (CFD) simulations of the internal flow of natural ventilation (ASCE-2005; IRWIN ET AL., 2013).

This same pressure model is also used to evaluate resultant pressure acting on the building envelope, i.e., cladding loads. This model has a density of pressure taps higher than the model used for HFPI (see [section 1.4.2.3](#)), and the outcome of this test includes doors operability, failures during extreme winds, and even internal wall failures when external pressures are higher than the loads for which these partitioning systems are designed (IRWIN ET AL., 2013).

1.4.2.1 *HFFB*

The HFFB consists of a stiff model attached to a base with a piezoelectric device or a strain gauge. The device can measure instantaneous base moments and sometimes shear forces at the base. After determining all aerodynamic coefficients and PSD of the wind loads, the building's response (drift, accelerations, and dynamic loads) can be obtained analytically using the structural data of the building (ASCE-2005; IRWIN ET AL., 2013).

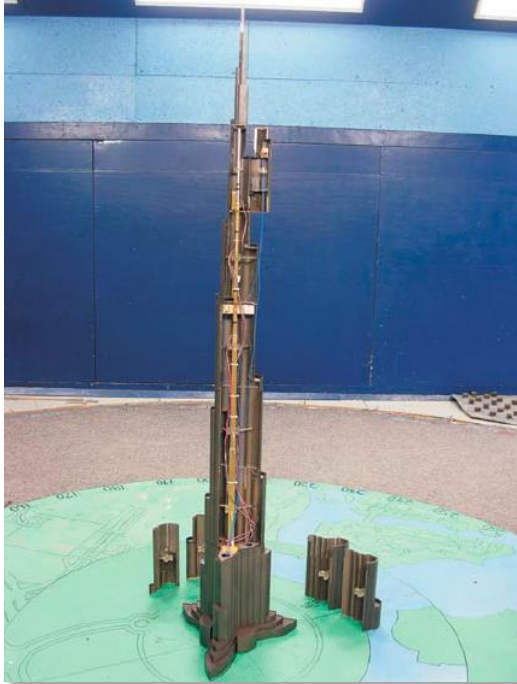
The “high-frequency” in the name of the method refers to the natural frequencies at the base of the model, which are considerably higher than the natural frequencies of the scaled-prototype studied. This directive allows for a correct measure of the fluctuating components of the wind load without contamination by resonant effects of the base model itself (IRWIN ET AL., 2013).

One of the advantages of the method is the simplicity, speed, and economy to build the tall building's scale model. It is an efficient tool to explore changes in the building's façade to achieve aerodynamic performance. However, this method is limited to the main sway modes in each direction and to the first torsional mode only (ASCE-2005; IRWIN ET AL., 2013). This means that higher modal contribution cannot be evaluated through HFFB.

1.4.2.2 *Aeroelastic models*

This WTT uses models with greater complexity than HFFB or HFPI models. Aeroelastic models are composed of outer shell parts connected by an inner spine with stiffness and mass distribution equivalent to a tall building in the scale of the WTT (see [Figure 1.17](#)). This test is important for tall buildings with aerodynamic damping, submitted to galloping, vortex shedding and other phenomena that cause this damping to assume negative values (IRWIN ET AL., 2013).

Figure 1.17 – Aeroelastic model testing.



Source: Irwin et al. (2013).

Since the structural damping presents itself with very low values, a building with negative aerodynamic damping tends to present even lower overall damping ratios. As a direct result, this may lead to structural instability or exaggerated amplitude of movement (BLESSMANN, 1988; IRWIN ET AL., 2013).

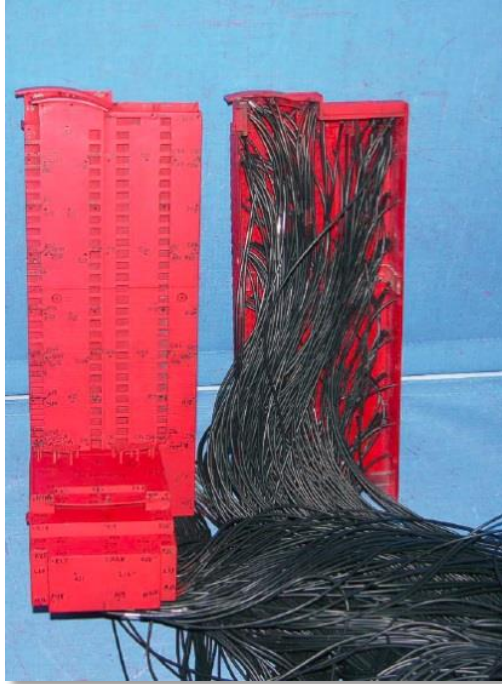
This test can simulate not only the lowest but also higher modes of vibration. The outcome of this test includes several of the building's dynamic responses, including accelerations, velocities, displacements, rotations, and dynamic loads (ASCE-2005). The aero elastic model testing is usually performed after a HFFB or a HFPI method has been applied, identifying potential negative aerodynamic damping (IRWIN ET AL., 2013).

1.4.2.3 HFPI

This test consists of a stiff model with hundreds of electronic pressure taps to measure mean and fluctuating loads on the building's envelope. *Figure 1.18* illustrates one of these models where a tributary area is assigned to each pressure tap. Each area is multiplied by the respective fluctuating pressures to create fluctuating wind loads. Each fluctuating load has its height and eccentricities with the reference axis, which generates respectively the bending moment at the base and

the torsional components discussed in [section 1.2.2.1](#) (eq. (1.1) to (1.5)). This geometry is better illustrated by [Figure 1.19](#) (ASCE-2005; IRWIN ET AL., 2013).

Figure 1.18 – Pressure study model.

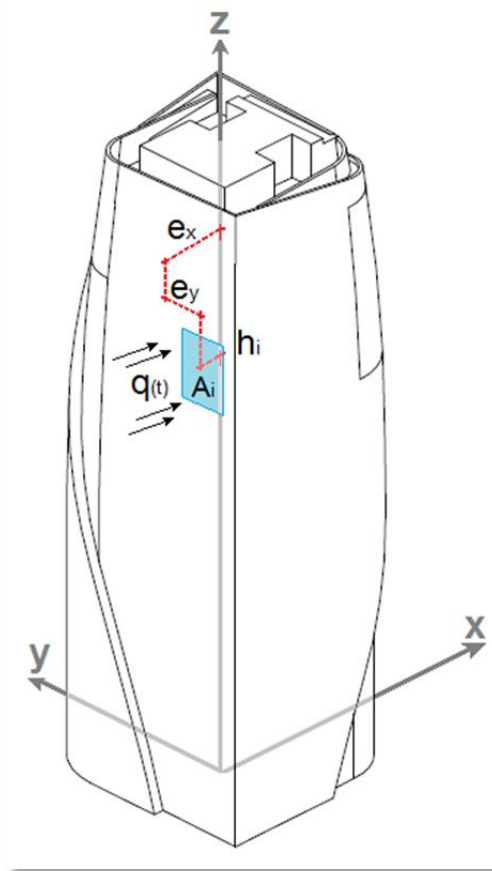


Source: Irwin et al. (2013).

Along with the building's structural data, this test can evaluate overall forces at the base (background and resonant) and modal loads acting on each mode of vibration. In addition, due to the precise torsional loads assessment over the building's height, this test allows a better evaluation of higher modal loads, i.e., for modes of vibration after each fundamental sway/torsional mode (IRWIN ET AL., 2013). The modal loads and modal responses approach will be better explained in [Chapter 2](#).

This test allows for a precise analytical assessment of each mode of vibration response, including higher modes. In addition, this test provides a detailed time history of load distribution on the building's façade, enabling a precise [time-domain analysis](#). These features make the HFPI a powerful tool to evaluate tall building's responses for wind-induced loads. Both tall building's WTTs studied in this thesis use the HFPI method. Further details on the results of these tests will be explored in [Chapter 7](#).

Figure 1.19 – Pressure taps eccentricities/heights/tributary areas.



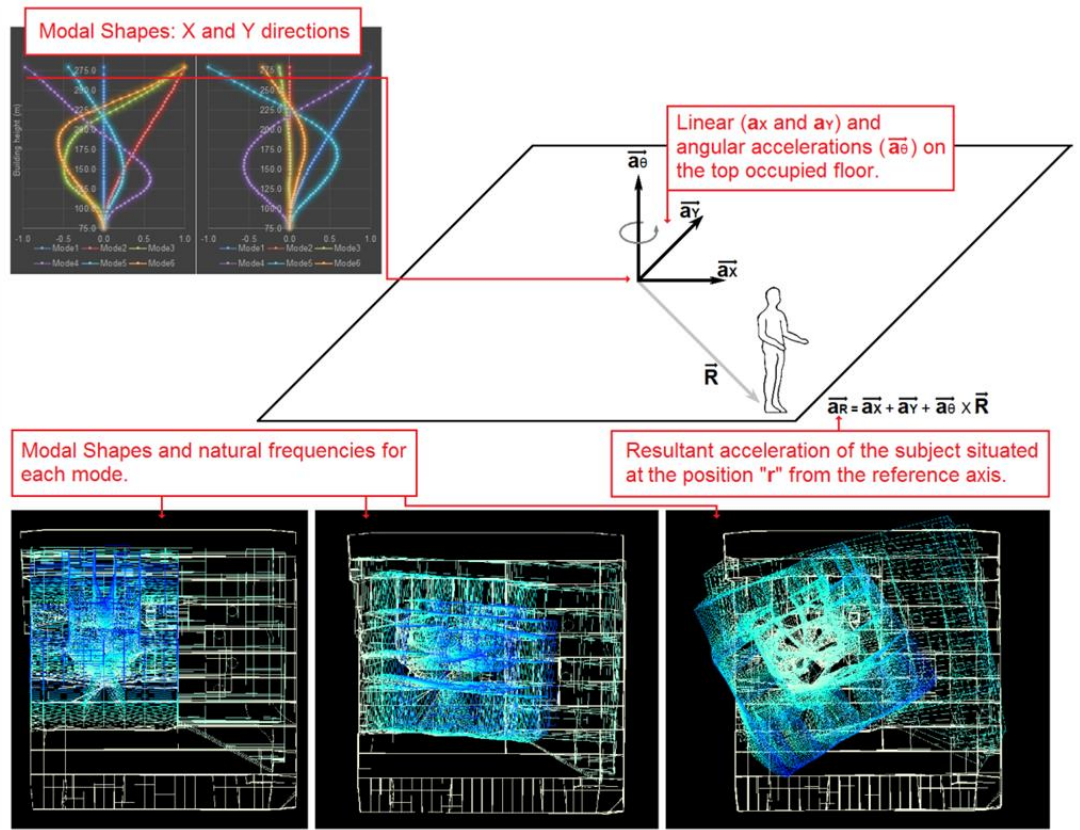
Source: Author.

1.5 INTRODUCTION TO COMFORT ASSESSMENT

The SLS of a tall building during wind-induced motion can be a critical design issue. Once the strength criteria are satisfied, the users' comfort must be assessed in order to validate the structural design.

A building's SLS for wind induced motion is usually verified by calculating the lateral drift between two consecutive stories or by the overall lateral displacement of the building, where these displacements are calculated using equivalent static wind loads from the local wind code (NBR6118-2014; GRIFFIS, 1993). These lateral displacements are verified to ensure that non-structural elements (such as cladding, partitions and elevators) will not be damaged during windstorms (GRIFFIS, 1993). Other criteria, such as creaking noises and feeling of self-movement, were documented by Hansen et al. (1973), although no comfort criterion was developed later based on these documented motion cues.

Figure 1.20 – Acceleration assessment overview.



Source: Author.

The users' comfort to motion is evaluated by the acceleration at the floor of interest. As a tall building may present mixed uses (Residential, Hotel and Offices) and the comfort threshold may be different for each one of these uses (as it will be discussed later in [Chapter 5](#)), the comfort verification may take place on the highest occupied floor (SARKISIAN, 2012) or on some residential/hotel floor on a lower story.

The current criteria to evaluate comfort are based on the users' perception of motion, which is assessed through acceleration curves (ISO6897, 1984; ISO10137, 2007; SARKISIAN, 2012; TAMURA, 2007). A precise explanation about the reason to use acceleration to evaluate comfort shall take place subsequently in [Chapter 5](#). [Figure 1.20](#) illustrates the situation considered in the design phase of a user on the target floor of a tall building.

According to Burton et al. (2006), motion can be perceived by several manners, such as vestibular organs, proprioceptive sensations, auditory cues, and visual cues. The interaction between these mechanisms of perception composes the sensing system, and determines a person's sensitivity to a building's motion.

In the 1950's and 1960's, the aerospace industry performed several experiments to predict the human response to vibration. However, the application of these results to tall buildings was questionable, since most of these experiences were made for frequencies higher than 1Hz (CHANG, 1973), while the first few natural frequencies of a tall building vary within the range of a small fraction of 1Hz to 1Hz.

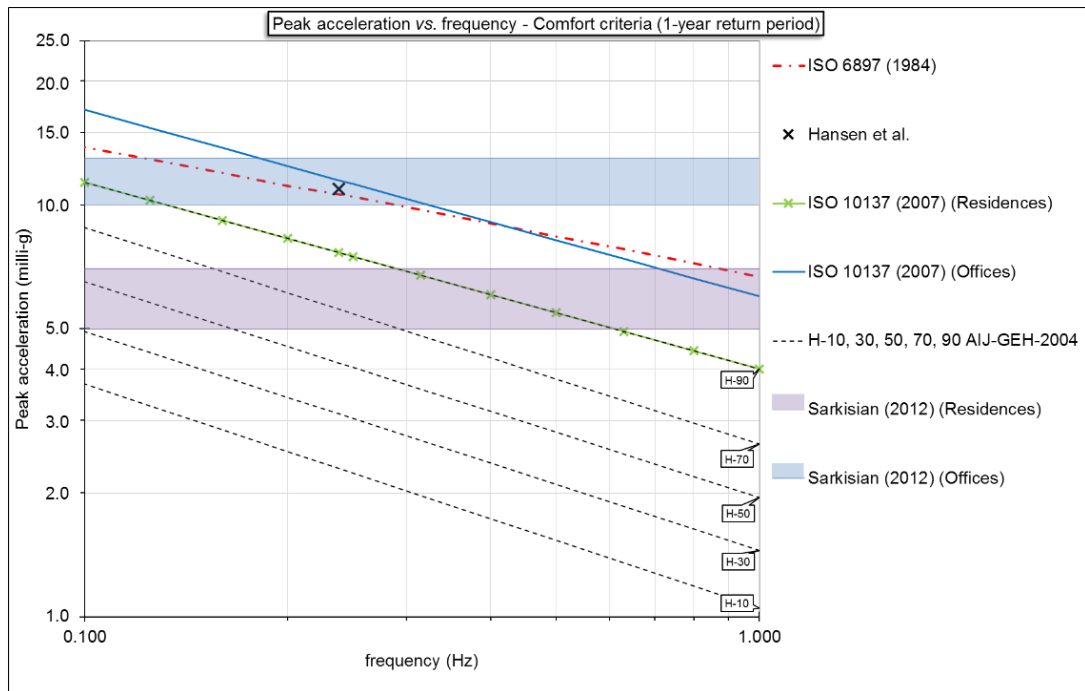
In the following decades, many experiments were carried out using motion simulators for tall building applications. These tests concentrated efforts on the relationships among a wide selection of variables and the thresholds of perception, comfort, and task-performance, like maximum peak acceleration, frequency, wave form (sinusoidal, random), movement direction (lateral, fore-aft), damping ratio, and biodynamic response (KWOK et al., 2009).

1.5.1 CURRENT APPROACH TO HUMAN COMFORT ASSESSMENT

The compilation of comfort criteria presented in this thesis (see [Figure 1.21](#) and [Figure 1.22](#)) includes the National Building Code of Canada (NBCC, 1990) and the CTBUH for residences and offices. It also includes the International Standardization Organization guidelines ISO10137 (2007) and ISO6897 (1984), adapted for a one-year recurrence interval with the peak factor proposed by Melbourne and Palmer (1992). The Guidelines for the Evaluation of Habitability to Building Vibration of the Architectural Institute of Japan (2004) is presented in this compilation. The criteria used by Hansen et al. (1973) were adapted for a one-year recurrence interval and for peak acceleration using 600 seconds of windstorm peak duration. For the sake of simplicity, only Sarkisian's (2012) one-year return period criteria are presented in the compilation (see [Figure 1.21](#)), since the ten-year period of return criteria was almost the same as the CTBUH criteria. The National Brazilian Wind Code (NBR6123-1988) comfort criteria appear with the same value of peak acceleration as the NBCC criteria for residences.

The level of users' complaints is currently the main indicator of human comfort assessment during wind-induced motion. Hansen et al. (1973) first established a comfort acceleration value of 5 milli – g based on a 2% level of users' complaints for a six-year return period (where 1.0milli – g stands for 1/1000th of the gravity acceleration).

Figure 1.21 – Comfort criteria benchmark (1-year return period).



Source: Ferrareto et al. (2015).

Most of the research and guidelines to assess the users' comfort to motion provide either a set of perception level curves (AIJ-GEH-2004; IRWIN, 1978; ISO6897, 1984) or a set of curves correlated to perception to motion (ISO6897, 1984; ISO10137, 2007).

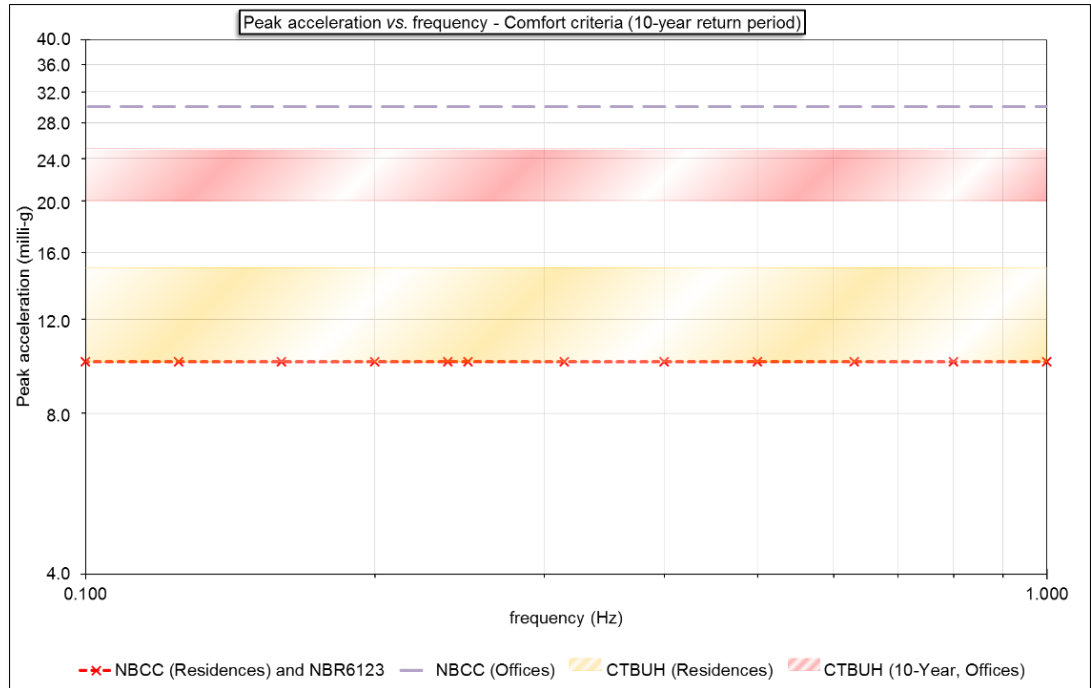
Perception thresholds to motion have been the primary concern of these studies, since it can be more easily quantified than complaint levels. In addition, peak acceleration criteria are more easily understood by building designers and building owners (TAMURA, 2007). Users' alarm and consequent objection to motion are caused by higher acceleration intensities than by those on perception levels (TAMURA, 2007).

AIJ-GEH-2004 provides five curves of motion perception where 10%, 30%, 50%, 70%, and 90% of people can perceive the vibration specified on each respective curve. The owner and the designers are to judge the suitable peak acceleration levels based on the users' perception (TAMURA, 2007).

Figure 1.23 shows accelerations of actual tall buildings in Japan. Some of the acceleration levels shown in the figure are higher than the 90% perception curve (H-90) from the AIJ-GEH-2004 standard. Nonetheless, society considers these

motion levels acceptable, in spite of how much bigger they are when compared to the perception curves presented in the Japanese standards (TAMURA, 2007).

Figure 1.22 – Comfort criteria benchmark (10-year return period).



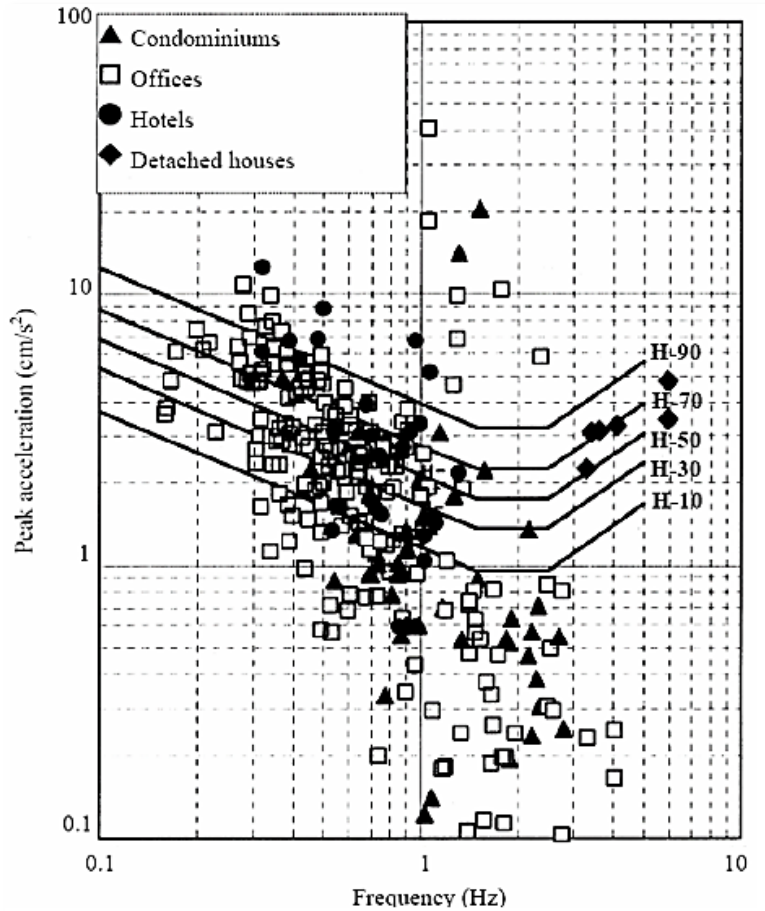
Source: Ferrareto et al. (2015).

Irwin (1978) proposed a frequency-dependent root-mean-square (rms) acceleration curve consistent with the criteria proposed by Hansen et al. (1973). Irwin's curve was adjusted to a five-year return period instead of six years. Later, ISO6897 (1984) adapted Irwin's curves to propose a comfort assessment for acceleration rms (see [Figure 1.21](#)).

Melbourne and Palmer (1992) related the response of return period "R" to the acceleration for a return period of five years (eq. (3.4)), while ISO6897 (1984) uses a 0.72 factor to convert the five-year return period assessment curve into a one-year return period curve.

The ISO10137 Standard (2007) proposes two evaluation curves for a one-year return period windstorm: one for residences and another for offices. The residence threshold of comfort curve is closer to Tamura's (2003) and AIJ-GEH-2004 90% perception curve, whilst the office threshold of comfort is 1.5 times the residential threshold.

Figure 1.23 – 1-year return period along-wind and crosswind peak accelerations of actual tall buildings in Japan.



Source: AIJ-GEH-2004.

Sarkisian (2012) suggested criteria of perception to motion in tall buildings. Peak accelerations of 5 to 7 milli – g or 12 to 15 milli – g for residences with a one-year or a ten-year return period wind, respectively. For offices, the peak accelerations are 10 to 13 milli – g for a one-year return period and 20 to 25 milli – g for a ten-year return period.

The criteria presented above are used in the deterministic evaluation of human comfort. An alternative approach is the probabilistic method, which is briefly discussed in this thesis. Further information on comfort criteria and kinematic/psychological properties of motion will be provided in [Chapter 5](#), along with the clarification on building acceleration to evaluate the SLS criteria.

1.6 OBJECTIVES

At this point of this thesis, it is clear how the interaction works among the different disciplines involved in the serviceability verification for wind-induced motion and about the role of each one of them in the procedure.

The main objective of this study is to offer better understanding of the criteria concerning these disciplines: structural engineering, wind engineering, and comfort criteria. This will allow for an increase in the accuracy of the procedure, bringing more precise designs through a set of criteria for the WTT's analysis of results, which should enable cost savings for future projects.

1.6.1 SPECIFIC OBJECTIVES – STRUCTURAL ENGINEERING

Primarily, the specific objective of this discipline is to bring precision to the FE model through modelling criteria. Both mass distribution and damping ratio shall not present any differences for the different finite element models created. The natural frequencies and mode-shapes, however, will present great differences due to the stiffening of certain structural elements.

Afterwards, the accuracy of dynamic analysis will be discussed according to two axes of investigation:

- Time-domain and frequency-domain analyses, using the time-series loading provided by the WTT through the HFPI method;
- Higher modal contribution evaluation, using final response for each analysis for three, six and nine modes of vibration.

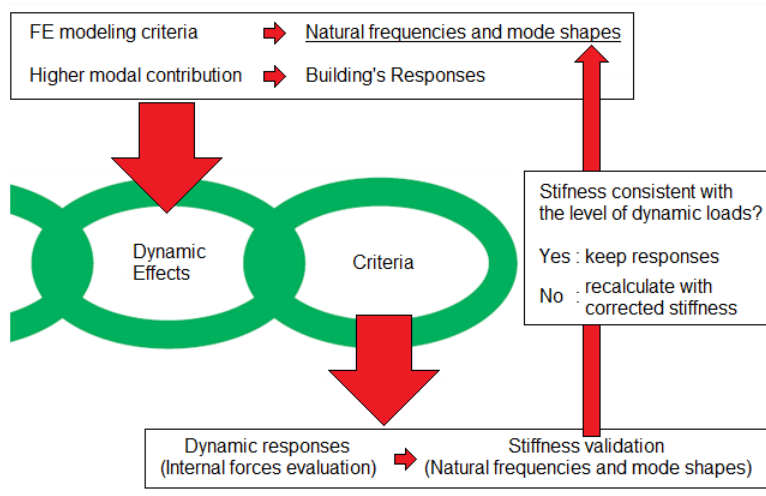
The number of modes of vibration used in the higher modal contribution evaluation is between six and nine. The justification lies in the PSD analysis of the buildings' responses, better explained in [sections 7.2.2.4](#) and [7.4.3](#).

Lastly, after precise evaluation of both buildings' dynamic responses, the calculation of the time history of internal loads in wind-resisting elements (such as shear walls) will take place. This time history will enable a verification of the stiffness reduction due to cracking when these structural elements are subjected to excessive loads.

This axis of investigation is vertical, analysing and validating specific criteria within the same discipline (structural engineering). The role of this axis of

investigation in the Davenport's chain of wind loading is better illustrated in [Figure 1.24](#). In this figure, it is possible to note the possible impact of each group of structural criteria in the final response. Hence, this figure brings a possible weak link in the chain (Dynamic effects) if the structural analysis and the structural data gathering are not carried out carefully enough.

Figure 1.24 – Davenport's possible weak link for structural criteria.



Source: Author.

1.6.2 SPECIFIC OBJECTIVES – WIND ENGINEERING

Predominantly, the design wind speed will be discussed in this study with different approaches. Directionality (see [Chapter 4](#)) will be discussed in this analysis using two main techniques: *worst-case* method and *up-crossings* method. Then, the different approaches will be evaluated according to their interaction with the unidirectional wind response. This work will discuss how the different directionality approaches (“Wind Climate” link, see [Figure 1.5](#)) affect the overall buildings’ responses (“Dynamic Effects” link). This axis of investigation deals with the objects of study horizontally, i.e., it exposes how the criteria impact the final results throughout different disciplines.

1.6.3 SPECIFIC OBJECTIVES – COMFORT CRITERIA

This part of the thesis discusses comfort criteria for wind-induced movement on tall buildings. [Chapter 5](#) of this thesis gathers data from the first studies on user’s

comfort to the current criteria used in the design of tall buildings, with the purpose of providing an overview of the most important research carried out in this field.

This part of the study also covers specific criteria to evaluate building motion: joint action factors, peak factors, torsional component of acceleration, and yaw, to name a few. Part of the discussion includes deterministic versus stochastic approaches for wind-induced acceleration: peak acceleration versus root-mean-square acceleration. Along with peak factors and joint action factors, this discussion represents an extension of the discussion on frequency-domain versus time-domain procedures, discussed in [Chapter 2](#). This topic is related to the last link of the Davenport's chain of wind loading: "Criteria".

1.6.4 FINAL STATEMENTS ABOUT THIS THESIS OBJECTIVES

Nowadays, most of the responsibility of the WTT's post-treatment results resides mainly on the hands of the wind tunnel facility, with exception of structural data. In addition, the backward verification of a building's stiffness (see [Figure 1.24](#)) in the Davenport's chain of wind loading is not carried out in most of the studies. Finally, the lack of interaction between the disciplines may bring several vulnerabilities to this chain.

With the set of criteria studied in this thesis, the BLWT's analyses may achieve more accurate results and so will structural engineers. Moreover, with the procedure to check internal loads, a suitable verification of a building's stiffness in SLS will be enabled.

As a final point, by bringing knowledge to different disciplines, this thesis proposes to offer better understanding and to provide verification tools for the whole procedure to all fields of study that take part in the WTT. For an instance, the dynamic analysis of the buildings' responses is essentially a field of structural engineering. Nevertheless, the structural engineer has too little control of this part of the procedure, since it is performed by the wind tunnel facility. This thesis provides tools to enable the control and responsibility, thereby increasing the role of the structural engineer during the WTT's analysis of results.

2 DYNAMIC ANALYSIS

2.1 INTRODUCTION

Wind tunnel facilities are usually in charge of this stage of the post-treatment of the WTT. This stage comprises all the steps of the dynamic response assessment, including: integration of fluctuating loads on a building's façade, transforming these loads into modal loads to apply the mode displacement superposition (see [section 2.2](#)) to evaluate the final building's response.

This study shall cover both approaches used to calculate the building's responses: deterministic/probabilistic in the *time domain*, and probabilistic in the *frequency domain*. The first paradigm will be addressed in this chapter, as it will bring up for discussion the dynamic approach for the assessment of the building's responses, instead of the equivalent static loads.

2.2 EQUATIONS OF MOTION AND MODE DISPLACEMENTS SUPERPOSITION

The viscously-damped equations of motion for a linear discretized model of a tall building subjected to wind-induced vibration can be written as:

$$[M]\{\ddot{u}(t)\} + [C]\{\dot{u}(t)\} + [K]\{u(t)\} = \{p(t)\} \quad (2.1)$$

where:

- $[M]$ is the mass matrix;
- $[C]$ is the viscous-damping matrix, assumed to be of the Rayleigh type (CLOUGH AND PENZIEN, 2010);
- $[K]$ is the stiffness matrix;
- $\{\ddot{u}(t)\}$, $\{\dot{u}(t)\}$ and $\{u(t)\}$ stand for the acceleration, velocity and displacement vectors, respectively;
- $\{p(t)\}$ stands for the dynamic loading applied to the structure by the wind.

In the mode superposition approach, the displacements of each DOF are given by the product of the mode-shape vector " $\{\Phi\}_j$ " by the respective modal amplitude " Y_j " (CLOUGH AND PENZIEN, 2010):

$$u_j = \{\Phi\}_j Y_j \quad (2.2)$$

The total displacement can be calculated by summing up each component (CLOUGH AND PENZIEN, 2010):

$$\{u(t)\} = \sum_{j=1}^n \{u_j(t)\} = \sum_{j=1}^n \{\Phi\}_j Y_j(t) = [\Phi]\{Y(t)\} \quad (2.3)$$

Similarly, since the mode-shapes do not vary with time, for the first and the second derivatives with time, acceleration and velocity vectors, can be calculated by (CLOUGH AND PENZIEN, 2010):

$$\{\dot{u}(t)\} = [\Phi]\{\dot{Y}(t)\} \quad (2.4)$$

$$\{\ddot{u}(t)\} = [\Phi]\{\ddot{Y}(t)\} \quad (2.5)$$

Replacing the displacement, velocity, and acceleration vectors by eq. (2.3), (2.4) and (2.5), respectively, eq. (2.1) becomes:

$$[M][\Phi]\{\ddot{Y}(t)\} + [C][\Phi]\{\dot{Y}(t)\} + [K][\Phi]\{Y(t)\} = \{p(t)\} \quad (2.6)$$

Multiplying each term on both sides by “[Φ]^T”, eq. (2.6) becomes:

$$[\Phi]^T[M][\Phi]\{\ddot{Y}(t)\} + [\Phi]^T[C][\Phi]\{\dot{Y}(t)\} + [\Phi]^T[K][\Phi]\{Y(t)\} = [\Phi]^T\{p(t)\} \quad (2.7)$$

The orthogonality property of vibration modes with respect to mass (CHOPRA, 2000; CLOUGH AND PENZIEN, 2010) provides:

$$\{\Phi\}_j^T [M] \{\Phi\}_k = 0, (j \neq k) \quad (2.8)$$

The stiffness matrix benefits from the same orthogonality property. Therefore, it can be assumed that the same orthogonality properties can be applied to the damping matrix for the Rayleigh damping. Each modal damping coefficient can be calculated by (CLOUGH AND PENZIEN, 2010):

$$C_j = \{\Phi\}_j^T [C] \{\Phi\}_j \quad (2.9)$$

Likewise, each modal mass/stiffness is (CHOPRA, 2000; CLOUGH AND PENZIEN, 2010):

$$M_j = \{\Phi\}_j^T [M] \{\Phi\}_j \quad (2.10)$$

$$K_j = \{\Phi\}_j^T [K] \{\Phi\}_j = M_j (\omega_j)^2 \quad (2.11)$$

The system of equations defined by eq. (2.7) can be simplified to an uncoupled system of equations of motion with one degree of freedom (DOF) for each mode of vibration used in the analysis:

$$\ddot{Y}_j(t) + 2\xi_j\omega_j\dot{Y}_j(t) + \omega_j^2Y_j(t) = \frac{P_j(t)}{M_j} \quad (2.12)$$

where:

- $C_j = 2\xi_j\omega_jM_j$;
- ξ_j stands for the modal viscous damping ratio;
- $P_j(t) = \{\Phi\}_j^T\{p(t)\}$;
- ω_j stands for the circular frequency of the “jth” mode of vibration.

In the design of tall buildings, the usual number of modes of vibration used in a dynamic analysis is 3 to 6 modes (HUANG AND CHEN, 2007; ROSA ET AL., 2012; FERRARETO ET AL., 2014), but other criteria, such as minimum participation factor, should be used to perform the analysis (AIJ-GEH-2004; CLOUGH AND PENZIEN, 2010). Some Brazilian BLWT already performs dynamic analyses taking into consideration the contribution of higher modes of vibration, usually with natural frequencies up to 1.00Hz. The relevance of these higher modes in Brazilian tall buildings can be explained by the slenderness of local buildings and it's impacts will be observed later in [section 7.4.2](#).

Current investigations indicate non-negligible differences if higher modal contributions are taken into consideration (HUANG AND CHEN, 2007; ROSA ET AL., 2012; FERRARETO ET AL., 2014). Overall building peak acceleration might increase up to 10%, according to Ferrareto et al. (2014), whilst torsional acceleration showed an increase of 36%, according to Huang and Chen (2007).

2.3 SOLUTION IN THE FREQUENCY DOMAIN

In order to assess the dynamic response, one may express the modal wind loads “ $P_j(t)$ ” as a series of harmonic loads in a [Fourier series](#) expression:

$$P_j(t) = a_{0,j} + \sum_{n=1}^{\infty} a_{n,j}\cos(\bar{\omega}_n t) + \sum_{n=1}^{\infty} b_{n,j}\sin(\bar{\omega}_n t) \quad (2.13)$$

where:

$$\bar{\omega}_n = n \frac{2\pi}{T_p} \quad (2.14)$$

In eq. (2.14), “ T_p ” stands for the duration of the loading. For the discrete Fourier transforms, the “ T_p ” duration can be divided into “ $T_p = N\Delta t$,” and coefficients “ $a_{0,j}$,” “ $a_{n,j}$,” and “ $b_{n,j}$ ” can be calculated as (CLOUGH AND PENZIEN, 2010):

$$a_{0,j} = \frac{2\Delta t}{T_p} \sum_{m=1}^N P_j(t)/2 \quad (2.15a)$$

$$a_{n,j} = \frac{2\Delta t}{T_p} \sum_{m=1}^N P_j(t) \cos(\bar{\omega}_n m \Delta t) \quad (2.15b)$$

$$b_{n,j} = \frac{2\Delta t}{T_p} \sum_{m=1}^N P_j(t) \sin(\bar{\omega}_n m \Delta t) \quad (2.15c)$$

For systems with proportional linear viscous damping, the dynamic response can always be obtained from the solution of the systems of equations such as eq. (2.12). Therefore, the response to the loads of Fourier series for an under-critically damped system is (CLOUGH AND PENZIEN, 2010):

$$\begin{aligned} \dot{Y}_j(t) = & \frac{-1}{\omega_j^2} \sum_{n=1}^N \left[\frac{\bar{\omega}_n^2}{(1 - \beta_{n,j}^2)^2 + (2\xi\beta_{n,j})^2} \right] \\ & \times \left\{ \left[2\xi a_{n,j} \beta_{n,j} + b_{n,j} (1 - \beta_{n,j})^2 \right] \sin(\bar{\omega}_n t) \right. \\ & \left. + \left[a_{n,j} (1 - \beta_{n,j})^2 - 2\xi b_{n,j} \beta_{n,j} \right] \cos(\bar{\omega}_n t) \right\} \end{aligned} \quad (2.16)$$

where:

$$\beta_{n,j} = \frac{\bar{\omega}_n}{\omega_j} \quad (2.17)$$

To assess the modal response rms through the Fourier series of the response, one can integrate eq. (2.16) over the duration of the load:

$$\sigma_{\dot{Y}_j} = \sqrt{\frac{\int_0^{T_p} \dot{Y}_j(t)^2 dt}{T_p}} \quad (2.18)$$

Only the squared terms in “ $\ddot{Y}_j(t)^2$ ” remain different from zero after the integration over the complete period of the Fourier series, i.e., only the terms multiplying “ $\sin(\bar{\omega}_n t)^2$ ” and “ $\cos(\bar{\omega}_n t)^2$ ”. Then, the result of the integration of eq. (2.18) can be simplified to:

$$\sigma_{\ddot{Y}_j}^2 = \frac{1}{2\omega_j^2} \sum_{n=1}^N \bar{\omega}_n^2 \left\{ \left[\frac{2\xi a_{n,j} \beta_{n,j} + b_{n,j} (1 - \beta_{n,j})^2}{(1 - \beta_{n,j}^2)^2 + (2\xi \beta_{n,j})^2} \right]^2 + \left[\frac{a_{n,j} (1 - \beta_{n,j})^2 - 2\xi b_{n,j} \beta_{n,j}}{(1 - \beta_{n,j}^2)^2 + (2\xi \beta_{n,j})^2} \right]^2 \right\} \quad (2.19)$$

2.3.1 ACCELERATION AND FORCES OVER THE BUILDING'S HEIGHT

According to Clough and Penzien (2010), any response “ $r(t)$ ”, which is linearly dependent on the generalized coordinates, can be assessed by the relation (CHOPRA, 2000; CLOUGH AND PENZIEN, 2010):

$$r(t) = \sum_{j=1}^n B_j \ddot{Y}_j(t) \quad (2.20)$$

where “ B_j ” is a coefficient that varies for each required response (acceleration, displacement, velocity, equivalent static forces, etc). To assess the acceleration on the floor of interest of the building using the results of eq. (2.20) and (2.22), one can use eq. (2.21) for the “ B_j ” coefficient:

$$B_j = \Phi_{(x,y,\theta),\ell_j} \quad (2.21)$$

where “ $\Phi_{(x,y,\theta)}$ ” stands for the “ j^{th} ” mode shape at the “ ℓ^{th} ” floor for the chosen direction (x and y translations or rotation θ). Then, the rms of the acceleration can be calculated using the mode superposition:

$$\sigma_a^2 = \sum_{j=1}^n (B_j \sigma_{\ddot{Y}_j})^2 \quad (2.22)$$

To calculate the resultant vector “ $\{f_s\}$ ” of the equivalent force on the building and to calculate the force “ $f_{s,\ell}$ ” on a single floor “ ℓ ”, the expressions are (CHOPRA, 2000; GOULD AND ABU-SITTA, 1980; CLOUGH AND PENZIEN, 2010):

$$\{f_s\} = [M] \sum_{j=1}^n \{\Phi\}_j (\omega_j)^2 Y_j \quad (2.23a)$$

$$f_{s,\ell} = m_\ell \sum_{j=1}^n \Phi_{j,\ell} (\omega_j)^2 Y_j \quad (2.23b)$$

where:

- m_ℓ is the element of the mass matrix “[M]” corresponding to the “ ℓ^{th} ” floor and to the desired DOF (x and y translations or rotation θ);
- $\Phi_{j,\ell}$ stands for the element of the mode shape vector “ $\{\Phi\}_j$ ” corresponding to the “ j^{th} ” mode, to the “ ℓ^{th} ” floor and to the desired DOF (x, y or θ).

2.3.2 PEAK ACCELERATION ASSESSMENT

Some standards allow the direct use of the rms acceleration for comfort assessment (ISO6897, 1984), whilst others require the peak acceleration (ISO10137, 2007). In order to transform the rms into peak acceleration, a peak factor “g” should be applied:

$$a_{\text{máx}} = g\sigma_a \quad (2.24)$$

The peak factor “g” was first proposed by Davenport and it usually assumes a value between three and four, typically 3.5 for wind-induced vibration (BOGGS, 1997; HUANG AND CHEN, 2007). The approximate value of the peak factor using the extreme-value as the probability function (CLOUGH AND PENZIEN, 2010) is:

$$g = \sqrt[2]{2\ln(v^{(n)}T)} + \frac{\gamma}{\sqrt[2]{2\ln(v^{(n)}T)}} \quad (2.25)$$

where:

- γ stands for the Euler’s constant, equal to 0.5772;
- T stands for the duration of the event, usually assumed to be 600s (HANSEN ET AL., 1973; MELBOURNE AND PALMER, 1992);
- and:

$$v^{(n)} = \sqrt[2]{\frac{\int_0^\infty f^{2(n+1)} S_z(f) df}{\int_0^\infty f^{2(n)} S_z(f) df}} \quad (2.26)$$

where “f” stands for the frequency of motion and the value of “n” refers to the derivative of the displacement with respect to time: “n = 0” for displacement; “n = 1” for velocity; “n = 2” for acceleration.

Since the response spectrum of a tall building has a high amount of energy concentrated around the natural frequency, the value of “v⁽ⁿ⁾” tends to be equal to the natural frequency itself (MELBOURNE AND PALMER, 1992).

2.4 SOLUTION IN THE TIME DOMAIN

In order to assess the wind-induced motion response of a multi DOF in the time domain, one can calculate a single DOF for each mode of vibration and then use mode superposition to assess the building’s response.

Using a simple *4th order Runge-Kutta*, (CHAPRA E CANALE; 2008) the time-domain response for a SDOF system on the nth time step is:

$$\ddot{Y}_{n,1} = \ddot{Y}_n(\dot{Y}_n; Y_n) \quad (2.27a)$$

$$\ddot{Y}_{n,2} = \ddot{Y}_n\left(\dot{Y}_n + \ddot{Y}_{n,1} \frac{\Delta t}{2}; Y_n + \dot{Y}_{n,1} \frac{\Delta t}{2}\right) \quad (2.27b)$$

$$\ddot{Y}_{n,3} = \ddot{Y}_n\left(\dot{Y}_n + \ddot{Y}_{n,2} \frac{\Delta t}{2}; Y_n + \dot{Y}_{n,2} \frac{\Delta t}{2}\right) \quad (2.27c)$$

$$\ddot{Y}_{n,4} = \ddot{Y}_n(\dot{Y}_n + \ddot{Y}_{n,3}\Delta t; Y_n + \dot{Y}_{n,3}\Delta t) \quad (2.27d)$$

$$\dot{Y}_{n,1} = \dot{Y}_n \quad (2.27e)$$

$$\dot{Y}_{n,2} = \dot{Y}_n + \ddot{Y}_{n,1} \frac{\Delta t}{2} \quad (2.27f)$$

$$\dot{Y}_{n,3} = \dot{Y}_n + \ddot{Y}_{n,2} \frac{\Delta t}{2} \quad (2.27g)$$

$$\dot{Y}_{n,4} = \dot{Y}_n + \ddot{Y}_{n,3}\Delta t \quad (2.27h)$$

where, for each mode “j” and step “n”:

$$\ddot{Y}_{j,n} = \frac{P_{j,n}}{M_j} - (2\xi_j\omega_j\dot{Y}_{j,n} + \omega_j^2 Y_{j,n}) \quad (2.28a)$$

$$\dot{Y}_{(n+1)} = \frac{(\ddot{Y}_{n,1} + 2\ddot{Y}_{n,2} + 2\ddot{Y}_{n,3} + \ddot{Y}_{n,4})}{6} \Delta t + \dot{Y}_n \quad (2.28b)$$

$$Y_{(n+1)} = \frac{(\dot{Y}_{n,1} + 2\dot{Y}_{n,2} + 2\dot{Y}_{n,3} + \dot{Y}_{n,4})}{6} \Delta t + Y_n \quad (2.28c)$$

Once a SDOF system is calculated for each mode, the mode superposition can be used to assess the acceleration:

$$a_{x,n}(t) = \sum_{j=1}^n \Phi_{\ell x j} \ddot{Y}_j(t) \quad (2.29a)$$

$$a_{y,n}(t) = \sum_{j=1}^n \Phi_{\ell y j} \ddot{Y}_j(t) \quad (2.29b)$$

$$a_{\theta,n}(t) = \sum_{j=1}^n \Phi_{\ell \theta j} \ddot{Y}_j(t) d \quad (2.29c)$$

where:

- $a_{x,n}$, $a_{y,n}$, and $a_{\theta,n}$ stand for the x, y and torsional components of the acceleration for “n” modes of vibration, respectively;
- d stands for the distance between the reference axis and the reference person on the floor (usually at the farthest point from the axis);
- $\Phi_{\ell x j}$, $\Phi_{\ell y j}$, and $\Phi_{\ell \theta j}$ are the components of the mode shape for the “ ℓ^{th} ” floor, “jth” mode of vibration and x, y or torsional direction.

2.5 DIFFERENCES BETWEEN TIME-DOMAIN AND FREQUENCY-DOMAIN RESPONSES

The time-domain analysis provides a time-history response that can be directly examined, whilst the frequency-domain analysis provides the rms response, which later needs to be multiplied by peak factors and joint-action factors (BOGGS, 1997; MELBOURNE AND PALMER, 1992). The difference in the use of the peak or rms response in the assessment of the user’s comfort will be explained later in [Chapter 5](#).

The results obtained by Wu et al. (2007) cover both time and frequency-domain analyses. The rms for the time-domain analysis is calculated using the time history response. The rms values for all responses are systematically higher for the frequency domain than they are for the time domain. This difference is due to the steady-state hypothesis assumed in the frequency-domain analysis (reminding that

eq. **(2.16)** is the steady-state response for the harmonic wind loads). The time-domain analysis allows the assessment of the transient behaviour of wind loads, enabling a more accurate assessment of a building's responses. As a result of this accuracy, lower responses can be achieved with the use of this procedure. Hence, additional accuracy is attained when combining the contributions of different modes, including lower ones, since the method allows for the assessment of exact values for each time step.

3 FE MODELLING CRITERIA

3.1 INTRODUCTION

Structural modelling criteria are of great importance for the reliable assessment of the response of a tall building subjected to wind loading. Dynamic properties of the building, such as natural frequencies, can be significantly miscalculated due to conservative assumptions (KIM ET AL., 2009).

Depending on the building height and use, the comfort performance for SLS may be the main issue in the structural design, leaving space for structural optimization and cost reduction (CHAN, HUANG AND KWOK, 2010). When the modelling criteria are too conservative or lack precision, wind-resistant structural elements may be penalized, leading to higher structural costs (JEARY ET AL., 1988).

Kim et al. (2009) performed field measurements in three buildings to acquire the first three natural frequencies of each building. Then, using FE models, the natural frequencies of these structures were obtained. The results showed great underestimation of the natural frequencies for the FE models. The authors investigated the phenomena using four main subjects:

- Beam-end offsets;
- Flexural stiffness of floor slabs;
- Influence of non-structural walls (NSW);
- Modulus of elasticity of concrete.

The results obtained by Kim et al. (2009) showed differences of up to 33% between the FE models and the measured natural frequencies. Four steps were then proposed to improve the FE models, one for each of the subjects investigated. After further enhancements on the structural models, the results showed slight differences ranging from 2% to 7%.

3.2 BEAM-END-OFFSETS

According to Kim et al. (2009), the connection between beams and columns has finite dimensions and has a behaviour similar to that of a rigid body. Therefore, beam-end offsets can be justified to achieve a more accurate performance between a finite element model and real scale measurements. Numerical results revealed an increase from 12% to 32% in the natural frequencies of the studied buildings.

This modelling directive has been taken into consideration for the last 50 years and the increase in the natural frequencies achieved is made explicit here for the sake of argument.

Therefore, today, it makes more sense to perform a tall building's dynamic analysis with this directive already included in the structural modelling criteria, which is the case of the investigation that will be presented later in this thesis.

3.3 *MODELLING FLOOR SLABS*

3.3.1 *VALIDITY OF THE RIGID DIAPHRAGM HYPOTHESIS*

As it will be discussed later in [section 3.3.3](#) ("*In-plane floor slab flexibility*"), the rigid diaphragm behaviour of the floor slab is compromised when floor plans have elongated shapes. These shapes present a semi-rigid behaviour and redistribute lateral loads differently than they would if they were a rigid diaphragm (MOON AND LEE, 1994). The effects of the semi-rigid diaphragm behaviour are referred to as in-plane floor slab flexibility and can be seen in [section 3.3.3](#).

The effect tends to be accentuated when the building presents fewer storeys (MOON AND LEE, 1994). The analysis performed in this thesis will not take these effects into consideration, for the target of this investigation will be tall and slender multi-storey buildings with non-elongated floor shapes.

There are different ways to apply these techniques to buildings with elongated floor shapes or connected twin towers, such as considering more than one axis of reference (RWDI, Issue number 26). However, they will not be further discussed in this study.

Using the rigid diaphragm hypothesis whilst neglecting the out-of-plane flexural stiffness in the FE model leads to smaller natural frequencies on the dynamic analysis, since it ignores the coupling between the exterior frames and the interior core walls (KIM ET AL. 2009; LEE, KIM AND CHUN, 2002).

For wind-induced motions, smaller natural frequencies mean lower stiffness, which may lead to larger responses (larger accelerations and larger displacements, which imply larger dynamic loads).

The explanation to the previous statement resides also in the wind power spectra. If the first natural frequency is low, the other natural frequencies will fall right

on the portion of the spectra with the higher amount of energy. If the first natural frequency is higher, the other natural frequencies will be closer to, or even after, the power spectral density decrease slope. This assertion will be verified later in this thesis through the dynamic analysis of the same building under several FE modelling assumptions, using a wide range of natural frequencies.

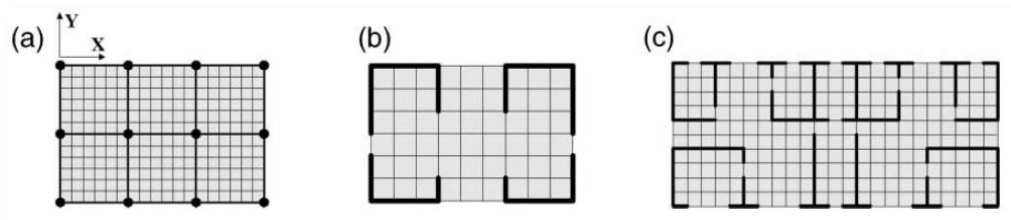
In addition, the rigid diaphragm assumption might cause some of the lateral load resisting elements to receive higher loads than expected with a semi-rigid floor diaphragm hypothesis (MOON AND LEE, 1994). The rigid diaphragm assumption, on the other hand, might overestimate the natural frequencies of the building.

Both reasons imply a loss of reliability of the dynamic response of the building. This is why floor slab modelling is an important part of the overall modelling criteria.

3.3.2 FLOOR SLAB FLEXURAL STIFFNESS

Lee, Kim and Chun (2002) performed a dynamic analysis of several different structures when they modelled the floor slab. Three different plans were used to create different structures. The plans in [Figure 3.1](#) were analysed with 10 and 20-storey structures under a seismic loading. Natural periods of vibration for FE models with modelled floor slabs showed a decrease of 30% when compared to FE models with rigid diaphragms. In addition, overall displacements and accelerations on the top floor showed decreases of 70% and 49%, respectively, for the FE model with modelled floor slabs.

Figure 3.1 – Structures with refined slabs.

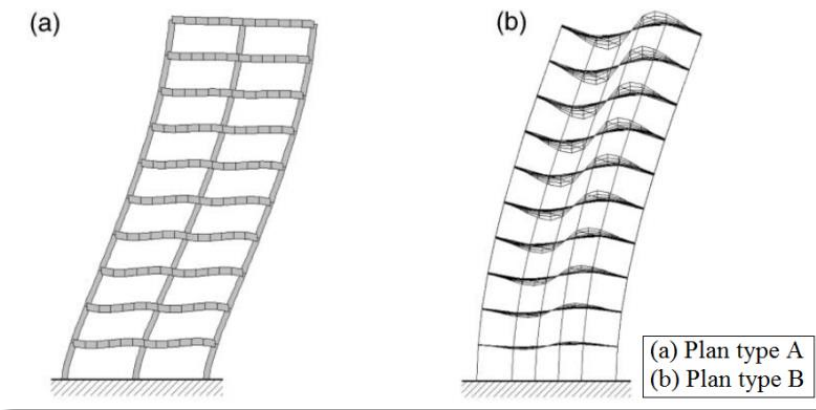


Source: Lee, Kim and Chun (2002).

[Figure 3.2](#) shows the lateral displacement of 10-story buildings with plan types (a) and (b), according to [Figure 3.1](#). In this figure, it is possible to observe the typical moment frame behaviour for plan type (a), where the floor slab follows the deformation pattern of the floor beams, where a larger deformation occurs on lower

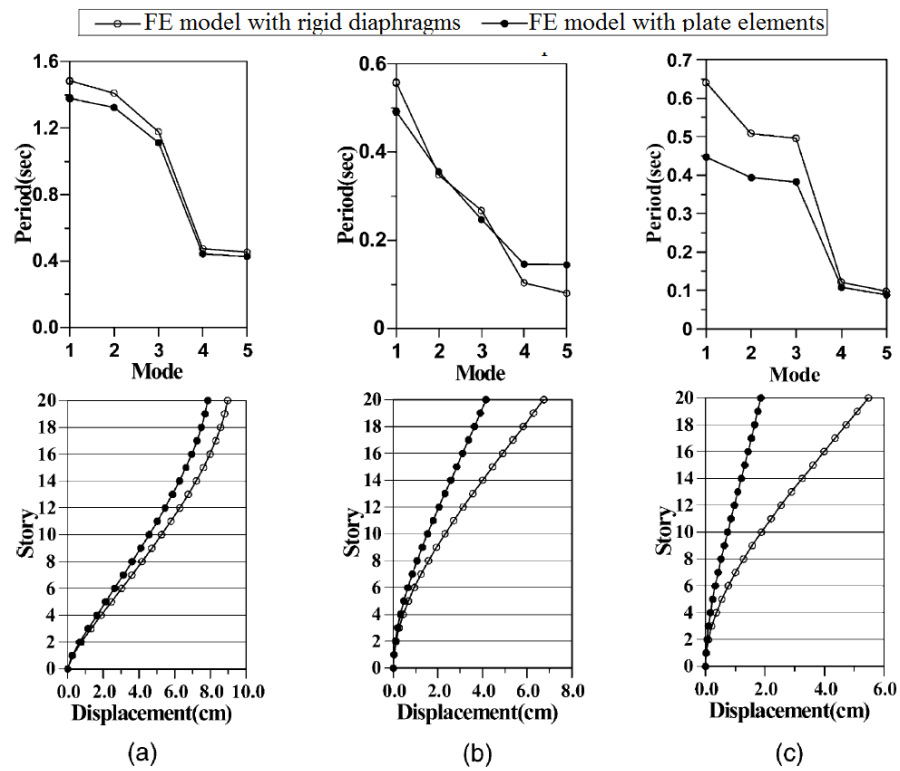
storeys. In the same figure, it is also possible to observe the structural behaviour of plan type (b), with shear walls.

Figure 3.2 – Deformed shape of building structures under lateral loads.



Source: Lee, Kim and Chun (2002).

Figure 3.3 – Natural periods and lateral displacements for 20-storey structures.



Source: Lee, Kim and Chun (2002).

For the second structure, plan type (b), the effect of the floor slab modelling is better noticed, since it provides a coupling between the shear walls, greatly

reducing the top displacement and the natural period, and also enabling a deformation shape more similar to the behaviour of a moment frame.

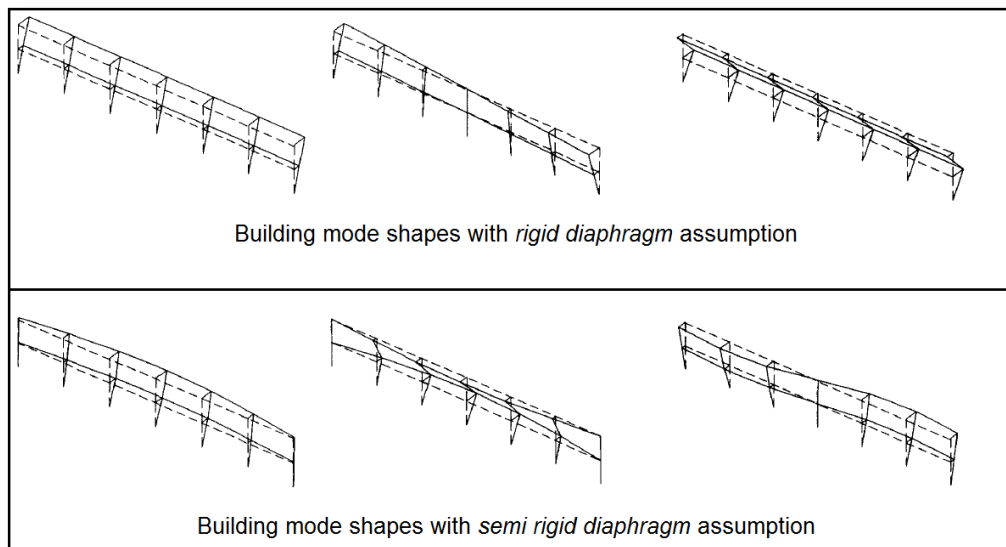
The moment frame behaviour, instead of the shear wall behaviour, is also illustrated in [Figure 3.3](#), mainly for structures (b) and (c). The coupling between the shear walls through the bending moment of the floor slab increases with the floor height, causing different displacements in models *D* (without modelling the floor slab) and *S* (modelling the floor slab) at higher storeys.

Kim et al. (2009) describe a similar effect for façade columns and internal concrete cores when the floor slab coupling enables *outrigger system behaviour*. This behaviour is not as effective as an outrigger system, but is sufficient to cause the 6% to 22% increase in the natural frequencies of the surveyed buildings in Korea.

3.3.3 IN-PLANE FLOOR SLAB FLEXIBILITY

Moon and Lee (1994) investigated the dynamic properties of the in-plane floor flexibility behaviour. Usually, reinforced concrete slabs and steel-deck-with-concrete-fill slabs are considered as rigid diaphragms. This hypothesis means that the floor has only three DOF per floor, two translations, and one rotation on the plan. On the other hand, for some buildings with floor plans in elongated shapes, a semi-rigid behaviour can be observed (see [Figure 3.4](#)). This flexibility of the floor affects the distribution of lateral loads over the resisting elements (MOON AND LEE, 1994).

Figure 3.4 – Rigid Diaphragm and Semi Rigid Diaphragm behaviours.

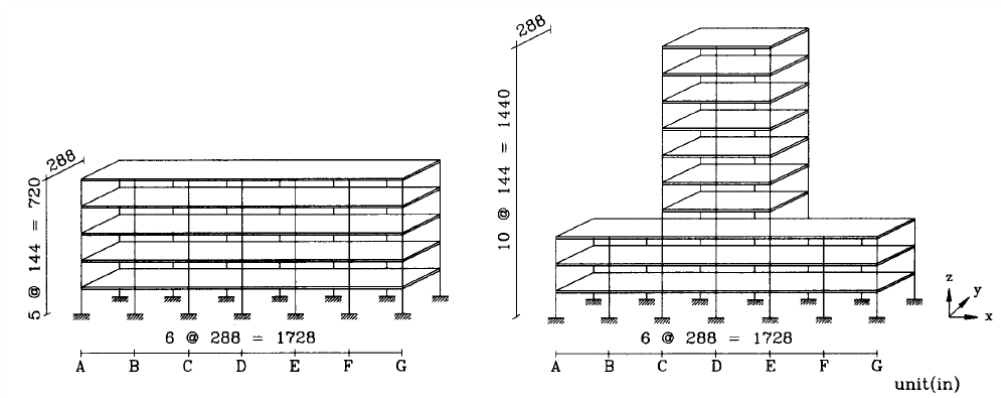


Source: Moon and Lee (1994).

Moon and Lee (1994) performed several numerical experiments with two types of structural systems: frame systems and frame-shear wall systems. The number of floors varied from two to 20 floors in the study, whilst the elongation varied from three to six bays. *Figure 3.5* shows some examples of the structures studied by Moon and Lee (1994).

The effects of in-plane floor slab flexibility seemed to be more distinct in buildings with lesser storeys and higher aspect ratio of the floor slab. Experiments showed a decrease in the natural frequency of the building for semi-rigid diaphragms. The decrease was more pronounced for higher modes of vibration.

Figure 3.5 – Example of building structures.



Source: Moon and Lee (1994).

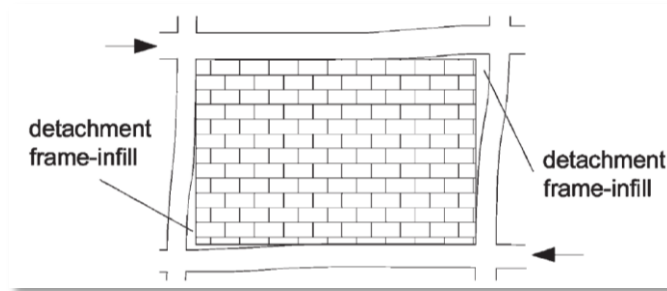
3.4 MODELLING NON-STRUCTURAL ELEMENTS

The use of a linear analysis to account for effects of NSW on the maximum response of the structure leads to unrealistic results, since the supporting structure might be working within the non-linear range of behaviour of the NSW (VILLAVARDE, 2006; KIM ET AL., 2009).

As the amplitude of deformation grows, the NSW may crack or separate from the neighbouring structural components (see *Figure 3.6*), leading to a loss of stiffness and incurring in non-linear behaviour (KIM ET AL., 2009).

However, the use of NSW in structural models under low stress levels, such as one-year-return-period wind loadings, might improve the accuracy of the structural response (KIM ET AL., 2009).

Figure 3.6 – Joint frame in-fill under horizontal loads.



Source: Cavaleri and Papia (2003).

Cavaleri and Papia (2003) presented a methodology to calibrate an already known strut model for in-filled frames with NSW. The study performed consisted of the analysis of the response of the frame submitted to lateral loads. The study showed linear behaviour of both the stiffness and the damping for the in-filled frames with NSW, provided that the range of amplitudes were low enough.

Kim et al. (2009) investigated the effects of NSW and plain concrete walls (PCW) in buildings under wind loads of approximately one-year-return-period winds. The walls were modelled with plate elements and stress values were verified to be lower than the cracking stress. The modelling of these elements increased by 14% the natural frequency of the FE model studied by Kim et al. (2009).

3.5 USE OF THE PROBABLE YOUNG'S MODULUS

Kim et al. (2009) examined the values of probable concrete strength. According to the Korean Building Code, an increase in the modulus of elasticity can be expected, since the probable concrete strength can be 21% higher than the one specified in design. As the modulus of elasticity is proportional to the square-root of the concrete strength, an increase of 10% can be estimated.

The results of Kim et al. (2009) showed an increase of 7 – 12% in the natural frequency of the tested buildings. In some cases, when the actual modulus of elasticity was available, the error between measured and calculated natural frequencies of the buildings ranged from 0% to 4%.

Eq. (3.1), from the Brazilian code NBR6118-2014, shows the increase in the elasticity modulus with the increase in the concrete age:

$$E_{Ci,\infty} = \lim_{t \rightarrow \infty} E_{Ci,28} \left\{ \exp\left\{s \left[1 - (28/t)^{0.5}\right]\right\} \right\}^{0.5} = E_{Ci,28} \exp(s/2) \quad (3.1)$$

where:

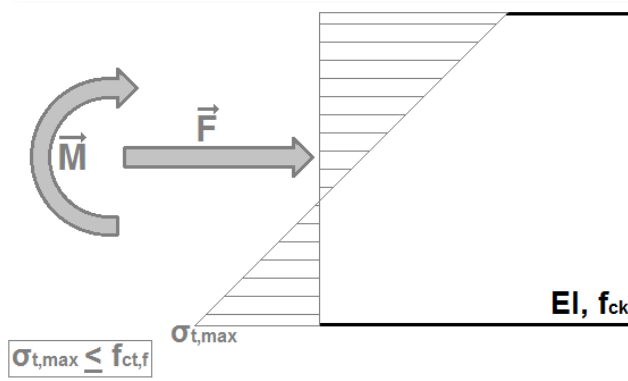
- $E_{Ci,28}$ is the Young's Modulus of the concrete after 28 days, according to NBR6118-2014;
- t stands for the age of the concrete, in days;
- s is a coefficient depending on the category of cement: in the tall buildings analysed in [Chapter 7](#), it assumes the value 0.25;
- $E_{Ci,\infty}$ stands for the Young's Modulus of the matured concrete: probable E .

3.5.1 STIFFNESS FOR CRACKED SECTIONS

Several building codes define an equivalent flexural stiffness for a concrete member when the bending moment acting on it causes the formation of cracking. A suitable illustration of NBR6118-2014's SLS for cracking formation (ELS-F) is given in [Figure 3.7](#).

In this figure, the internal forces are characterized by the bending moment " M " and axial force " F ," generating a maximum tensile stress " $\sigma_{t,max}$ ". This tensile stress should not exceed the maximum value " $f_{ct,f}$ " in order to keep the original flexural stiffness " EI " for the concrete member.

Figure 3.7 – ELS-F cracking formation.



Source: Author.

The " $f_{ct,f}$ " value stands for the tensile strength of the concrete members subjected to bending moment solicitations. The moment " $M(t)$ " at each time step shall obey the relation in eq. (3.2) to keep a full flexural stiffness (NBR6118-2014).

$$\frac{M(t)c}{I} \leq \sigma_c(t) + 0.3f_{ck}^{2/3} \quad (3.2)$$

where:

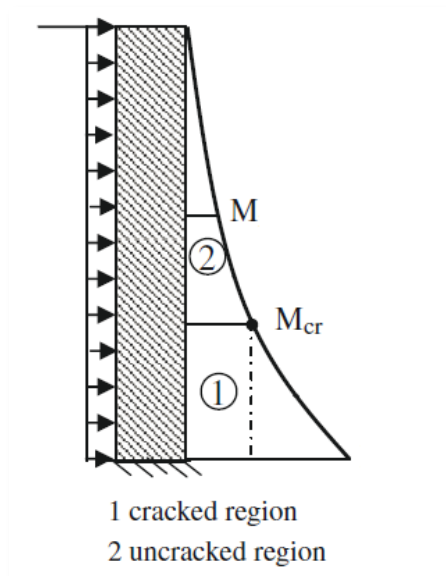
- f_{ck} is the concrete's characteristic strength after 28 days, according to NBR6118-2014;
- $\sigma_c(t)$ is the compression stress due to the axial force "F(t)" at each time step;
- c stands for the distance from the neutral axis with pure bending to the most distant point in the section of the concrete member.

It is important to note that for beams and floor slabs, the axial force effects tend to be negligible, leading to a shortened form of eq. (3.2):

$$M(t) \leq 0.3f_{ck}^{2/3} \frac{I}{c} \quad (3.3)$$

Lee, Kim and Chun (2002) analysed the effect of cracked sections for the floor slabs of three different buildings, modelling them with an overall stiffness of "0.3EI". In the results, the natural frequencies of shear wall structures decreased in up to 16% due to the decrease of the flexural stiffness of floor slabs. Even so, the natural frequencies presented an increase around 66% in some cases, when compared to models without modelling out-of-plane stiffness of floor slabs, even with reduced stiffness for these elements.

Figure 3.8 – Shear wall modelling with cracked and uncracked regions.



Source: Kara and Dundar (2009).

Kara and Dundar (2009) performed a series of tests to assess more accurately the shear wall displacements under severe loads and compared it with ACI stiffness models. Primarily, these shear walls were modelled as cantilever beams, with two different load intensity regions, leading to two different stiffness models for these structural elements along the building's height. In [Figure 3.8](#), the “ M_{cr} ” value represents the maximum value “ $(\sigma_c(t) + 0.3f_{ck}^{2/3})I/c$ ” (see eq. (3.2)) above which the cracked section occurs in the shear wall element.

The discussion about the use of the characteristic concrete strength “ f_{ck} ” or the probable concrete strength “ $f_{cj}, j \rightarrow \infty$ ” to calculate the maximum bending moment of structural elements still remains (eq. (3.2) and (3.3)). To calculate these strengths, the most reliable models today use the characteristic concrete strength and so will the studies in this thesis. The Young's modulus, however, remains calculated with the concrete ageing to validate the modelling criteria, since the contribution of this criterion to the building's natural frequencies have been tested by now (KIM ET AL, 2009).

3.6 SYNTHESIS ABOUT STRUCTURAL CRITERIA

A wide range of possibilities can interfere with the assessment of a tall building's stiffness, natural frequencies, and dynamic responses. These possibilities begin with the modelling criteria (MOON AND LEE, 1994; LEE, KIM AND CHUN, 2002; CAVALERI AND PAPIA, 2003; VILLAVERDE, 2006; KIM ET AL., 2009), passing through material properties (LEE, KIM AND CHUN, 2002; KARA AND DUNDAR, 2009; NBR6118-2014), and include strong interferences from calculation methods (HUANG AND CHEN, 2007; WU ET AL., 2007; ROSA ET AL., 2012; FERRARETO ET AL., 2014), as observed in [Chapter 2](#).

A building's stiffness can vary up to 33% due to FE modelling criteria, whilst the acceleration results can vary 10% due to higher modal contribution ([Chapter 2](#)). In addition, the lack of material properties to be used and the choice of the appropriate analysis might aggravate the imprecision of the dynamic analysis of a tall building. Building codes and wind codes have suitable criteria to evaluate the SLS in slender tall buildings and to verify these responses along with WTTs. What remains an issue, however, is the lack of a proper link between these criteria to strengthen the link “Dynamic Effects” in the Davenport's chain (see [Figure 1.24](#)).

4 WIND MODELLING CRITERIA

4.1 INTRODUCTION

Part of the results of the wind tunnel testing procedures is overall building's responses over the different azimuths normalized by the wind pressure at a certain height. Acceleration and angular velocity are the main concern for comfort, as it will be seen in this thesis, and in order to assess the final response one should multiply it by the wind pressure for that sector, introducing the wind climate data in the analysis according to the Davenport's chain of wind loading (see [Figure 1.5](#)).

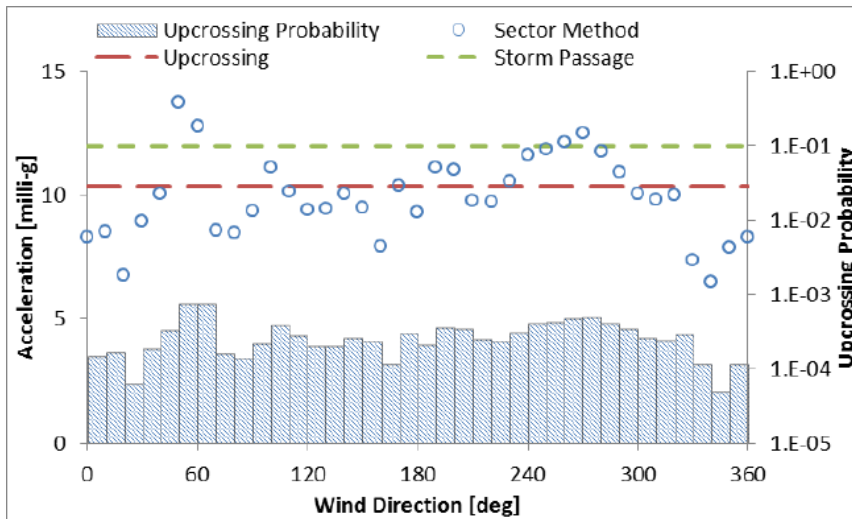
The worst-case method (see [section 4.2](#)) is straightforward, since it suffices to multiply the responses by the wind pressure, taking into consideration the terrain roughness, fetch, and topography for each wind sector. The sector-by-sector methods (see [section 4.3](#)) use a different approach by considering that the wind pressure varies according to the wind climate preference on each sector, presenting an independent statistical distribution for each sector of the compass. The up-crossing-method (see [section 4.4](#)) requires an additional statistical analysis and will be concisely discussed here.

Simiu and Scanlan (1996) illustrate the directional dependency behaviour of structures subjected to wind loads. The illustration consists of a circular flag pole in a horizontally homogenous terrain, anchored on its foundation by four anchor bolts onto a squared base plate. Despite of the constant values for the bending moment at the base and for the base shear force over different directions of the wind compass, the response of some structural members is highly directional. For example, the uplift force acting on the anchor bolts have a ratio of $\sqrt{2}$ between the responses when the wind is parallel to the diagonal of the base plate and when compared to the response where the wind is parallel to its side. A building's acceleration for human comfort purposes is no different and may benefit from a directional approach.

According to Isyumov et al. (2014), the sensitivity of tall buildings to wind direction is customarily examined in wind tunnels. Burton et al. (2015) analysed different approaches to evaluate directionality effects on wind-induced responses of tall buildings and brought five different scenarios: non-directional building in a non-directional wind climate (1), non-directional building in a directional wind climate (2), directional building in a non-directional wind climate (3), directional building in a

directional wind climate with prevailing wind direction different from the critical direction for the building's response (4), and directional building in a directional wind climate with prevailing wind direction equal to the critical direction for the building's response (5). The results were evaluated by the same methods described by Isyumov et al. (2014), with the exception of the worst-case method. The results for the third scenario are presented in *Figure 4.1* and show that even for a non-directional wind climate, when the building's response is directional, a noticeable reduction in its final response occurs when a directional approach like the up-crossing method is applied.

Figure 4.1 – Acceleration results for scenario 3.



Source: Burton et al. (2015).

This reduction can be explained by the contribution of the building's response from each sector in the overall failure probability. Simiu and Scanlan (1996) described the general principle of the methods using the feature of different sector contributions, considering the results of each sector statistically independent.

$$F_Q(Q < R) \cong \prod_i \text{Prob}(v_i < v_i^l) \quad (4.1)$$

where:

- $F_Q(Q < R)$ is the cumulative probability of the largest yearly wind effect "R";
- $\text{Prob}(v_i < v_i^l)$ is the probability of wind speed " v_i " in sector " i " of to cause effect "R" when reaching value " v_i^l ".

The first approach proposed by Simiu and Scanlan (1996) considered the division of the 360° compass in eight equal portions ($1 \leq i \leq 8$), whilst current sector-by-sector methods propose a 22.5° division (16 sectors), and the up-crossing method can be performed with smaller sectors (10°, for example).

In *Figure 4.1*, it is possible to verify that the results of the up-crossing method, for example, stand between the lowest building response and the highest one. It should be noted that the sector-method responses for a non-directional wind climate are equivalent to the worst-case method. In this case, the up-crossing method definitely represents a reduction in the overall response, since the comfort assessment via building's accelerations is made using the most severe azimuthal result. This method will assess a level of acceleration for a given return period, extending the reliability concept of failure probability (SLS failure, only) for all azimuths, as in the eq. (4.1) models.

It is clear that a directional approach to evaluate the overall building's acceleration at the floor of interest might be beneficial. The features of each method shall be briefly described in this chapter.

4.2 WORST-CASE METHOD AND NBR6123-1988

The worst-case method assumes that the wind approaches the structure from the azimuth for which the building's response is the most severe. It is currently used in several normative codes, like the National Building Code of Canada (NBCC, 1990) and the National Standard of People's Republic of China (NSPRC, 2012), to name a few. The Brazilian national wind code (NBR6123-1988), in addition to directional methods, also proposes the worst-case method, where the wind speed is based on a statistical approach using the annual maxima (ISYUMOV ET AL., 2014). The extreme distribution is usually a Type I with Gumbel parameters (ISYUMOV ET AL., 2014), whilst NBR6123-1988 uses a Weibull distribution, as it can be seen in eq. (4.3).

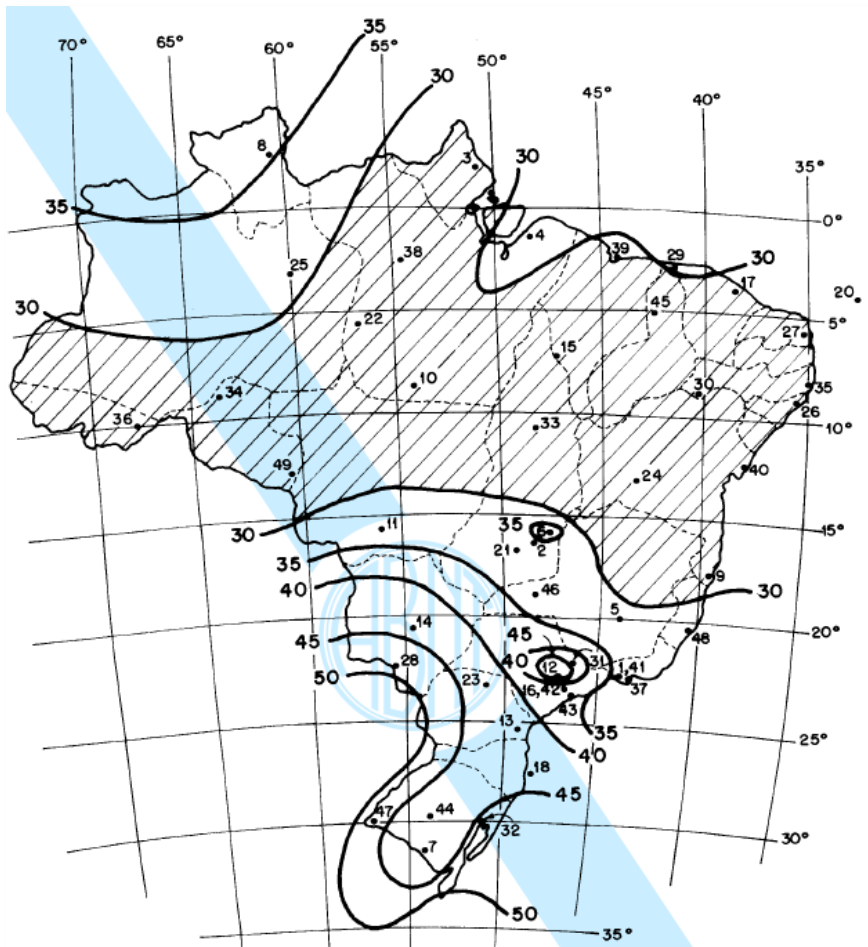
$$V_k = V_0 S_1 S_2 S_3 \quad (4.2)$$

$$S_3 = 0.54 \left[-\frac{\ln(1 - P_m)}{m} \right]^{-0.157} \quad (4.3)$$

where:

- V_k is the characteristic wind speed to calculate the wind pressure;
- V_0 stands for the basic wind speed at the chosen location, regardless of the terrain roughness, return period, topography, or height, and can be assessed using the isocurves in *Figure 4.2*;
- S_1 is the factor to evaluate the effects of topography changes in the wind speed profile;
- S_2 is the factor that takes into account the wind speed variation with height and terrain roughness factors;
- S_3 is the factor that takes into account the return period, also called the “statistical factor”;
- P_m and m are, respectively, the cumulative probability and the return period.

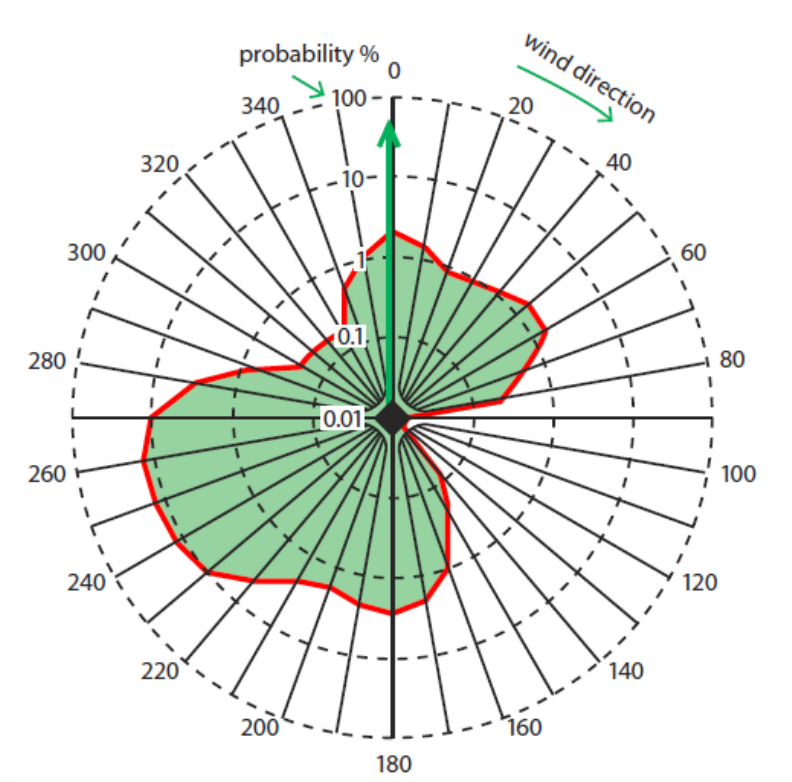
Figure 4.2 – Isocurves for V_0 , in m/s.



Source: NBR6123-1988.

This is a straightforward method, since the aerodynamic data just need to be multiplied by a value of wind pressure for a given return period. The only problem of this method is that it doesn't take into consideration the sensitivity of the tall building's responses concerning different azimuths, and the preferences of the wind climate for strong synoptic winds for certain sectors of the compass (ISYUMOV ET AL., 2014) (see [Figure 4.3](#)).

Figure 4.3 – Example probability exceedance for wind speed above the value for 50-year return period.



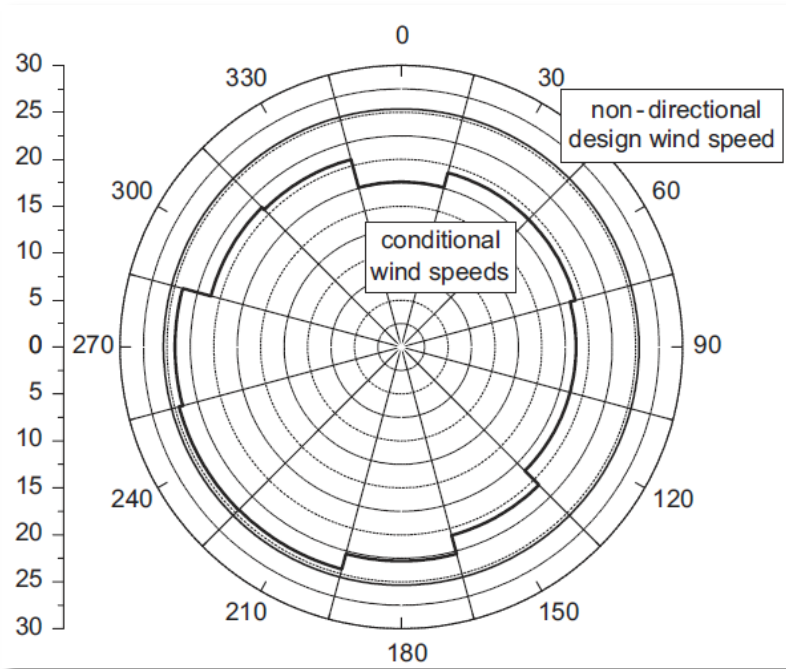
Source: Irwin et al. (2013).

Since the annual maxima is not gathered from only one sector, the distribution using the annual maxima from different sectors leads to greater values than the highest design wind speed assessed by the sector-by-sector methods (see [Figure 4.4](#)), which are further discussed in [section 4.3](#).

This wind speed distribution, along with the consideration that the wind will approach the structure from the azimuth where its responses are greater, lead to very conservative results (ISYUMOV ET AL., 2014; BURTON ET AL., 2014). The ASCE7 (2010) guideline uses the “ K_d ” factor to take into consideration the

directionality effects on structures (BURTON ET AL., 2015), reducing the overall wind loads in tall buildings in up to 15%, as it assumes the value of 0.85 for this category of structure.

Figure 4.4 – Comparison between non-directional and conditional wind speed per sector in Düsseldorf.



Source: Kaspersky (2007).

4.3 SECTOR-BY-SECTOR METHODS

The sector-by-sector methods present several variations, with the common feature that they are all based on extreme values of wind speed for each sector for a given site (HOLMES AND BEKELE, 2015), where the sectors are considered as being statistically independent from each other (ISYUMOV ET AL., 2014; HOLMES AND BEKELE, 2015).

Holmes and Bekele (2015) describe a few sector-by-sector methods in their study, starting from the worst-case method, which is a particular sector method that was already presented in the previous section.

Subsequently, Holmes and Bekele (2015) presented the sector-22.5° method, an approach where the wind speeds " $V(1/R; \delta\theta_i)$ " are analysed separately for each sector " $\delta\theta_i$ " and return period "R" (or annual probability of exceedance " $1/R$ "). These sector wind speeds are lower than the overall reference wind speed

“ $V(1/R)$ ”, since the annual probability of exceeding “ $V(1/R)$ ” in the course of a year is smaller for one sector than it is for all sectors combined. The worst sector wind speed “ $[V(1/R; \delta\theta_i)]_{MAX}$ ” is replaced by the overall wind speed for the given return period “ $V(1/R)$ ” and the remaining sectors’ wind speed are given by eq. (4.4) (IRWIN ET AL., 2005).

$$V_{Des}(1/R; \delta\theta_i) = \frac{[V(1/R; \delta\theta_i)]}{[V(1/R; \delta\theta_i)]_{MAX}} V(1/R) \quad (4.4)$$

The method proceeds by multiplying the building response by the matching wind pressure for each azimuth.

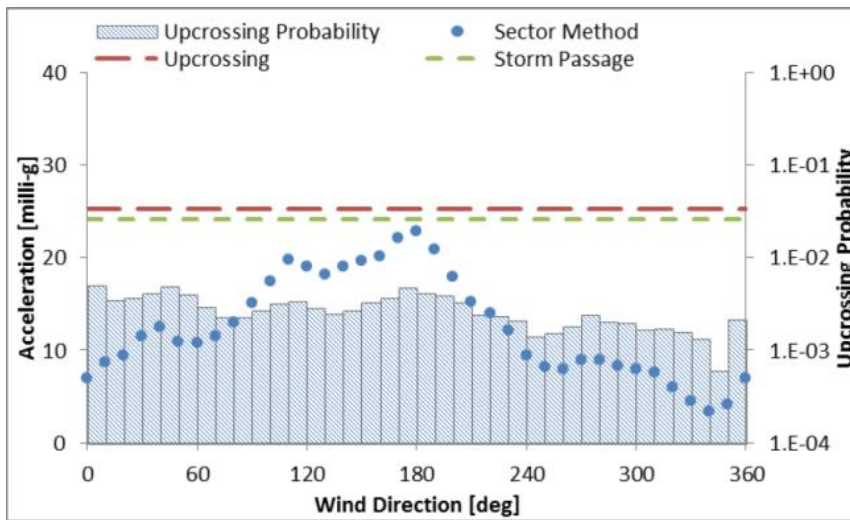
Holmes and Bekele (2015) use 22.5° sectors arguing that it is the standard sector interval used by meteorological agencies that provide data to wind studies. In addition, it is an interval for which extremes from adjacent sectors can be considered as statistically independent (HOLMES AND BEKELE, 2015). Kaspersky (2007) used 30° sectors (see [Figure 4.4](#)), whilst Simiu and Scanlan (1996) suggested 45° sectors in their statistical approach (not exactly a sector method). Irwin et al. (2005) state that some structures’ responses can greatly vary over a 5° or a 10° direction change, and sector methods consider a severe response of the structure over the entire extension of the sector used (22.5°, 30° or 45°), instead of only the corresponding 5° or 10° sector, leading to conservative results. This great variability in the responses over the azimuths is quite typical for tall buildings’ structures and is going to be verified in [Chapter 7](#).

One of the main problems of using sector methods to evaluate acceleration is that it doesn’t take into consideration the contributions of all the responses in the final assessment. Therefore, it often presents conservative results when compared to other procedures, such as the up-crossing method (ISYUMOV ET AL., 2014; BURTON ET AL., 2015; HOLMES AND BEKELE, 2015). Burton et al. (2015) noticed that the sector-by-sector method presented smaller responses for scenario 4 (see [Figure 4.5](#)). Isyumov et al. (2014) reached similar results by assessing base moments of a generic building’s response data in the studied wind climates. Fewer results were achieved for the sector-by-sector method after a comparison with the

up-crossing method, when the critical direction for the base moment response was distinct from the wind climate direction of preference.

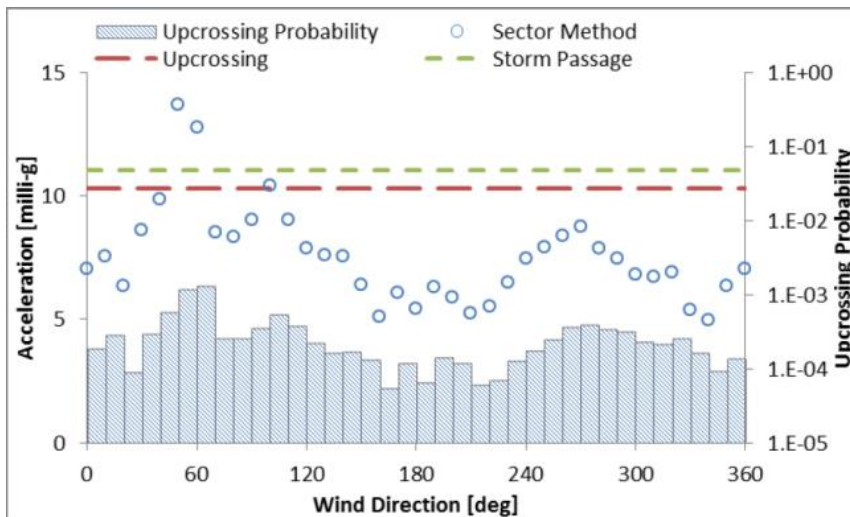
On the other hand, the results obtained by Burton et al. (2015) and Isyumov et al. (2014) for the sector-by sector method presented a greater response when compared to the up-crossing method for scenario 5 (see [Figure 4.6](#)).

Figure 4.5 – Acceleration results for scenario 4.



Source: Burton et al. (2015).

Figure 4.6 – Acceleration results for scenario 5.



Source: Burton et al. (2015).

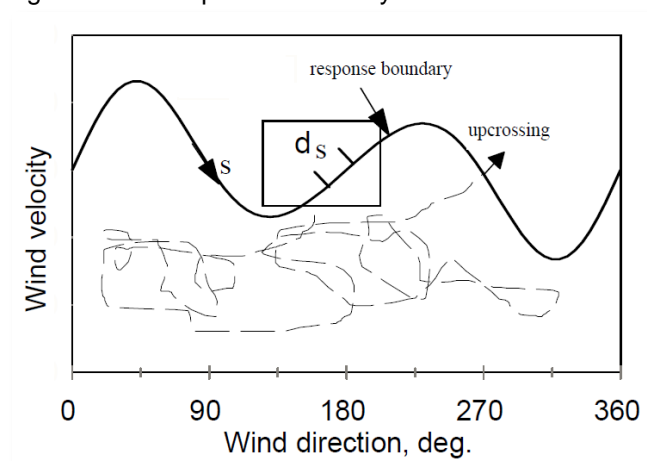
Another factor that contributes to the lack of precision of the sector methods lies in the following fact: if all sectors are independent from each other, when the

probability of exceedance is “ $1/R$ ” for each sector, the overall probability exceedance is “ N/R ”, where “ N ” is the number of sectors (IRWIN ET AL., 2005). This time, the contribution is for the non-conservatism of the method, since the overall probability is greater than the sector probability, which indicates a smaller return period for the response. Adjusting each ratio “ $[V(1/R; \delta\theta_i)]/[V(1/R; \delta\theta_i)]_{MAX}$ ” from eq. (4.4) in order to achieve an overall probability of “ $1/R$ ” instead of “ N/R ” is one possibility. However, it requires an element of judgement from the wind engineer (IRWIN ET AL., 2005).

4.4 UP-CROSSING METHOD

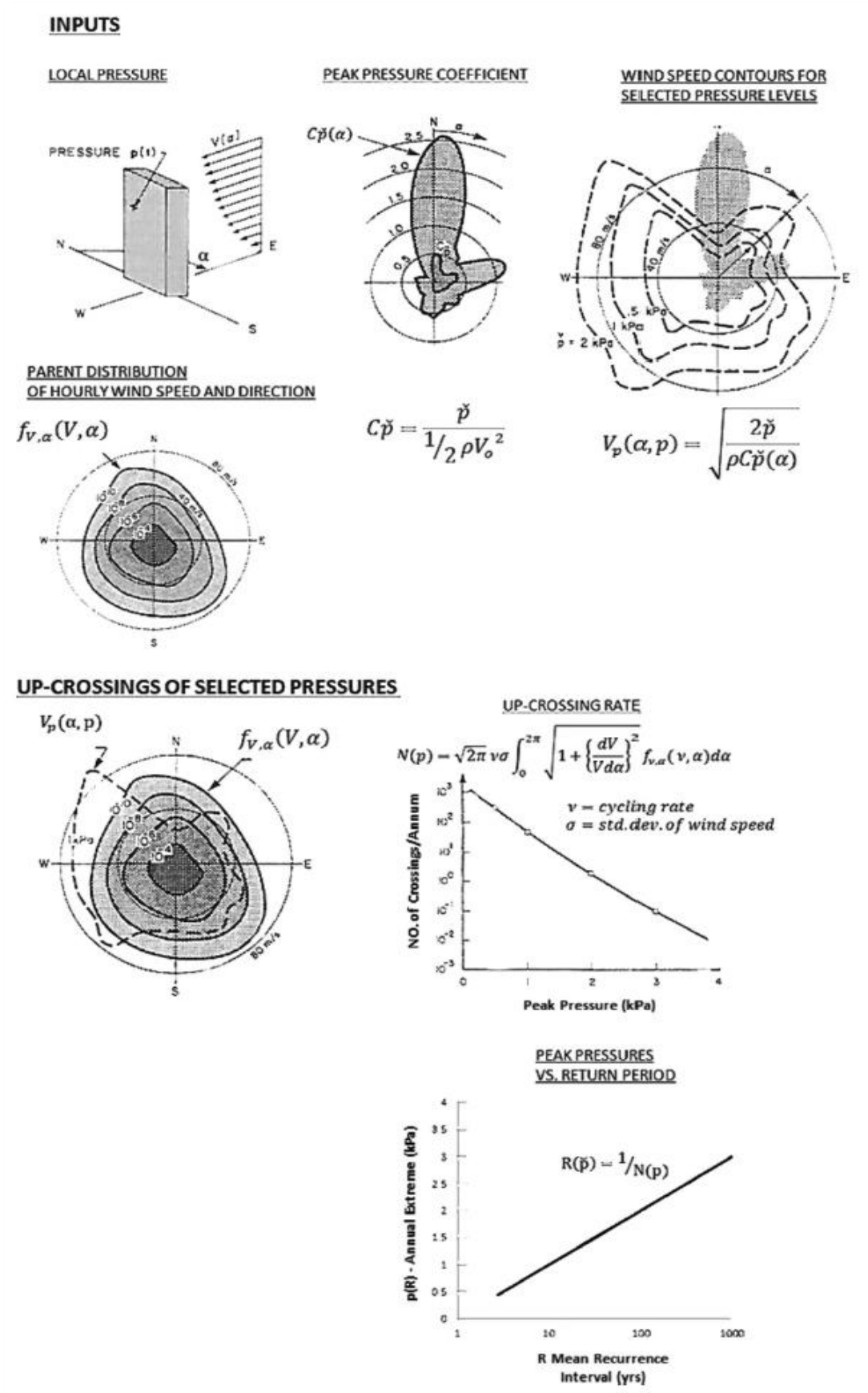
According to Irwin et al. (2005), the question directly asked by the up-crossing method is “*How often a given response magnitude will occur*”. Differently from the sector methods, which attribute a different response to each direction, the up-crossing method looks for the asked magnitude of the response regardless of the direction. To develop a better understanding of the procedure, one might observe the wind speed associated with a given building’s response magnitude (for example, a 5.0milli – g overall acceleration) for each sector of the compass. This curve is denominated ‘response boundary’ and can be seen in [Figure 4.7](#).

Figure 4.7 – Response boundary.



Source: Irwin et al. (2005).

Figure 4.8 – Up-crossing method overview.



Source: Adapted from Isyumov et al. (2014).

The response boundary formulation is better illustrated in [Figure 4.8](#), along with a general overview of the procedure. In this figure, the response analysed is the peak suction pressure “ \check{p} ” in the building’s façade, calculated by eq. (4.5):

$$\check{p} = C\check{p} \frac{\rho V_0^2}{2} \quad (4.5)$$

where “ $C\check{p}$ ” is the pressure coefficient directly measured in the wind tunnel, “ ρ ” is the air density, and “ V_0 ” is the wind speed associated with the response “ \check{p} ”, which can be calculated by rearranging eq. (4.5) into:

$$V_0(\alpha; \check{p}) = \sqrt{\frac{2\check{p}}{\rho C\check{p}(\alpha)}} \quad (4.6)$$

The analysis of the up-crossing method proceeds by analysing wind climate data, which can be fitted by a Weibull expression (IRWIN ET AL., 2005):

$$P_i(V) = A_i e^{-\left(\frac{V}{C_i}\right)^{k_i}} \quad (4.7)$$

where “ $P_i(V)$ ” stands for the probability that the wind speed will exceed value “ V ” at sector “ i ” whilst “ A_i ”, “ C_i ” and “ k_i ” stand for the Weibull parameters for each sector (IRWIN ET AL., 2005). From eq. (4.7), the probability density function “ $p_i(V; \alpha_i)$ ” can be deduced:

$$p_i(V_i; \alpha_i) = \frac{1}{\Delta\alpha_i} \frac{A_i k_i}{C_i} \left(\frac{V_i}{C_i}\right)^{k_i-1} e^{-\left(\frac{V_i}{C_i}\right)^{k_i}} \quad (4.8)$$

Then, according to Irwin et al. (2005), the rate “ R ” at which the magnitude of the response will happen is:

$$R = \sum_{i=1}^N \frac{1}{2} |\overline{\check{V}}|_i \sqrt{1 + \frac{|\overline{\check{\alpha}}|_i^2 \left(\frac{dV_i}{d\alpha}\right)^2}{|\overline{\check{V}}|_i^2} \frac{A_i k_i}{C_i} \left(\frac{V}{C_i}\right)^{k_i-1} e^{-\left(\frac{V}{C_i}\right)^{k_i}}} \quad (4.9)$$

Parameters “ $|\overline{\check{\alpha}}|$ ” and “ $|\overline{\check{V}}|$ ” can be calculated by empirical expressions as functions of wind speed “ V ”, and are suitable for extra-tropical winds (IRWIN ET AL., 2005):

$$|\overline{\check{V}}| = 0.065V + 0.5e^{-0.252V} \quad (4.10a)$$

$$\overline{|\alpha|} = 6.5(1 + 3.3e^{-0.252V}) \quad (4.10b)$$

Finally, return period “T” associated with the magnitude of the response chosen is calculated by (IRWIN ET AL., 2005):

$$T = \frac{1}{8760R} \quad (4.11)$$

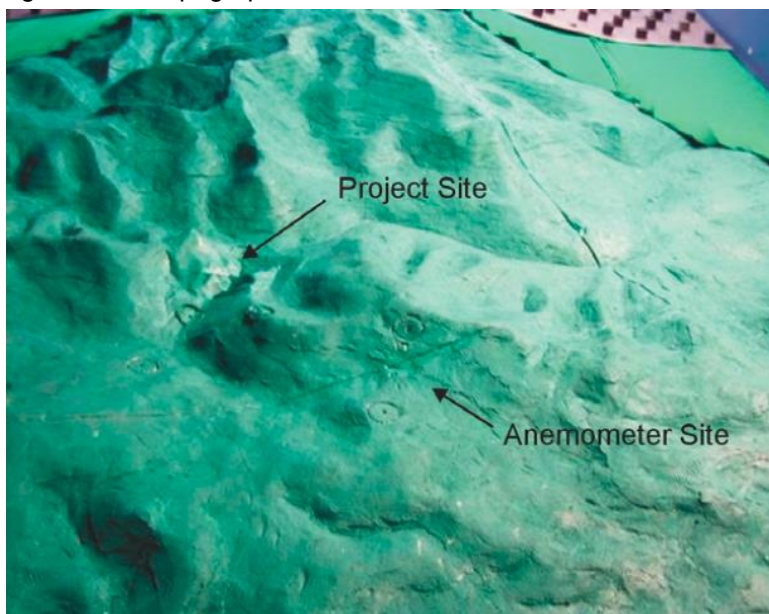
A series of response magnitudes can be tested in order to create a table of return period versus response magnitudes and interpolated for the required values.

4.5 WIND SPEED IN OPEN TERRAIN VS. WIND SPEED ON SITE

One of the most essential steps in the Davenport’s chain is the introduction of the wind speed data from the building’s site, since the wind pressures that generate the façade loads are proportional to the square of the design wind speed. Therefore, the quality of the derived directional model is governed by the quality of the measured data (IRWIN ET AL., 2005).

According to Irwin et al. (2005), the exposure of the anemometers to obtain wind records needs to be considered and appropriate corrections must be made when the exposure is less than ideal. An ideal exposure is a standard open field terrain, with roughness parameter “ $z_0 = 0.02m$ ” in all directions.

Figure 4.9 – Topographic model to transfer anemometer data.



Source: Irwin et al. (2005).

When the exposure is less than ideal (in a mountainous terrain, for example), other techniques (like a topographic model, for instance, as in [Figure 4.9](#)) can be used to provide better correlation between the anemometer's site and the tall building's site.

The final result of this operation may be a table correlating the wind speed at the tall building's site with the wind speed at the anemometer's site for each studied azimuth.

4.6 WIND MODELLING IN BRAZILIAN WIND CLIMATE

Today, there is a debate about the applicability of the directional wind approach to the Brazilian wind climate. The criticism of directional methods lies mainly in the non-synoptic characteristic of the winds in certain regions of the country, where downbursts have been observed. Moreover, the temperature increase in the Atlantic Ocean due to recent climatological changes has enabled the formation of hurricanes in the southeast and south coasts of Brazil. These climatological changes were discussed in the [14th International Conference on Wind Engineering \(ICWE\)](#), in Porto Alegre (Brazil), where hurricane Catarina (March, 2004) was cited in the opening ceremony. The main argument is that these non-synoptic winds have no directional preference when they hit the structure and, therefore, they compromise the applicability of directionality methods. Holmes (2001) explains the extreme winds in Brazil as a mixture of large extratropical depression systems and local thunderstorm downdrafts. Holmes (2005) also states that thunderstorm winds are dominant in most places.

Yet, Brazilian wind code NBR6123-1988 allows the use of directionality to assess building's responses if properly justified. Hence, the procedures provided by this wind code to assess wind loads refer to synoptic winds, conflicting with the previous statements about Brazilian wind climate. Finally, one might recall the results obtained by Burton et al. (2015) on directional structures in non-directional wind climates, where the use of the worst-case method is conservative and when the use of the up-crossing method may lead to smaller responses.

The semi-probabilistic approaches with partial safety factors currently used by structural engineers feature a very definite line between actions and strengths (SCHNEIDER, 2006). In these methods, for some azimuths, the probability of failure

or wind effect occurrence will have exactly the required value. However, for the remaining azimuths the result might be too conservative, leading to overall conservative results. Directional approaches like the up-crossing method or the storm passage method allow for a direct relation between the response magnitude and the return period (ISYUMOV ET AL., 2014; BURTON ET AL., 2015), leading exactly to the response magnitude or occurrence probability sought.

5 COMFORT CRITERIA

5.1 INTRODUCTION

Human comfort in a tall building's wind-induced motion is a very complicated subject of analysis due to the extensive range of variables on which it relies. Previous sections of this thesis explained several of these variables purely from the mechanical and statistical points of view, whilst this chapter will cover the same variables from the users' viewpoint (see *sections 5.2 "Kinematic properties of the motion," 5.3.2 "Return period," 5.3.3 "Duration," and 5.3.4 "Peak, rms and waveform."* Moreover, psychological features, biodynamic amplification and visual cues will also be discussed (see *section 5.3 "Structural, psychological and statistical properties of motion"*) along with the latest research in this field.

5.2 KINEMATIC PROPERTIES OF THE MOTION

According to Taranath (2012), the users' comfort during wind-induced motion in tall buildings can be assessed through several indicators, such as displacement, velocity, acceleration, and the derivative of acceleration. Acceleration, however, has become the standard measure of comfort due to the facility of its field measurements and analytical verification. Chang (1973) explored each of these indicators in his work. In this chapter, each of these kinematic properties will be briefly presented.

5.2.1 AMPLITUDE OF MOTION

Chang (1973) used the amplitude of motion and the fundamental frequency of the building to estimate the acceleration, assuming a sinusoidal vibration. Afterwards, Chang (1973) made a comparison with a set of comfort curves to categorize comfort levels of a building: "non-perceptible," "perceptible," "annoying," "very annoying," and "unbearable."

The amplitude of motion provides the subject with apparent visual cues of the building's movement, such as visual parallax. It may also trigger noise cues, such as the creaking noises documented by Hansen et al. (1973). These visual and sound cues may confirm and/or increase the feeling of motion by other mechanisms of perception (KWOK et al., 2009).

5.2.2 VELOCITY

5.2.2.1 Linear velocity

Chang (1973) stated that individuals cannot feel velocity directly; they can only feel the indirect effects of it, such as the wind pressure on the body. Naturally, people free from atmospheric effects, vibrations, sounds, and visual cues cannot tell if they are moving at a constant speed or standing still.

Chang (1973) cited researchers who affirmed that the threshold depends on velocity for vibrations between 20Hz to 60Hz (frequencies far above the range of wind-induced vibrations in studies of comfort in tall buildings).

5.2.2.2 Angular velocity

Sarkisian (2012) presented from the Council of Tall Buildings and Urban Habitat (CTBUH) some criteria regarding torsional velocity: 1.5 mili – radians/s for one-year return period windstorms; 3.0 mili – radians/s for ten-year return period windstorms. In many cases, torsional velocities and accelerations can be more important than linear accelerations, since the slightest angular velocities can cause the user to see changes from a point of reference on the neighbouring structures (ISO10137, 2007; SARKISIAN, 2012).

5.2.3 ACCELERATION

5.2.3.1 Linear acceleration

The otolith organs, in the vestibular system, are deeply responsible for the detection of accelerations (CHANG, 1973; BURTON ET AL., 2006). In the ISO6897 Standard (1984), the main motion-perceiving cues are assumed to be those from the proprioceptive sensations and from the vestibular organs and, therefore, linear acceleration is the chosen property to evaluate comfort and perception of motion in that document, and the parameter of comfort evaluation for several other normative codes.

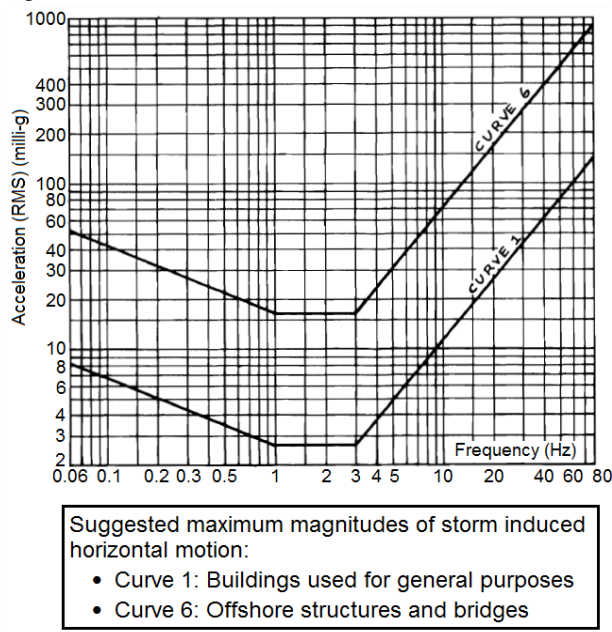
Chen and Robertson (1972) also concluded that the second or the third derivatives of displacement with time (see [Section 5.2.4 “Derivative of acceleration \(Jerk\)”](#)) are the most important for the users' discomfort.

The thresholds proposed by Chang (1973) for acceleration “a,” using a theoretical extrapolation of the aerospace industry’s data, are:

- Non-perceptible: $a < 5\text{milli} - g$;
- Perceptible: $5\text{milli} - g < a < 10 - 15\text{milli} - g$;
- Annoying: $10 - 15\text{milli} - g < a < 50\text{milli} - g$;
- Very Annoying: $50\text{milli} - g < a < 150\text{milli} - g$;
- Unbearable: $150\text{milli} - g < a$.

Chang (1973) recommended that, for accelerations of long duration (more than 5s), the threshold should be near $10\text{milli} - g$. Chang also suggested that acceleration levels equal to or greater than $10\text{milli} - g$ in a sinusoidal vibration of frequencies between 0.1Hz and 0.3Hz could easily induce sickness symptoms.

Figure 5.1 – RMS acceleration levels.



Source: Adapted from Irwin (1978).

Irwin (1978) used acceleration to evaluate the motion comfort/perception, and affirmed that it was the best parameter due to several reasons, emphasizing the simplicity of the use of only one parameter for motion. Irwin (1978) proposed different curves to evaluate both vertical and horizontal rms acceleration levels for different types of structures. *Figure 5.1* shows horizontal motion thresholds (acceleration) for offshore structures and buildings used for general purposes.

5.2.3.2 Angular acceleration (Yaw)

The angular acceleration can be noticed either by the vestibular system (CHANG, 1973; IRWIN, 1981) or by means of visual cues (IRWIN, 1979; ISO6897, 1984). Even a small torsional oscillation might cause exaggerated visual cues and such visual amplification would considerably reduce the threshold curves proposed by another assessment curve (IRWIN, 1978; ISO6897, 1984). The semi-circular canals of the hearing system are in charge of detecting the angular acceleration. For angular accelerations that last more than eight seconds, the threshold is about $0.5^\circ/s^2$ ($0.080\text{rad}/s^2$), according to Chang (1973).

Irwin (1981) built a room to study low-frequency pure-yaw vibration thresholds of perception and recurrent, equal sensations. The tests performed by Irwin included the effects of visual cues, a prejudice to the performance of tasks, and an evaluation of the combinations of linear and angular accelerations. From these tests and other unpublished results, Irwin (1981) proposed a base of perception for pure-yaw vibrations and adjusted a frequency-dependent coefficient to match the angular accelerations to a set of linear accelerations. Then, the author was able to create an assessment to combine both linear and angular accelerations (see eq. (5.1)).

$$V = h + r \times \ddot{\theta} \quad (5.1)$$

where “ $\ddot{\theta}$ ” stands for the rms yaw acceleration (rad/s^2) in a vibration frequency “ f ” (Hz), and “ h ” stands for the resultant horizontal rms linear accelerations (milli – g). Variable “ r ” stands for a factor that assesses the equivalency of the yaw vibration and the translational vibration (see [Figure 5.2](#)). This “equivalent” acceleration is then added to the horizontal resultant acceleration “ h ”.

“ V ” stands for the final combined acceleration to be compared with the criterion presented by Irwin (1981). Dimensionally, “ r ” is expressed in meters, as in eq. (5.1) and (5.2).

$$r = \left[\left(\frac{1}{f} \right) + \left(\frac{0.57}{\sqrt{f}} \right) \right] + 0.2 \times \left(1 - \frac{0.8}{f} \right) \quad (5.2)$$

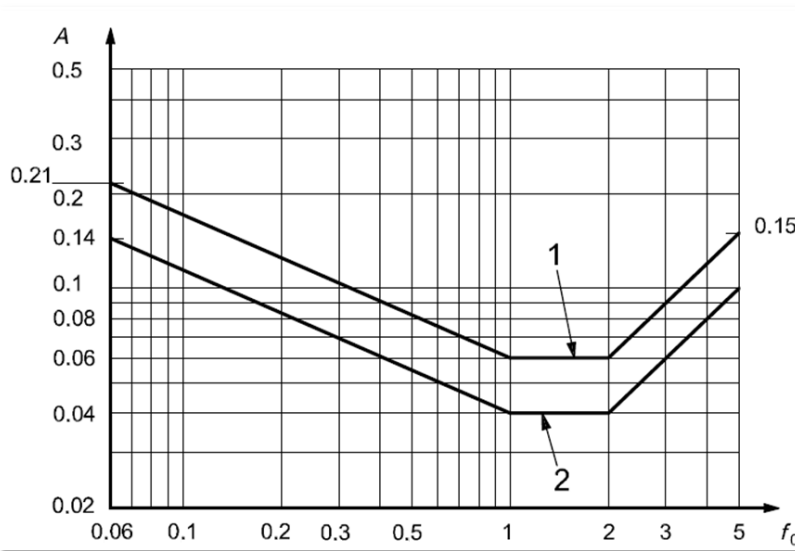
The angular acceleration is also responsible for causing the linear acceleration of “ $\vec{a}_\theta \times \vec{R}$ ”, where “ \vec{a}_θ ” stands for the torsional acceleration vector and

the range of frequencies of resonance of the eyeball is around 60 – 90Hz, and for the thorax-abdomen’s system, that value is around 3.0 – 4.0Hz.

Irwin (1978, 1981) took into consideration the frequency dependence and carried out studies with a range of frequencies between 0.063Hz and 1.0Hz.

The international standards of ISO6897 (1984) and ISO10137 (2007) predict a strong dependence between the threshold of comfort and the frequency of vibration. They consider a decreasing threshold curve between 0.063Hz and 1.0Hz, with a minimum value between 1.0Hz and 2.0Hz, and a further increase for frequencies greater than 2.0Hz (see [Figure 5.3](#) and [Figure 5.4](#)).

Figure 5.3 – Human comfort acceleration assessment (peak).



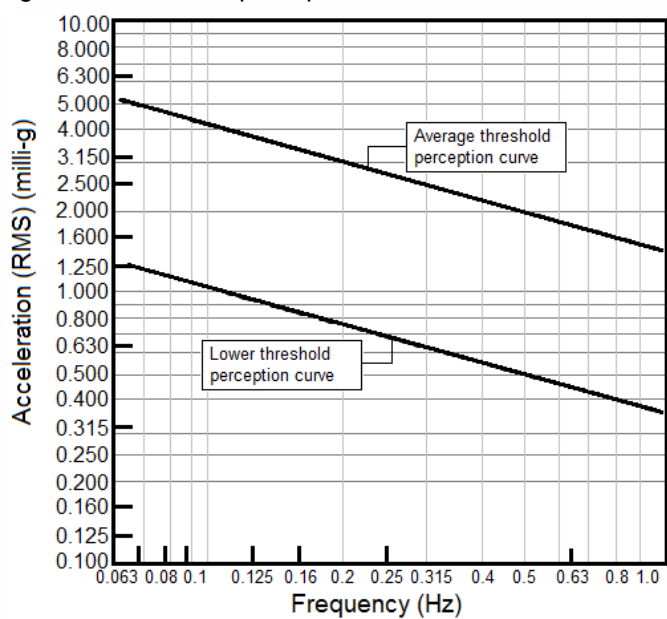
Source: ISO10137 (2007).

where:

- A stands for the peak acceleration (m/s²);
- f_0 is the natural frequency of the first torsional mode of vibration;
- 1 and 2 stands respectively for the thresholds for offices and residences/hotels.

In [Figure 5.4](#), the frequency used to evaluate the comfort level is the fundamental frequency of the building, considered to be the frequency of oscillation of the entire structure. Two standards are given: one higher threshold for offices (1), and a lower threshold for residential buildings (2).

Figure 5.4 – Human perception acceleration assessment (rms).



Source: Adapted from ISO6897 (1984).

Denoon et al. (2000) conducted field experiments on three wind-sensitive towers equipped with accelerometers and anemometers:

- Sydney Airport Control Tower: first natural frequency of 0.94Hz;
- Brisbane Airport Control Tower: first natural frequency of 0.54Hz;
- Port Operation Control Centre: first natural frequency of 0.39Hz.

Sydney's air traffic controllers were subjected to a long-term observation and to end-of-shift questionnaires, while Brisbane's air traffic controllers had vibration ranking push buttons, and the subjects at the Port Operation control had end-of-shift questionnaires only. The occupant perception was found to be frequency-dependent and consistent with ISO6897 (1984). [Table 5.1](#) shows the results for the three locations.

Table 5.1 – Results: accelerations, durations and complaints.

Location	Natural frequency (Hz)	rms acceleration threshold (milli-g)	Peak acceleration threshold (milli-g)	Hours/year perceptible acceleration	Days/year perceptible acceleration	Complaints
Brisbane Airport	0.54	0.65	2.5	30	20	No
Sydney Airport	0.94	0.65	2.4	705	185	Yes
POCC	0.39	0.80	2.8	897	187	?

Source: Denoon et al. (2000).

Burton et al. (2006) performed a landmark experiment on ten subjects in a shaking room to study uni-axial, fore-aft, and lateral biodynamic responses. The group was composed by ten subjects aged between 22 and 32 years old with a mean age of 27, which included men and women.

The test consisted in watching a video on a 430mm screen placed at a distance of 1.25m from the person, with their feet resting on the floor and seating on a stool with their hands between their knees, while the room would simulate the motion. Two digital video recorders documented peak head displacements, eliminating maximum and minimum values.

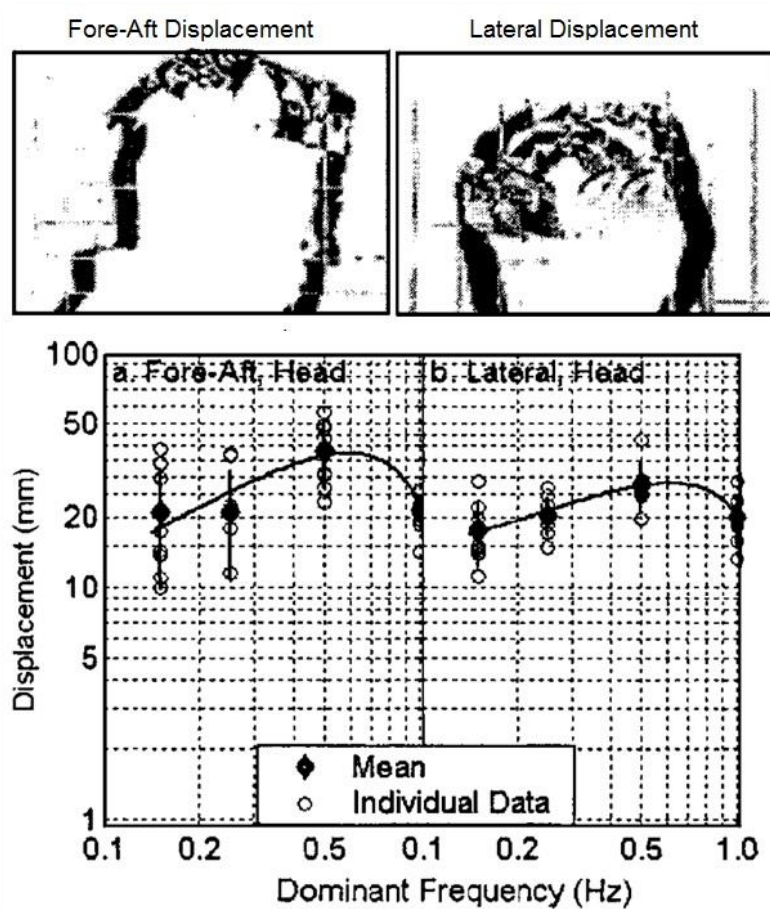
Figure 5.5 shows the mean peak-to-peak displacements of the head for each tested frequency. For each tested individual and each of the motion condition, the peak displacement was captured from the recorded videos and then turned into black and white images. In order to provide a displacement scale to these images, grids of 5mm squares were attached to the wall on the left and back sides of the subject. Finally, the peak images were superposed to create this figure. The peak displacement of each subject was calculated by the average value of the peak displacements for all the recorded cycles.

The displacement curve seems to increase up to the frequency value of 0.50Hz, from which it drops 45% toward the fore-aft direction, and 26% toward the lateral direction at 1.00Hz. The peak-to-peak displacement values were relatively small when compared to the moving room displacements. The peak-to-peak displacements in the moving room were calculated for each frequency by the harmonic motion equation:

$$D = \frac{(2 \times A)}{(2 \times \pi \times f)^2} \quad (5.3)$$

where “A” is the acceleration (13.5milli – g for the displacement studies) and “f” stands for the vibration frequencies: 0.15Hz, 0.25Hz, 0.50Hz, and 1.00Hz. The room displacements were 298mm, 108mm, 26mm, and 7mm for each respective frequency. In spite of the small head displacement values, the perception of motion or an enhanced perception due to a visual parallax is possible.

Figure 5.5 – Displacement results under sinusoidal vibration.

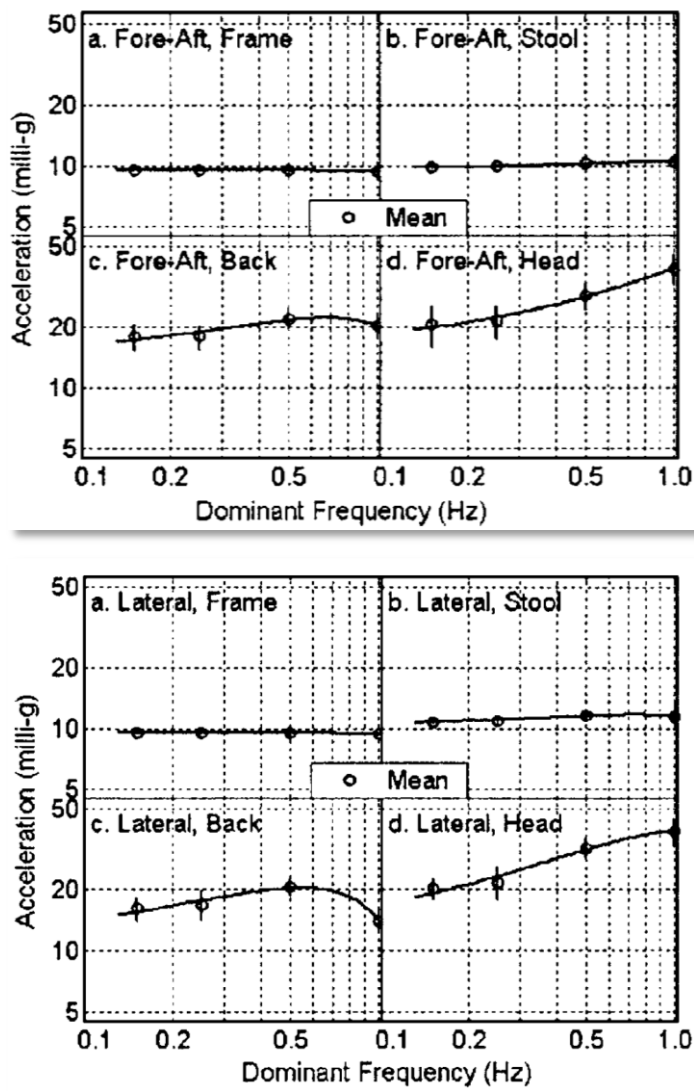


Source: Adapted from Burton et al. (2006).

To measure the acceleration magnification, four triaxial accelerometers weighing 50g each were used on the human subjects to measure fore-aft and lateral accelerations during the motion of the moving room. Two accelerometers were used on each subject: one was placed between the shoulder blades, while the other was placed on the top of their heads. The rms of the acceleration was used to evaluate body and head motions. Two other accelerometers were used to measure the accelerations of the stool and the frame.

The frame acceleration was assumed as the reference, and then used to divide the other accelerations in order to find the magnification factor for each movement and for each part of the body. The acceleration of the stool was almost constant and near to the values of the frames, and served to disregard important magnifications from this element. The accelerations and magnification factors are given in [Figure 5.6](#) and [Figure 5.7](#).

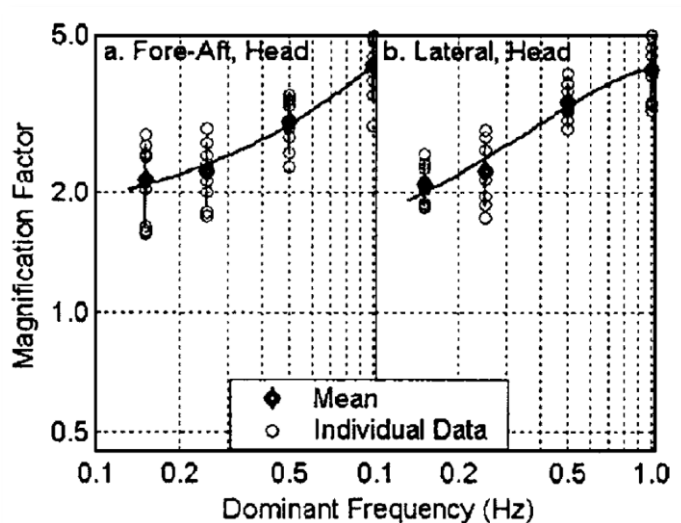
Figure 5.6 – Acceleration results.



Source: Burton et al. (2006).

The results showed that the acceleration of the head increases as the frequency of oscillation increases for both fore-aft and lateral motions. The head acceleration is also the most significant magnification factor observed, where values varied within the range of [2; 4] at the lowest frequency (0.15Hz) and at the highest (1.00Hz) frequency of oscillation, respectively.

Figure 5.7 – Magnification factors for the head.



Source: Burton et al. (2006).

Burton et al. (2006) also concluded that:

- After 0.50Hz, the para-spinal muscles become stiffer and increase the damping effects on body motions. A decrease in the magnification factors are to be expected for frequencies above 1.0Hz;
- The vestibular system is the primary indicator of motion in the human body, and its frequency dependence is the same as that of the head;
- The frequency-dependent peak-to-peak displacement for a constant acceleration is probably responsible for the visual parallax during motions in tall buildings.

5.3 STRUCTURAL, PSYCHOLOGICAL AND STATISTICAL PROPERTIES OF MOTION

5.3.1 PSYCHOLOGICAL AND PHYSIOLOGICAL FACTORS

Irwin (1978) summarized accurately the most important psychological factors involved in the occupants' perception of motion:

- People sensitive to vibration can trigger perception to motion in others;
- Noise cues: noises caused by winds, either on poorly insulated buildings or by frame joints, claddings, and other building elements;
- Sounds originated from traffic;
- Sounds created by air flow through air-conditioning ducts;

- Observation of relative motion, especially during torsional movements;
- Expectation of movement.

All of the following factors can exaggerate or trigger the fear of motion on the occupants, along with psychological factors: body posture (sitting, standing up, or lying down), gender, and age (TARANATH, 2012). These physiological factors, particularly the body posture, represent one of the reasons why the comfort threshold for offices is higher than the threshold for hotels and residences (see [Figure 1.21](#) and [Figure 1.22](#)), along with the duration of the motion (see [section 5.3.3.1](#)).

5.3.1.1 *Visual cues*

Visual cues are a major concern in several studies carried out by different authors (IRWIN, 1981; TAMURA, 2006) and are somewhat assessed by several standards and guidelines for human comfort (ISO10137, 2007; SARKISIAN, 2012).

Visual cues can reduce the threshold of perception to motion, as demonstrated by Irwin (1981), and they can reach the SLS even if the acceleration is below the comfort threshold. Visual cues are usually assessed through the angular velocity (see [section 5.2.2.2 “Angular velocity”](#)).

5.3.2 *RETURN PERIOD*

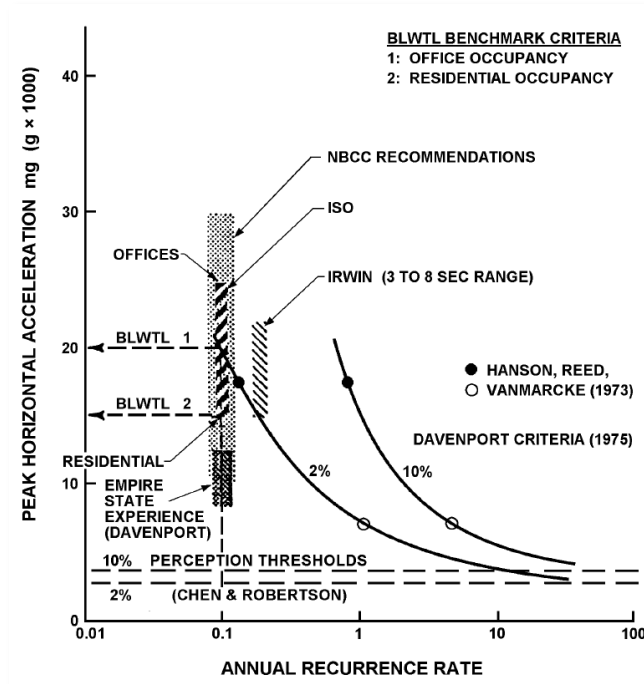
Hansen et al. (1973), in a survey on two different buildings after a windstorm, proposed a methodology and a criterial format to analyse the discomfort level in tall buildings. Based on the surveys, the comfort criteria for wind-induced vibration in tall buildings were proposed.

The two buildings showed different thresholds main motion cues. One of them showed audible cues, such as creaking, while the other showed motion cues, like the feeling of self-movement and sickness symptoms.

A few subjects of the test in both buildings were asked about how many times a year they would consider objectionable if a similar motion experience occurred. The answers were categorized from no objection at all to once every 5 years. In addition, 70% of the subjects were accurate in their answers within one hour of the peak motion periods. Within this period, the rms acceleration was measured for an instrumented building and calculated for a second non-instrumented building, based on wind-tunnel loading estimations. The result was a percentage

curve of people objecting to motion, versus the recurrence time for the two peak accelerations (measured and estimated).

Figure 5.8 – Davenport's benchmark criteria.



Source: Boggs (1997).

Boggs (1997) cited Davenport (1975) to propose two different curves and relate the acceleration to the recurrence interval. These curves were calculated to represent the 10% and 2% rates of objection to movement perceived on the floors in the top third of the building height. They were also drawn to agree with the criteria proposed by Hansen et al. (1973). Another criterion brought by Melbourne and Palmer (1992) related the return period “R” to the acceleration in the following equation:

$$\frac{\text{response for return period R years}}{\text{response for return period 5 years}} = 0.68 + \frac{\ln(R)}{5} \quad (5.4)$$

The acceleration proposed by Hansen et al. (1973) for 2% of the users' complaints is 7.0milli – g for a one-year return period (see [Figure 5.8](#)). Applying eq. (5.4) twice, so as to adapt a one-year to a five-year return period, and subsequently, a five-year to a six-year return period, the result obtained is $[0.68 + \ln(6)/5]/[0.68 + \ln(1)/5] \times 7 = 10.6\text{milli} - \text{g}$. The result is far lower than the

value of 17.5milli – g for a six-year period of return for 2% of users' complaints (see [Figure 5.8](#)). The results suggest that Melbourne and Palmer's (1992) criterion, used to combine comfort thresholds for different return periods, is more conservative than the criterion of Hansen's et al. (1973). The criterion from eq. **(5.4)** provides more conservative results as the return period increases.

5.3.3 DURATION

Some researchers believe that when the vibration lasts more than 5 to 8s, its duration does not affect human responses. For a duration of less than 5s, the allowable acceleration can be increased by the same ratio (10milli – g for 5s and 20milli – g for 2,5s of duration). Since most of the cases of wind-induced vibrations have vibration that last longer than 5s, the omission of the duration in the comfort criteria is not totally unjustified (CHANG, 1973).

5.3.3.1 Duration of the windstorm

Melbourne and Palmer (1992) stated that the 10min duration is used because it is typical of extreme responses in areas where thunderstorm activities dominate the wind-loading design. Melbourne and Palmer (1992) also proposed a peak factor (see eq. **(5.5)**) that is strongly dependent on the duration of the motion for normally distributed accelerations:

$$g = \sqrt{2 \times \ln(nT)} \quad (5.5)$$

where:

- T is the duration of the motion (normally 600s);
- n stands for the frequency of the building's motion (Hz).

Another formulation to assess the peak factor was developed and used thereafter, as discussed in [section 2.3.2](#) (see eq. **(2.25)**).

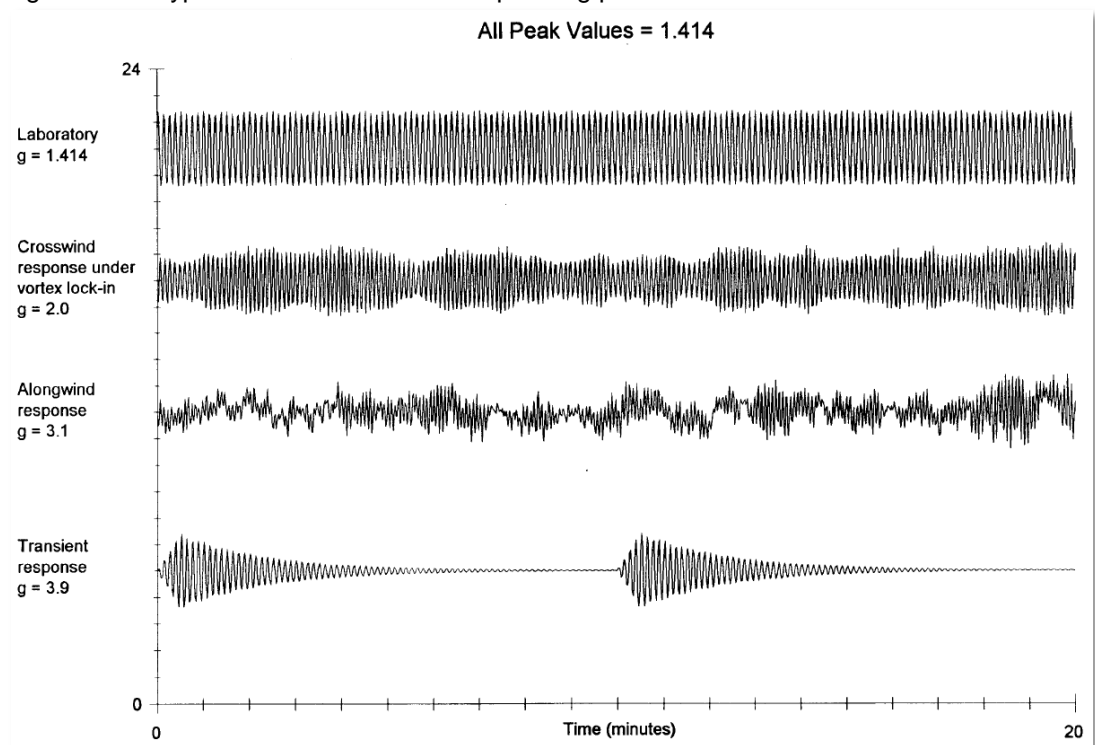
Hansen et al. (1973) also affirmed that the 20min duration is due to the "spectral gap" in the Van der Hoven power spectrum, as mentioned above (see [section 1.2.2.2](#)). Denoon et al. (2000), during field experiments, found that both Sydney's and Brisbane's Airport Control Towers had acceleration levels considered acceptable per ISO6897 (1984). However, the Sydney Tower registered more complaints about motion. It was assumed that the higher number of complaints was

due to the characteristic of winds in Sydney, which blow for hours during winter, while wind in Brisbane is characterized by infrequent short bursts with a high peak acceleration and a high peak factor. This suggests that both duration and waveform are important contributions to the movement perception/tolerance threshold.

5.3.4 PEAK, RMS AND WAVEFORM

There are two different schools of thought on the assessment of building acceleration: the peak acceleration, which occurs within a period of 20min to one hour, and the rms over the same period. The first believes that people remember only the strongest cycle and have a tendency to forget smaller ones. In this case, the peak value would be the measure for the effects of motion. The second believes that the number of cycles above a given threshold and the intensity of those cycles determine the degree of objection to the building motion. For the sake of simplicity, the rms was chosen as a concise measure (BOGGS, 1997). Boggs (1997) also discussed the peak factors for four different waveforms: sinusoidal vibration ($g = \sqrt{2}$), crosswind vibration ($g = 2.0$), along-wind vibration ($g = 3.1$), and transient response ($g = 4.0$).

Figure 5.9 – Types of vibration and corresponding peak factors.

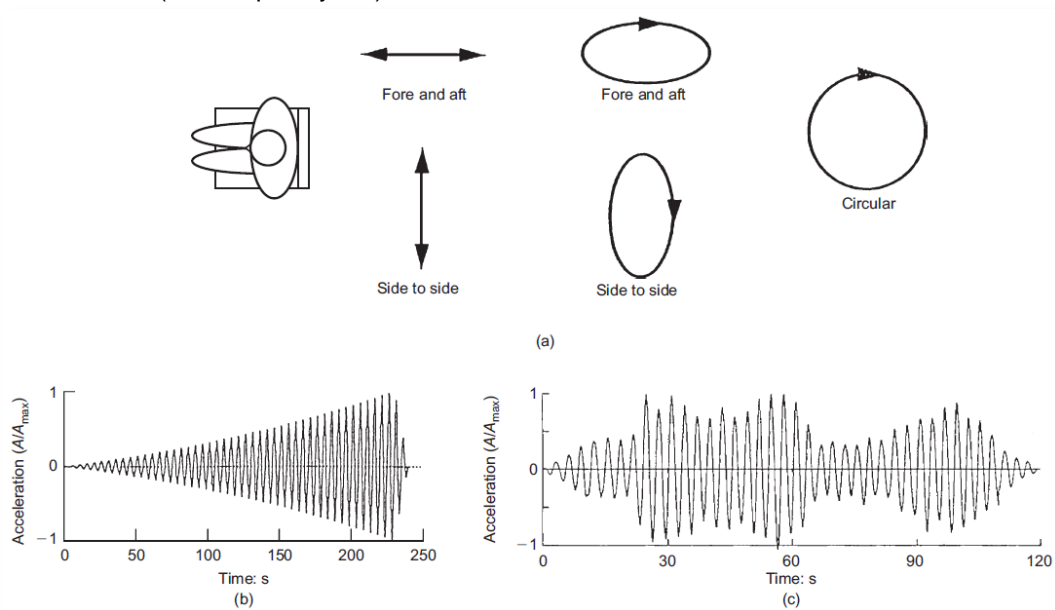


Source: Boggs (1997).

Figure 5.9 shows different waveforms with the same peak values and different peak factors and rms values. Boggs (1997) also discussed the typical peak factor of 3,5 for tall buildings, used to adjust the rms assessed by Hansen et al. (1973) to the peak values proposed by Davenport (1975). This typical value is used to divide the true peak value to assess a pseudo rms value as reliable as the one proposed by Hansen et al. (1973).

According to Melbourne and Palmer (1992), an acceleration criterion based on the rms ignores the probability distribution of peak values, which fluctuates significantly between a sine waveform and a normally distributed waveform.

Figure 5.10 – Motion shapes (a); time histories of sinusoidal (b) and random (c) motions of the test room (low-frequency set).



Source: Tamura et. al (2006).

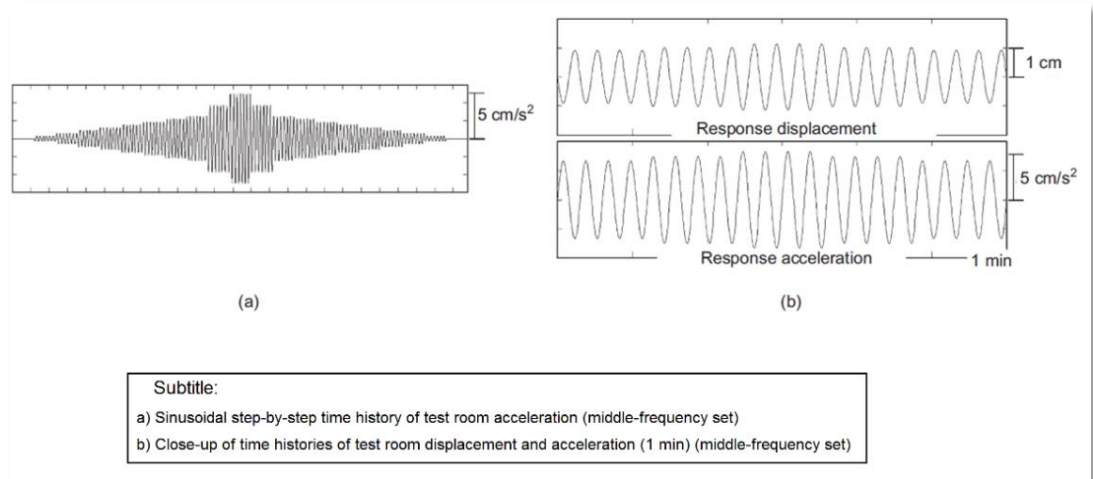
Tamura et al. (2006) carried out an experiment to evaluate the sensitivity of the motion perception according to the following factors:

- direction of motion at a sitting position (fore-aft or lateral);
- motion waveform (sinusoidal or normally distributed);
- subjects were tested within three ranges of frequencies;
- low-frequency set: 0.125 – 0.315Hz;
- middle-frequency set: 0.33 – 2.0Hz;
- high-frequency set: 1.0 – 6.0Hz.

Sinusoidal motions were simulated with the low-frequency set, while both sinusoidal and random waveforms were tested with the middle-frequency set. The sinusoidal motion generated a time-history ascending waveform, while the random motion was generated using a time-history of a single degree-of-freedom system with a damping ratio of 1%. The motion shapes and waveforms are shown in [Figure 5.10](#) and in [Figure 5.11](#).

The test subjects were quite accurate in recognizing the direction of motion (fore-aft or lateral), but most of them could not distinguish uniaxial motions from elliptical motions.

Figure 5.11 – Examples of sinusoidal acceleration responses of test rooms.

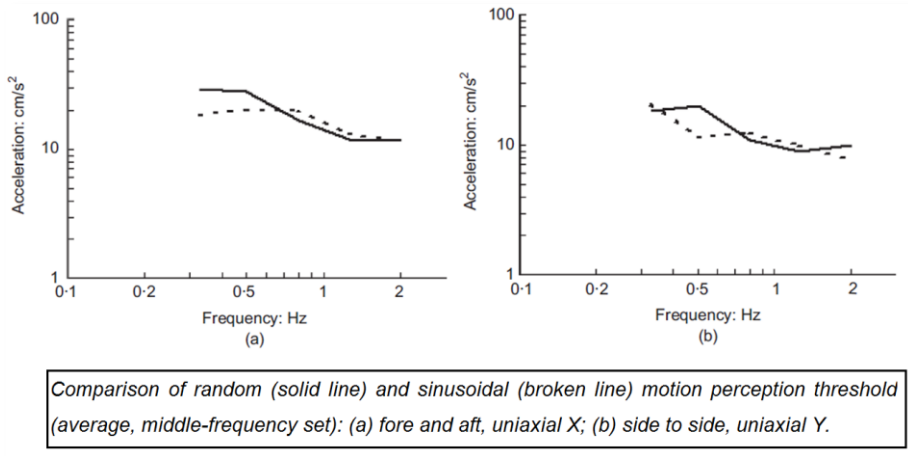


Source: Tamura et. al (2006).

For the middle-frequency set, the presented results also showed that sinusoidal waveforms had no significant difference from random motion waveforms concerning the perception threshold (see [Figure 5.12](#)).

The subjects were instructed to press the “ON” button immediately after perceiving the movement. The acceleration corresponding to the cycle would be recorded as the subject’s perception threshold. Consequently, the acceleration assessed was the peak acceleration.

Figure 5.12 – Comparison of random and sinusoidal motion perception.



Source: Tamura (2006).

5.3.5 PROBABILISTIC EVALUATION OF HUMAN COMFORT

This method was first proposed by Kanda et al. (1993) and later discussed and used by several authors (TAMURA ET AL., 2006; TAMURA, 2007). It starts by calculating the probability of the wind pressure distribution based on statistical meteorological data. The building’s dynamic characteristics can be obtained through boundary-layer wind-tunnel tests and through the building’s structural analysis. Once these dynamic characteristics are correctly assessed, the maximum annual acceleration “A” of the target floor is calculated as a function of the wind dynamic pressure (TAMURA, 2007).

Table 5.2 – Target reliability index β_T .

Perception index β_T	Possible occupants’ reactions
$\beta_T < 0$	Complaints will occur
$0 \leq \beta_T < 1$	Complaints may occur
$1 \leq \beta_T < 2$	Perceptible but no complaints
$2 \leq \beta_T$	Not perceptible in majority

Source: Tamura et al. (2006).

The perception limit “P” of the users is modeled by a log-normal distribution with mean “ μ_p ” and coefficient of variation “ ζ_p ” (TAMURA et al., 2006). The parameter “A” needs to be equivalent to the sinusoidal motion in order to be comparable with a random variable “P” obtained from experiments. This parameter

was first proposed by Kanda et al. (1993) and is equal to “ $2\sigma_a$ ”, where “ σ_a ” is the standard deviation of the acceleration response. “A” is also modeled by a log-normal distribution, which allows the calculation of reliability index “ β ” (TAMURA ET AL., 2006):

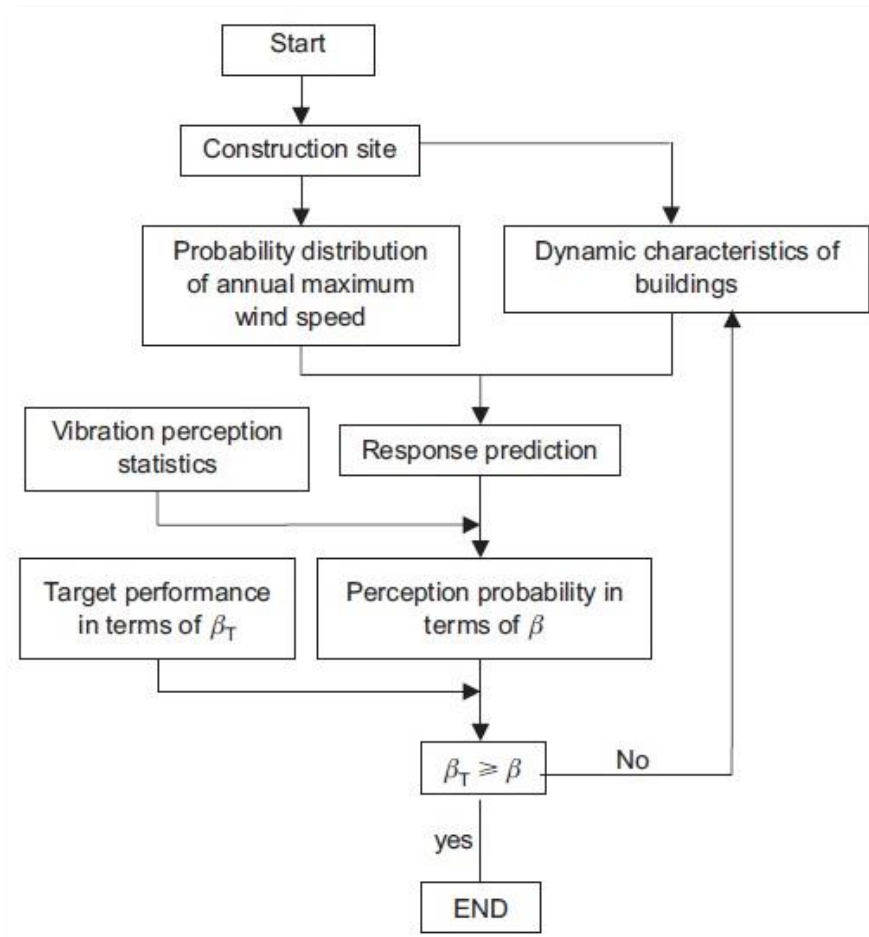
$$\beta = \frac{\lambda_P - \lambda_A}{\sqrt{\zeta_P^2 + \zeta_A^2}} \quad (5.6)$$

where:

$$\lambda = \ln \mu - (1/2)\zeta^2 \quad (5.7)$$

$$\zeta^2 = \ln[1 + (\sigma/\mu)^2] \quad (5.8)$$

Figure 5.13 – Schematic flow of the probabilistic comfort evaluation method.



Source: Tamura et al. (2006).

Subsequently, the reliability index “ β ” is compared with the target reliability index “ β_T ”, from [Table 5.2](#). If “ $\beta < \beta_T$,” the design parameters require changes. [Figure 5.13](#) shows the schematic flow for this method.

5.4 DISCUSSION

5.4.1 PSYCHOLOGICAL AND STATISTICAL SIGNIFICANCE FOR USER'S COMFORT

5.4.1.1 Peak and rms accelerations

The sinusoidal waveform in [Figure 5.11](#), used by Tamura et al. (2006), is similar to the transient waveform in [Figure 5.10](#), used by Boggs (1997) to explain the peak factors. This similarity implies that the waveform used by Tamura et al. (2006) for the sinusoidal motion has a peak factor not very far from 3.9, which is the peak factor for Boggs's transient response. As for the random waveform used by Tamura et al. (2006), it is quite similar to the second waveform used by Boggs (1997), as recorded from a crosswind vibration with the use of an accelerometer ($g = 2.0$).

The accelerations to assess perception in the studies performed by Tamura et al. (2006) were peak values, with no significant difference between the sinusoidal and the random waveforms in the subjects' perception. Both waveforms have clearly different but not precisely assessed peak factors, implying different rms values for the same peak acceleration levels. Taking only these results into consideration, the use of the peak acceleration seems to be more suitable to assess perception levels, and consequently, comfort levels of motion.

Denoon et al. (2000), after the field experiments, concluded that the waveform and duration might be important factors to assess the human comfort. However, it was not clear how different the waveform was or the duration of the event that caused the air traffic controllers in Sydney to lower their comfort thresholds.

An uncertainty remains on how many cycles above the subjects' threshold are necessary to cause alarm, or if only one value would be sufficient. Lenzen (1966) concluded that when a vibration persists for more than 12 cycles, the response would be the same as that of a steady-state vibration. However, these studies were made for vertical vibration. As far as the perception criteria for horizontal vibration are concerned, the vestibular organs involved are the same, but

further and more specific investigations about horizontal vibrations would be necessary.

Once these cycles are correctly evaluated to allow for a careful comparison with national and international standards, the question remains on how many of these smaller groups of cycles above the threshold would be necessary to alarm the occupants during a bigger event.

Kwok et al. (2009) affirm that peak accelerations trigger the fear of vibration, while the rms gives a more direct assessment of sustained vibration, being more suitable for the verification of comfort, which was already used by Irwin (1978) to evaluate the perception and comfort of occupants.

5.4.1.2 *Assessing complex motion*

As for complex motion, the assessment of the resultant rms acceleration may be even harder. Melbourne and Palmer (1992) discussed three factors that might lead to further difficulties in the assessment of comfort :

- when the peak accelerations of a motion are not normally distributed;
- when the accelerations result from a complex mode;
- when the rms acceleration from one mode of vibration is not dominant over any others.

For tall buildings, the maximum accelerations usually come from a cross-wind response and, for this kind of wind excitation, the probability of peak distribution is considerably far off the Gaussian distribution. Therefore, the usual peak factors given by eq. (5.5) or (2.25) are not suitable for assessing peak values alone.

When the motion of a mode shape is purely a sway mode, the resulting acceleration value is easier to measure. However, when the building motion occurs in complex mode shapes (with torsional effects, for example), the resulting acceleration due to the angular acceleration at a distance from the reference axis must be added vectorially to the resultant horizontal acceleration of the floor about the same reference axis (see [Figure 1.20](#)). The vectorial sum of two perpendicular peak accelerations is given by:

$$\ddot{x}_y = \sqrt{\ddot{x}^2 + \ddot{y}^2} \quad (5.9)$$

The rms resultant accelerations are given by:

$$\sigma_{xy} = \sqrt{\sigma_x^2 + \sigma_y^2} \tag{5.10}$$

Using the same formulation, the evaluation of the resultant rms might lead to several mistakes, particularly when the frequencies of each orthogonal mode shape are different. The results of the difference between the calculations of eq. (5.9) and (5.10) are given in [Table 5.3](#).

Table 5.3 – Comparison of peak accelerations.

Frequency ratio $\frac{n_y}{n_x}$	Standard deviation ratio $\frac{\sigma_x}{\sigma_y}$	σ_x	σ_y	Peak acceleration from component standard deviations $\sigma_{xy} = \sqrt{\sigma_x^2 + \sigma_y^2}$		Peak acceleration from resolved acceleration $\dot{x}\dot{y} = \sqrt{\dot{x}^2 + \dot{y}^2}$		Ratio $\frac{\widehat{x\dot{y}} \text{ resolved acceleration}}{\widehat{x\dot{y}} \text{ components } \sigma}$
				average peak factor g_{av}	peak acceleration $\widehat{x\dot{y}} = g_{av}\sigma_{xy}$	Peak factor g	Peak acceleration $\widehat{x\dot{y}} = g\sigma_{xy}$	
1.00	2.96	28.07	9.47	3.66	108.85	3.72	110.63	1.02
1.00	0.41	6.41	15.80	3.72	63.43	3.64	62.06	0.98
1.08	2.33	27.92	11.97	3.72	113.09	3.72	113.09	1.00
1.18	2.99	30.89	10.34	3.61	117.58	3.54	115.29	0.98
1.00	0.82	12.11	14.79	3.75	71.81	3.95	75.64	1.05
1.08	0.96	11.45	11.96	3.58	59.39	3.36	55.74	0.94
1.18	0.95	11.25	11.85	3.45	56.51	2.46	40.30	0.71
1.23	0.96	4.95	5.17	3.72	26.63	2.87	20.55	0.77
1.33	0.84	4.59	5.47	3.64	25.99	2.90	20.71	0.80
1.50	0.73	4.96	6.78	3.51	29.48	2.84	23.86	0.81
1.70	0.87	5.14	5.92	3.35	26.26	2.89	22.66	0.86

Source: Melbourne and Palmer (1992).

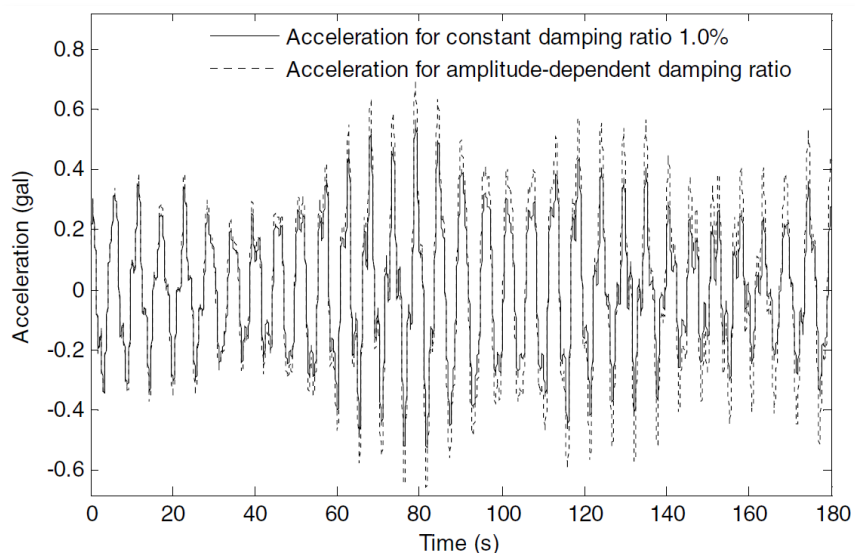
The accelerations in [Table 5.3](#) are determined at the top of the building from component rms accelerations and continuously-resolved accelerations (time domain). Boggs (1997) discusses the concept of the joint action factor “ φ ” and peak factors for each direction “ g_x ” and “ g_y ”, where:

$$\widehat{x\dot{y}} = \varphi \times \sqrt{(g_x \times \sigma_x)^2 + (g_y \times \sigma_y)^2} \tag{5.11}$$

Boggs (1997) also mentions that the values for the joint action factor fall between 0.7 and 1.0, with typical values ranging from 0.8 to 0.9, in close agreement with the right-most column of Melbourne and Palmer' (1992) table. These joint-action factors might provide criteria to complement the peak factors given in eq. (5.5) and (2.25).

The greater the damping, the faster a peak or a transient vibration decays, which means a smaller rms value and a bigger peak factor. These results, along with those obtained from Wu et al. (2007), confirm the importance of the damping coefficient to the waveform.

Figure 5.14 – Crosswind responses for 1% damping ratio.



Source: Wu et al. (2007).

Despite the close agreements found in the results from Wu et al. (2007) for SLS (1% damping ratio) and for ULS (2 – 3% damping ratio), the assessed peak factors were different in many cases, implying different waveforms and, consequently, a possible difference in the motion perception/comfort threshold. [Table 5.4](#) shows peak factors varying from 3.05 to 3.63 when the damping ratios vary from 1% to 2%, respectively (with 32 m/s wind speed) ([Figure 5.14](#)).

The best way to evaluate the building acceleration is to calculate the acceleration vectorially, including yaw effects and extra-horizontal accelerations from the torsional motion on the floor perimeter for each time step. Then, with the time-

history of the floor of interest completed, the evaluation can be done with the use of either the peak or the rms acceleration.

Table 5.4 – Crosswind responses: accelerations and displacements.

Wind speed (m/s)	Damping ratio	Results from the time domain method						Results from the frequency domain method	
		Displacement (mm)			Acceleration (gal)			RMS for displacement (mm)	RMS for acceleration (gal)
		RMS value	Maximum value	Peak factor	RMS value	Maximum value	Peak factor		
15	NL	2.93	8.20	2.79	0.26	0.81	3.10		
	1%	2.86	8.03	2.81	0.24	0.84	3.50	2.90	0.23
	2%	2.78	7.50	2.66	0.19	0.69	3.56	2.70	0.16
	3%	2.66	7.05	2.68	0.16	0.58	3.60	2.58	0.13
27	NL	13.60	34.90	2.56	0.82	2.71	3.30		
	1%	14.10	36.60	2.59	1.20	3.12	2.60	14.47	1.30
	2%	12.65	33.83	2.59	0.77	2.51	3.26	13.02	0.91
	3%	11.65	31.79	2.54	0.65	2.40	3.70	12.09	0.74
32	NL	22.10	62.24	2.81	1.36	4.86	3.57		
	1%	23.19	68.56	2.95	1.69	5.16	3.05	24.92	2.03
	2%	21.94	62.79	2.86	1.32	4.79	3.63	22.60	1.50
	3%	20.41	60.13	2.95	1.16	4.75	4.09	21.30	1.22
37	NL	33.54	97.26	2.91	2.19	8.04	3.67		
	1%	36.38	100.68	2.76	2.74	9.46	3.45	37.05	3.26
	2%	29.83	83.82	2.83	2.09	7.94	3.79	32.19	2.29
	3%	26.91	78.85	2.91	1.74	6.11	3.51	28.13	1.87
48	NL	65.10	187.04	2.87	4.63	14.09	3.03		
	1%	75.74	208.94	2.75	6.82	17.55	2.57	79.69	6.93
	2%	67.21	189.02	2.81	5.14	15.37	2.99	68.35	5.38
	3%	63.42	188.69	2.97	4.16	12.86	3.09	63.03	4.27

Source: Wu et al. (2007).

5.4.2 FREQUENCY BIODYNAMIC AMPLIFICATION

The dependence of the motion threshold of perception/comfort on the frequency has been taken into consideration since the very first experiments: Chang (1973), Irwin (1978, 1982). However, they were clarified by the investigations of Burton et al. (2006).

The studies carried out by Burton et al. (2006) consider the subjects sitting on a stool to study their dynamic amplification to motion response. An interesting way to observe this amplification phenomenon is to imagine that the comfort/perception threshold is approximately constant, with frequency changes for the acceleration of the head, where the vestibular organs are located.

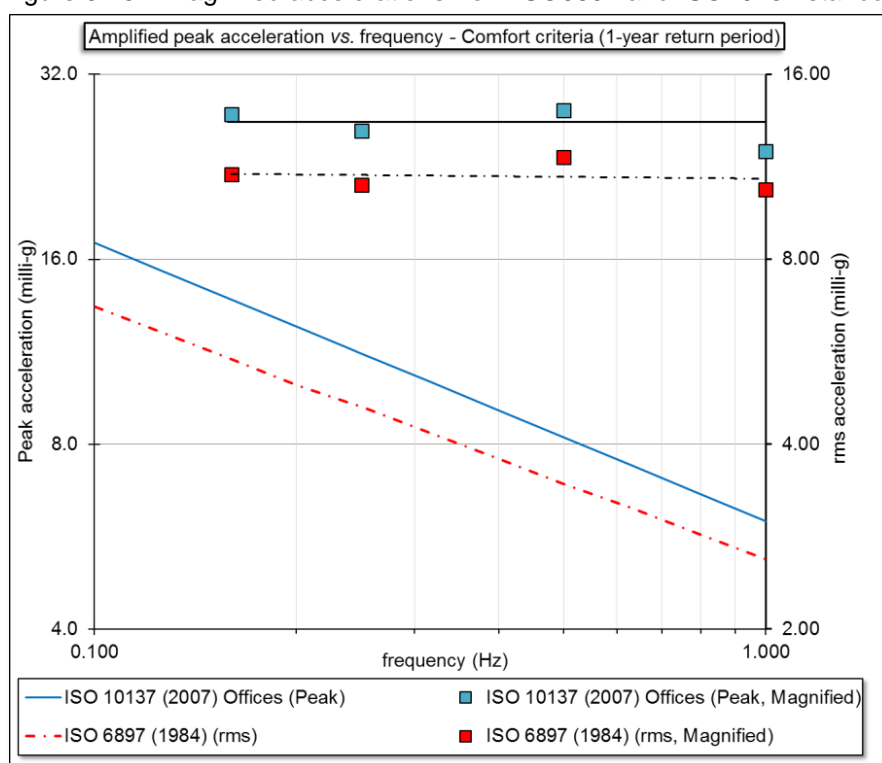
Table 5.5 – ISO Standards multiplied by head magnification factors.

(a)	(b)	(c)	(d)	(e)	(f)
Frequency (Hz)	Burton et al. (2006) Magnification factor _(head)	ISO6897 (mg)	ISO6897 Magnified (mg)	ISO10137 Offices (mg)	ISO10137 Offices Magnified (mg)
0.160	2.0	5.5	11.0	13.8	27.5
0.250	2.3	4.6	10.6	11.2	25.9
0.500	3.4	3.5	11.7	8.2	27.9
1.000	4.0	2.6	10.4	6.0	24.0

Source: Author.

Then, if this assumption is correct, the acceleration levels established in ISO10137 (2007) and in ISO6897 (1984) (*Figure 5.3* and *Figure 5.4*) multiplied by the magnification factor presented in the studies of Burton et al. (2006) (*Figure 5.7*) should result in a nearly constant value for the head acceleration.

Figure 5.15 – Magnified accelerations from ISO6897 and ISO10137 standards.



Source: Author.

The values shown in

Table 5.5 are relatively close to each other for columns (d) and (f) when the frequency changes. *Figure 5.15* illustrates these results: the magnified acceleration might be well represented by a straight horizontal line in the log-log graph for each

magnified curve. Only one comfort curve from ISO10137 Standard (2007) was used, since the office curve is 1.5 times the residence curve, meaning that both curves present the same behaviour. This comparison used the rms value of acceleration from ISO6897 (1984) (curve 1, for general purposes) for five-year return period. This relation provides the evidence that the frequency dependence on the motion threshold of perception/comfort might be governed mostly by biodynamic amplification.

However, the results presented by Burton et al. (2006) do not cover all ranges of possible frequencies and accelerations that might affect the occupants of a tall building. Further investigations are needed in this area to analyse the linearity or non-linearity of these amplification factors with different amplitudes and frequencies of motion.

5.4.3 ALTERNATIVE APPROACH TO HUMAN COMFORT ASSESSMENT OF MOTION

According to Lamb et al. (2013), the level of users' complaint might be a poor indicator to assess the human comfort during wind-induced motion. Moreover, there are several psychological and physiological effects caused by the horizontal motion of the floor, such as dizziness, compensatory behaviours, reduction of task performance, difficulty to concentrate, motion sickness, and nausea.

Goto (1983), in a study that consisted of a survey on six buildings after a windstorm, succeeded to gather different types and degrees of building responses during wind-induced building motion events. The results indicated thresholds for perception and physical symptoms. Compensatory behaviours, such as stop working and descending to a lower level of the building, were observed during the survey.

Jeary et al. (1988) performed a study with an artificially excited building (sinusoidal vibration). The goal was to study the effects of acceleration levels on human task performance. No significant results concerning a decrease in task performance were observed. According to the authors, the tasks were too simple and the subjects were able to counterbalance the motion effects by "concentrating harder". In addition, the vibration did not persist long enough to cause any fatigue symptoms in the users. However, seven of the 24 subjects who participated in the

experiment claimed to have experienced motion sickness at the highest amplitudes of motion.

Lee (1983) calculated the acceleration of a seventy-eight-meter high building after a windstorm. The calculation used a wind tunnel modelling system and showed good agreement with full-scale data. The peak accelerations for the two modes of vibration during the windstorm peak were 3.9milli – g for the E-W mode and 5.5milli – g for the N-S mode. The resultant peak acceleration can be estimated by a simple vectorial addition:

$$\ddot{x}_{\text{Resultant}} = \varphi \times \sqrt{(\ddot{x}_{\text{N-S}})^2 + (\ddot{x}_{\text{E-W}})^2} \quad (5.12)$$

The result needs to be multiplied by a joint-action factor “ φ ” (Boggs, 1997). The joint-action factor used in Lee’s (1983) results is 0.7 (based on [Table 5.3](#)).

Denoon (2000) performed an extensive survey of three wind-sensitive structures: Brisbane Airport Control Tower, Sydney Airport Control Tower, and Port Operations Control Centre (POCC). The results included a study of motion tolerance thresholds (including perception) in a great range of work conditions, such as temperature of the room, fatigue, concentration, and body posture effects on these thresholds. Initially, 39% of the users of the Sydney’s Airport Control Tower reported that the motion was disturbing or frightening. After being educated about the building motion and learning that it was safe and could not affect the structural integrity of the tower, this group of users showed an adaptation to the motion effects. These users reported a strong decrease (50%) in the frequency of how often they felt disturbed or frightened due to the building motion. In addition, 40% of these users reported that they came to find the level of motion less disturbing or frightening. Annoyance thresholds rose since annoyance complaints rate dropped 40% with user’s acquaintance to the environment.

Denoon (2000) actually got to measure a tolerance level for a disturbing, frightening, or nauseating feeling. However, most of the reports of “disturbing / frightening / nauseating” sensations described symptoms of nausea, such as headaches or queasiness, leading to an acceleration peak level close to 4,0milli – g at a frequency of 0,94Hz for nausea symptoms. [Figure 5.16](#) shows a compilation of the results obtained by Goto (1983), Lee (1983), Jeary et al. (1988), and Denoon (2000).

5.4.3.1 *Alternative assessment of human comfort*

Burton et al. (2006) affirmed that the vestibular system is the primary indicator of the body to motion perception and its frequency dependence is the same as that of the head.

Assuming a constant comfort threshold for the head acceleration, the acceleration value for a certain level of comfort/discomfort at 1.0Hz should be half of that for the value for 0.15Hz, since the magnification factor for 1.0Hz is twice as large as the factor for 0.15Hz (4 and 2, respectively). This analysis will consider a set of log-log straight lines with the angular coefficient “m” consistent with the magnification factors found in the studies of Burton et al. (2006). The angular coefficient “m” is calculated by:

$$m = \frac{\ln(2/4)}{\ln(1/0.15)} = -0.37 \quad (5.13)$$

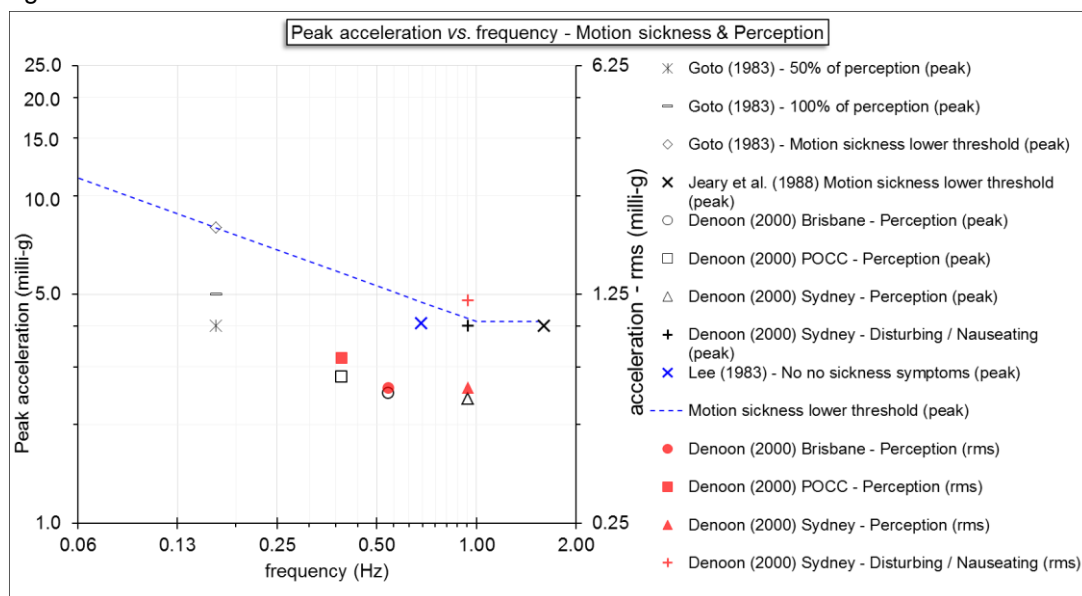
In addition, for accelerations at frequencies higher than 0.50Hz, para-spinal muscles become stiffer and increase the damping effects on body motions. A decrease in the magnification factors is to be expected for frequencies above 1.0Hz (BURTON et al. 2006).

These lines stop at the frequency of 1.0Hz, since the range of frequencies tested does not go any further. Yet, a change of behaviour in the magnification factor is expected above 1Hz, as previously stated by Burton et al. (2006).

When close attention is given to the exact line that passes through Goto’s (1983) lower motion sickness threshold (see [Figure 5.16](#)), it can be observed that Denoon’s (2000) nausea threshold is very close to that line. The line was drawn with a constant acceleration value between 1.0Hz and 2.0Hz, the same behaviour of ISO10137 (2007), to fit in the results from Jeary et al. (1988).

The assessed peak acceleration from Lee’s (1983) survey results is 4.09milli – g for a frequency of 0.68Hz, below the lower nausea threshold (see [Figure 5.17](#)). It is important to point out that no episodes of nausea or motion sickness were noted during Lee’s (1983) survey.

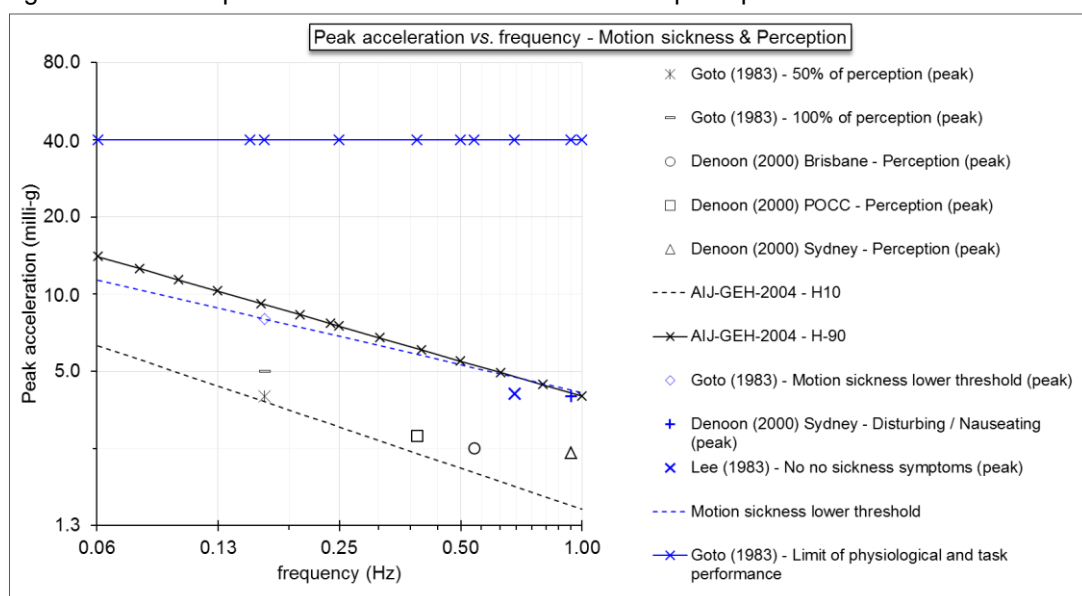
Figure 5.16 – Alternative acceleration assessment curve.



Source: Ferrareto et al. (2015).

Angular coefficients neighbouring the value of -0.365 appear in standards ISO6897 (1984) and in ISO10137 (2007), -0.32 and -0.45 , respectively, which might indicate a similar behaviour between the thresholds of perception and nausea in the range of frequencies between 0.15Hz and 1.0Hz. However, the thresholds of nausea and motion sickness are clearly higher than perception thresholds.

Figure 5.17 – Comparison between motion sickness and perception thresholds.



Source: Ferrareto et al. (2015).

The lower threshold of motion sickness is above Tamura's (2003) 30% perception threshold (see *Figure 5.17*). At the same time, the "limit of physiological task performance" is 40milli – g for peak acceleration (Goto 1983), far above the NBCC upper threshold for comfort (offices) and from the AIJ-GEH-2004 H-90 curve (see *Figure 5.17*).

These results confirm that nausea/task performance thresholds are much higher than the perception thresholds. Therefore, the assessment of comfort through perception thresholds might lead to more conservative results.

5.4.3.2 *Probabilistic method application and future research*

The target coefficient " β_T " of the method introduced by Tamura (2006, 2007) is calibrated by the perception curves from GEH-AIJ-2004. This coefficient can be calibrated using nausea/reduced task performance thresholds. Hence, these data are already partially available in the literature on full scale measurements (GOTO, 1983; JEARY ET AL., 1988; DENOON, 2000), as they are used to encourage a deterministic method approach to nausea and task performance in this thesis.

This possible new use of the probabilistic method would *allow for the comfort assessment to track actual comfort thresholds instead of tracking perception thresholds*, which are considerably lower than nausea/reduced task performance thresholds. By adopting higher thresholds for motion, less conservative results can be achieved and consequently lower material consumption can be expected if the strength criteria are met.

5.5 CHAPTER SYNTHESIS

Normative documents around the world are not consistent with each other. At the present time, linear and angular acceleration are the most significant kinematic properties of motion for comfort assessment. The derivative of acceleration "jerk" might be an alternative for future comfort assessments to solve the problem of peak versus rms criteria. In addition, the peak acceleration is more closely related to the perception of motion, whilst the rms acceleration is better suited to evaluate comfort during sustained motion (compensatory behaviour, motion sickness, annoyance levels).

There is strong evidence that biodynamic amplification might be one of the major factors that contribute to the the dependency of comfort thresholds on frequency frequency dependency on comfort thresholds.

The assessment of comfort through the level of perception/complaint may lead to conservative results, which on its turn leads to a higher consumption of structural and consequently higher costs. An alternative approach that might provide less conservative results is the comfort evaluation through motion sickness, compensatory behaviours, and task performance reduction. This approach requires trained users, i.e., users educated about the building motion and familiarized with the fact that the wind-induced motion does not affect its structural safety.

6 METHODOLOGY

6.1 FE MODELLING

FE models were developed using a Brazilian software for commercial structural, generally used in the modelling of tall buildings: TQS. The same building was modelled using each of the sets of criteria shown in [Chapter 3 “FE modelling criteria”](#). Three different structural models were created for each building studied as a result of the application of these criteria: one structural model with beam-end offsets (1); one structural model with an increased modulus of elasticity (2); and one structural model with the floor slab discretized by a 50cm × 50cm mesh of rod elements to simulate a grid (3).

Each structural model incorporates the previous criteria, since this methodology intends to build them with an increasing precision/complexity at each step of the procedure. This indicates that the second structural model has the beam-end offsets modelled along with the increased modulus of elasticity and that the third model has both the first and the second criteria, as well as the the floor slab modelling as a third criterion.

6.1.1 BEAM-END-OFFSETS

Previously, in the 2007 International Conference on Wind Engineering, Kijewski-Correa et al. (2007) evaluated tall buildings' structures using this modelling concept and showed considerably different results.

The first structural model studied has its columns and beams modelled as linear elements (beams). It already has beam-end-offsets, since only the beams that resist the horizontal forces acting on the building are connecting the shear walls in the worked examples (see [Figure 6.2](#) and [Chapter 7, “Case study”](#)). These beams were modelled between the shear-wall-element limits, as shown in [Figure 6.2](#), and modelling them connecting the centre of mass of each shear wall element would generate a very questionable structural model. In addition, the use of these offsets is already a common practice in structural modelling of tall buildings. This model is considered the basis of comparison for the subsequent models, as it makes use of the simplest criteria for the structural modelling of tall buildings currently used in Brazil.

6.1.2 USE OF PROBABLE YOUNG’S MODULUS

The second model has the modulus of elasticity for “ $t \rightarrow \infty$ ” in eq. (3.1). The results of the concrete’s Young’s modulus at day “j” for each category of the concrete’s strength used in this equation are given in Table 6.1.

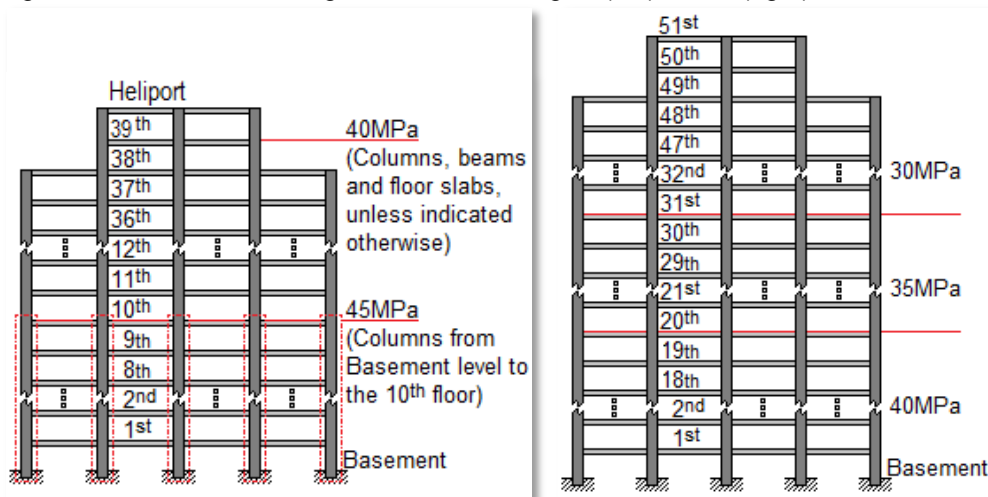
Table 6.1 – Modulus of elasticity results for “ $t \rightarrow \infty$ ”.

f_{ck} (MPa)	E (GPa)	
	t_{28}	$t \rightarrow \infty$
30	30.7	34.8
35	33.1	37.5
40	35.4	40.1
45	39.1	44.4

Source: Author.

The schematics of the categories of strength of concrete for each structural element are given in the Figure 6.1 for both buildings (buildings A and B).

Figure 6.1 – Concrete strength for each building: A (left) and B (right).



Source: Author.

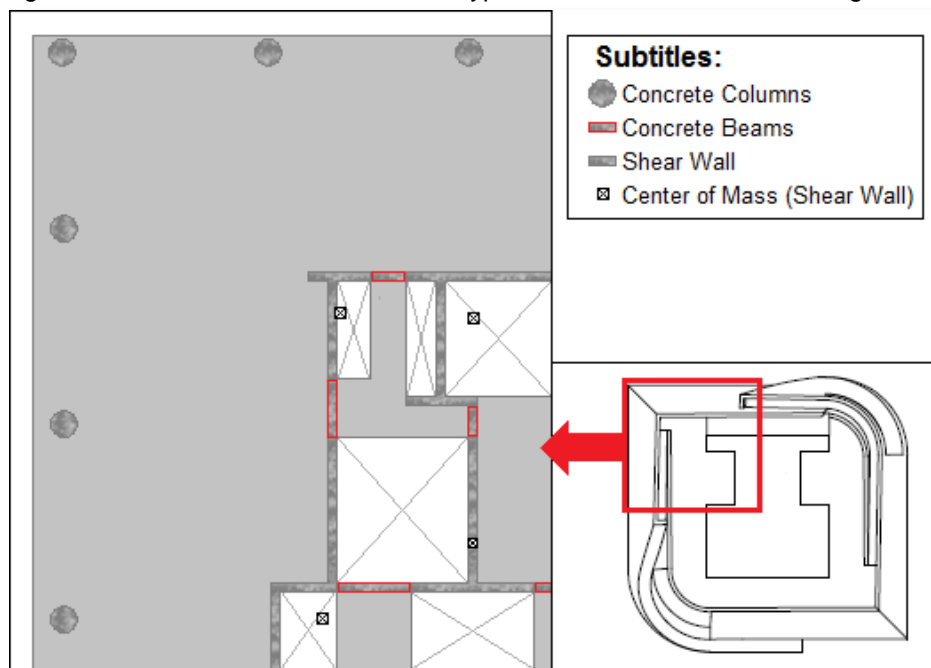
6.1.3 FLOOR SLAB MODELLING

The third model has the floor slabs modelled with shell elements in order to provide the coupling between two shear walls and between shear walls and the

external columns, creating a kind of outrigger system on every floor of the tall building (see [Figure 3.2](#)).

As it can be seen in the [Figure 6.2](#), the floor slab of building A has no elongated dimensions. As it was previously discussed in [section 3.3.3](#), the effects of in-plane floor slab flexibility are accentuated in buildings with fewer storeys and higher aspect ratio of the floor slab. Since the floor slab of building A has an almost square shape (aspect ratio $\sim 1:1$) and 39 stories, the effects of in-plane floor slab flexibility are not relevant. It means that the modelling of in-plane deformations through a rigid diaphragm system or through shell elements generates the same results in terms of natural frequencies and mode shapes.

Figure 6.2 – Structural elements of the typical floor of the studied building.



Source: Author.

Thus, only the flexural stiffness of the floor slabs is significant in the case study. To avoid any misinterpretation, “flexural stiffness” in this thesis must be understood as “out-of-plane stiffness,” or even as the stiffness related to forces and deformations out of the floor plane. The same conclusion may be reached analogously for building B, which presents the same behaviour for the aspect ratio on the typical floors and more stories (51) than the first building studied (see [Chapter 7](#)).

6.1.4 STRUCTURAL DYNAMIC DATA

Each structural model generated a set of dynamic data that characterizes its performance during the dynamic analyses presented later in this chapter. These dynamic data consist of:

- a lumped mass matrix: lumped masses on each floor, with elements for each DOF (see eq. (6.1)), through juxtaposition of the mass matrix of each storey of the building (see eq. (1.19));
- structural damping: this assumes the value of 1.00% and 1.25%, as discussed in [section 1.3.3, “Damping – \$\xi\$ ”](#);
- mode shapes with three DOF per floor (eq. (1.20)) for the first six or nine modes of vibration;
- natural frequencies of the first six or nine natural modes of vibration.

The dynamic data from each model are calculated using the structural analysis software TQS. A Microsoft Excel (2013) worksheet, “[Structural_Data.xlsx](#),” was used to gather and document the dynamic data from the structural analysis.

$$[M] = \begin{bmatrix} m_m & 0 & 0 & & 0 & 0 & 0 \\ 0 & m_m & 0 & \dots & 0 & 0 & 0 \\ 0 & 0 & I_{zm} & & 0 & 0 & 0 \\ & \vdots & & \ddots & & \vdots & \\ 0 & 0 & 0 & & m_1 & 0 & 0 \\ 0 & 0 & 0 & \dots & 0 & m_1 & 0 \\ 0 & 0 & 0 & & 0 & 0 & I_{z1} \end{bmatrix} \quad (6.1)$$

6.2 DYNAMIC ANALYSES

All of the post-processing was performed using the commercial software Microsoft Excel (2013), which includes time and frequency-domain analyses, acceleration assessment, and wind climate analyses, to name a few. Mode deflection shapes and natural frequencies of the building structure for each set of modelling criteria were assessed using the commercial software TQS. The complete formulations and schematics used in the accelerations’ assessment on the building floor of interest will be further explained in this chapter.

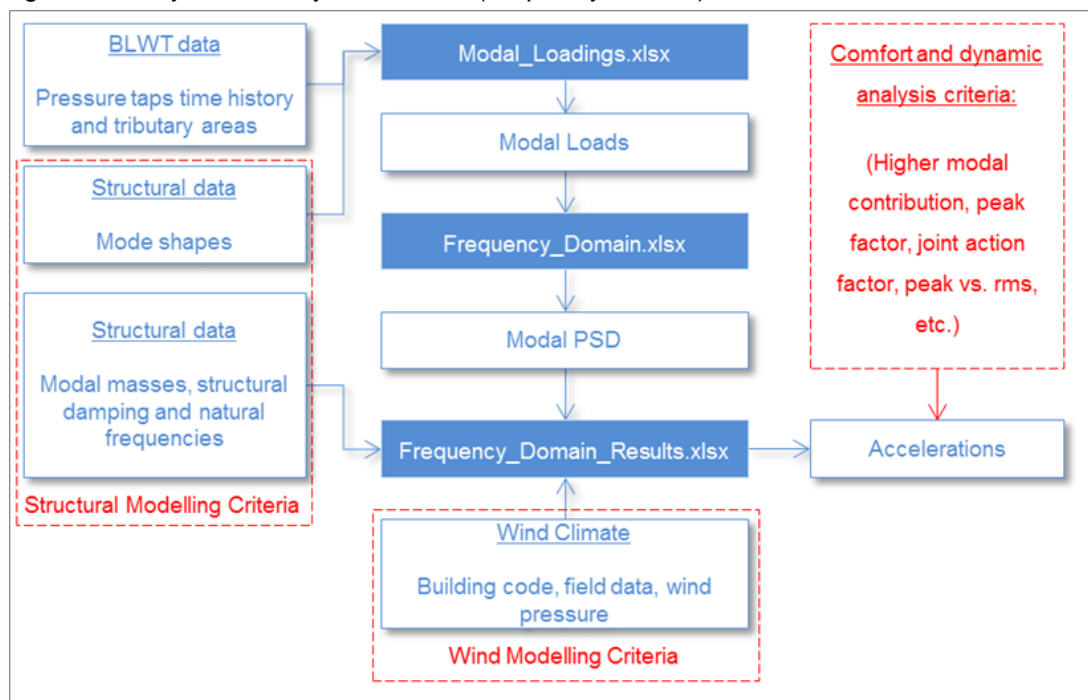
The technique of mode displacement superposition used in both the frequency-domain and the time-domain analyses is validated in [Chapter 7](#), where a

linear behaviour is observed for structural members for SLS winds. The worksheets used in the frequency-domain analyses were:

- *Modal_Loadings.xlsx*: creates the six modal loads out of the mode shapes and synchronous pressure measurements from the BLWT (time history loads);
- *Frequency_Domain.xlsx*: generates the Power Spectral Density (PSD) from the modal loads through a Fourier transform;
- *Frequency_Domain_Results.xlsx*: uses the method presented in [section 2.3](#), “Solution in the frequency domain,” to find the final accelerations of the building in each direction.

The Fourier transform coefficients of the generalized forces acting on the tall building’s façade are used to evaluate the final accelerations and angular velocities, according to the workflow for the frequency-domain analysis presented in [Figure 6.3](#).

Figure 6.3 – Dynamic analysis workflow (frequency domain).



Source: Author.

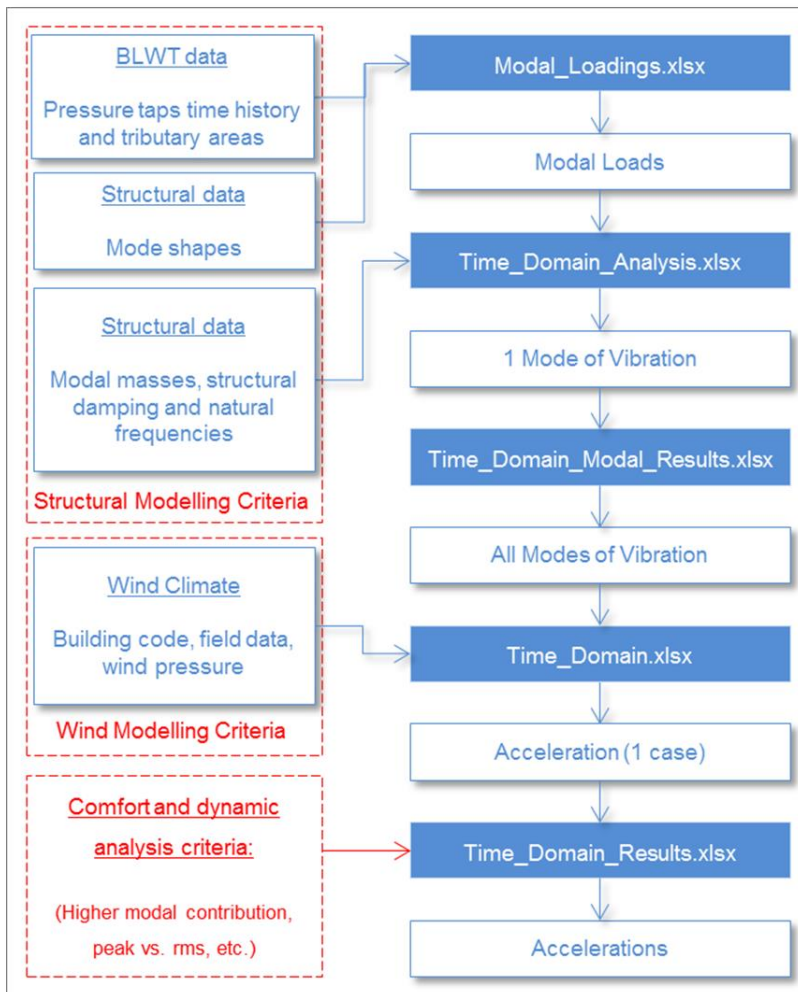
The worksheets used in the time-domain analyses were:

- *Modal_Loadings.xlsx*;

- *Time_Domain_Analysis.xlsx*: uses the 4th Order Runge-Kutta to find the modal response for each mode of vibration;
- *Time_Domain_Modal_Results.xlsx*: stores all modal responses for each wind load direction;
- *Time_Domain.xlsx*: generates the final accelerations in eight different positions of the floor using the modal responses. In addition, it assesses *Peak and RMS* from the time-history accelerations calculated;
- *Time_Domain_Results.xlsx*: stores all of the results of accelerations from the time-domain analysis.

The procedure described in this section is performed using Microsoft Excel (2013) worksheets and assesses eight possible accelerations for one wind direction at a time (see *Figure 6.8*). The final workflow for the time-domain analysis is presented in the *Figure 6.4*.

Figure 6.4 – Dynamic analysis workflow (time domain).



Source: Author.

6.2.1 MODAL LOADS

The BLWT data for building A corresponds to a time-history of 222 pressure taps over 4920s of duration for each azimuth multiple of 10° starting from the north. Building B has a time-history of 363 pressure taps during 13894s, also for each azimuth multiple of 10°. The angle gaps chosen for this study follow the same interval as the BLWT studies, since a tall building's response can greatly vary between two 10° azimuths (IRWIN ET AL., 2005). The only exceptions for the abovementioned rule are the directions between 150° and 200°, and between 350° and 360° for building A, due to the lack of BLWT time-series data between these azimuths. For these azimuths, the responses were interpolated. Building A was studied by Rowan Williams Davies and Irwin Inc., whilst building B WTT was studied by the Davenport Wind Engineering Group.

Each pressure tap has a tributary area and eccentricities “ $e_{x,\ell}$ ” and “ $e_{y,\ell}$ ” from the vertical axis of reference Z and storey “ ℓ ” above the ground (see [Figure 6.5](#) and [Figure 1.19a](#)). Combining eq. (1.1), (1.2), and (1.5) with (2.12), one can find the modal loading for each mode of vibration “ j ” studied (eq. (6.2)). In this thesis, six modes were considered in the analysis for building A, and nine for building B (as it will be explained later in this chapter).

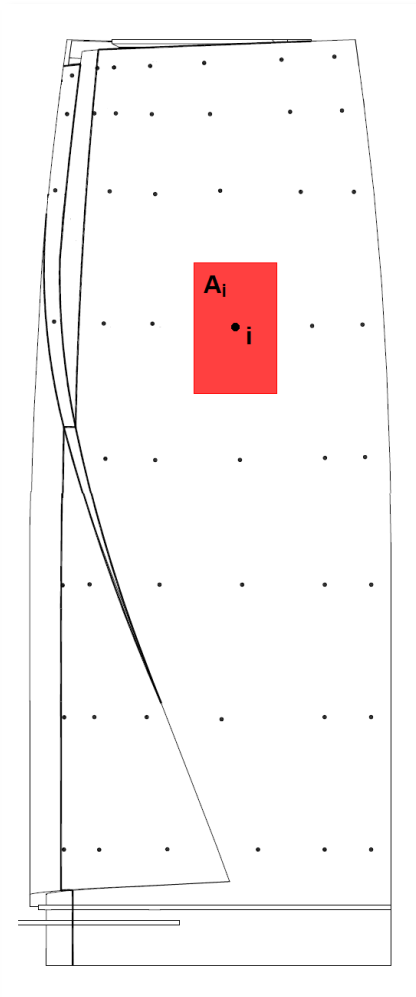
$$P_j(t) = \{\Phi\}_j^T \{p(t)\} = \sum_{\ell=1}^m [(\Phi_{\ell,x,j} + e_{y,\ell} \Phi_{\ell,\theta,j}) p_{x,\ell}(t)] + \sum_{\ell=1}^m [(\Phi_{\ell,y,j} + e_{x,\ell} \Phi_{\ell,\theta,j}) p_{y,\ell}(t)] \quad (6.2)$$

To fit the methodology of this study, eq. (6.2) needed to be slightly changed for three main reasons: the pressure taps have tributary areas representing more than one floor (see [Figure 6.5](#)); there are more than one pressure tap for each building height level (see [Figure 6.5](#)); the pressure-tap heights do not correspond exactly to the heights of the building floors. The adaptation of eq. (6.2) leads to:

$$\begin{aligned}
 P_j(t) = & \sum_{i=1}^{222} \{ [\Phi_{x,j}(h_i) + e_{y,i} \Phi_{\theta,j}(h_i)] p_{x,i}(t) \} + \\
 & + \sum_{i=1}^{222} \{ [\Phi_{y,j}(h_i) + e_{x,i} \Phi_{\theta,j}(h_i)] p_{y,i}(t) \}
 \end{aligned}
 \tag{6.3}$$

where “ $\Phi_{x,j}(h_i)$ ”, “ $\Phi_{y,j}(h_i)$ ” and “ $\Phi_{\theta,j}(h_i)$ ” are the values of the eigenvectors for height “ h_i ” of pressure tap “ i ” (eq. (6.4)). These values are assessed through interpolation of the eigenvector components. The horizontal components of the normal force acting on the building façade, “ $p_{x,i}$ ” and “ $p_{y,i}$ ”, are calculated by pressure “ $q_i(t)$ ” (at the pressure tap “ i ”) multiplied by the corresponding tributary area “ A_i ” (see [Figure 1.19](#)).

Figure 6.5 – Pressure taps layout (building A).



Source: Author.

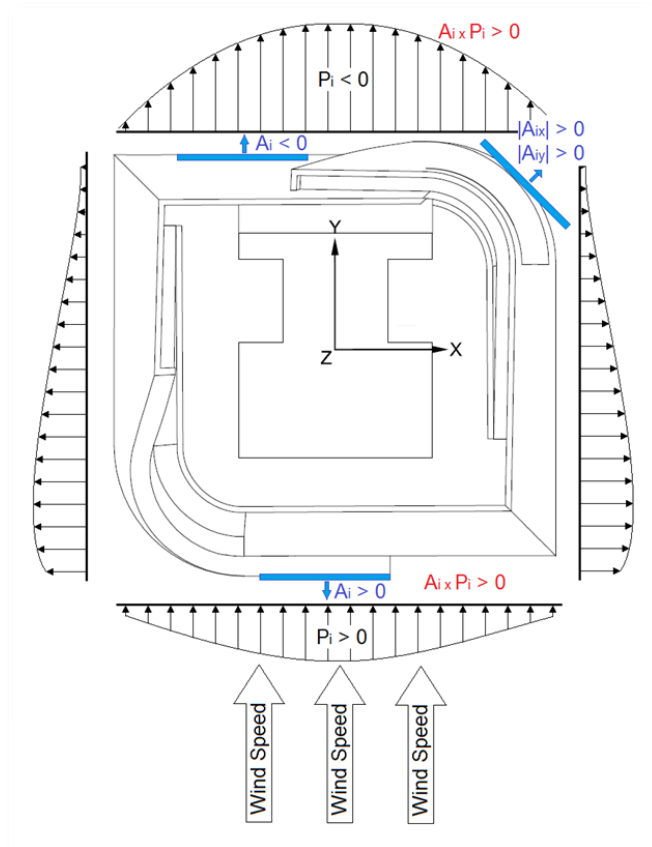
The eigenvector value interpolated for height “ h_i ” is given by:

$$\Phi_{x,j}(h_i) = \frac{\Phi_{x,j}(h_{\ell+1}) - \Phi_{x,j}(h_{\ell})}{h_{\ell+1} - h_{\ell}} (h_i - h_{\ell}) + \Phi_{x,j}(h_{\ell}) \quad (6.4)$$

where:

- h_{ℓ} stands for the highest level of the building below pressure tap “ i ”;
- $h_{\ell+1}$ is the height of the subsequent structural level;
- $\Phi_{x,j}(h_{\ell})$ and $\Phi_{x,j}(h_{\ell+1})$ are the respective values of the eigenvector for the known heights “ h_{ℓ} ” and “ $h_{\ell+1}$ ”;
- Eq. (6.4) is analogous for y and torsional DOF’s.

Figure 6.6 – Tributary areas and pressures on the building’s façade (building A).



Source: Author.

There are two possible components for the tributary area “ A_i ”, associated with the local building coordinates x and y (see [Figure 6.6](#)). For the pressure taps on the north/south façade, “ A_i ” assumes negative/positive values for the “ $p_{y,i}$ ” component, whilst it is nullified for the “ $p_{x,i}$ ” component. Analogously, these areas

are null for the “ $p_{y,i}$ ” component and negative/positive for the “ $p_{x,i}$ ” component on the east/west façade. Some pressure taps are located on the round corners of the building’s façade and therefore present absolute positive values for these areas, since the vector representing the normal surface have components in both x and y directions.

The area sign depends on the façade orientation:

- Positive for the façade oriented towards negative values of the Y axis (south façade);
- Negative for the north façade;
- Positive for the west façade (oriented towards negative values of the X axis);
- Negative for the east façade.

One might consider a wind blowing towards positive values of the Y axis to better understand these signs. On the façade facing the wind (south façade), the wind pressure is positive and the area is positive as well, whilst on the façade facing the opposite direction (north façade), both the area and the wind pressure assume negative values (negative values for pressure meaning “suction” on the façade when the internal wind pressure is higher than its external pressure). These values of wind pressure and area generates a resultant force towards positive values of the Y axis, which is reasonable considering that this resultant force is oriented to the same direction of the wind speed. [Figure 6.6](#) illustrates this situation, where the resultant along-wind force is oriented to positive values of the Y axis along with the wind speed.

The reasoning is analogous to the wind blowing onto the north façade. In this case, there would be suction on the south façade (which has positive area values) and positive pressure on the north façade (which has negative area values). The resultant force would be negative (towards negative values of Y axis).

Crosswind forces result from the unbalanced forces in the perpendicular direction of the wind due to two main reasons: asymmetric geometry leading to unbalanced crosswind force in the same direction; wind pressure fluctuations due to turbulence of the wind, leading to fluctuating crosswind forces in both directions.

This dense approach to the calculation of resultant forces and modal loads is justified by the amount of data to be processed in the case study. There is a total of six modes of vibration per structural model for building A and 36 wind loads (one for each 10° azimuth gap). Considering different mode shapes for each one of the three structural models of each building (as it will be seen in [Chapter 7](#)), the number of modal loads to be calculated is 648 only for building A. As for building B (with a total of nine analysed modes), the total number of modal loads to be assessed is at least 1620.

The resultant methodology is an automatic procedure to calculate all required modal loads for each wind direction. This automatic procedure is shown in the Microsoft Excel (2013) worksheet “[Modal_Loadings.xlsx](#)” and is designed to prevent human errors in the process. The final result of this procedure is a set of time-history modal loads to be used in the subsequent time-domain analysis (see [sections 6.2.2](#) and [6.2.3](#)).

6.2.2 FREQUENCY-DOMAIN ANALYSIS

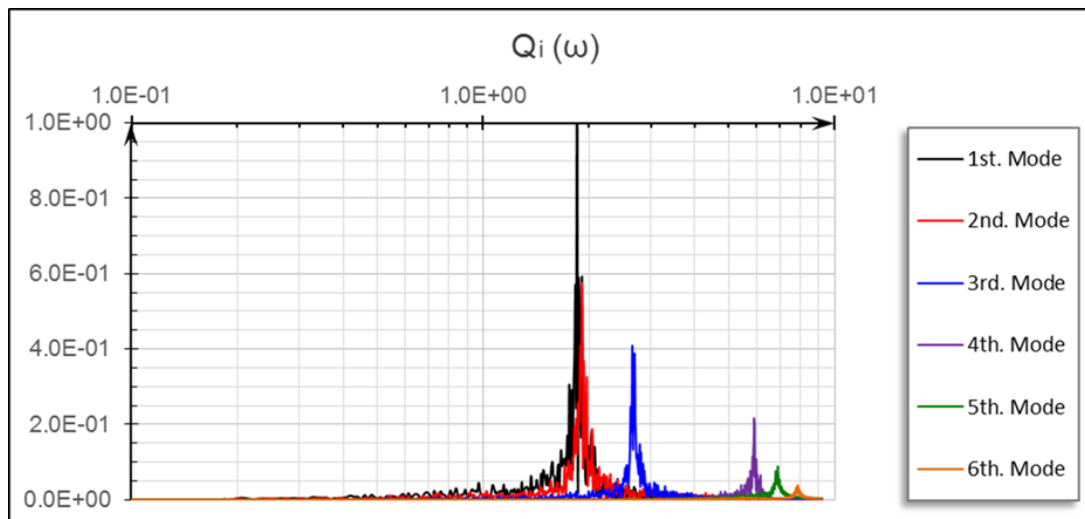
Once the modal loads are correctly assessed, a Fourier transform is used to find the respective coefficients, applying eq. [\(2.15a\)](#) to [\(2.15c\)](#) to each load. The period of integration was reduced to increase the precision of the Fourier transform and to achieve lower values for the harmonic frequencies (see eq. [\(2.14\)](#)). The value for period “ T_p ” was high enough for both buildings to allow for the ergodic hypothesis discussed in [section 1.2.2.2](#).

The overall damping ratio is 1.25% for building A and the first natural angular frequency of the first structural model (beam-end offset, only) is 1.858 rad/s for building A. For building B, these values are 1.00% and 1.150 rad/s , respectively. The first structural model was used to define the minimum period of integration, since it is the less stiff one. Considering the given natural angular frequencies, the overall damping ratio, and eq. [\(1.8\)](#), the minimum time span for the Fourier transform is 200s for building A and 320s for building B. A 889s period was used in both analyses, meeting both requirements. The variances between buildings A and B can be explained by the difference in height and structural materials used in their construction. These differences will be addressed in more details in the building’s description in [Chapter 7](#) ([sections 7.1.1](#) and [7.3.1](#)).

The 889s period led to a precision of 0.0071 rad/s or 0.0011 Hz for the frequency gap in the Fourier transform, where 3186 harmonics were obtained to perform the frequency-domain analysis later.

The procedures described in this section and in [section 2.3](#) (eq. **(2.13)** to **(2.17)**) were performed in the Microsoft Excel (2013) worksheet “*Frequency_Domain.xlsx*”. The results of the generalized accelerations for the 10° azimuth are given in [Figure 6.7](#), from which it is plausible to infer that the sixth mode already has very little participation in the final acceleration on the floor of interest for building A (which is going to be better detailed in [Chapter 7](#)). These results support the justification to study higher modal truncation in the sixth mode of vibration for the current case study of building A. However, studies carried out with other tall buildings might need even higher modal truncation to provide reliable results. As far as building B is concerned, it follows the same rule of higher modal truncation with three extra modes (up to the ninth mode) with a little more relative importance for the seventh mode, as it will be better detailed in [Chapter 7](#).

Figure 6.7 – PSD of the modal accelerations Q_i for 10° azimuth (Building A).



Source: Author.

Modal results in the frequency domain (generalized accelerations) are assessed by eq. **(2.19)**. When each modal result is correctly assessed, eq. **(2.21)** and **(2.22)** are used to calculate the final accelerations in each direction (X, Y, and

torsional components). Finally, when all components of acceleration are correctly evaluated, the final peak acceleration “ a_{Peak} ” is calculated using eq. (6.5).

$$a_{\text{Peak}} = \Phi \sqrt{(a_x)^2 + (a_y)^2 + (a_{\theta}R)^2} \quad (6.5)$$

where:

- a_x , a_y , and $a_{\theta}R$ are the peak X axis, Y axis, and torsional components of acceleration, in milli-g;
- $a_{\theta}R$ is the product of the angular acceleration “ a_{θ} ” times the radius “ R ” to compose the linear acceleration (see [Figure 1.20](#));
- Φ is the joint-action factor, explained in [section 5.4.1.2](#).

Initially, the joint-action factor assumes a unitary value. After evaluating the building’s final responses in the time domain (see [section 6.2.3](#)), this factor will be calibrated and discussed in [Chapter 7](#).

Peak accelerations shall be calculated from rms values using eq. (2.24) to (2.26) (see [section 2.3.2](#)). The procedure for the assessment of peak acceleration components “ a_x ”, “ a_y ,” and “ $a_{\theta}R$ ” and final acceleration results (eq. (2.19) to (2.26) and 6.5) is performed using the Microsoft Excel “[Frequency_Domain_Results.xlsx](#)” worksheet.

6.2.3 TIME-DOMAIN ANALYSIS

Once the time-history of the generalized forces is obtained, a [4th Order Runge-Kutta](#) takes place to find each modal response of the building (see eq. (2.27a) to (2.28c)). This part of the analysis is done using the Excel (2013) worksheet “[Time_Domain_Analysis.xlsx](#)”.

For the method applied, the acceleration of the generalized coordinate is already a part of the result (see eq. (2.27a)). Therefore, the results of this stage are six generalized accelerations. These accelerations were later stored in the Microsoft Excel (2013) worksheet “[Time_Domain_Modal_Results.xlsx](#)”.

The “ j ” acceleration for each generalized coordinate generates three components: “ $a_{x,j}$ ”, “ $a_{y,j}$,” and “ $a_{\theta,j}R$ ” (see [Figure 1.20](#)). As described in [section 2.4](#) (see eq. (2.29a), (2.29b), and (2.29c)), this procedure transforms the acceleration of

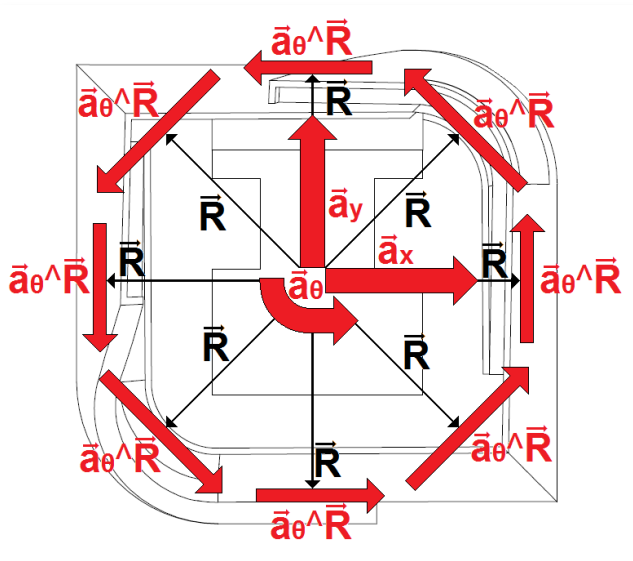
each generalized coordinate into three components and stacks them together for all modes of vibration (“ $a_x = \sum_{j=1}^6 a_{x,j}$ ”, “ $a_y = \sum_{j=1}^6 a_{y,j}$ ” and “ $a_\theta = \sum_{j=1}^6 a_{\theta,j}$ ”).

Once the three components are assessed, the vectorial sum requires some elaboration in order to compose the complex movement. At each time-step, one has the final acceleration over the X axis and the Y axis, but the issue of adding the torsional contribution is not unique, as there are several possible locations where the user might be located. In order to solve this indetermination, the acceleration was calculated at eight different locations of the building floor (see *Figure 6.8*).

The idea behind this procedure is to take full advantage of the benefits of the time-domain analysis. The time-domain analysis allows for a precise assessment of all components of the building floor acceleration without no need for artificial coefficients, such as joint action factors and peak factors. This procedure enables the calculation of each possible x and/or y component of the acceleration originated from the torsion of the building within 45° sectors. This angular vector size was chosen in order to provide a detailed assessment of these accelerations without prejudice to the procedure by rendering it extremely heavy or excessively slow. The final acceleration for each time-step is calculated by eq. (6.6).

$$|\vec{a}_{Peak}| = |\vec{a}_x + \vec{a}_y + (\vec{a}_\theta \times \vec{R})| \tag{6.6}$$

Figure 6.8 – Locations for resultant acceleration assessment.



Source: Author.

6.3 WIND LOAD MODELLING

6.3.1 WORST CASE METHOD

Initially, the worst-case method (described in [section 4.2](#)) was used to calculate the final responses. This approach allows one to properly observe the directional dependency of the building's response and compare the three different structural models for each building.

For the worst-case method, the data from the pressure taps were normalized by the dynamic pressure of the wind tunnel at "1.52m" for building A. In order to find the pressure at the real scale, the final recorded value on each tap needed to be multiplied by the dynamic pressure of the wind speed at a height of "1.52m × 400 = 608m" (since the model scale is 1:400). This pressure must also take into consideration the "fetch" of the oncoming terrain roughness for each azimuth. For building B, the reference dynamic pressure is set at 500m as the standard open exposure.

The normalization of the pressure data allows the return period to be a final input in the procedure, along with the time step. The design wind speed could be set up to the respective return period and subsequently the equivalent dynamic pressure could be calculated using the formulations of NBR6123-1988 for both buildings:

$$q(T) = 0.613 \left[V(T) b F_r \left(\frac{608}{10} \right)^p \right]^2 \quad (6.7)$$

$$q(T) = 0.613 \left[V(T) b F_r \left(\frac{500}{10} \right)^p \right]^2 \quad (6.8)$$

where "q(T)" is given in N/m² and "b", "F_r," and "p" stand for the NBR6123-1988 parameters to calculate the wind speed at a given height for a specific design roughness of terrain. "V(T)" is the wind speed at the height of reference (10m) for the period of return "T" for a 3s gust.

The time scale must be adjusted between the WTT and the full scale model for each wind speed, which is a direct result from return period. Linear scale of the simulation "λ_L" was briefly discussed in [section 1.4.1](#), whilst the time scale for full scale model can be expressed by eq. (6.9).

$$\Delta t = \frac{S}{V(T)} \quad (6.9)$$

where:

- Δt stands for the time scale (or time gap between two consecutive wind loads);
- S is a variable depending on each azimuth.

The variable “ S ” and wind speed in the WTT are fixed. When the full scale wind speed increases, its time scale decreases. Therefore, a return period increase leads to changes in the PSD of wind loads, bringing the resonant response to a portion of the power spectra with higher energy density and, consequently, increasing the sensitivity of the structure to the dynamic effects of the wind loads.

6.3.2 UP-CROSSING METHOD

The methodology described in [section 4.4](#) is used in this analysis. To begin the procedure, the response boundary (see [Figure 4.7](#)) is assessed for several required pressures corresponding to several velocities (see [Figure 4.8](#)).

The probability density function “ $p_i(R; \alpha_i)$ ” given in eq. [\(4.8\)](#) uses the parameters shown in [Table 6.2](#). Then, parameters “ $|\bar{\alpha}|$ ” and “ $|\bar{V}|$ ” are obtained by eq. [\(4.10a\)](#) and [\(4.10b\)](#) using the wind speed “ V ,” which corresponds to the response boundary. Finally, crossing rate “ R ” is obtained using eq. [\(4.9\)](#), and return period “ T ” is obtained by eq. [\(4.11\)](#).

Several pairs of acceleration “ a_T ” vs. return period “ T ” are obtained in a tabular form and plotted into a chart, where a regression curve takes place to interpolate these values and provide the final resultant acceleration level for the sought return period.

The method will be applied to two sets of wind climate: the data provided by [Table 6.2](#) and a non-directional wind climate for São Paulo. In this sense, it is possible to present three different output scenarios: one for the worst-case method and two for the up-crossing method, including a directional building in a directional wind climate, and a directional building in a non-directional wind climate (BURTON ET AL.. 2015). These directives allow for the evaluation of the impact of criteria from the wind climate and the assessment method (up-crossing and worst-case methods).

Table 6.2 – $p_i(R; \alpha_i)$ parameters for São Paulo.

Azimuth	A_θ	CL_θ (km/h)	KL_θ	CU_θ (km/h)	KU_θ	U_{th_θ} (km/h)	V_{open}/V_{site}
10	1.80%	10.28	1.49	10.02	1.47	21.00	1.37
20	1.60%	9.24	1.44	9.16	1.43	21.00	1.36
30	1.60%	8.41	1.37	8.22	1.36	21.00	1.37
40	1.40%	7.94	1.33	7.20	1.26	21.00	1.38
50	1.70%	7.87	1.33	6.34	1.18	16.00	1.39
60	2.70%	8.13	1.36	6.46	1.18	21.00	1.38
70	2.70%	8.55	1.38	7.58	1.26	21.00	1.38
80	3.20%	9.12	1.41	8.65	1.32	21.00	1.39
90	4.30%	9.75	1.44	9.17	1.32	26.00	1.38
100	4.00%	10.32	1.47	9.32	1.30	31.00	1.35
110	3.70%	10.80	1.49	9.34	1.27	26.00	1.30
120	4.60%	11.18	1.52	9.29	1.27	21.00	1.27
130	4.30%	11.51	1.57	9.10	1.28	31.00	1.26
140	5.00%	11.88	1.64	8.95	1.30	31.00	1.26
150	7.20%	12.31	1.72	9.09	1.35	41.00	1.23
160	8.10%	12.62	1.78	9.31	1.38	31.00	1.20
170	7.40%	12.70	1.80	9.48	1.40	26.00	1.20
180	6.20%	12.54	1.77	9.83	1.43	16.00	1.23
190	3.40%	12.20	1.72	10.38	1.49	21.00	1.29
200	2.10%	11.71	1.66	10.68	1.52	21.00	1.30
210	1.10%	11.08	1.60	10.47	1.51	16.00	1.26
220	0.60%	10.30	1.53	10.09	1.50	21.00	1.22
230	0.40%	9.56	1.49	9.94	1.52	21.00	1.23
240	0.40%	9.11	1.47	10.25	1.57	21.00	1.29
250	0.50%	8.97	1.45	10.66	1.59	26.00	1.35
260	0.60%	8.99	1.41	10.49	1.52	26.00	1.36
270	0.80%	9.08	1.35	9.84	1.40	26.00	1.34
280	1.00%	9.31	1.32	9.48	1.33	26.00	1.33
290	1.20%	9.67	1.33	9.51	1.31	21.00	1.34
300	1.80%	10.21	1.40	9.46	1.30	21.00	1.32
310	1.40%	10.93	1.49	9.27	1.28	21.00	1.29
320	1.90%	11.57	1.54	9.35	1.27	26.00	1.26
330	3.00%	11.94	1.52	9.83	1.28	26.00	1.28
340	3.40%	12.03	1.50	10.32	1.34	26.00	1.33
350	2.90%	11.82	1.51	10.58	1.41	21.00	1.37
360	2.30%	11.23	1.52	10.53	1.47	31.00	1.38

Source: Author.

6.4 COMFORT EVALUATION OF ASSESSED ACCELERATIONS

6.4.1 DETERMINISTIC COMFORT ASSESSMENT

The accelerations assessed by the methodology explained in this chapter are evaluated based on the comfort curves studied in [section 1.5.1](#), “*Current approach to human comfort assessment*”.

There are several human comfort assessment curves to evaluate serviceability during wind-induced motion. In this thesis, they were organized in two figures: [Figure 1.21](#) and [Figure 1.22](#). The first gathers comfort assessment curves for a 1-year return period, whilst the second collects comfort assessment curves for a 10-year return period.

Later, the same results are compared with the comfort curves in [Figure 5.17](#). These curves are not related to a return period, as in [Figure 1.21](#) and [Figure 1.22](#). The purpose of these curves is to show the differences between comfort assessments via motion perception versus comfort assessments via actual comfort parameters. Despite the extensive data gathering for these curves, these data had no further survey with the building users as did Hansen et al. (1973) in their studies. These studies presented specific questionnaires for the users to relate the level of acceleration to the return period.

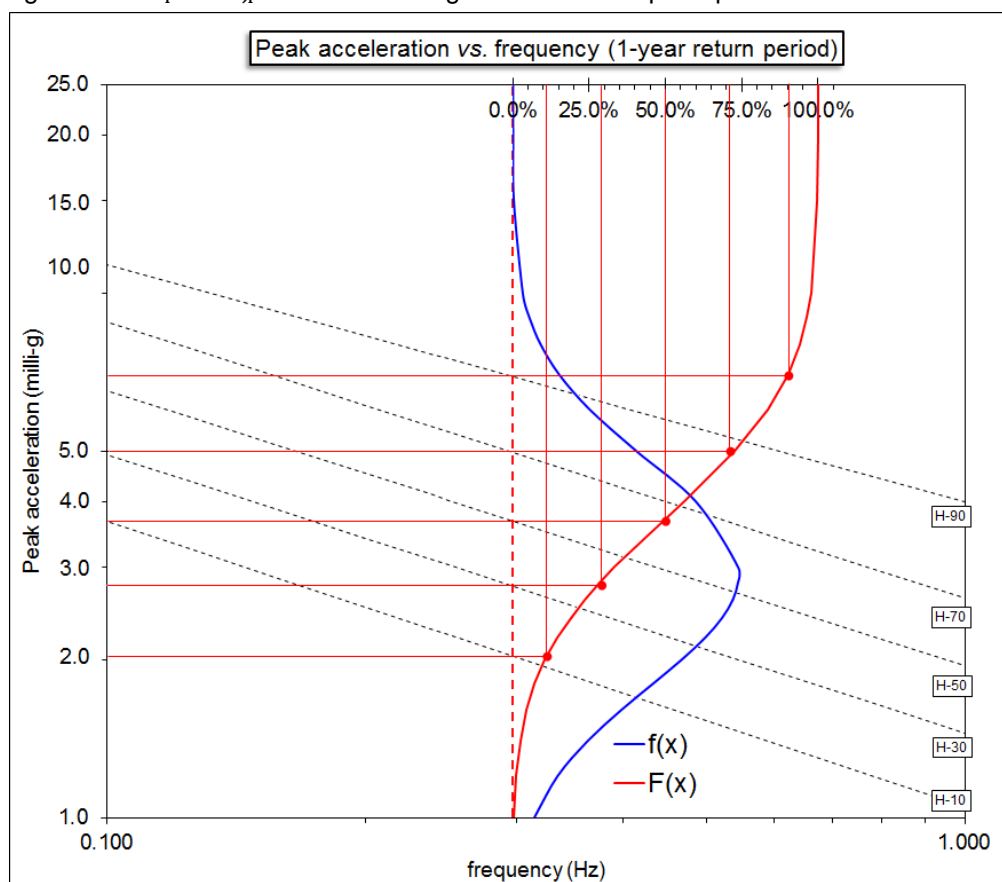
6.4.2 PROBABILISTIC COMFORT ASSESSMENT

The probabilistic comfort assessment will be presented later herein, with the procedure described in [section 5.3.5](#). The “ λ_p ” and “ ζ_p ” coefficients were calibrated using the AIJ-GEH-2004 curves, whilst the “ λ_A ” and “ ζ_A ” were calculated from the rms acceleration assessed in the numerical simulations previously described in the subsections of this chapter.

Table 6.3 – Coefficients λ_p and ζ_p vs. buildings’ first natural frequency.

$f_{(Hz)}$	λ_p	$(\zeta_p)^2$
0.2957	0.204	0.132
0.3123	0.175	0.140
0.3262	0.156	0.146

Source: Author.

Figure 6.9 – λ_p and ζ_p calibration using AIJ-GEH-2004 perception curves.

Source: Author.

The natural frequencies of interest for this analysis are the first natural frequencies of each building model. These frequencies will be shown and discussed later (in [Chapter 7](#)). Nonetheless, the first natural frequency of each building model will be shown in [Table 6.3](#), along with the respective " λ_p " and " ζ_p " coefficients, based on the perception curves from AIJ-GEH-2004, as shown in [Figure 6.9](#). In this figure, " $f(x)$ " is the log-normal function consistent with the curves of AIJ-GEH-2004 for the given natural frequency, whilst " $F(x)$ " is its cumulative function.

Parameter " μ_A " is calibrated as " $2\sigma_A$ ", following the suggestion presented by Tamura et al. (2006), where " σ_A " is the rms acceleration of the building floor studied.

6.5 MODULUS OF ELASTICITY FOR COMFORT ANALYSIS

Once the final accelerations are assessed, the worst case can be detected (wind load direction). Then, through the time-history of displacements for each vibration mode, the time-history of elastic modal forces can be assessed using eq. (6.10).

$$\{f_s\}_j(t) = [M]\{\Phi\}_j(\omega_j)^2 Y_j(t) \quad (6.10)$$

By applying each normalized modal load “ $\{f_s\}_{N,j} = [M] \times \{\Phi\}_j(\omega_j)^2$ ” without the “ $Y_j(t)$ ” factor, one can reprocess the building’s structure. The overall normalized bending moment “ $M_{N,j}$,” normalized shear force “ $V_{N,j}$,” and normalized axial force “ $N_{N,j}$ ” can be read for the main structural elements that participate in the structural system resisting lateral forces. Then, the final time-history of internal-forces can be assessed by eq. (6.11a) to (6.11c).

$$M(t) = \sum_{j=1}^n M_{N,j} Y_j(t) \quad (6.11a)$$

$$V(t) = \sum_{j=1}^n V_{N,j} Y_j(t) \quad (6.11b)$$

$$N(t) = \sum_{j=1}^n N_{N,j} Y_j(t) \quad (6.11c)$$

The procedure is carried out using linear transformations of the basic equation of equilibrium of elastic forces:

$$\{f_s\}(t) = [K]\{u\}(t) \quad (6.12)$$

where “[K]” is the stiffness matrix of the building and “ $\{u\}(t)$ ” is the displacement vector for each time step. Replacing eq. (6.10) in eq. (6.12), one obtains:

$$\{u\}(t) = [K]^{-1}[M] \sum_{j=1}^n \{\Phi\}_j(\omega_j)^2 Y_j(t) = \sum_{j=1}^n [K]^{-1}[M]\{\Phi\}_j(\omega_j)^2 Y_j(t) \quad (6.13)$$

Then, internal forces can be obtained directly from vector “ $\{u\}(t)$ ” and from the physical/geometrical (“EA”, “EI”) constant properties of the internal structural elements.

The procedure described in eq. (6.11a) to (6.11c) is equivalent to calculating the parcel “[K]⁻¹[M]{ Φ }_j(ω_j)²” of the eq. (6.13), and then multiplying it by the respective generalized coordinate “ $Y_j(t)$ ” for each time step.

The time-history of internal forces from each relevant structural element is analysed and the domain of stress (both tension and compression) in their sections is

evaluated. If the value of cracked regions is high enough, for example, the overall flexural stiffness “EI” must be multiplied by a factor smaller than the unitary value and the whole procedure must be performed with this new stiffness value for each relevant structural member.

On the other hand, if the results show maximum tension values below “ $f_{ct,f}$ ” (see [section 3.5.1](#)) for these relevant structural members, the model remains validated. This step represents the final verification from the Davenport’s chain (see [Figure 1.5](#)) and ensures the coherence of structural models regarding the dynamic analysis criteria and wind climate modelling (return period, wind pressure).

7 CASE STUDY

7.1 BUILDING A

7.1.1 GENERAL INFORMATION

The building is 137.30m high, with five basement levels, which results in a structure 157.50m high. The building has 29 typical floors, with a 4.28m floor-to-floor height each, and two technical levels on the top, including a heliport. The total number of structural levels of this tall building is 40.

Figure 7.1 – Studied Building (nearly finished, on the right).

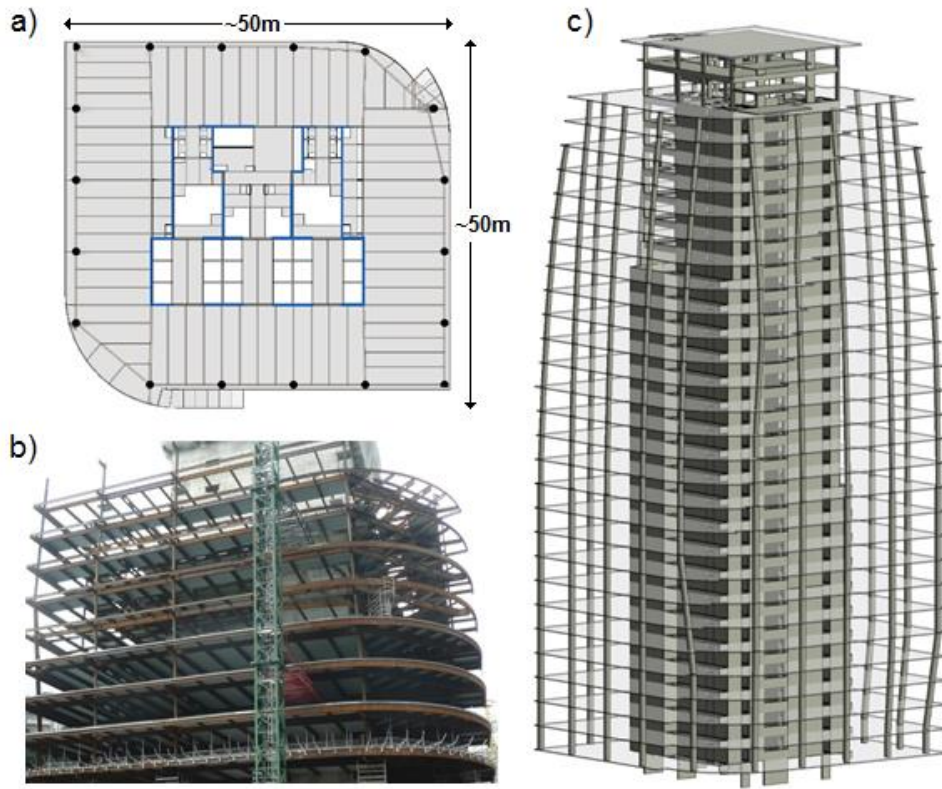


Source: CTBUH.

The structural design of the building is based on gravity columns near its façades with a stiff concrete core in the centre (see [Figure 7.2](#)). This concrete core works for both vertical loads and horizontal loads (wind loads). The structure supporting the floor slab is a composite structure with a steel deck and built-up steel sections with a 8.0cm concrete screed. The live loads acting on the typical floors is 5.0 kN/m².

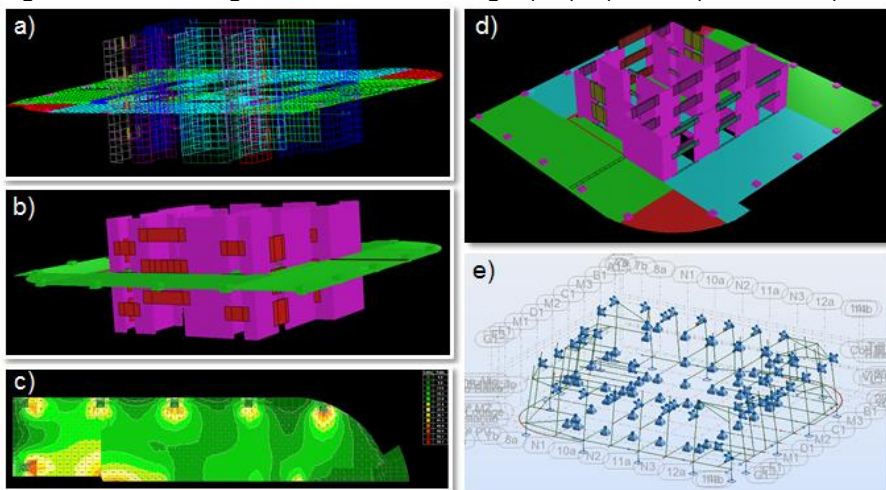
The building's structure and constructive method themselves present interesting features, such as climbing formwork for the concrete core and important transitions in the gravity columns to be properly balanced by floor slab horizontal reactions. However, the technical matter that will be meticulously examined for this building will be the dynamic behaviour due to wind-induced motion.

Figure 7.2 – Building's structure: a) blueprint; b) construction photo; c) 3D model.



Source: Author.

Figure 7.3 – Building's structural modelling: a), b), c), and d) STRAP; e) Robot.

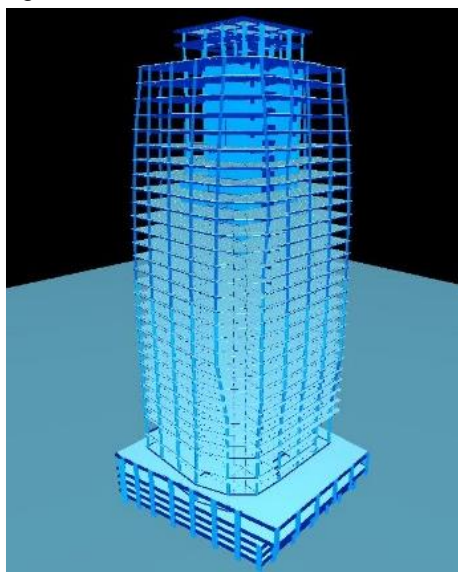


Source: Author.

Most part of the building structure was calculated with the commercial software TQS. Further structural modelling was carried out with the commercial software STRAP and ROBOT (see [Figure 7.3](#)) in order to support the TQS software structural model.

Figure 7.3 a), b), and d) show the rendering of the structural model, while Figure 7.3 c) shows the stress on the floor slab due to horizontal forces from gravity columns' transitions. Figure 7.3 e) shows the ROBOT structural model for the heliport area. The building's dynamic properties (natural frequencies and mode shapes) were calculated using TQS (see Figure 7.4).

Figure 7.4 – Structural model of the building using TQS software.



Source: Author.

7.1.2 BUILDING'S DYNAMIC AND MECHANICAL PROPERTIES

The mass distribution, natural frequencies, and mode shapes of the building were calculated based on the modelling criteria described in section 6.1.1. The building's natural frequencies, angular frequencies, and the respective periods are shown in Table 7.1.

Table 7.1 – Building's natural frequencies and periods of vibration.

Mode	$f_{(Hz)}$	$T_{(s)}$	$\omega_{(rad/s)}$
1	0.2957	3.382	1.858
2	0.3032	3.298	1.905
3	0.4282	2.335	2.691
4	0.9409	1.063	5.912
5	1.092	0.916	6.859
6	1.247	0.802	7.835

Source: Author.

The building's inertial properties (floor mass, moment of inertia, and height) are given in *Appendix 1* (see *Table A1.1*), where the structure's mass is calculated with 30% of the live loads, which leads to a total mass of 100000ton and an approximate building density of 250 kg/m³.

The building's mode shapes for three DOF are also given in *Appendix 1* (*Figure A1.1* to *Figure A1.3*). For the sake of simplicity, this building model will be called building A1, whilst the subsequent application of the structural modelling criteria explained in *sections 6.1.2* and *6.1.3* will generate buildings A2 and A3, respectively. These mode shapes were normalized to meet the terms of the eq. (1.21).

7.2 RESULTS FOR BUILDING A

7.2.1 STRUCTURAL MODELLING CRITERIA

7.2.1.1 Natural frequencies

Building A's natural frequencies of vibration showed a significant increase due to the structural modelling criteria (see *Table 7.2*). Each step presented a different increase in the building's overall stiffness for each mode of vibration for the criteria previously explained in *section 6.1*.

Table 7.2 – Comparison of natural frequencies for the structural models A1, A2, and A3.

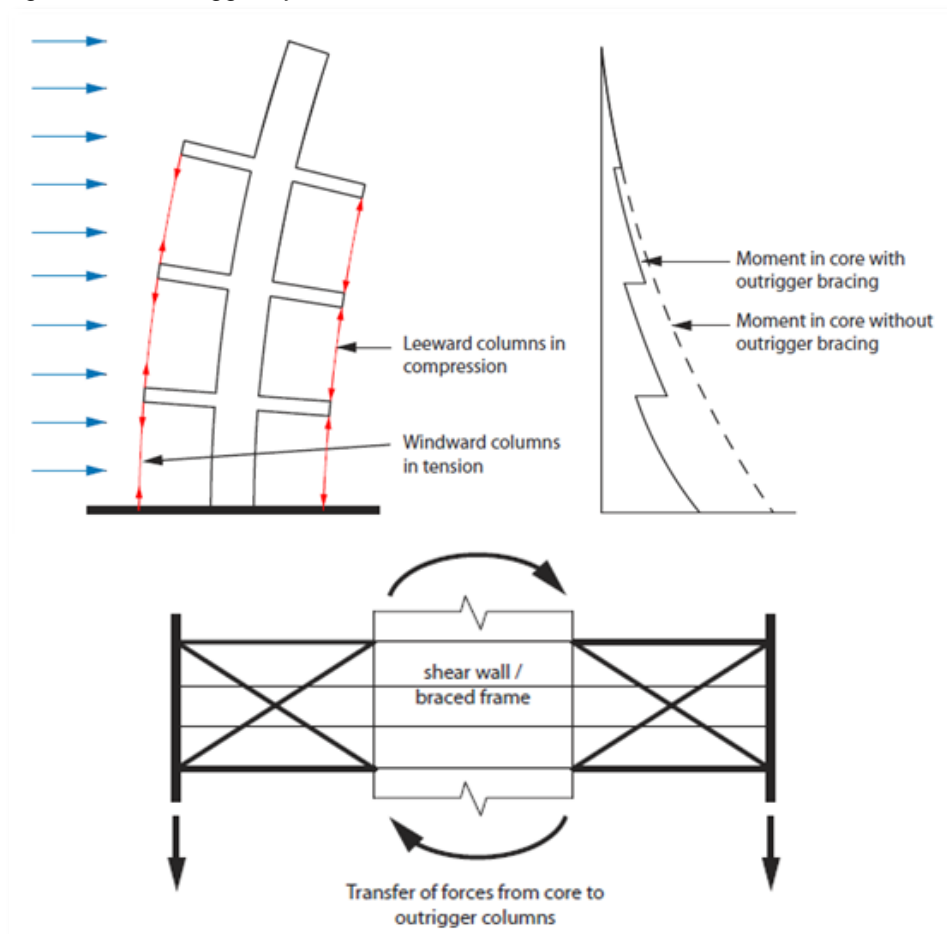
Mode	f_n (Hz)					
	A1	i_{1-2}	A2	i_{2-3}	A3	i_{1-3}
1	0.2957	+ 5.61%	0.3123	+ 4.45%	0.3262	+ 10.31%
2	0.3032	+ 5.71%	0.3205	+ 3.71%	0.3324	+ 9.63%
3	0.4282	+ 5.14%	0.4502	+ 13.82%	0.5124	+ 19.66%
4	0.9409	+ 4.46%	0.9829	+ 10.29%	1.0840	+ 15.21%
5	1.0920	+ 5.22%	1.1490	+ 6.61%	1.2250	+ 12.18%
6	1.2470	+ 4.65%	1.3050	+ 13.79%	1.4850	+ 19.09%

Source: Author.

The first structural model A1 already presents beam-end-offsets, and the first step to increase the precision of the natural frequency assessment is the use of the probable Young's modulus, generating the A2 structural model. The 4th step of structural modelling described by Kim et al. (2009) also used the probable's Young's modulus, where it represented an overall increase of 7% to 12% in the natural

frequencies of the first three natural modes of vibration (two translational modes and one torsional mode). The increase in the natural frequencies of Building A2 is slightly smaller than that of Kim et al.'s (2009) for the probable Young's modulus criterion: around 5.5% for the three first modes. This discrepancy is due to the different formulation of the concrete strength/Young's modulus in both the Korean Building Code (2005) and NBR6118-2014, leading to a different increase in the final compression strength over time.

Figure 7.5 – Outrigger system.



Source: Taranath (1998).

The second step is modelling the floor slab in order to generate the structural model A3. In the research by Kim et al. (2009), this was step two and represented an overall increase between 3% and 11% in the natural frequencies of the translational natural modes of vibration. For the torsional mode, it represented an overall increase between 16% and 23% in the natural frequency. For building A3, the translational modes presented an increase between 3.71% (2nd mode) and 10.29%

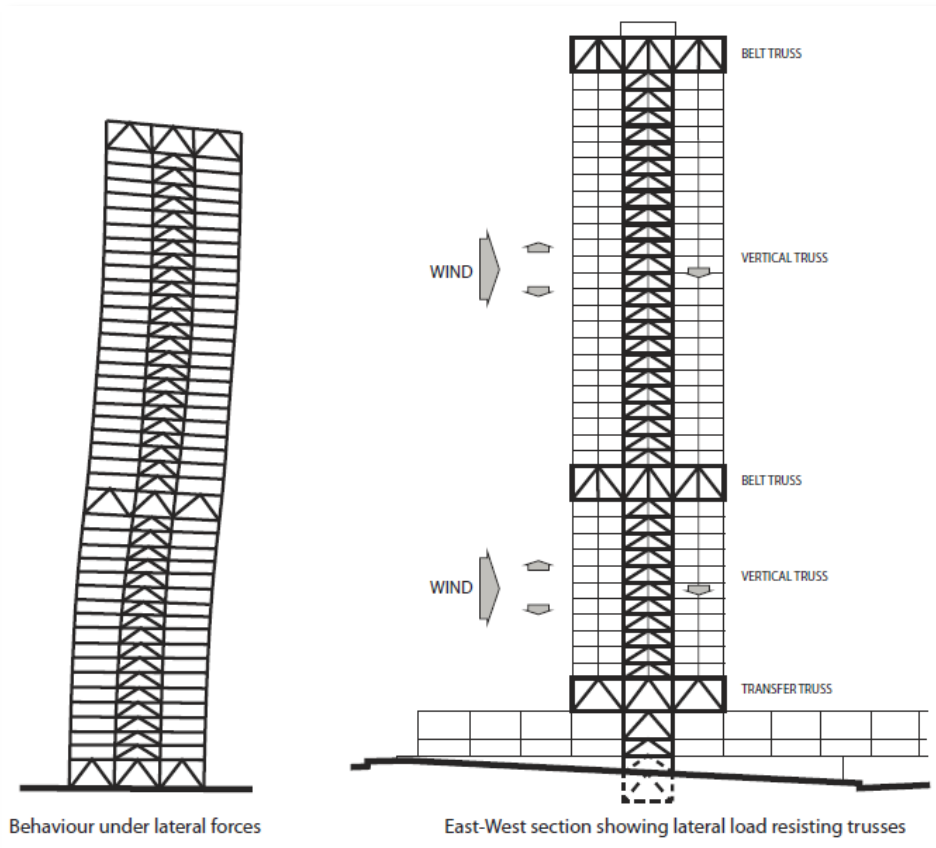
(4th mode, also a torsional mode). For this same building, the torsional modes presented an increase of 13.8% in average. This result is consistent with building C in the research of Kim et al. (2009), which present a structural system that is similar to of the building studied in this thesis.

The increase in the natural frequencies of translational modes can be explained by two main effects (KIM ET AL., 2009):

- Transfer of axial forces from the exterior frame, generating a resistant moment on the core walls in an effect analogous to an *outrigger system* (CHOI ET AL., 2012), but slightly less substantial than the actual system (see *Figure 7.5*);
- Increased coupling between the shear walls through the floor slab.

Both effects have a tendency to approximate the mode deformation shapes of the structure to the ones of a moment resisting frame (see *Figure 7.6*). The features of mode shapes for buildings A1 to A3 will be systematically discussed in *section 7.2.1.2*.

Figure 7.6 – Structural behaviour of an outrigger system under lateral loads.



Source: Beedle and Iyengar (1982).

There is a significant increase in the natural frequencies of torsional modes when compared with the translational ones. According to Kim et al. (2009), the warping rigidity of the diaphragm is related to its out-of-plane rigidity, and the floor slab modelling (which generated building A3) presents an important increase in the stiffness of the vertical direction of the floor slab. This new feature (floor slab modelling) is responsible for the average 13.8% increase in natural frequencies of torsional modes for building A3.

Together, the criteria presented in section 6.1 indicated overall increases in the natural frequencies of building A, varying from 9.63% to 19.66%.

7.2.1.2 Mode shapes

The mode deflection shapes for building A1 are presented in [Appendix 1: Figure A1.1](#) for modal displacements in X axis, [Figure A1.2](#) for modal displacements in Y axis, and [Figure A1.3](#) for modal torsional components. Both the X and Y components are very similar to natural modes 3 to 6 for the three structural models, and therefore require no further presentation (since they were already presented in [Appendix 1](#) for building A1).

Building A2 was generated by a simple increase in the Young's modulus of the structural elements of the building. Even when all the structural elements receive a linear increase due to the increase in the Young's modulus, eq. (1.14) (used to generate the mode shapes) will not behave with the same linearity, as it is a polynomial equation. Therefore, some differences are expected even for this step.

The greater differences, however, are expected for the second step, which generates the structural model for building A3, when compared with the previous step, due to the outrigger-like behaviour and the shear wall coupling explained in the previous section. The mode deflection shapes for the two first natural translational modes of vibration are presented in [Figure 7.7](#), whilst the torsional components of the first six natural modes of vibration are given in [Figure 7.10](#).

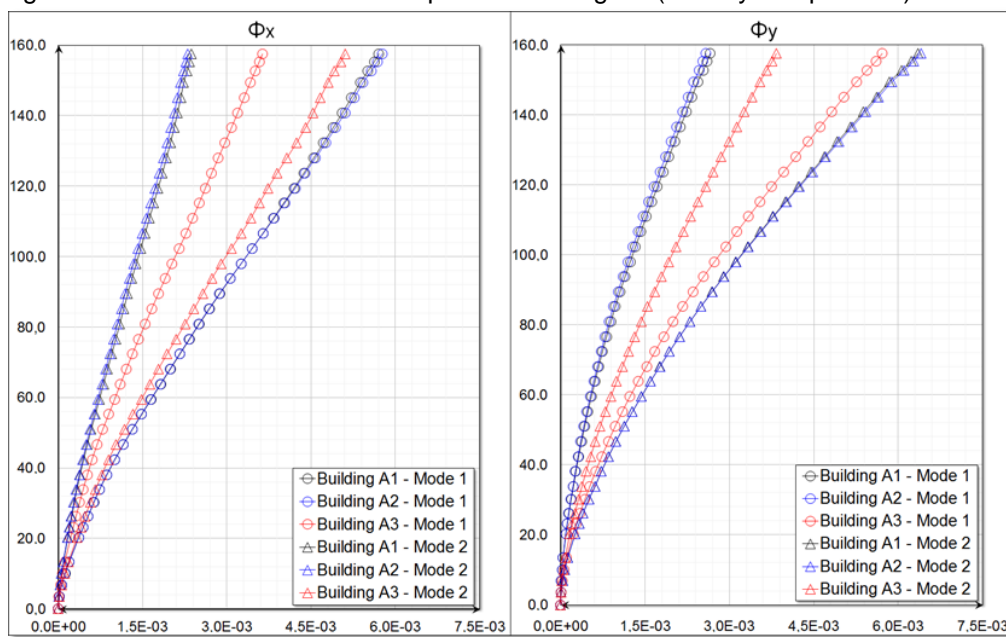
In a preliminary examination, it seems that there are greater differences in the mode deflection shapes in step two (between buildings A3 and A2) and nearly no difference in step one (between buildings A2 and A1). The first mode of vibration for buildings A1 and A2 occurs predominantly in the X axis (with a significant component

in the Y axis), whilst the second modes for both of them occur predominantly in the Y axis (with a smaller component in the X axis).

Building A3, however, seemed to have these directions inverted. After a careful analysis, it was detected that the first two natural frequencies for buildings A1 and A2 are very close, separated only by a 0.082Hz frequency gap (nearly 2.63% of the first natural frequency value). The subsequent increase in the natural frequencies due to the step two of this methodology is higher for the first mode than it is for the second mode, shifting the places of these two modes for building A3.

After visually rearranging the translational components of the mode shapes by shifting the first and the second modes, this modification becomes clearer (see [Figure 7.8](#)).

Figure 7.7 – Translational mode shapes for building A3 (x and y components).

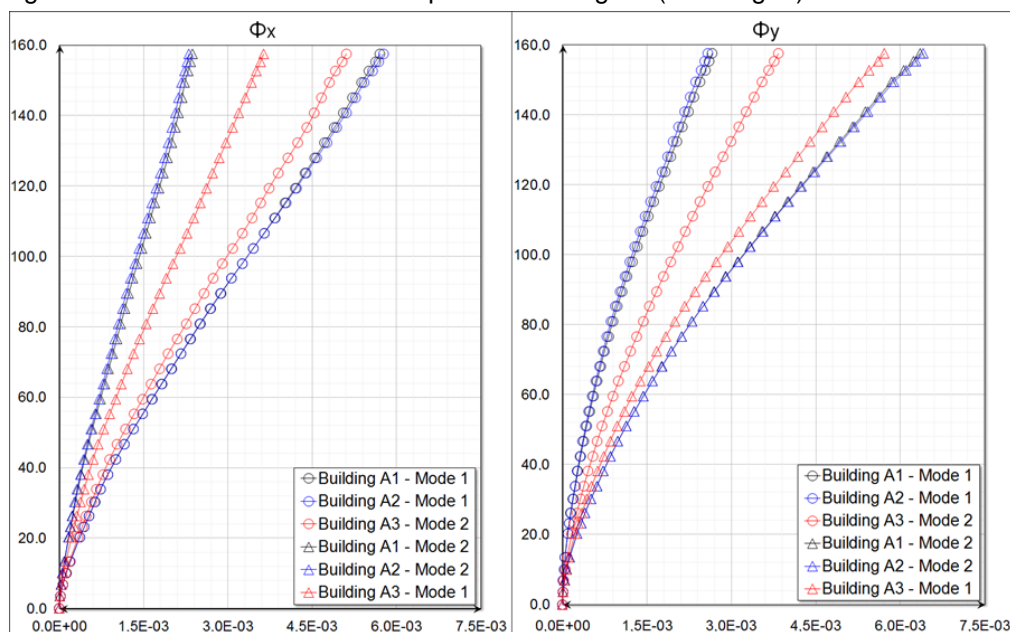


Source: Author.

In [Figure 7.8](#), it is possible to verify that the main component of the mode deflection shapes for the first two natural modes of vibration have a considerable difference, although not as large as that shown in [Figure 7.7](#).

Based on this rearrangement, [Table 7.2](#) can also be rearranged for the Building A3, with the description of the type of movement (see [Table 7.3](#)).

Figure 7.8 – Translational mode shapes for building A3 (rearranged).



Source: Author.

Table 7.3 – Natural frequencies comparison rearranged.

Mode	f_n (Hz)						Type
	A1	i_{1-2}	A2	i_{2-3}	A3	i_{1-3}	
1	0.2957	+ 5.61%	0.3123	+ 6.44%	0.3262	+ 7.59%	Translational y dir.
2	0.3032	+ 5.71%	0.3205	+ 1.78%	0.3324	+ 12.41%	Translational x dir.
3	0.4282	+ 5.14%	0.4502	+ 13.82%	0.5124	+ 19.66%	Torsional
4	0.9409	+ 4.46%	0.9829	+ 10.29%	1.0840	+ 15.21%	Tors. with transl. in x dir.
5	1.0920	+ 5.22%	1.1490	+ 6.61%	1.2250	+ 12.18%	Tors. with transl. in y dir.
6	1.2470	+ 4.65%	1.3050	+ 13.79%	1.4850	+ 19.09%	Tors. with transl. in y dir.

Source: Author.

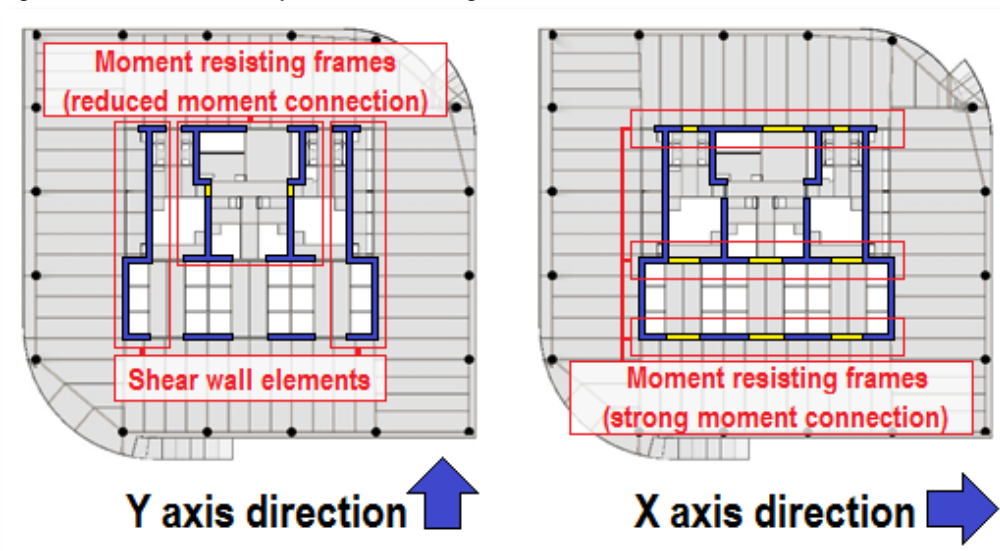
Along with the apparent predisposition of the step two criterion, which increases the natural frequency of the first vibration mode with a value higher than the second vibration mode, the considerable differences between the increases in the natural frequencies for the first two natural modes can be explained with a closer look at the structural system for horizontal loads in building A (see [Figure 7.9](#)).

Horizontal forces in the Y axis are resisted mainly by shear wall elements (highlighted in blue in [Figure 7.9](#)) and two moment resisting frames (where the beam element is highlighted in yellow in [Figure 7.9](#)). One of the moment connections of this moment frame system is not connected with a portion in the strong axis of the shear wall and, therefore, it is a flexible (not hinged, but less stiff) connection.

On the other hand, the structural system for horizontal forces in the X axis is mainly composed by moment resisting frames with connections along the strong axis of the shear walls.

Looking again at *Figure 7.8*, it can be observed that the behaviour of the mode shape components in the Y axis is similar to a cantilever beam, whilst their behaviour in the X axis has a small “S-shaped” distortion (similar to the building’s displacement with an outrigger system, as in *Figure 7.6*).

Figure 7.9 – Structural system of building A.



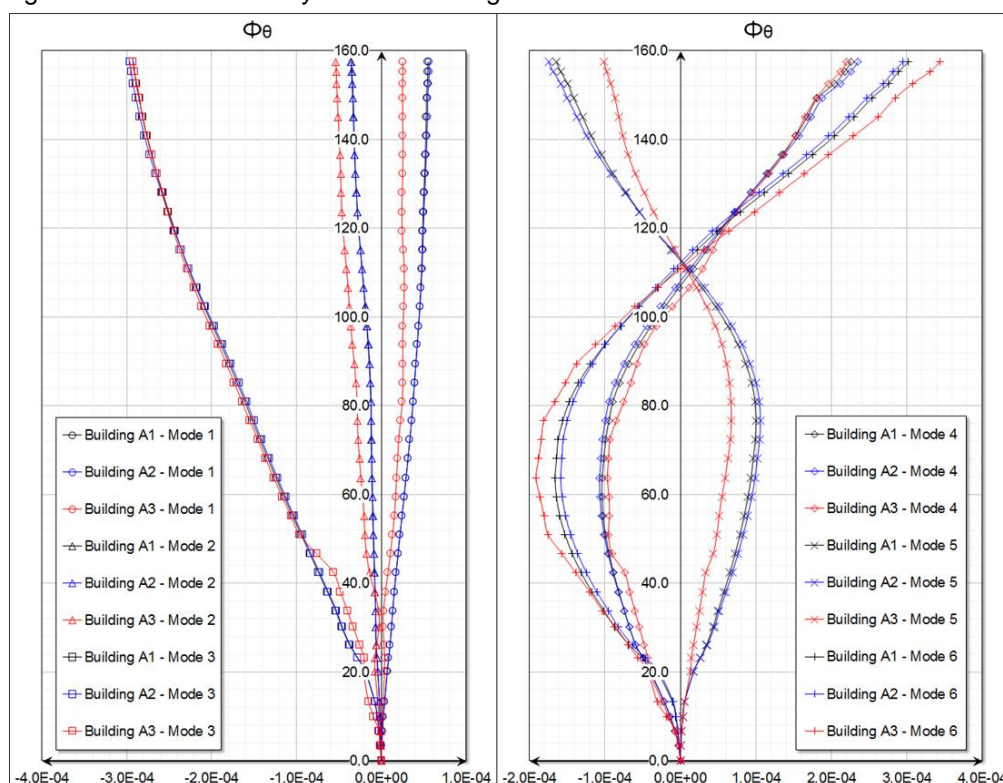
Source: Author.

The coupling between the shear walls can be slightly increased through the floor slab only in the X axis, as it is the only direction with short spans between shear wall elements. The stiffness increase due to the previously explained outrigger effect is reduced for this building due to the geometry of the floor slab. Since the floor system is composed of a steel deck with an 8.0cm concrete screed, the moment connecting the internal concrete core to the external columns needs to pass through a very long span (more than 10.0m) and a very slender shell (8.0cm). This combination of factors favours the stiffness increase in the X axis more than it does in the Y axis.

The remaining mode deflection shapes are either purely torsional (3rd mode) or very much stiffer than the first two modes (4th to 6th modes), with a natural frequency ratio higher than 3.1 between the 4th mode and the 1st mode and up to 4.55

between the 6th mode and the 1st mode. The stiffer modes are much less sensitive to smaller stiffness increases, such as the outrigger effect or the shear wall coupling, and do not present any significant changes in the mode deflection shapes neither for X nor Y axes. These modes (3rd to 6th), however, are purely or highly torsional and very sensitive to the warping rigidity increase and present minor changes in the torsional components (see [Figure 7.10](#)).

Figure 7.10 – Structural system of building A.



Source: Author.

These changes in the mode shapes might be responsible for a change in the modal loads (through eq. (2.7)), whilst the changes in the natural frequencies might bring the resonant response to different values of the PSD of the wind loads. When combined, these features might change the modal responses and their sensitivity concerning the azimuth, even changing the critical direction of the building's response. These changes will be presented in [sections 7.2.1.3](#) and [7.2.1.4](#).

The shear walls in this tall building are asymmetric and so are the beam connections between them. This kind of element often presents big displacements in orthogonal directions (it can be illustrated by a cantilever with an "L" or a "C" section

subjected to a concentrated load on the opposite end). This condition generates mode displacement shapes that do not comply with the traditional Cartesian directions usually presented in wind load studies: mode displacement shapes for translation in the x direction, translation the in y direction, and torsional.

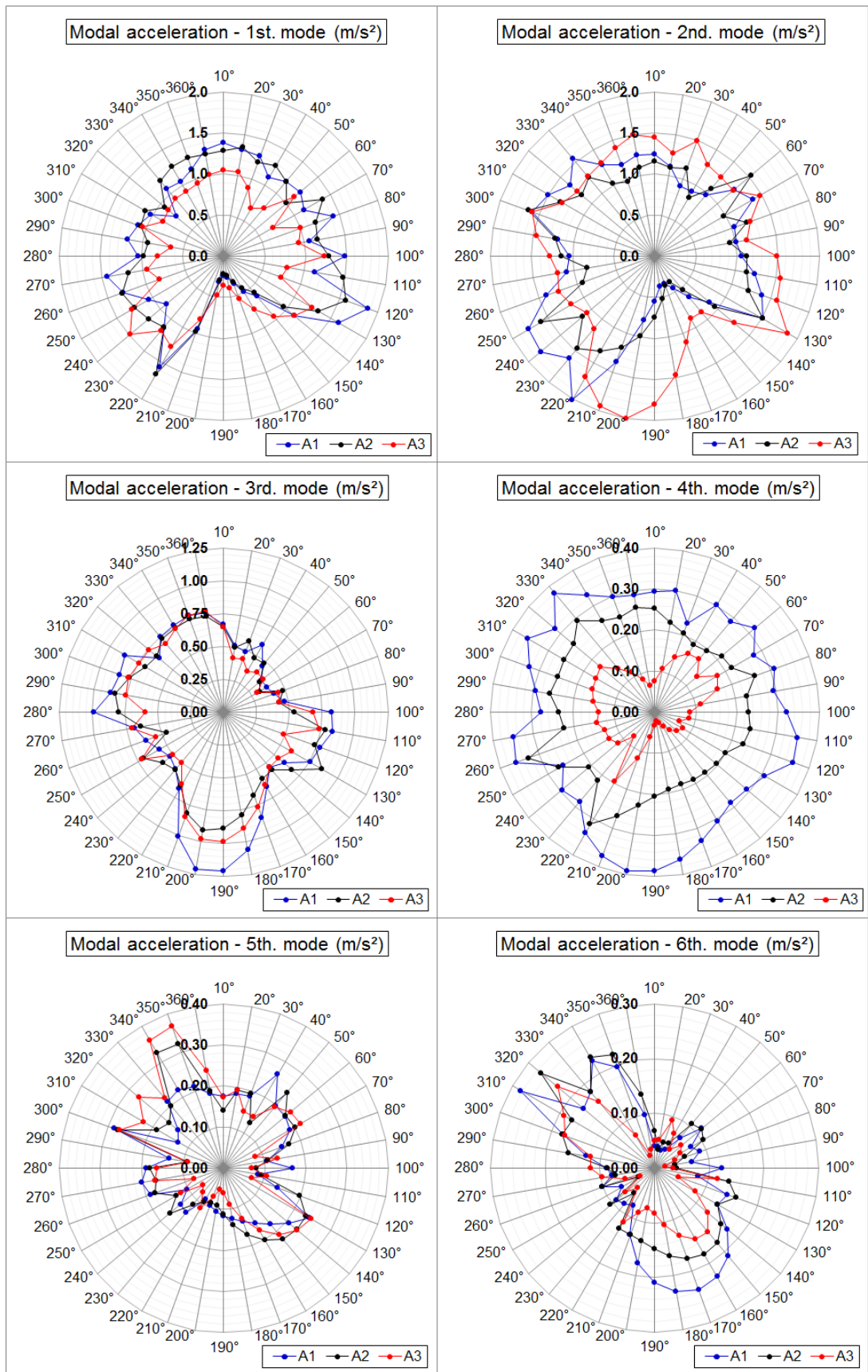
The mode shapes presented for this building have important components in the orthogonal direction and always present some moderate to high torsional participation. This behaviour is due to these highly asymmetrical structural elements that happen to work always in both x and y directions together. Hence, any rigidity increase in the X axis will influence the behaviour of the Y axis, generating the substantial differences found in the mode shapes of buildings A2 and A3 during the step two of this methodology, differing from the results presented by Kim et al. (2009) for mode shapes in this specific case.

The interference between the X and Y axes shall be clearer after a close observation of the internal forces (bending moment diagrams) on the asymmetric shear walls (see [section 7.2.5.2](#)). The view from the top of the building of the six modal loads, including all translational components and torsional effects, is presented in [Appendix 2](#) (see [Figure A2.1](#) for modes 1-3 and [Figure A2.2](#) for modes 4-6).

7.2.1.3 Modal results (frequency domain)

Modal results are presented separately in this chapter and acceleration will be the focal attribute for the ongoing SLS analysis, as previously discussed in this thesis. The analyses of each modal result separately allow for the verification of previously discussed features of the structural modelling criteria, in particular the impact of the changes in the mode displacement shapes and natural frequencies in the modal accelerations. Another feature to be observed not only in the modal results but also in the final accelerations (see [section 7.2.1.4](#)) is the change in the critical azimuth of the building. These results are presented in [Figure 7.11](#) for each of the six modes of vibration and for the three structural models studied (A1, A2 and A3).

Figure 7.11 – Modal accelerations (rms) for buildings A1, A2 and A3.



Source: Author.

The *rms* results are given in m/s^2 because they are in the generalized coordinates still to be multiplied by the eigenvector component of the floor of interest (according to eq. (2.20) and (2.21)). The abovementioned multiplication transforms the generalized accelerations into real scale acceleration components (X, Y, and torsional), bringing the final values to the usual unit of measure for the accelerations of tall buildings: milli – g.

In *Figure 7.11*, the response corresponding to the first mode of vibration displays the results of the second mode of vibration for building A3, continuing the discussion from *section 7.2.1.2*. Likewise, the results corresponding to the second mode of vibration display the first modal accelerations for building A3. It can be observed in this same figure that the behaviour of each mode of vibration follows the same pattern along the azimuths for each single building (A1, A2 and A3), including the first two modes, which have the exchanged responses between modes one and two. This feature supports the hypothesis of the interchange between the first two natural modes of vibration discussed in *section 7.2.1.2*.

As discussed in *section 1.2.2.2*, the accelerations of a tall building subjected to dynamic wind loads are highly dependent on the natural frequencies of the structure due to the resonant response (see *Figure 1.11*). The PSD of the wind loads tends to present smaller values as the frequency increases, therefore presenting lower resonant responses as the natural frequencies of the buildings increase. Since each step of the structural modelling leads to a substantial increase in the natural frequencies of vibration of the building models, building A3 is expected to present the lower results, then building A2, and finally building A1 with greater modal accelerations.

The pattern “A1>A2>A3” is observed almost systematically for the modal responses corresponding to modes 4 and 6. This pattern is respected in most of the sectors for modes 1 and 3. However, some greater values in some azimuths can be explained by two main reasons:

- According to Huang and Chen (2007), the result of the PSD of a generalized force over a short period of time is quite jaggy, which means that an increase in the natural frequency might carry the resonant response from a local

minimum in the PSD function to a local maximum, being responsible to a minor increase in the modal response;

- Different mode displacement shapes bring different modal loads and therefore different modal results, exempting each of the three models' behaviours from completely complying with each other.

This might be the case for modal accelerations corresponding to mode 2, where there is a similar pattern throughout the azimuths, but not identical. The greatest differences in the mode shapes are seen in the first two natural modes of vibration.

In these responses, one can see how much a tall building's response can change over a 10° azimuth change, agreeing with Irwin et al. (2005). It is possible to verify in mode 4, building A3, azimuth 220°, a ratio higher than 3 between the response of that azimuth and the response of neighbouring azimuths. This same variability can be observed for the generalized accelerations for all modes, in particular for mode 1 (220°) and mode 2 (130°), which are the modes with the highest participation in the final response.

The final analysis of the modal responses brings to attention the changes in the critical directions of the modal responses. To illustrate these changes, for each mode of vibration:

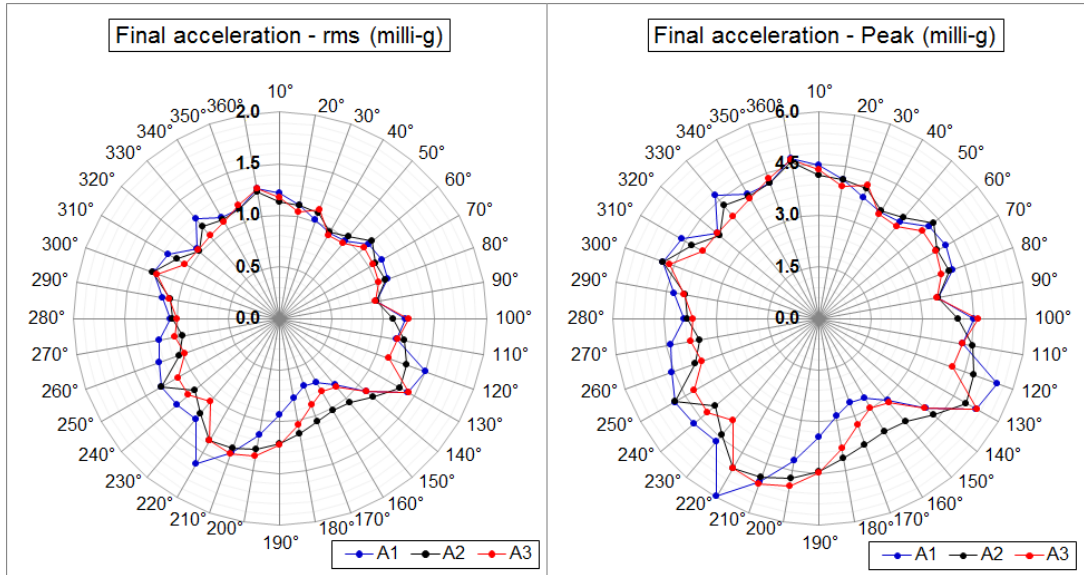
- Mode 1: 120° for building A1 and 240° for building A3;
- Mode 2: 220° for building A1 and 200° for building A3;
- Mode 3: 190° for building A1 and for building A3 (same critical direction);
- Mode 4: 200° for building A1 and 220° for building A3;
- Mode 5: 300° for building A1 and 350° for building A3;
- Mode 6: 310° for building A1 and 320° for building A3.

A similar behaviour with a slight reduction in the final acceleration between buildings A1 and A3 and same critical direction is observed for mode 3. This is an expected result, as the respective mode displacement shapes present little to no changes between structural models, along with an increase in the natural frequency. The impact of structural modelling criteria on the final accelerations is presented in [section 7.2.1.4](#).

7.2.1.4 Final acceleration results for each structural model

Resultant accelerations using the presented methodology are given for all azimuths and the three structural models in *Figure 7.12*. Peak results were obtained through eq. (2.24), (2.25), and (2.26).

Figure 7.12 – Resultant accelerations for buildings A1, A2, and A3.



Source: Author.

As expected, the pattern “A1>A2>A3” is respected for most of the azimuths, including the maximum acceleration. The critical direction for building A1 is 220°, where the peak acceleration on the floor of interest is 5.96mili – g. For building A3, these results are 130° and 5.28mili – g.

The way in which the wind climate will be introduced to the procedure will define how this change in the critical direction can impact the final acceleration assessment.

For the worst-case method, the results are given and a *reduction of 11.4%* is observed in the results due to the use of the structural modelling criteria presented in this thesis.

For both the sector methods and the up-crossing method, the outcome of the procedure would depend on the directional features of the wind climate and building responses: if the critical wind direction matches the critical direction of the building; or

if the contribution of other lower building responses within the other non-critical wind sectors is significant. However, the lack of precision in the use of 22.5° or 30° sectors can be observed in [Figure 7.12](#), where a great changeability in the responses can be observed within a 10° angle gap.

These and other features of the wind climate with the structural modelling criteria are explored in [section 7.2.3](#). This is a strong evidence of how the structural modelling criteria can influence the Davenport's chain of wind loading.

7.2.2 DYNAMIC ANALYSIS CRITERIA

7.2.2.1 Validation of results

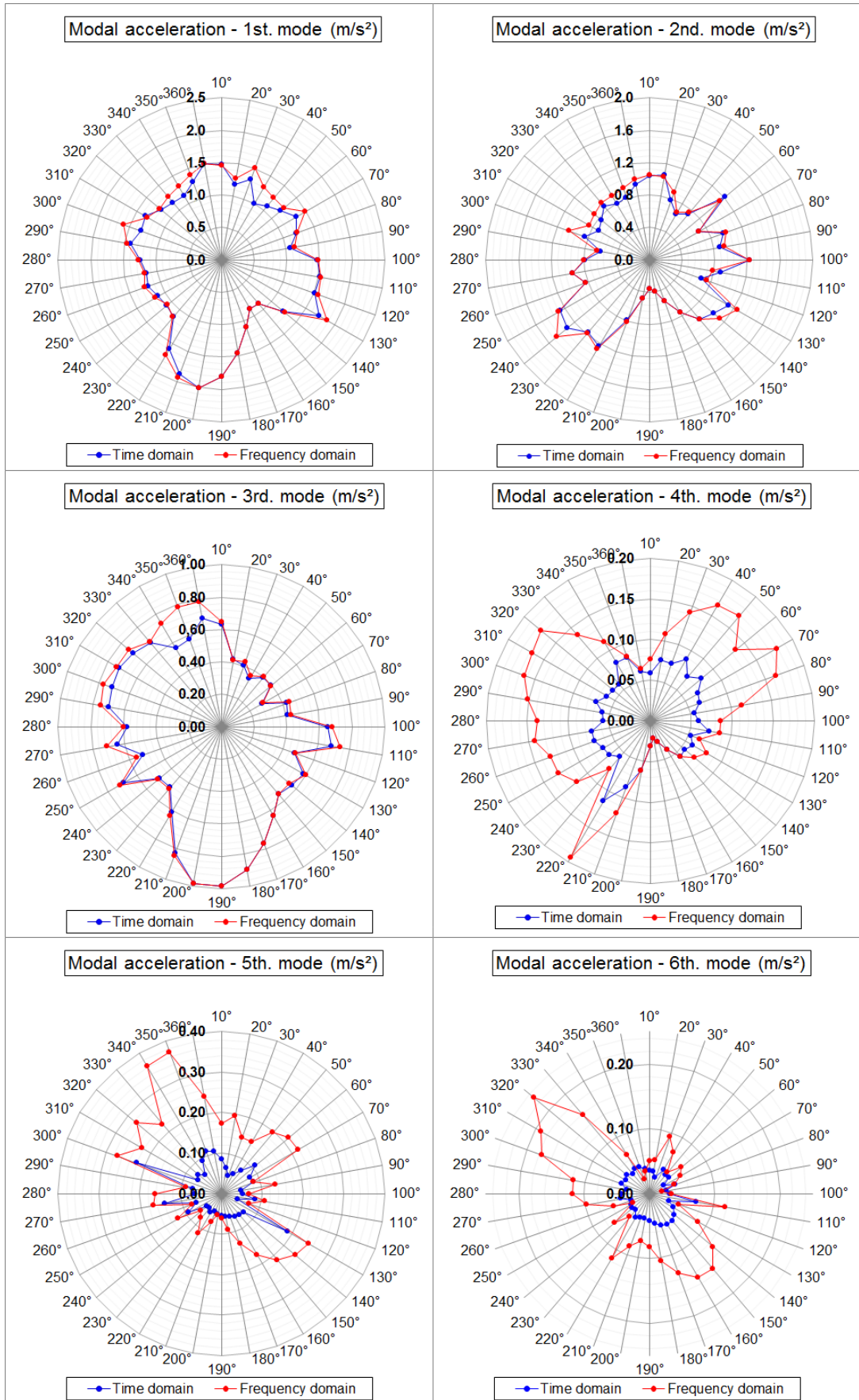
The time-domain analysis was performed throughout the entire duration of the experiment. However, in order to establish a proper comparison, the same time interval used in the frequency-domain was used in a second time-domain analysis just for this validation.

According to Jeary (2003), a structure with an angular natural frequency “ ω_n ” and a damping ratio “ ξ_0 ” has a time constant “ τ ” that can be calculated by:

$$\tau = \frac{1}{\omega_n \xi_0} \quad (7.1)$$

For a linearly damped system subjected to a simple sine wave loading, the time-domain response might achieve nearly 99.3% of the steady-state response after 5 time constants. For more complex dynamic loads, the ratio between the time-domain and the frequency-domain responses can be even lower, as the ratios presented for the rms accelerations by Wu et al. (2007). It is important to state that the “ 5τ ” time length is quite close to the minimum duration discussed in [section 1.2.2.2](#), to ensure steady-state responses for the frequency-domain analysis. The values for the time constant “ τ ” for each mode of vibration from 1 to 6, in that order, are: 39.0 s/rad, 38.3 s/rad, 24.8 s/rad, 11.75 s/rad, 10.39 s/rad, and 8.574 s/rad.

Figure 7.13 – Modal acceleration (rms): time vs. frequency domain (Building A3).

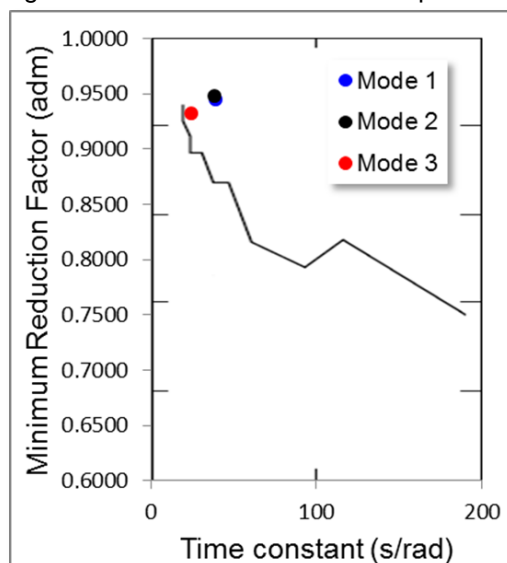


Source: Author.

The rms of modal responses for each azimuth is presented in [Figure 7.13](#), for both the frequency domain and the time domain. This figure shows how modal responses (generalized accelerations) follow the same pattern throughout the azimuths. This feature endorses the methodologies proposed in this study, since the time-domain and the frequency-domain analyses use very different formulations and produce very similar (sometimes equal) patterns in their responses.

In addition, the time-domain response is systematically below the frequency-domain response for all modes of vibration and azimuths (except for one azimuth in the first mode of vibration and two azimuths in the second one). This behaviour corroborates the steady-state theory (JEARY, 2003) despite the few azimuths where it is not observed, as it was also observed in the results found by Wu et al. (2007) for rms accelerations. A comparison between the reduction *factors vs. time constants* for each mode of vibration is established in [Figure 7.14](#), along with the results of Wu et al. (2007).

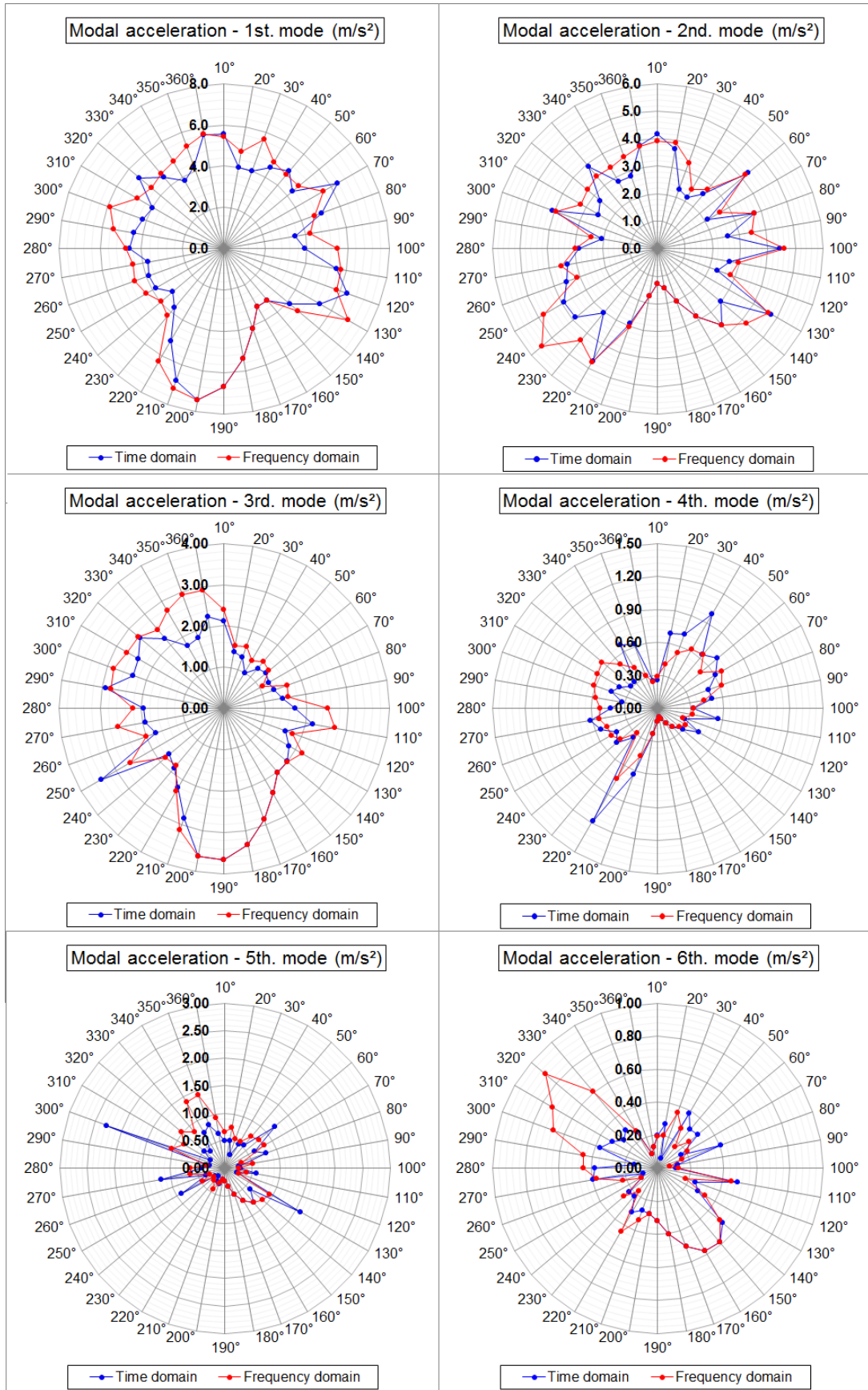
Figure 7.14 – Reduction factor comparison.



Source: Author.

Average reduction factors between rms responses for time and frequency domains show agreement with the results obtained by Wu et al. (2007) for each of the three first modes of vibration. In addition, the reduction factors for the first three modes remained above 0.73, as debated by Wu et al. (2007).

Figure 7.15 – Peak modal accelerations: time vs. frequency domain (Building A3).

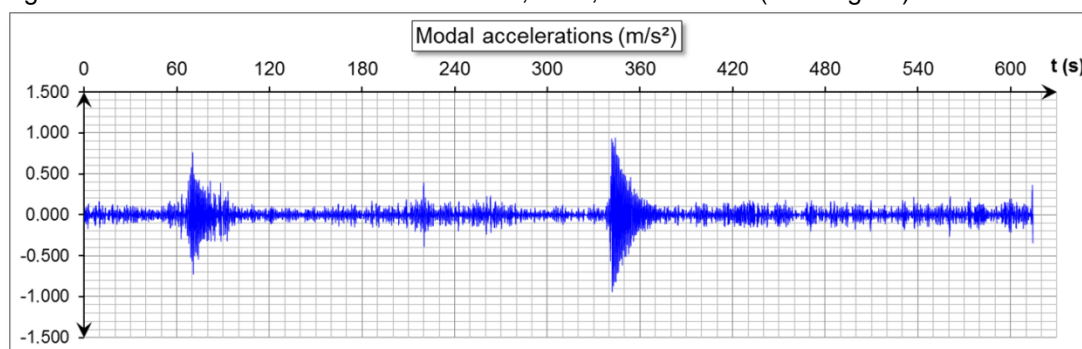


Source: Author.

Peak acceleration responses showed very similar behaviour for the first three natural modes of vibration for both the time-domain and the frequency-domain analyses, where the time-domain results were systematically lower than the frequency domain's results (see [Figure 7.15](#)). Modes 4 to 6, on the other hand, showed a comparable behaviour, but often a higher peak acceleration for the time-domain analysis.

This feature can be explained by the transient behaviour of the responses in this latest group of modes of vibration (see [Figure 7.16](#)), where the decay of gust loads is faster due to greater overall damping (eq. (2.12)) and higher cycling rate, both resulting from higher natural frequencies of these modes (causing lower rms and consequently higher peak factors).

Figure 7.16 – Modal accelerations: 5th mode, 300°, time domain (Building A3).



Source: Author.

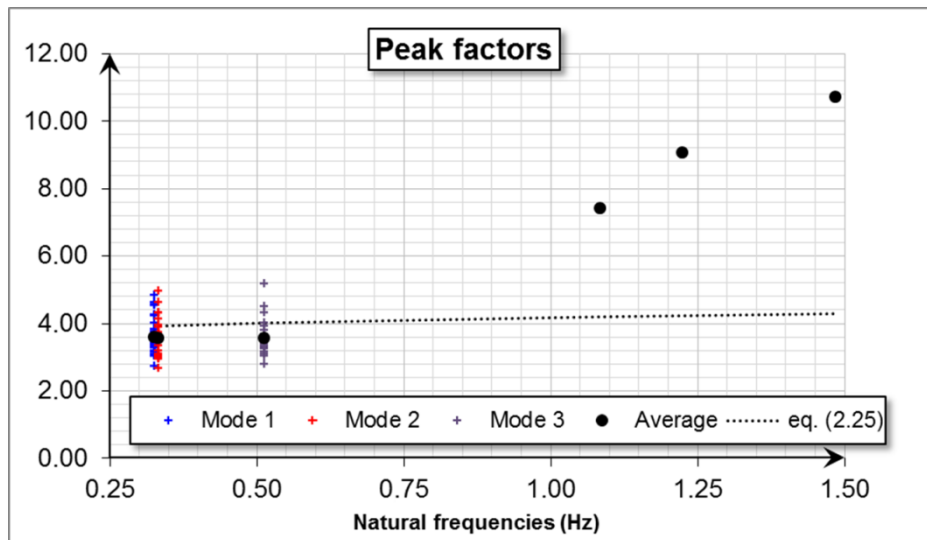
7.2.2.2 Peak factors and joint action factors

The peak factors for each mode of vibration were calculated throughout this analysis. The results of the calculated peak factors are shown in [Figure 7.17](#). The peak factors shown in this figure were obtained from the assessment of the time-domain analysis for the duration of 889s for all azimuths and from eq. (2.25) as well. These two different sources for the peak factor assessment will allow for comparisons between time-domain and frequency-domain analyses.

The first important feature is the average peak factors assessed for the 1st, 2nd, and 3rd modes of vibration. These peak factors were also compared with the results from eq. (2.25) (used in the frequency-domain analysis). The results show that some of the peak factors were above the results of eq. (2.25), explaining why

some of the modal peak accelerations were higher for the time-domain analysis when compared with the frequency domain (see [Figure 7.15](#)), despite of having lower rms. The average value of the peak factor calculated from the time-domain results (between 3.64 and 3.58) are significantly lower than the peak factor obtained from eq. (2.25) (between 3.91 and 4.03). In addition, peak factors often assumed values under 3.5, which is a peak factor usually expected and used for accelerations in tall buildings (BOGGS. 1997). These peak factors assumed values as low as 2.77, in agreement with the results of Wu et al. (2007).

Figure 7.17 – Peak factors (Building A3, all azimuths).



Source: Author.

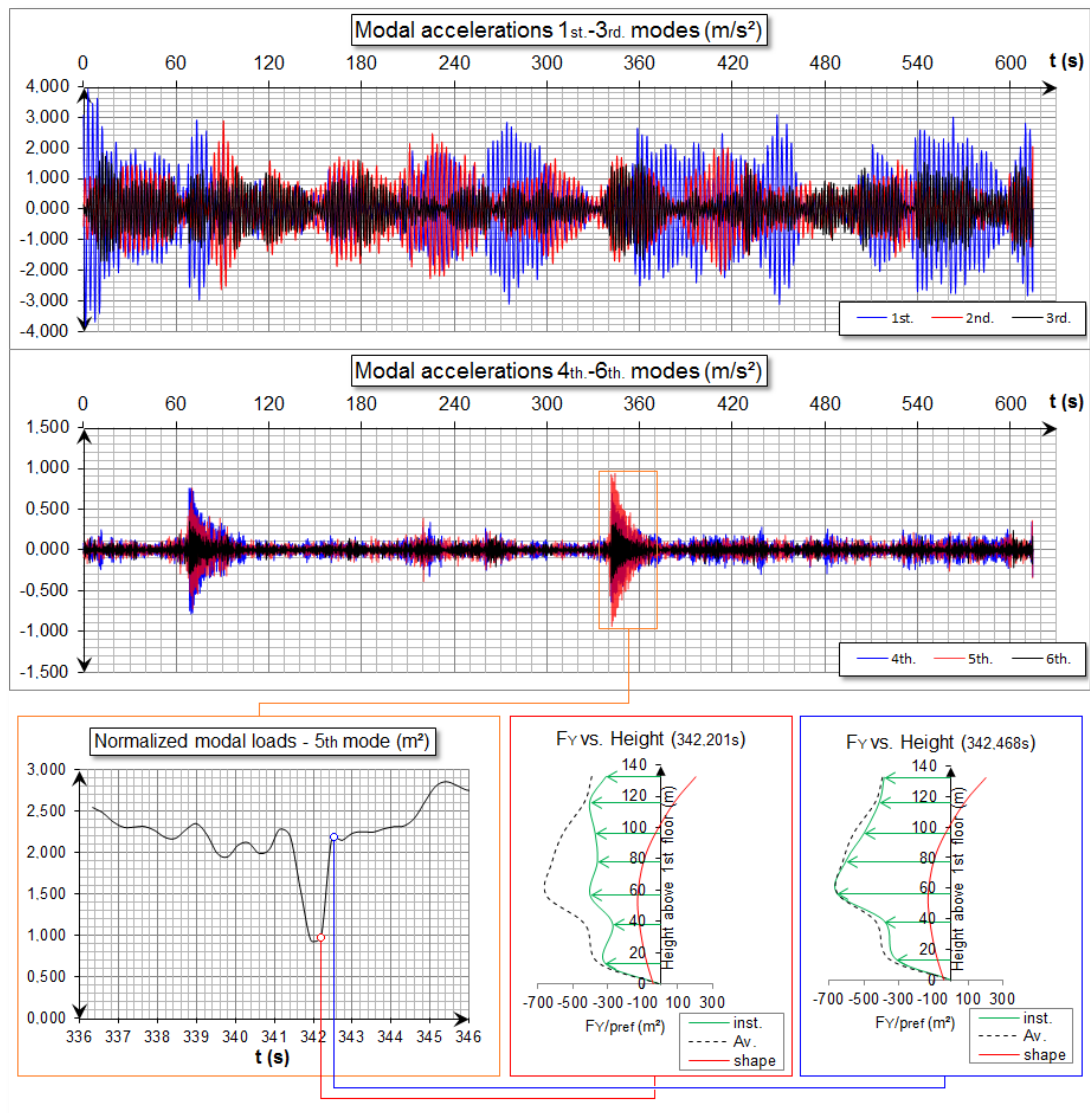
The peak factors for higher modes (4th, 5th, and 6th modes) are not in agreement with eq. (2.25). This dissimilarity occurs due to the transient behaviour of higher modes of vibration responses (see [Figure 7.18](#)).

This transient behaviour can be explained by a small variation in the modal load, generating an instant peak acceleration that is later damped by the system. In the example set in [Figure 7.18](#), the variation is generated by a temporary reduction in the wind loading profile in the Y axis, with lower correlation to the mode shape in the same direction, followed by an increase in this correlation and in the load values.

The wind loading and the mode deflection shape in the Y axis are presented in [Figure 7.18](#) because they have the most significant participation in the final modal load in this case. It is also interesting to note that it is not the absolute value of the

load but the absolute value of the variation of the load that causes the peak acceleration, as one may see in this figure, where the loads that caused this peak are below the average in that 10s time-span.

Figure 7.18 – Transient behaviour (Building A3, 340°).



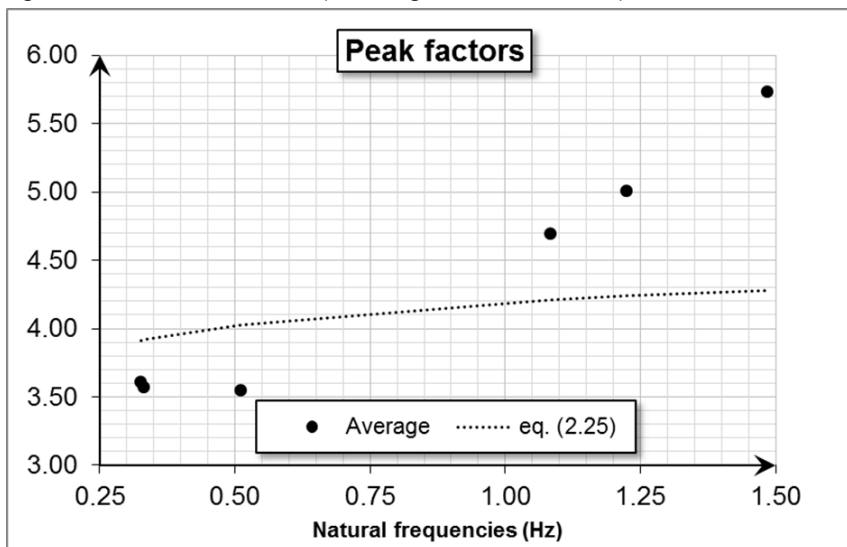
Source: Author.

These transient patterns were caused by a gust wind with a 25% variation from the average and a 2s duration, which is a conceivable situation for the turbulence in a tall building's design and will therefore be kept for the final acceleration assessment. The modal load and along-wind loads in *Figure 7.18* were normalized by dividing these values by the pressure of reference (i.e., loads without the wind climate data). Average peak factors excluding these transient responses

are provided in [Figure 7.19](#), in closer agreement with results from eq. (2.25) when compared with previous results. The highest values of peak factors for the higher modes of vibration (specially the 6th mode) still indicate a strong transient behaviour for them.

The final accelerations calculated in both time and frequency domains for all azimuths for building A3 are given in [Figure 7.20](#), where it can be observed that the peak responses for the same time-span are similarly smaller for the time-domain than they are for the frequency domain.

Figure 7.19 – Peak factors (Building A3, all azimuths).



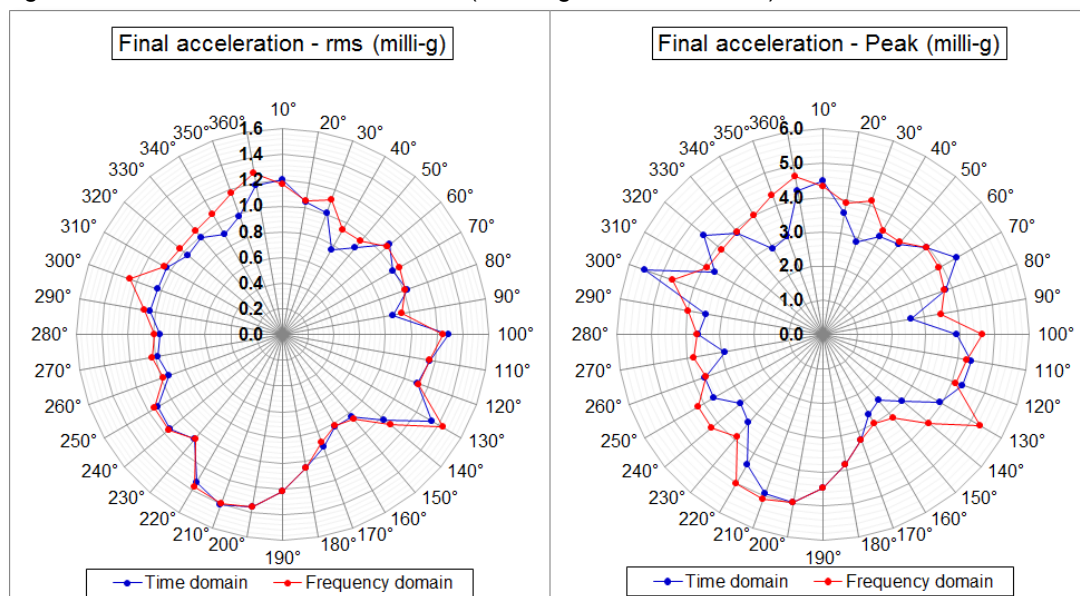
Source: Author.

Some of the azimuths present responses that are bigger for the time domain when compared with the frequency domain (300°, 320° and 70°). In some cases, this can be explained by the higher modal contribution, which often presents peak accelerations above those for the same modes in the frequency domain analysis. Higher modal truncation will be discussed in [section 7.2.2.3](#).

Peak factors of the final acceleration vary between 2.75 and 4.70, with an average value of 3.55, whilst joint action factors vary between 0.72 and 1.17, with an average value of 0.92 (see [Figure 7.21](#)). The highest peak factor value of 5.33 for the 300° azimuth is due to the contribution of the 5th mode of vibration with a transient

along-wind contribution for the acceleration (as previously explained for the 340° azimuth in *Figure 7.18*).

Figure 7.20 – Final acceleration results (Building A3, all azimuths).



Source: Author.

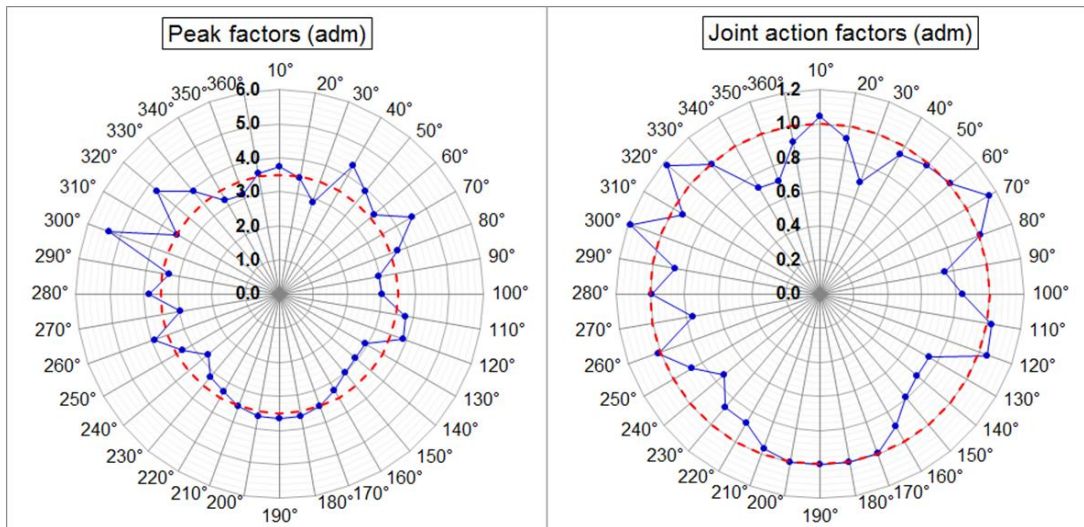
The correlation factor between the modes in this study is 0.20 between the two first natural modes of vibration and 0.00 for all other combinations of modes of vibration. Huang and Chen's (2007) results for their second situation of study have a similar behaviour between different modes of vibration and present joint-action factors around 0.88. The joint-action factors presented for building A3 to relate final accelerations of the frequency domain (using the rule of "square-route-of-sum-square") to the time domain, leading to an average value of 0.92, consistent with Huang and Chen's (2007) results.

Some joint-action factors, on the other hand, presented themselves above the unitary value. This result agrees with Melbourne and Palmer's (1992) results presented in *Table 5.3* for the assessment of complex motions between two orthogonal directions. Melbourne and Palmer's (1992) assessment of joint-action factors assumed values up to 1.05 in cases where the natural frequencies were equal.

One can easily explain this situation with two sinusoidal waves with the same phase, angular frequency, and amplitudes with peak to peak amplitude equal to 2.0.

The rms of each wave is $\sqrt{2}/2$ and the peak factor is $\sqrt{2}$. Using the rule of “square-route-of-sum-square” and later multiplying it by each peak factor, the peak result using the rms approach would be equal to $\sqrt{2}$. Analysing the actual resultant wave, the real peak value is 2, forcing the joint-action factor to assume the value of $\sqrt{2}$ in order to correctly assess the final acceleration in the frequency domain.

Figure 7.21 – Peak and joint action factors (Building A3, all azimuths).



Source: Author.

The previous example has only an educational value. However, along with this studied case, it perfectly illustrates the added value of the time-domain analysis when assessing complex motions.

7.2.2.3 Higher modal contribution

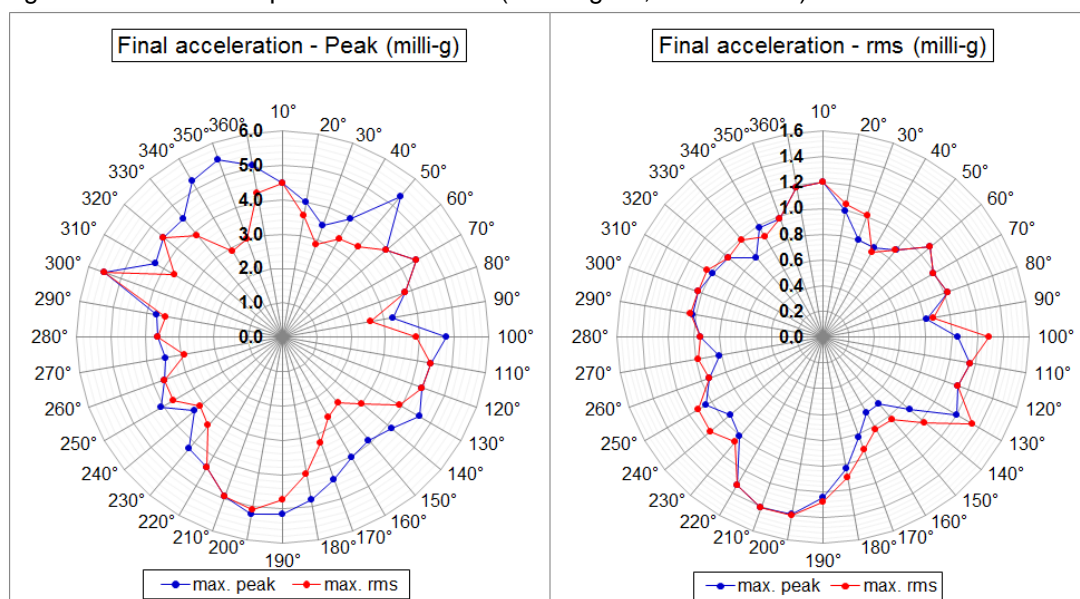
Previous analyses took into consideration the time intervals (10 minute time windows within the approximately 1 hour data) that could generate the highest rms in the frequency domain. These results were later multiplied by the respective peak factor for each mode of vibration (eq. (2.25)) and then compared with the time-domain results for the same time interval for building A3.

The highest resultant peak acceleration, however, was obtained in another time interval for most of the sectors and is shown in [Figure 7.22](#). In this figure, the maximum peak accelerations are displayed for both scenarios. Despite of presenting

very similar behaviours, the analysis of the maximum peak presented higher results when compared with the analysis with a higher rms.

The consequence of this examination is that the most severe response in the time domain for this building presents slightly higher peak factors and peak accelerations than the results previously evaluated.

Figure 7.22 – rms and peak accelerations (Building A3, all azimuths).



Source: Author.

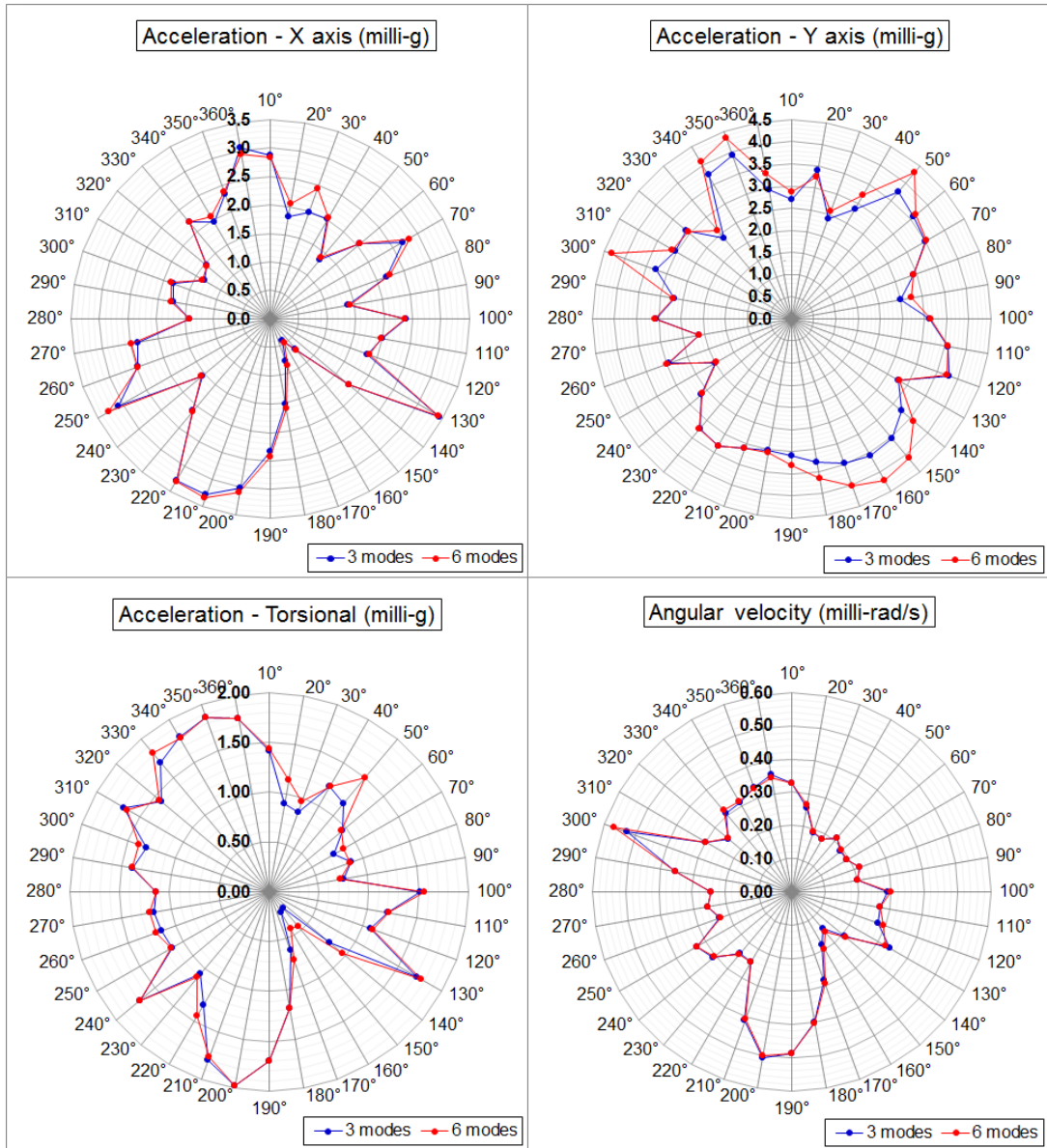
The peak acceleration presented an important, higher modal contribution, mostly in the cross-wind directions and in the torsional component of the motion, in agreement with Aly (2013).

The higher modal contribution presented the following increases in the maximum value for each acceleration component:

- X axis component (300° and along-wind direction for this sector): 0.34%;
- Y axis component (300° and cross-wind direction for this sector): 10.3%;
- Torsional component: 1.05%.

The overall resultant acceleration presented an increase of 9.47% in the maximum value, due to a higher modal contribution from Y axis for the 340° azimuth (cross-wind contribution).

Figure 7.23 – Higher modal contribution (components of acceleration).



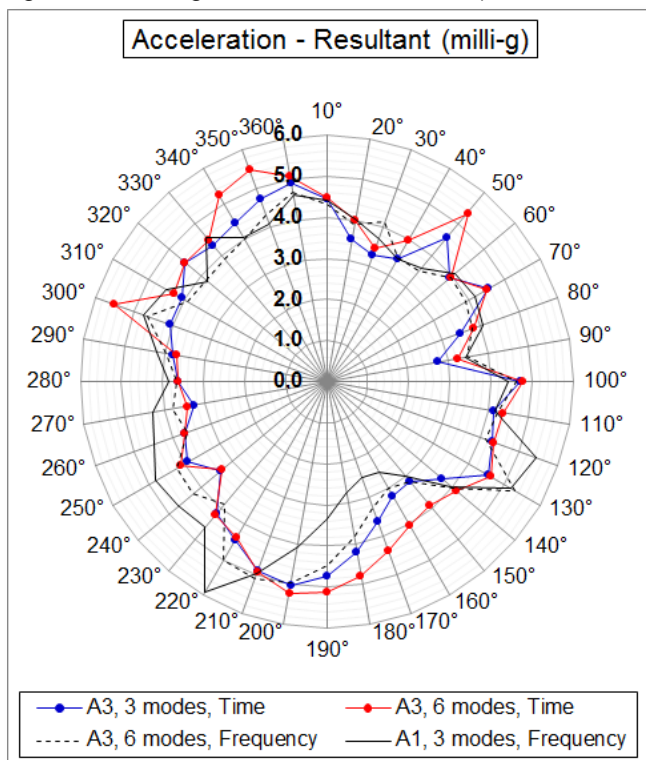
Source: Author.

On the other hand, the angular velocity showed a smaller increase (7.71%). A smaller increase – due to a higher modal contribution is expected for smaller derivatives of displacement. Huang and Chen’s (2007) and Aly’s (2013) (see [Table 7.4](#)) results of higher modal contribution for displacements are significantly less important when compared with the results for accelerations. [Figure 7.23](#) shows the results for each component, whilst [Figure 7.24](#) shows the overall results.

[Figure 7.24](#) also shows a comparison with resultant accelerations in the frequency domain. The comparison is established with 6 modes of vibration in the frequency domain for building A3, and with 3 modes of vibration for building A1,

similar to the frequency domain, which represents the most common set of criteria used in WTT.

Figure 7.24 – Higher modal contribution (overall and comparison).



Source: Author.

In this figure, one can observe that even with higher peak factors and higher modal contribution, the last model A3 in the time domain presents lower results than model A1 in the frequency domain for most of the sectors. In addition, the change in the behaviour of the response throughout the sectors previously discussed in [section 7.2.1.3](#) can be observed. The critical direction for resultant acceleration changes from 220° for the building A1 in the frequency domain to 300° for the building A1 in the time domain.

There is one last observation of the higher modal contribution analysis that relates it to the peak factors for three modes and six modes of vibration. For three modes of vibration, the peak factor of the resultant acceleration varied between 3.35 and 5.36, with an average value of 4.01. For six modes of vibration, the peak factor varied between 3.54 and 5.93, with an average value of 4.25.

This increase observed in the peak factor is explained by the participation of higher modes, which contribute poorly to the overall rms values but presents higher

peaks as mentioned above in [section 7.2.2.2](#). The same increase pattern can be observed in Aly's (2013) results from the analysis of the contribution from modes one to nine in a tall building (see [Table 7.4](#)).

Aly's (2013) peak factors for along-wind accelerations for three modes of vibration is 3.42, and 3.93 for cross-wind accelerations. For six modes and for nine modes, these values are, respectively 3.42, 3.98, 3.52, and 4.17. The overall increase of 2.93% and 6.11% in these peak factors could be justified by the same behaviour described in [section 7.2.2.2](#) for the contributions of higher modes in the peak accelerations.

Table 7.4 – Higher modal contribution (acceleration and displacements).

Response of the top corner of the building tower for an incident angle of 270°.										
Mode	σ_x, m		X_{mean}, m		X_{max}, m		$\sigma_x, m/s^2$		$\ddot{X}_{max}, m/s^2$	
	A	C	A	C	A	C	A	C	A	C
1	0.0003	0.1509	0.0000	0.0098	0.0013	0.5911	0.0004	0.1637	0.0014	0.6424
1:2	0.1177	0.1509	0.2818	0.0098	0.7510	0.5911	0.1805	0.1637	0.5616	0.6424
1:3	0.1188	0.1516	0.2770	0.0113	0.7350	0.5894	0.2018	0.1670	0.6904	0.6567
1:4	0.1188	0.1513	0.2770	0.0107	0.7350	0.5845	0.2018	0.1683	0.6904	0.6561
1:5	0.1182	0.1513	0.2696	0.0107	0.7243	0.5845	0.2037	0.1683	0.6693	0.6560
1:6	0.1183	0.1513	0.2701	0.0105	0.7257	0.5847	0.2071	0.1688	0.7079	0.6729
1:7	0.1183	0.1512	0.2701	0.0106	0.7257	0.5858	0.2071	0.1678	0.7079	0.7026
1:8	0.1183	0.1512	0.2708	0.0106	0.7270	0.5858	0.2078	0.1678	0.7315	0.7026
1:9	0.1183	0.1512	0.2708	0.0106	0.7270	0.5856	0.2078	0.1684	0.7316	0.7018

σ_x is the root mean square value of the fluctuating deflection, A means along-wind and C means cross-wind.

Source: Aly (2013).

Building A3's acceleration components for the most critical sector (300°) are given in [Table 7.5](#). The peak factors are higher for building A3 due to its higher natural frequencies when compared with the building studied by Aly (2013). The tall building studied by Aly (2013) is taller, slender, and therefore presents lower natural frequencies, which leads to lower peak factors in eq. (2.25).

Table 7.5 – Higher modal contribution on acceleration components (Building A3).

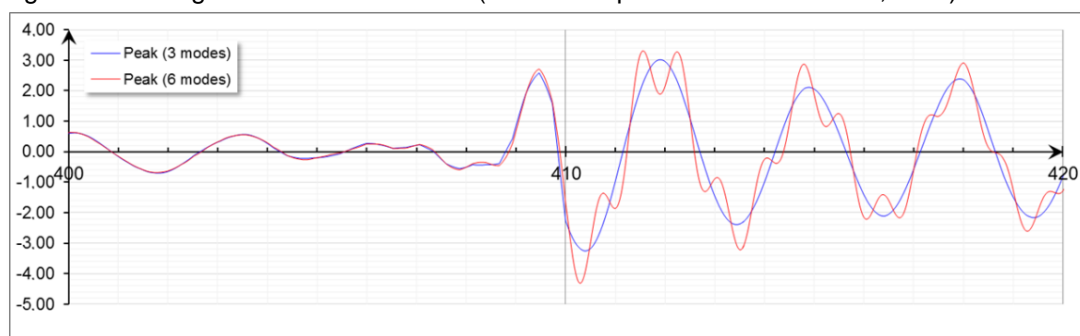
Modes	σ_X (milli-g)	σ_Y (milli-g)	\hat{a}_X (milli-g)	\hat{a}_Y (milli-g)	g_X adm)	g_Y (adm)
1:3	0.5371	0.7896	1.8145	3.2528	3.3786	4.1196
1:6	0.5388	0.7957	1.8586	4.3131	3.4495	5.4207

Source: Author.

The exact point in time where the higher modal contribution takes place can be seen [Figure 7.25](#). The resultant peak is formed by peak accelerations in three different modes simultaneously: 1st, 2nd, and 5th modes.

The discussion about considering or not the peak represented in this figure was already presented in [section 5.4.1.1](#) and it remains uncertain how many peaks below 12 cycles would be required for the user to perceive motion as a steady-state vibration. Hence, there is a considerable number of peaks with similar magnitudes following the peak in this figure and, therefore, they might represent a steady-state vibration for the user, which justifies keeping it for the comfort analysis.

Figure 7.25 – Higher modal contribution (Y axis component of acceleration, 300°).



Source: Author.

The peak acceleration presented in the 300° sector is a product of the turbulent wind load distribution in the building's façade randomly generating simultaneous pulses which lead to the resultant peak acceleration of 5.51 milli – g.

The BLWT can generate a steady average value for the wind loads for the whole WTT and, therefore, it would not make sense to argue about the duration of the analysis and the Van der Hoven power spectrum (see [section 1.2.2.2](#)). The random association of the modal responses, on the other hand, even in a very steady flow, generates these peak values, which must be considered in the analysis. The assumption of using the whole time of the WTT to generate the response values might lead to a lower rms and same peak values, leading to higher and incorrect peak factors.

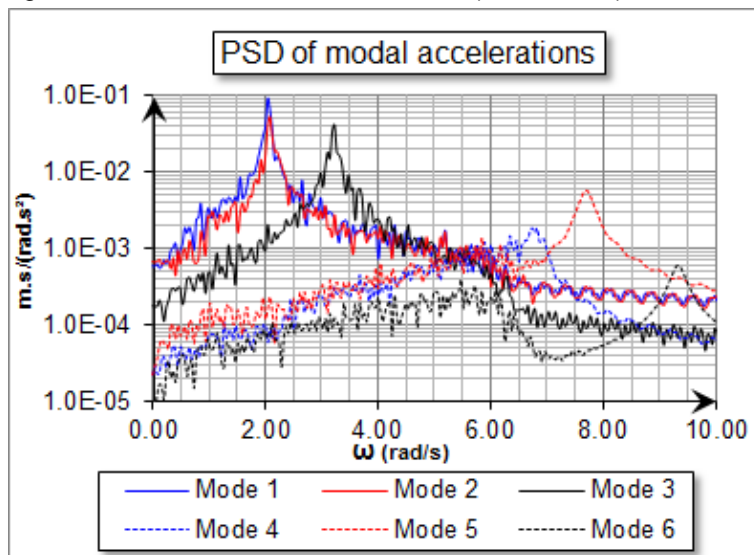
That is the reason why consideration should be given to the worst 10 – 20min time duration of the WTT around the highest peak value. This duration is

based on the time constants of the tall building analysed and is supported by the Van der Hoven power spectrum of the wind loads in real scale structures.

7.2.2.4 PSD of the time-domain results

The PSD of the modal accelerations was conducted for the time-domain responses for all sectors, and the results were obtained from sector 300°. [Figure 7.26](#) shows the PSD of the modal accelerations for this sector only (the most critical sector). This spectral analysis serves as a confirmation for the modal truncation at the sixth mode of vibration for this building. In effect, the highest mode with significant contribution to the final response is the fifth mode. However, the analysis will follow with six modes, since it was already calculated with all their contributions.

Figure 7.26 – Modal accelerations PSD (300° sector).



Source: Author.

7.2.2.5 Location of the user

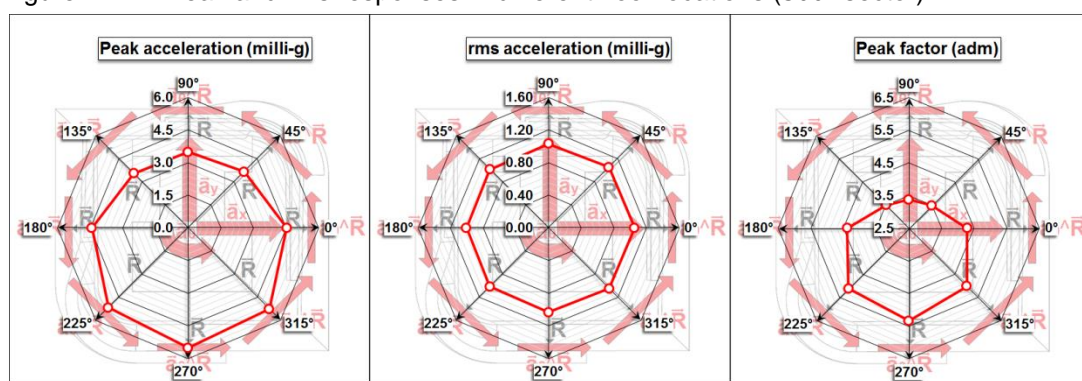
[Figure 7.24](#) shows the worst peak resultant acceleration considering the most critical location of the user on the highest occupied floor. This section will explore the aspect of this location in order to evaluate the human comfort during wind-induced motions. The other peak and rms accelerations for the other top occupied floor positions are provided in [Figure 7.27](#).

In this figure, one can observe that the rms accelerations don't present significant variation over the floor positions, whilst the peak accelerations do. The

rms accelerations adopt an almost constant value with an average of 1.03milli – g throughout the positions, whilst the peak accelerations vary between 3.49milli – g and 5.52milli – g.

This variation occurs due to the torsional components from both torsional and translational modes of vibration, which is particularly significant in this project. The constructive interference between the translational and the torsional components in one position of the floor is a destructive interference in the opposite direction, generating these discrepancies.

Figure 7.27 – Peak and rms responses in different floor locations (300° sector).



Source: Author.

As a result, the peak factors for this floor also vary greatly. The peak factor presented for sector 300° (critical sector in the final analysis of building A3) in the previous sections is 5.34 and corresponds to the highest peak acceleration, whilst the average peak factor for this floor is 4.31.

The discussion about use the most severe result of the floor was already conducted in this thesis, in [Chapter 5](#). To correctly evaluate the comfort level of the user, one must define whether the perception of movement or the annoyance levels will be assessed. If the annoyance levels are chosen, the average value and probably the rms acceleration should be used.

However, if the perception of movement is chosen, then there is a chance that the occupants in the region with the most severe result will perceive the motion and alarm the other occupants on the floor. In this case, the peak acceleration is probably the most suitable way to evaluate comfort.

Brazil has a recent practice with tall buildings and currently there is no acceptance to a building's movement by its occupants. Thus it is reasonable to pursue comfort through the perception of motion until this practice is better developed in the country. The most severe peak acceleration of the floor will be used based on the location of the building (Brazil) and on the type of assessment (perception).

Another relevant analysis of the user's location is related to the floor height. As it was discussed in [section 1.5](#), the acceleration for comfort evaluation must be calculated on the floor of interest. If the project presents mixed use (hotel and offices, for example), the comfort verification might take place on the highest occupied floor or on some hotel floor on a lower storey.

Let's consider *just for the sake of the analysis* that the entrepreneur wants to build a tower with hotel rooms up to the 13th floor (20th structural floor, counting from basement levels), where the height above ground is 60.7m. The overall resultant accelerations for this situation are given in [Figure 7.28](#).

Peak and rms accelerations of this floor are 3.13milli – g and 0.50milli – g, respectively, both corresponding to the sector of 340° and with a peak factor of 6.24. Similarly to the previous analysis, the average peak and rms values (over the floor perimeter) are 2.45milli – g and 0.45milli – g, respectively, for the same azimuth, with an average peak factor of 5.39. The contribution of higher modes to the resultant acceleration is 12.54%.

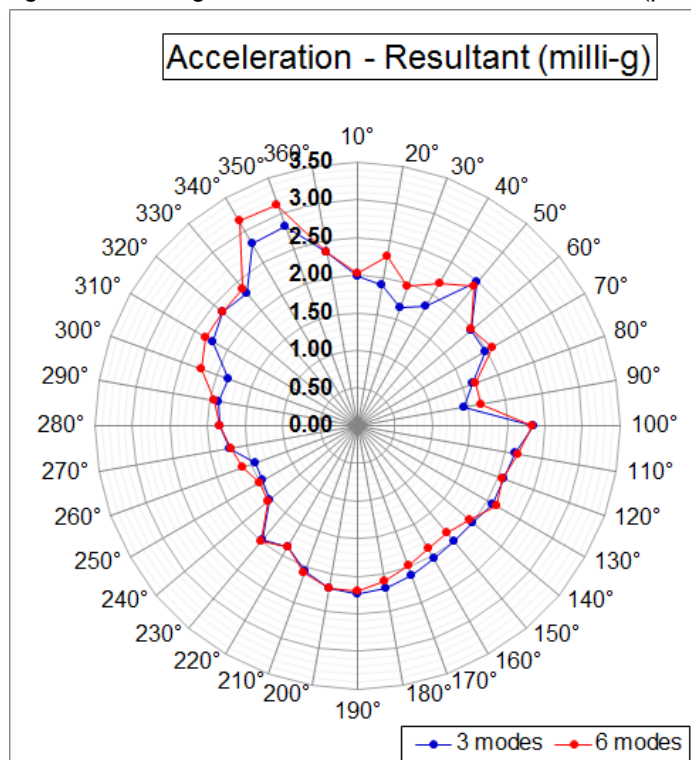
When compared with the results of a higher modal contribution to the top occupied floor (129.2m), these results establish the following scenario:

- Peak accelerations: 3.13milli – g (60.7m) and 5.51 milli – g (129.2m);
- Higher modal contributions: 12.54% (60.7m) and 9.47% (129.2m);
- Average peak factors: 5.39 (60.7m) and 4.25 (129.2m).

The increase in the higher modal contribution (from 9.47% to 12.54%) is due to the mode deflection shapes of the building. On lower levels, these shapes present smaller values for the fundamental sway and torsional modes when compared with the values on the top occupied floors, whilst for the higher modes they may show

similar values for both heights (see [Figure A1.1](#) to [Figure A1.3](#)). These values are used in eq. (2.29a) to (2.29c) for the time-domain results.

Figure 7.28 – Higher modal contribution: level 60.70m (peak acceleration).



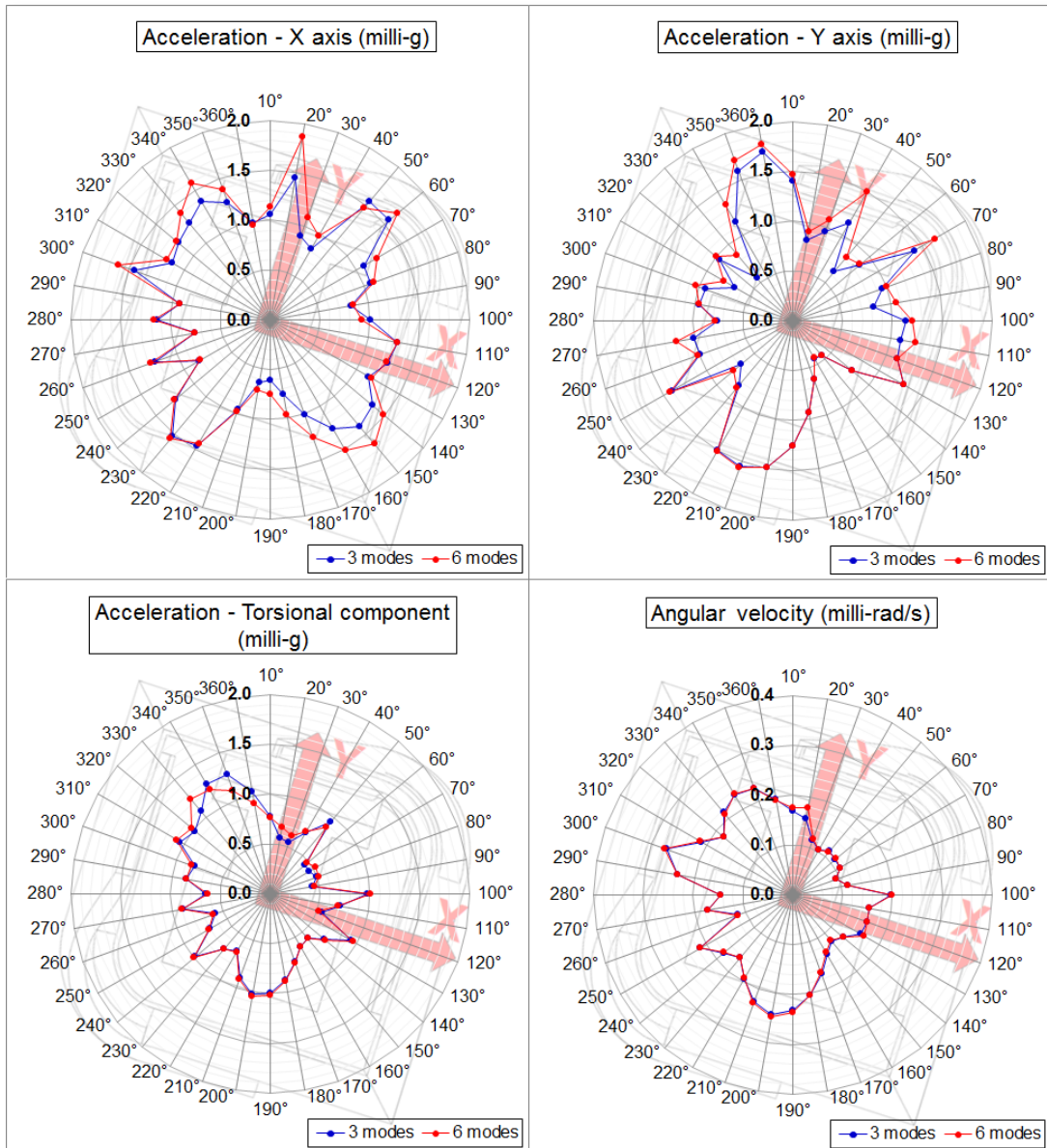
Source: Author.

As a result of the increased relevance of the contribution from higher modes of vibration, the average peak factor is higher for the acceleration in the lower section of the tower.

As expected, the peak acceleration showed to be lower for the lowest tower level where the acceptance level is also lower for the hypothetical hotel use. It is also relevant to point out that the critical azimuth of the worst acceleration changes from 300° at 129.2m to 340° at 60.7m.

A higher modal contribution is significantly more relevant for crosswind accelerations. [Figure 7.29](#) shows components of acceleration, where it can be observed that the X axis acceleration has a higher modal contribution for the 20° sector (29% increase).

Figure 7.29 – Higher modal contribution: level 60.70m (acceleration components).



Source: Author.

7.2.2.6 Summary of structural modelling criteria and dynamic analysis

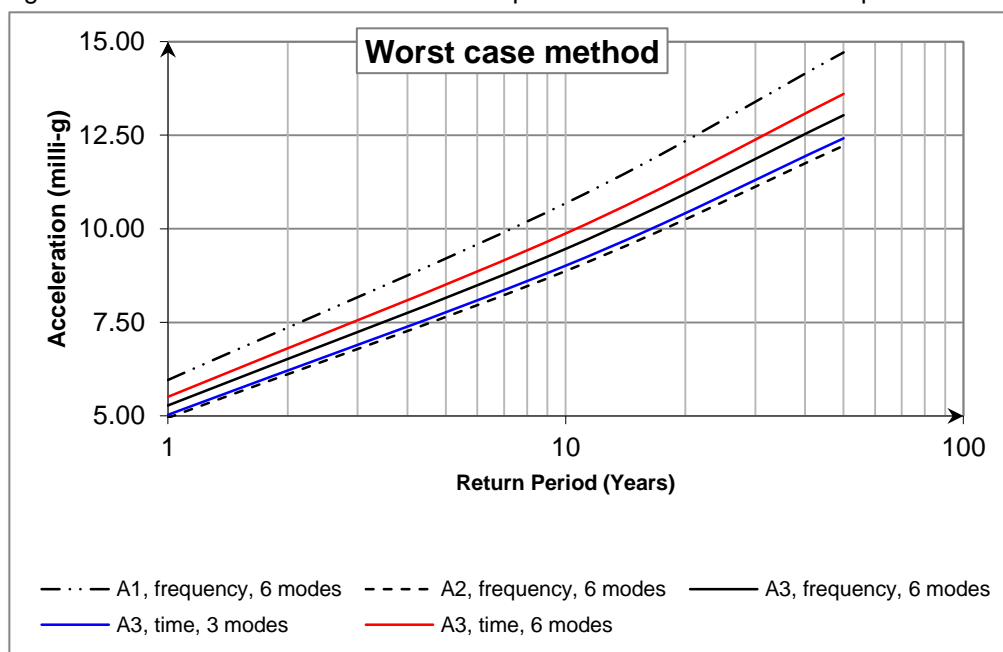
Both structural modelling and dynamic analysis criteria are structural engineering subjects and therefore should be under direct appreciation by the structural engineer, strengthening the links in the Davenport’s chain.

The resultant acceleration for each building model using the main dynamic analysis criteria is presented in *Figure 7.30*, where the worst-case method was applied and the results for 10 and 50-year return periods were obtained.

This figure shows that the most severe acceleration happens to building A1 in the frequency domain, which happens to be the most common criteria used by BLWT and structural engineers around the world. Little difference was obtained from the use of either three or six modes in the frequency domain for this building. Therefore, six-modal results and three-modal results are quite similar in this specific analysis.

Reasonable reduction was obtained by improving the models and later shifting from the frequency domain to the time-domain analysis. The three-mode analysis in the time domain showed one of the highest levels of reduction. However, a higher modal contribution showed to be quite relevant in these resultant accelerations and neglecting it would lead to less reliable results.

Figure 7.30 – Worst case method resultant peak accelerations vs. return period.



Source: Author.

The most precise set of criteria did not present smaller results. In this case, the time-domain analysis with a higher modal contribution for building A3 presented resultant accelerations higher than the resultant accelerations in the frequency domain for both buildings A2 and A3. The worst case method was used in this analysis and generated the results presented in [Figure 7.30](#). However, different results are expected when using not only the most severe acceleration, but also the

contribution from each sector to the final response. The results of the up-crossing method will be presented in [section 7.2.3](#).

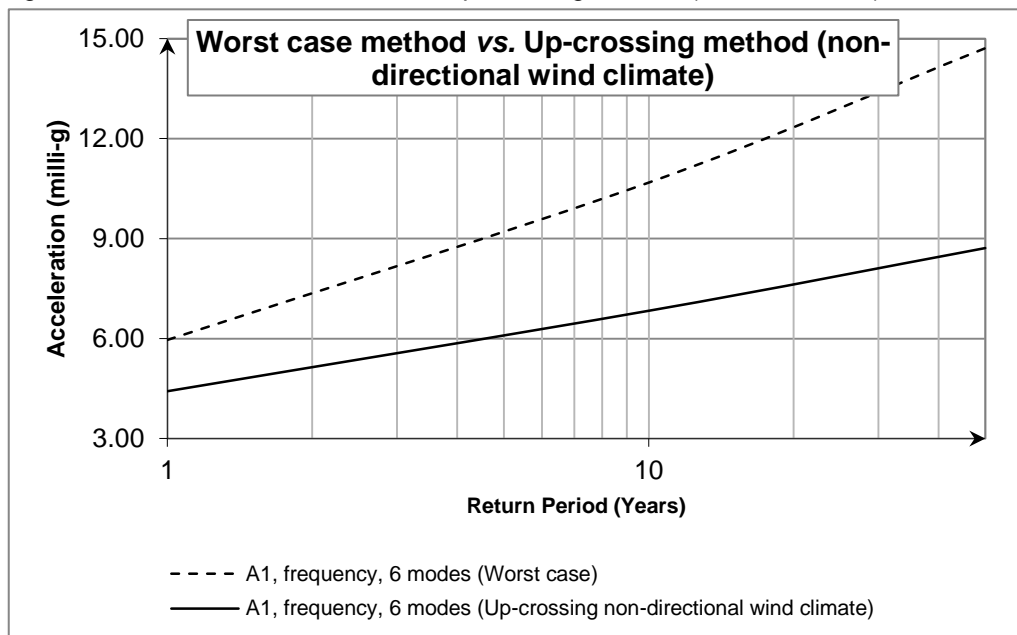
The dispersion of results is clearly great for this kind of analysis and, therefore, consolidating criteria between structural engineers and WTT facilities should be a priority when it comes to structural modelling and dynamic analysis.

7.2.3 WIND MODELLING CRITERIA

7.2.3.1 Up-crossing method results (non-directional wind climate)

In [Chapter 4](#), the results of directional buildings in non-directional wind climate were discussed. In this discussion, the results of Burton et al. (2015) showed that the azimuths with a smaller contribution (smaller results) tend to reduce the overall probability of exceedance of the building acceleration for a certain threshold.

Figure 7.31 – Worst case method vs. Up-crossing method (non-directional).



Source: Author.

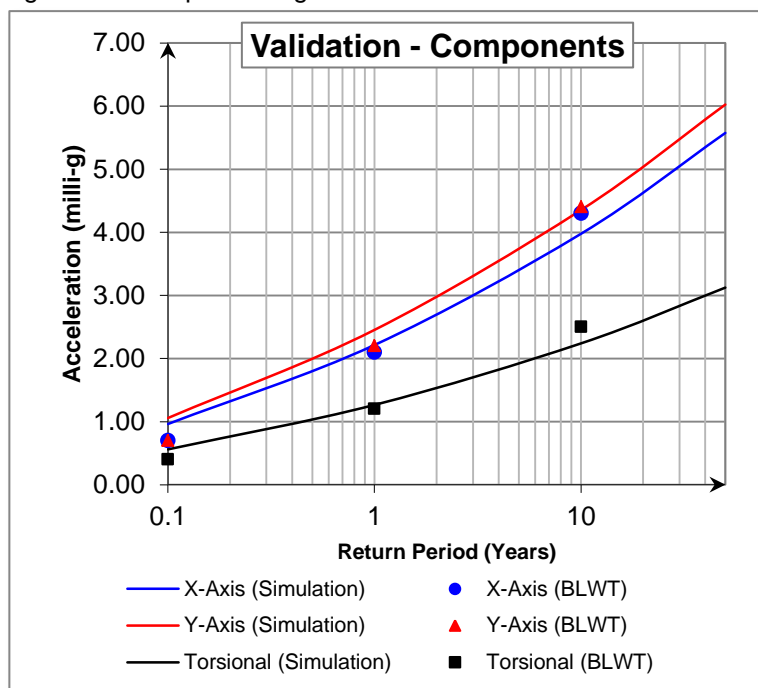
The same analysis was performed for buildings A1 to A3. [Figure 7.31](#) shows the results for building A1. This figure shows results considerably smaller for the up-crossing method, even in a non-directional wind climate, due to the lower contributions from the sectors with results smaller than the maximum response.

These results corroborate the discussion from [Chapter 4](#) and the results obtained by Burton et al. (2015).

7.2.3.2 Up-crossing method results (directional wind climate)

Using eq. (4.9) to (4.11) in the results of the frequency domain for three modes of vibration for building A1, the up-crossing method was first validated with the BLWT results shown in [Figure 7.32](#). The validation was made for each component and marked as “simulation” results in this figure. The same criteria were used for both the simulated results in this thesis and the BLWT (structural modelling criteria and dynamic analysis criteria). This is why this validation occurs in the frequency domain and with lower modal truncation (3 modes, only).

Figure 7.32 – Up-crossing method validation with BLWT results.



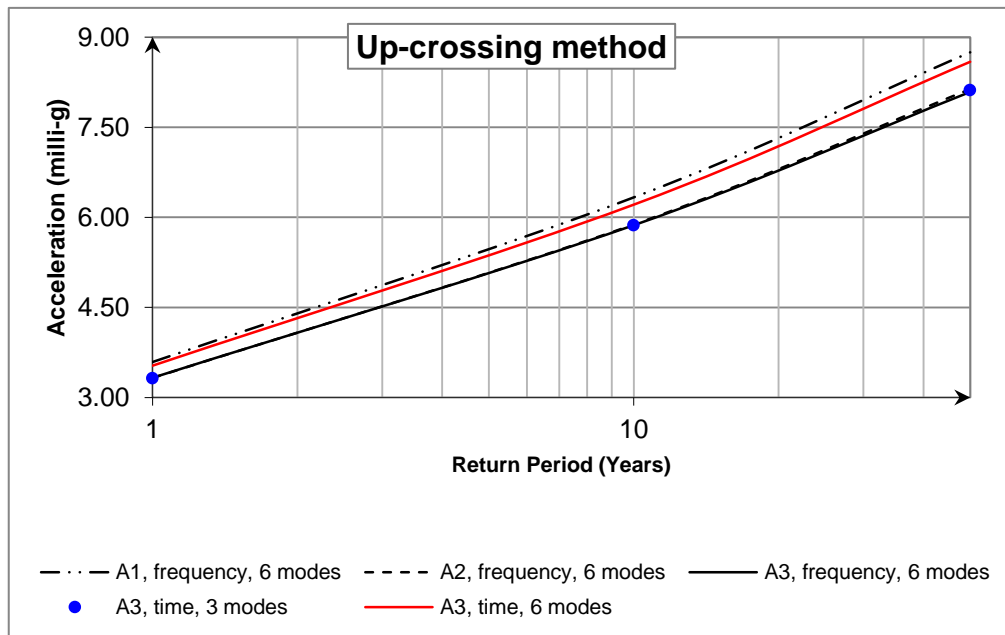
Source: Author.

These results endorse even further the methodology used in this thesis. Quite a few validation arguments have been presented to this point of the text, like the similar response behaviour between modal results for time domain when compared with the frequency domain, and the smaller rms response for time domain when compared with frequency domain ([section 7.2.2.1](#)). These results show that the outcome of the whole procedure is quite the same when compared with the

BLWT's, and serves as final validation. In other words, starting from the integration of pressures on the building's tributary façade areas at the WTT, the dynamic analysis (modal loads, modal results, and modal combinations) and wind climate modelling (up-crossing method) were performed in parallel and achieved similar results.

The results for buildings A1 to A3, for both frequency and time domain, are presented in [Figure 7.33](#). These results follow the "A1>A2>A3" pattern, whilst the time-domain results for building A3 are closer to the frequency domain results for building A1 and higher than those for A2 and A3 building.

Figure 7.33 – Up-crossing method results (Building A).



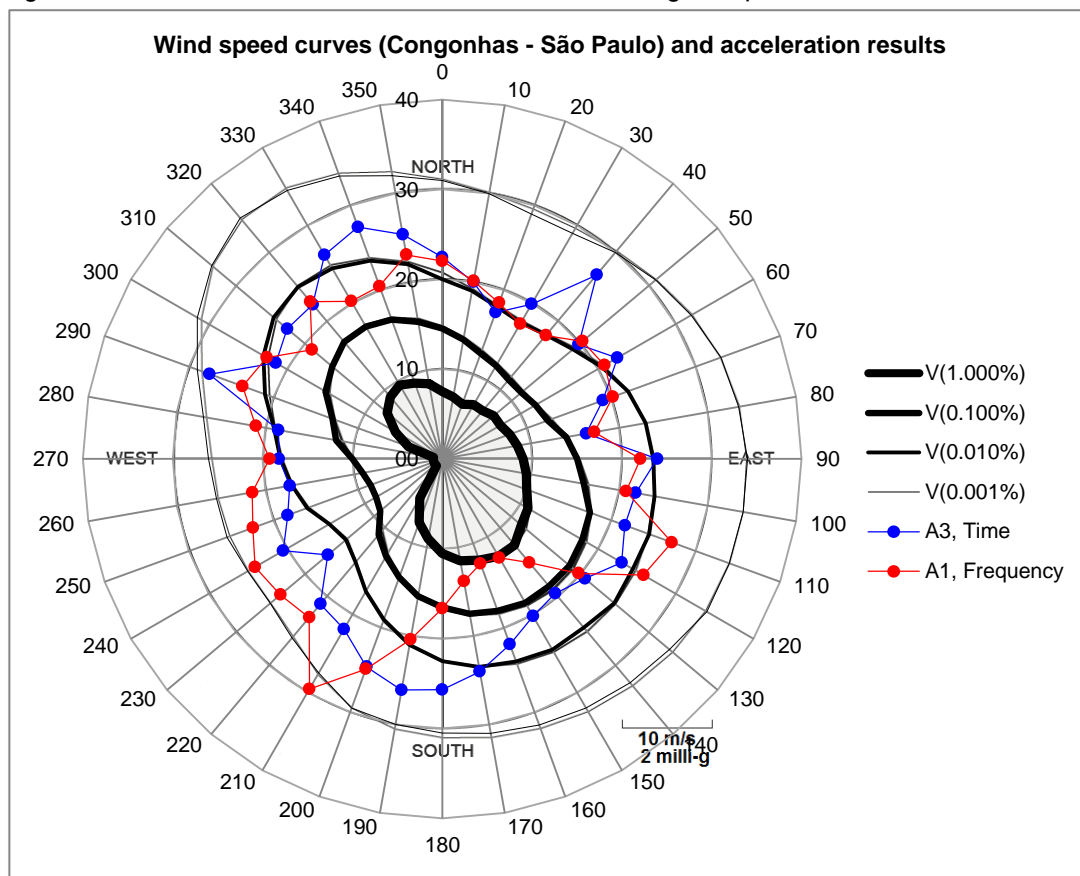
Source: Author.

There is a significantly smaller result (nearly 7% smaller) for building A3 in the time-domain (5.52milli – g) when compared with building A1 in the frequency domain (5.92milli – g) –see [Figure 7.24](#) – for six modes of vibration. However, building A3's accelerations response has a critical direction equal to the critical direction of the wind climate, whilst these directions are different for building A1 (see [Figure 7.34](#)).

[Figure 7.34](#) shows the probability of exceedance of the wind speed for [Congonhas Airport](#), in São Paulo (Brazil). The curves from the most central to the

most external positions represent the probabilities of exceeding that velocity (these probabilities are, respectively, 0.001%, 0.010%, 0.100%, and 1.000%).

Figure 7.34 – Critical directions: wind climate and building's responses.



Source: Author.

In this figure, one can also read the resultant acceleration response for building A1 in the frequency domain and for building A3 in the time domain for six modes of vibration.

By overlapping these curves, one can verify that the stronger contributions of building A3 to the final response are in azimuths 40° , 190° , and 290° , where the wind speed of the probability curves have their maximum values (or where they are closer to their maximum values). In contrast, the stronger contribution of building A1 to the final response is between azimuths $210^\circ - 260^\circ$, where the wind speed of these curves has their minimum values. Hence, the contribution of building A1's responses between azimuths $130^\circ - 190^\circ$ (one of the critical azimuth gaps for wind climate) are much smaller than building A3's contribution.

This is one of the results of the change in the modal deflection shapes discussed in [section 7.2.1.2](#). The modal-deflection-shape change led to a change in the critical direction of the building and in the building's response distribution over the different sectors which, in turn, led to different results in the application of the up-crossing method.

7.2.4 COMFORT AND SLS CRITERIA

7.2.4.1 Peak and rms acceleration analysis (deterministic)

The peak acceleration analysis for time domain is presented in [Figure 7.35](#), where it shows five main results:

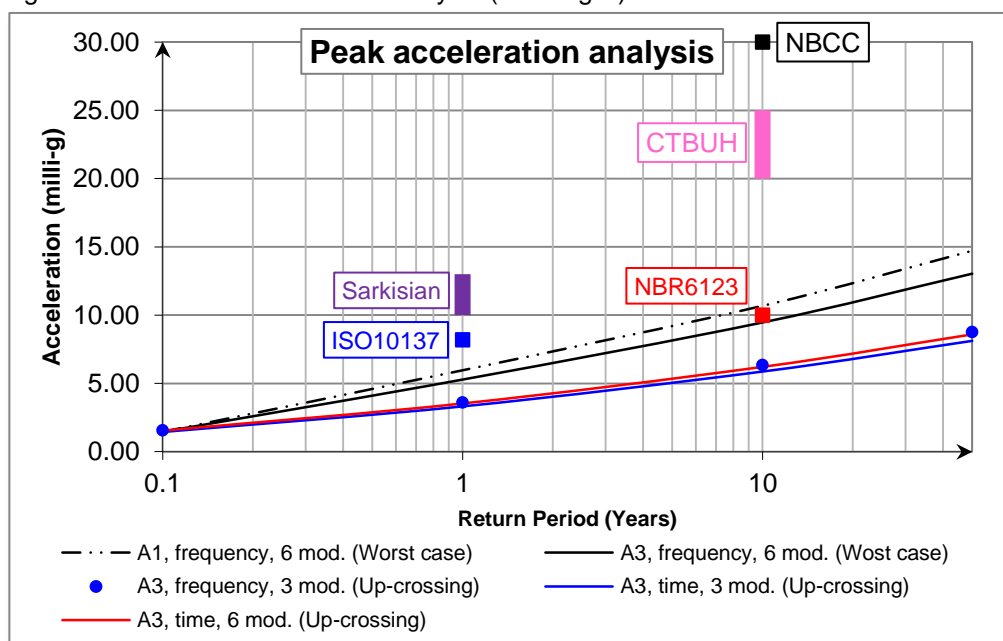
- Building A1, frequency domain, worst-case method, six modes of vibration: these results appear in this figure because they represent the most conservative set of criteria in terms of structural modelling, dynamic analysis, and wind modelling;
- Building A3, frequency domain, worst case method, six modes of vibration: these results represent the most conservative set of criteria for wind modelling and still allow for a comparison between structural modelling criteria;
- Building A1, frequency domain, up-crossing method, three modes of vibration: this set of criteria represents the methodology used by the BLWT;
- Building A3, time domain, up-crossing method, six modes of vibration: this set of criteria represents the most precise results in terms of structural modelling, dynamic analysis, and wind modelling;
- Building A3, time domain, up-crossing method, three modes of vibration: these results establish a comparison between the final results of time-domain and frequency-domain for three modes of vibration and to establish a comparison for higher modal contributions.

Looking at this figure, it is important to reiterate the lack of consistency between the comfort criteria. This lack of consistency can still be justified by the different tolerance to motion in different countries. The user of a building in Chicago, traditionally a very windy city of high-rises, may have more tolerance to motion than the user of a building in São Paulo, a city with a recent culture of high-rises and with

much lower design wind speeds. Therefore, the comfort thresholds in the building codes of these two cities/countries should be different as well.

The inconsistency in overall criteria, conversely, is more concerning. This building in the most conservative set of criteria doesn't pass the comfort verification using the threshold defined in NBR6123-1988. On the other hand, using more precise parameters and comparing them with codes with higher thresholds, like the NBCC (1990), the resultant acceleration achieves a ratio where the acceleration is only 29% of the comfort threshold for the same return period (10 years). Hence, all sets of criteria pass in the comfort verification for a smaller return period (1 year).

Figure 7.35 – Peak acceleration analysis (Building A).



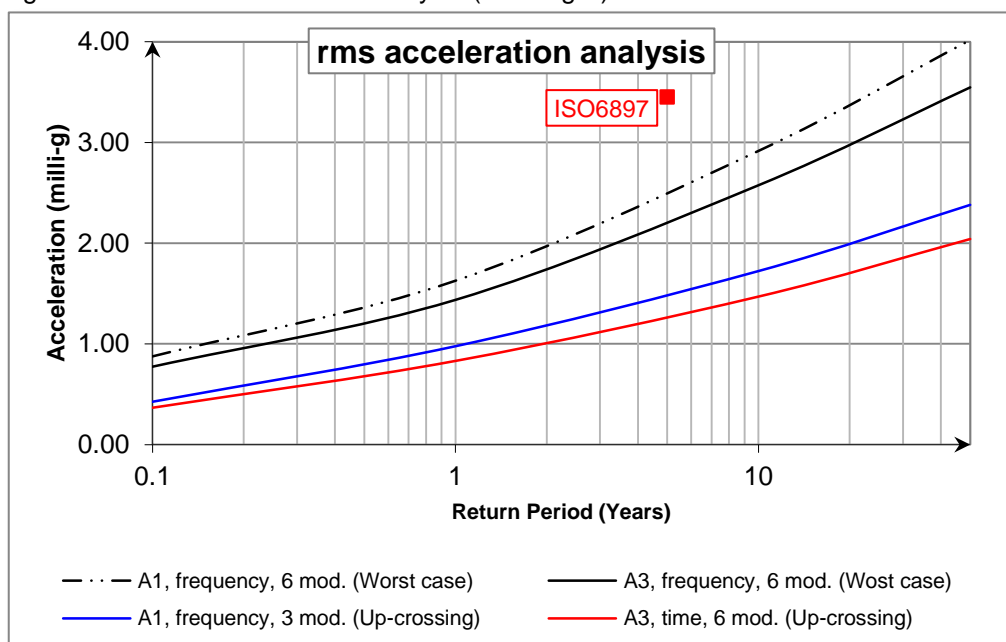
Source: Author.

ISO10137 (2007) and NBR6123-1988 are related to perception, whilst NBCC (1990) and CTBUH criteria are related to comfort. As said before, the verification of comfort in tall buildings in Brazil should be looking for perception thresholds for the next years, due to its recent history with high-rises. NBR6123-1988 is currently under revision to integrate more recent and precise thresholds and dynamic analysis criteria.

Comparing three modal responses to time domain (building A3) and frequency domain (building A1), the time-domain response is even lower and should

lead to a more economic design (allowing further structural optimization). However, considering higher modal contributions, the final acceleration for building A3 is quite similar to the criteria of the BLWT. This means that this could be the case where “two wrongs made a right,” and the different response behaviour throughout the azimuths and higher modal contributions (which lead to higher responses) balanced the reduced response with the use of structural modelling criteria and time-domain analysis (which lead to lower responses).

Figure 7.36 – rms acceleration analysis (Building A).



Source: Author.

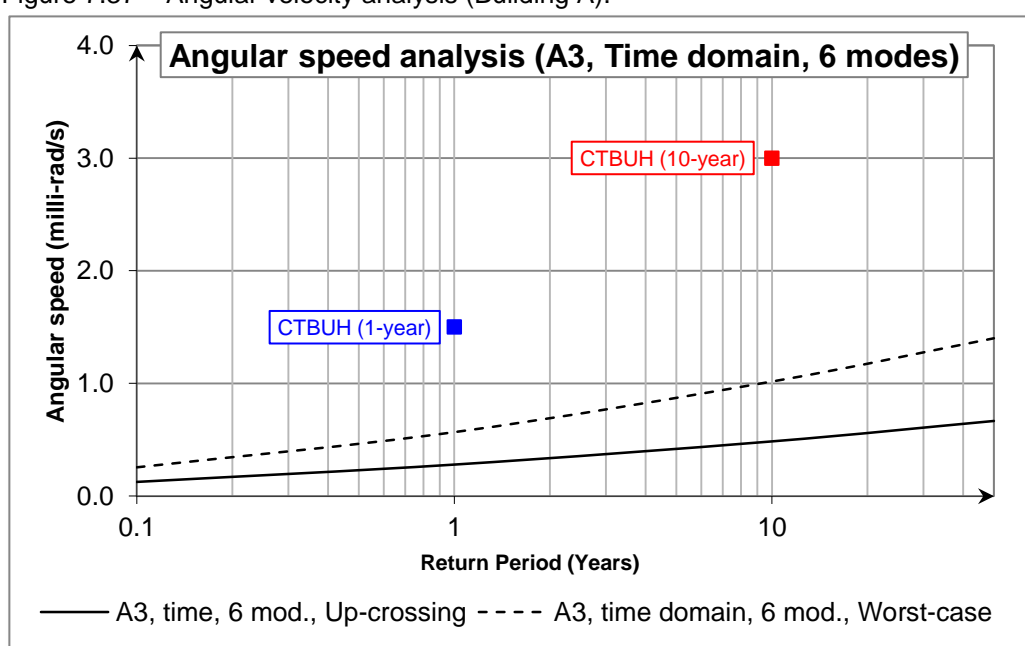
The rms analysis is presented in [Figure 7.36](#), where several features can be observed. First, the time-domain response is significantly lower than the frequency domain response (as expected, due to its higher precision). This means that a comfort analysis performed for comfort using rms accelerations should always use time-domain results for extra precision while taking advantage of lower design accelerations. Subsequently, the higher modal contribution is quite minor for rms results, which is why there is no comparison for higher modal contribution in [Figure 7.36](#). Third and last, the results fall further away from the threshold for the rms analysis than they are for the peak analysis, which also means a more economical

design with further structural optimization (if strength criteria are met after this design with the maximum displacement or acceleration).

7.2.4.2 Peak angular velocity analysis (deterministic) and lateral drift

The main difference in this verification involves the wind modelling criteria between up-crossing and worst-case methods. Higher modal contribution showed little difference in only one azimuth (300°, see [Figure 7.23](#)). This is an expected result, since lower derivatives of displacement, including the displacement itself, have very little contribution from higher modes (HUANG AND CHEN, 2007). [Figure 7.37](#) shows the final results of angular velocity and comfort thresholds for building A3 in the time domain. The angular velocity isn't the most critical parameter for this building, as shown in this figure.

Figure 7.37 – Angular velocity analysis (Building A).



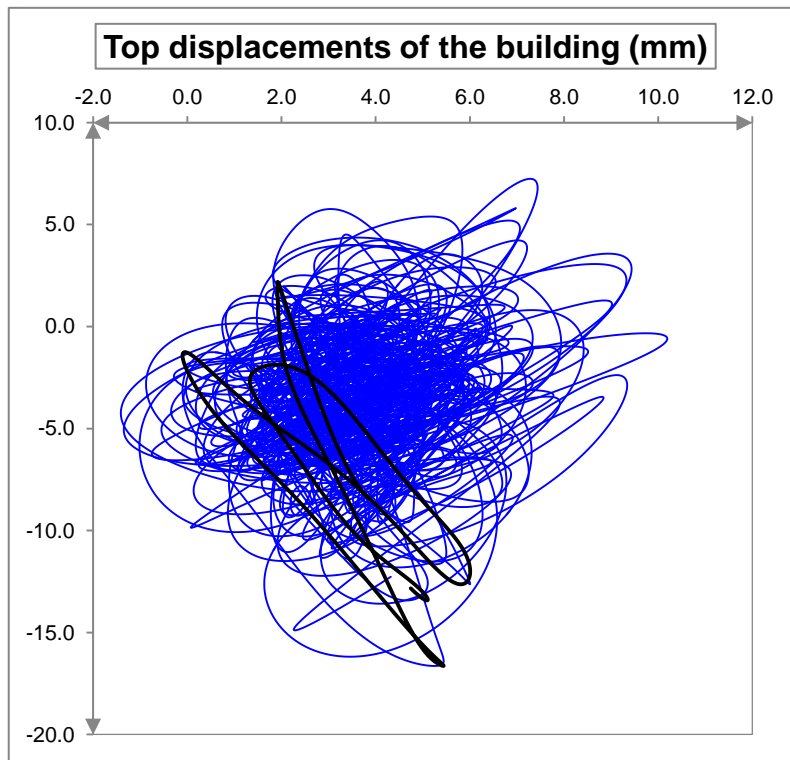
Source: Author.

Sometimes the displacement represents important verifications for internal partitions and cladding where problems may occur due to the exaggerated drift and torsion between floors, as explained in [section 1.5](#). The Brazilian code for mixed/composite structures, NBR8800-2008, requires that the top lateral displacement be limited to “H/400” for a 50-year return period wind load, where “H” is the building height. Other limits are set by this same code, like the maximum inter-

storey drift, for example. Nonetheless, “H/400” is the most critical parameter in this case and therefore should be retained as a design criterion.

Figure 7.38 shows the maximum displacement for a 1-year return period wind and for the worst-case method in the 300° sector, which is the sector with the most severe accelerations and displacements. Building A3 was used in this analysis in the time domain for six modes of vibration, which is the most precise set of criteria for structural modelling and dynamic analysis. The displacement was taken on the building’s façade, where torsional effects contribute significantly.

Figure 7.38 – Top displacement at the building’s façade (1-year return period).



Source: Author.

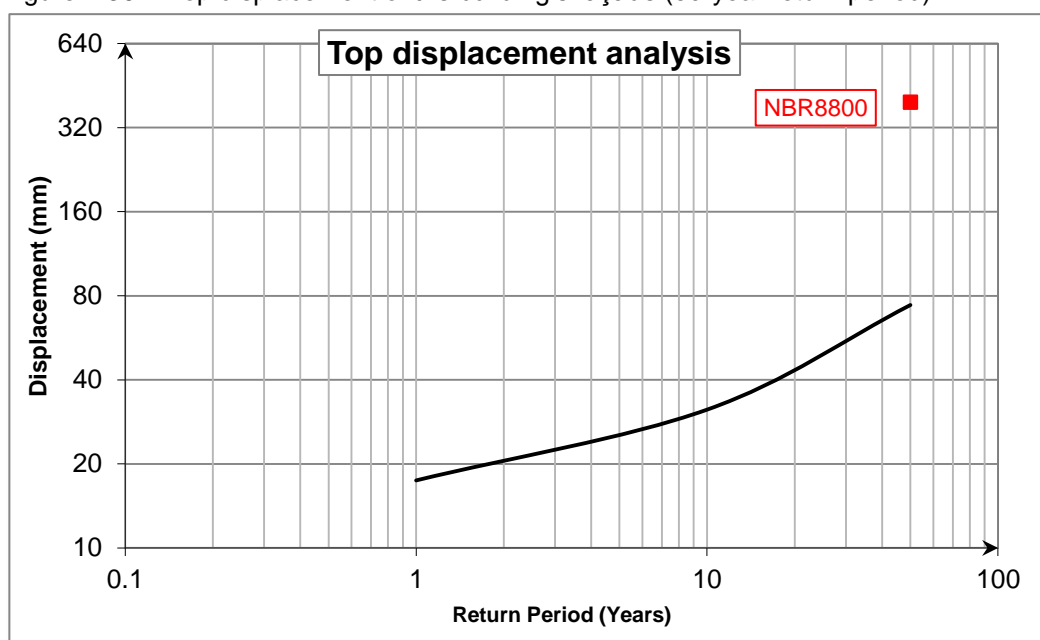
The peak response for the 1-year return period was adapted for a 50-year return period adapted for displacement. The results are shown in *Figure 7.39*, along with the practical limit specified by NBR8800-2008.

The highest values of displacement in *Figure 7.38* were highlighted in black. It is important to note that the movement is nearly oval with a very elongated shape, which means that despite the complex combination of six modes of vibration, the user will perceive an uniaxial movement (TAMURA ET AL., 2006). In this figure the

movement trajectory is highlighted in black for the most critical acceleration/displacement time lapse.

The higher modal contribution showed little to no contribution to the displacement response. The top displacement for the 50-year return period is 43mm when the practical limit for this building, according to NBR8800-2008, is 400mm.

Figure 7.39 – Top displacement of the building's façade (50-year return period).



Source: Author.

7.2.4.3 Probabilistic comfort assessment

This assessment used the perception curves from AIJ-GEH-2004 for habitability to calibrate a log-normal function for the acceleration acceptance (see [Figure 6.9](#)). The frequency used was obtained from the first torsional mode of vibration, as recommended by standard ISO10137 (2007).

The curves from AIJ-GEH-2004 are for habitability, while ISO10137 (2007) multiplies the residential comfort threshold (H90 curve in AIJ-GEH-2004) by 1.5 to calculate the comfort threshold for offices. In order to calibrate the acceptance parameters " λ_p " and " ζ_p^2 ", curves H10 to H90 were also multiplied by 1.5. This is done only to represent higher thresholds for offices, with academic purpose only. Specific comfort curves should be tailored for comfort in offices.

Then, the rms acceleration for a 1-year return period was used to calculate parameters “ λ_A ” and “ ζ_A^2 ” according to eq. (5.7) and (5.8). At that juncture, parameter “ β ” was calculated to finally evaluate the comfort by comparing it with the “ β_T ” values from Table 5.2.

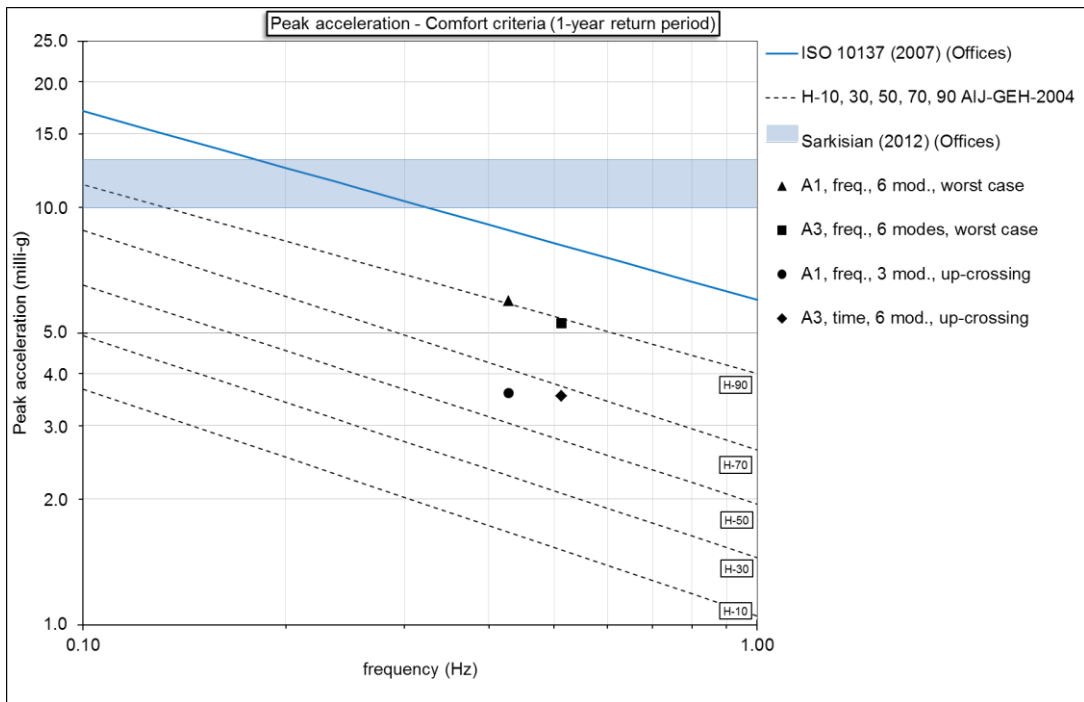
Table 7.6 – Probabilistic comfort assessment for different criteria.

Parameters							
Comfort			Acceleration			Results	
f (Hz)	λ_P	ζ_P^2	Model	λ_A	ζ_A^2	β	Description
0.5124	1.425	0.279	A1, frequency, 6 modes, worst case	1.07	0.223	0.503	Complaints will occur
	1.359	0.285	A3, frequency, 6 modes, worst case	0.94	0.223	0.678	Complaints will occur
	1.425	0.279	A1, frequency, 3 modes, up-crossing	0.56	0.223	1.223	Perceptible but no complaints
	1.359	0.285	A3, time, 6 modes, up-crossing	0.40	0.223	1.451	Perceptible but no complaints

Source: Author.

Table 7.6 shows these results where, for the worst-case method (all models), there will be complaints from the user. For the up-crossing method, the perception of movement occurs but no complaints should be made by the users.

Figure 7.40 – Deterministic comfort/perception evaluation (1-year return period).



Source: Author.

Despite the approximated approach given to the acceptance criteria in this probabilistic analysis, these results are actually quite accurate and consistent with

the deterministic analysis. As shown in *Figure 7.40*, for the up-crossing method (both analyses) there will be at least 50% of users or more that will perceive movement. However, the comfort threshold is moderately far from these results. For the same models, the probabilistic result is “perceptible by most users, but with no complaints”.

Looking at *Figure 7.35*, one may notice that building A1, for the worst-case method, doesn't pass in a comfort evaluation and building A3 is moderately close to the comfort threshold.

Looking at *Figure 7.40*, one may notice the models analysed with the up-crossing method (criteria with lower responses). These results are far from the comfort thresholds, but should be perceived by at least 50% of the users, in accordance with the probabilistic criteria.

This approach is a very powerful tool and might allow for a *full probabilistic approach* for human comfort in tall buildings during wind-induced motion. For this to happen, the acceptance curves must be calibrated for actual comfort (compensatory behaviour, dizziness, productivity at work) and a probabilistic approach to the actions is required (up-crossing method, for example).

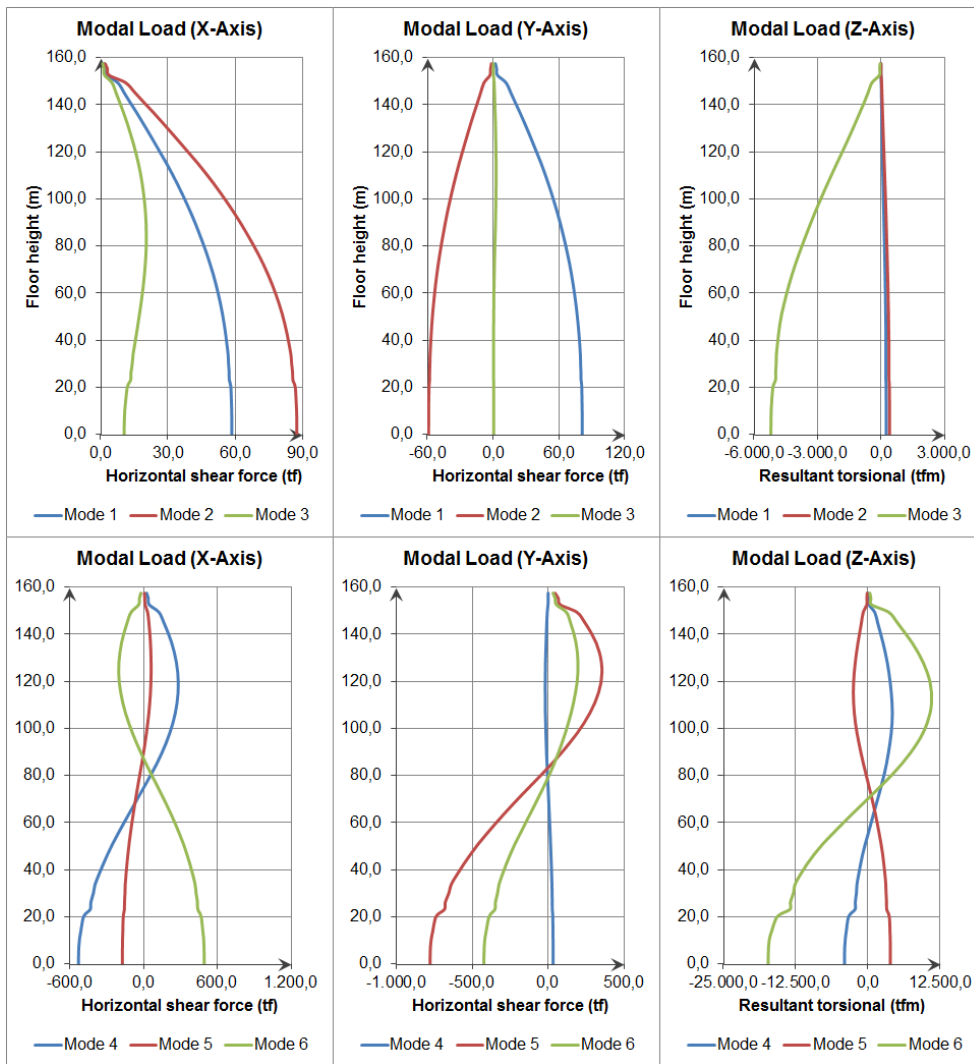
7.2.5 STIFFNESS VALIDATION

7.2.5.1 Modal normalized loads

Each normalized load was generated with the use of eq. (6.10). Then, each group of floor loads (two orthogonal shear forces and one torsional moment) was applied to the reference axis on each floor. *Figure 7.41* shows these modal shear forces on both X and Y axes and the torsional moment around the reference axis (in this figure represented as “Z axis”) using a unitary value for modal amplitude “ Y_j ”.

Regardless of the large value of the normalized loads for modes 4-6 in comparison with the loads for modes 1-3, the participation of modes 4-6 is smaller than the participation of modes 1-3. This is due to the proportion of modal amplitude “ Y_j ” for these modes, which is much higher for modes 1-3 in comparison to modes 4-6. Nevertheless, the contribution of higher modes revealed itself to be fairly relevant to the final response, with an overall increase of nearly 30,8% for the base shear force and 6,5% for the base torsional moment in the most critical direction.

Figure 7.41 – Modal shear forces and torsional moments vs. building heights.



Source: Author.

These resultant forces were assessed using the modal amplitudes obtained from the time-domain analysis and the modal superposition method. Vis-à-vis this relevance, a total of six modal loads was applied to the structure of building A3 in order to verify critical moments on flexural members and validate the overall stiffness.

Before this thesis proceeds to the time-history analysis of internal forces in flexural members, it is timely to present some results and observations about the behaviour of the structure under these modal loads. These structural behaviours help corroborating the discussion carried out in [sections 7.2.1.1](#) and [7.2.1.2](#).

Even with a ringed connection between the floor slab and the concrete core, the flexural behaviour of the lateral portion of the floor slab carries shear loads to the external columns in an outrigger-like behaviour pattern. These ringed connections

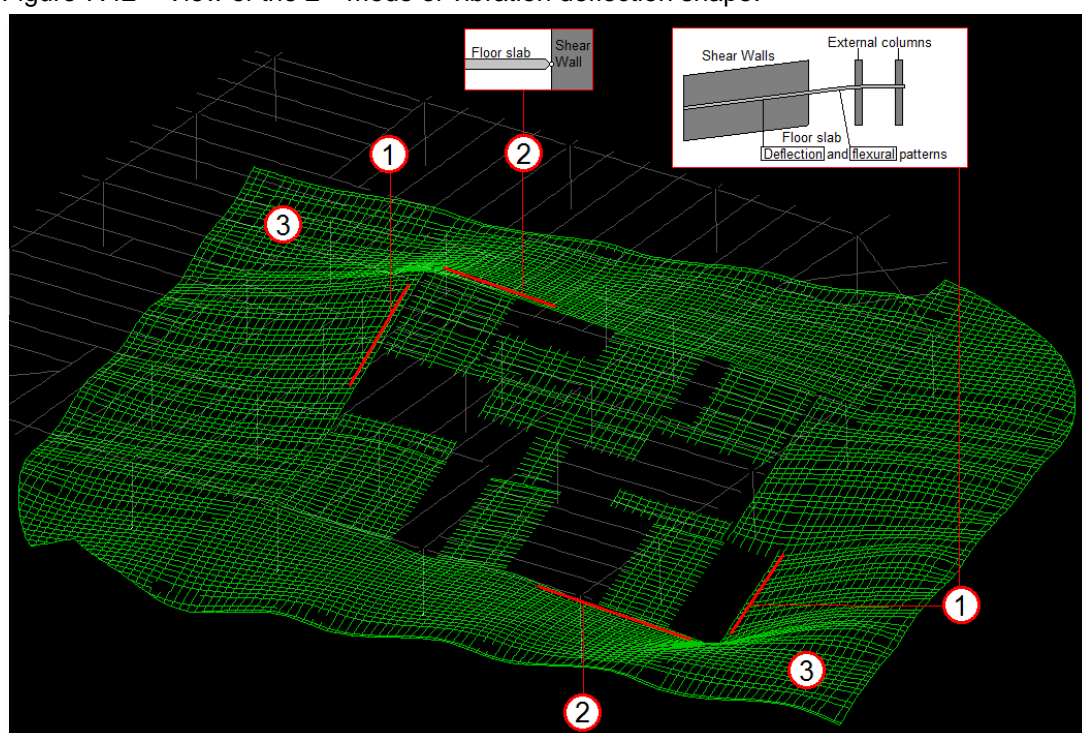
were already included in all studied models due to the constructive method used in this project. However, they did not prevent the contribution from the floor slab modelling to the overall building stiffness.

Figure 7.42 shows this feature for the second mode of vibration, which according to previous discussions in *section 7.2.1.2*, is the mode of vibration more susceptible to benefit from an outrigger-like behaviour of the floor slab. In this figure, one can observe:

- 1: Floor slab deflection pattern following shear-wall connections in a straight line;
- 2: Hinged connection rotation pattern between concrete-core shear walls and the floor slab;
- 3: Clamped portion of the floor slab to the external columns.

Despite the very low values of bending moment acting on the floor slabs, the cumulative effect on every building floor is very expressive and, for this building, it generates the differences in the mode deflection shapes and in the natural frequencies presented in *section 7.2.1.1*.

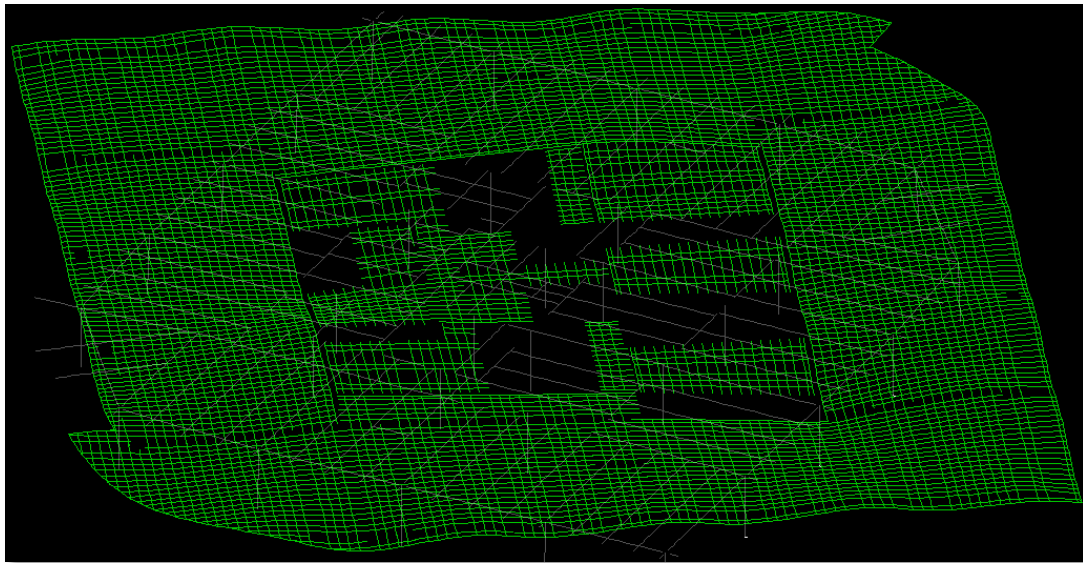
Figure 7.42 – View of the 2nd mode of vibration deflection shape.



Source: Author.

Finally, the mode deflection shape of the 3rd mode of vibration is discussed, which is a mode ruled by torsional behaviour. As previously discussed in [section 7.2.1.2](#) and presented by Kim et al. (2009), the warping stiffness of the building's floor slab stores elastic strain energy by a distortion effect. This effect can be seen in [Figure 7.43](#) for the structure of building A3.

Figure 7.43 – View of the 3rd mode of vibration deflection shape.



Source: Author.

7.2.5.2 Stiffness validation for shear walls

Structural members were classified in two main categories: (1) shear walls; (2) concrete beams connecting shear walls and floor slabs.

The structural members chosen for this analysis are presented in [Appendix 3 – “Building A” studied shear walls](#). They are the sections at the base level for a group of five shear wall elements: P21 and P24 ([Figure A3.1](#)); P25 ([Figure A3.2](#)); P32 ([Figure A3.3](#)); and P3 ([Figure A3.4](#)).

These structural elements are representative enough to allow for a complete stress analysis in the shear wall elements, where the base section was used in the analysis as it is, where the effects of bending moments in these elements are the most critical. In these figures, one can also identify the points of calculation of stress values for the verification of cracked sections.

For a shear wall element, the gravity loads act by preventing cracks from opening by adding compression. In this sense, the stress analysis proposed in eq. (3.3) was made by adding effects of gravity load, as shown in eq. (7.2).

$$\frac{M_x(t)c_x}{I_x} + \frac{M_y(t)c_y}{I_y} + \frac{N_z(t)}{A_z} \leq \sigma_{c,g} + 0,3f_{ck}^{2/3} \quad (7.2)$$

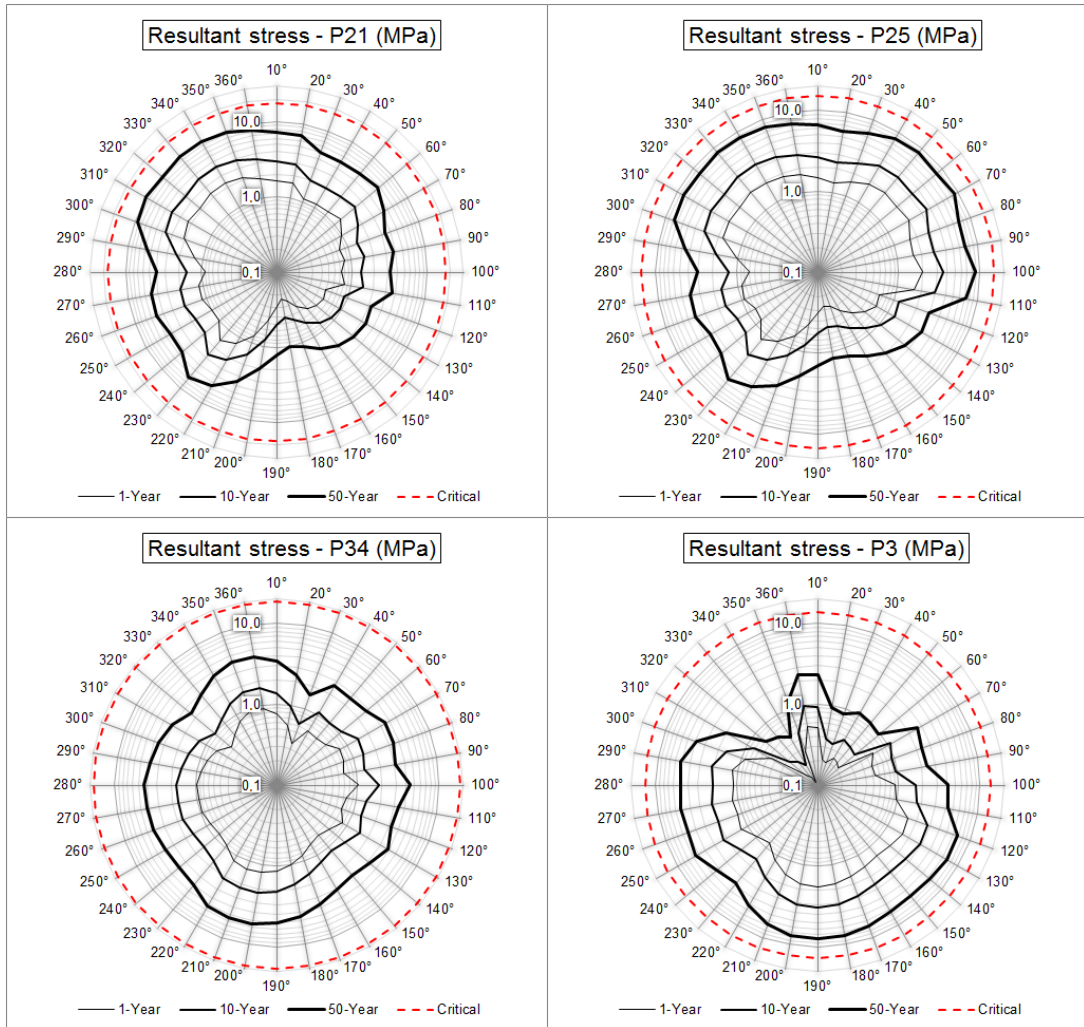
where:

- $M_x(t)$, $M_y(t)$, and $N_z(t)$ are the resultant bending moment in each orthogonal axis and the axial force due to wind loads, respectively;
- I_x , I_y , and A_z are the moments of inertia and the area of the shear-wall cross-section, respectively, corresponding to each described load;
- c_x , c_y distances from the neutral axes to the point of interest of the section studied;
- $\sigma_{c,g}$ is the stabilizing compression stress due to gravity loads (with 30% of live loads);
- f_{ck} is the concrete compression strength.

Maximum tensile stresses are shown in [Figure 7.44](#) for “P21,” “P25,” “P34,” and “P3,” using eq. (7.2) for each time step and six modes of vibration. In addition, the wind climate modelling was included with the worst-case method. The highest tensile stress was obtained for shear wall “P24” (see [Figure 7.45](#)).

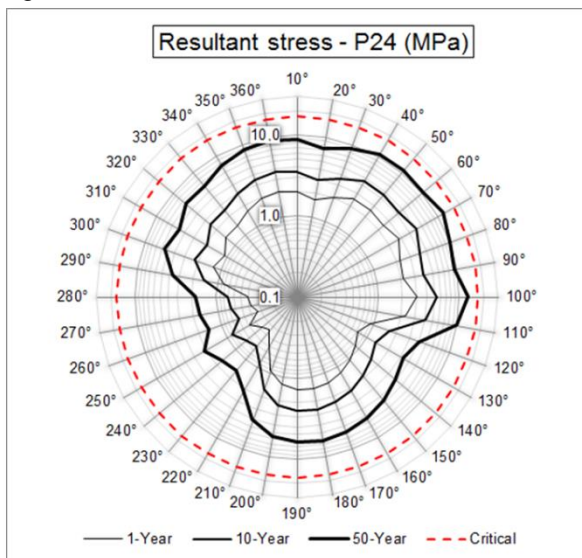
All shear walls presented tensile stresses much below the cracking limit for all return periods. This happens due to the stabilizing effect of the gravity loads on the shear wall elements. These results serve to validate the stiffness used in the shear walls for building model A3.

Figure 7.44 – Peak tensile stress for each structural member (shear walls).



Source: Author.

Figure 7.45 – Peak tensile stress for P24.



Source: Author.

7.2.5.3 Stiffness validation for beams and floor slabs

Several concrete beams connecting shear walls were examined in this validation (see [Figure 7.9](#) for beam location). These beams were analysed according to the highest ratio of “ M_j/W ,” where “ M_j ” is the bending moment generated in the studied structural element by the j^{th} modal load, and “ W ” is its elastic section modulus.

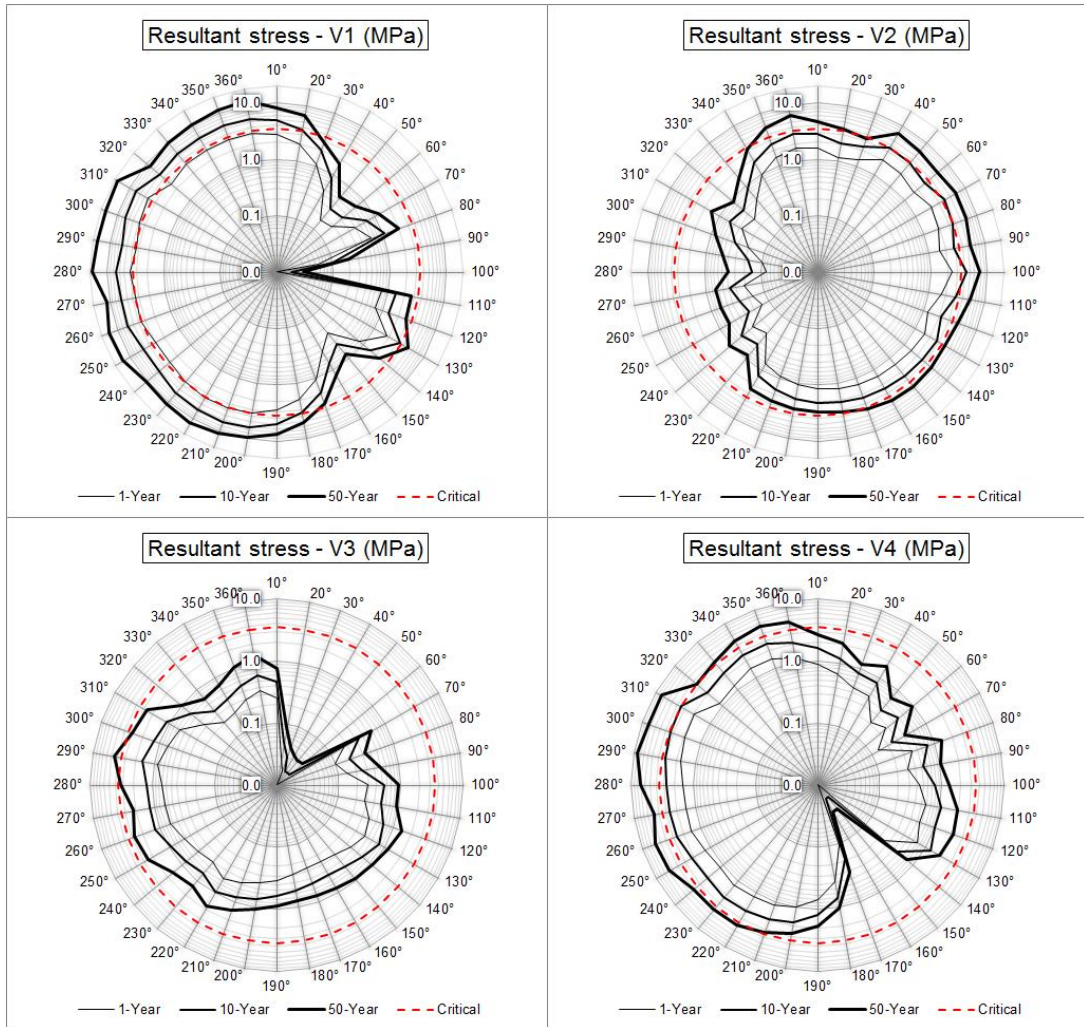
Four beams were retained for the time history analysis. They all have rectangular cross sections ($b \times h$) with a concrete strength of 40MPa. For the sake of simplicity, they will be called V1-V4 and their sections are listed below:

- V1: $b = 30\text{cm}$, $h = 88\text{cm}$, located on first underground level;
- V2: $b = 30\text{cm}$, $h = 425\text{cm}$, located on ground level;
- V3: $b = 30\text{cm}$, $h = 367\text{cm}$, located on typical floors;
- V4: $b = 30\text{cm}$, $h = 178\text{cm}$, located on typical floors.

The beams of the typical floors presented the most severe responses at the top of the first third of the building’s height. The results from four beams along with their (critical) cracking stress are shown in [Figure 7.46](#). V1 presented the highest tensile stresses, to a point where it would not be able to sustain full stiffness against winds with 10-year return periods and above due to the formation of cracked sections. V2 and V4 followed the same pattern, but only for 50-year return period winds. Finally, V3 was able to work with a full stiffness value for all design wind speeds, which is the same behaviour as that of the building floor slabs (see [Figure 7.47](#)).

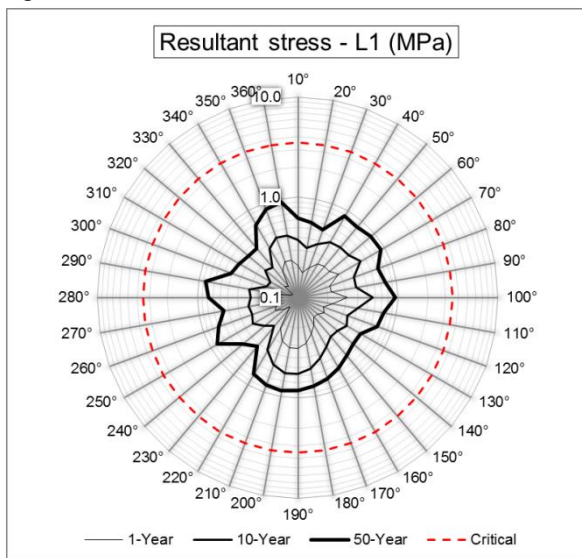
The building’s floor slabs presented the most severe bending moment results for the middle third section of the building. Nevertheless, tensile stresses in these structural elements showed to be fairly below the critical value.

Figure 7.46 – Peak tensile stress for each structural member (beams).



Source: Author.

Figure 7.47 – Peak tensile stress for the floor slabs.



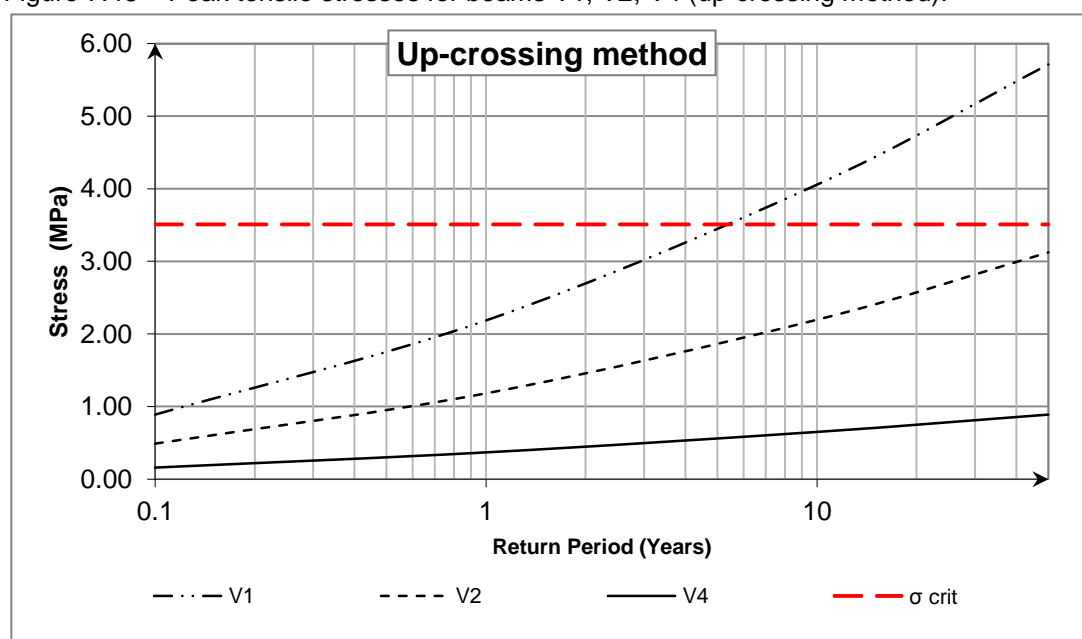
Source: Author.

A partial conclusion of the results presented above would be that the stiffness of the floor slabs is adequate to the structural model, whilst some beams (V1, V2, and V4) would need modelling with a lower stiffness due to cracked sections (KARA AND DUNDAR, 2009). Then, the dynamic properties (natural frequencies and mode deflection shapes) would need to be generated once more for a new building model A3-1. Subsequently, the dynamic loads would need to be re-evaluated and a validation would be required to confirm the effective stiffness used in the model.

This procedure is iterative and leads to one more important conclusion. For each return period, the effective stiffness requires a specific stiffness assessment for certain structural elements. This could mean, for instance, a different structural model with full stiffness for SLS loads and another structural model for ULS purposes with reduced effective stiffness.

As a final and important link between wind climate and structural modelling in the Davenport's chain, one may apply directionality effects to this analysis. The results of the application of eq. (4.9) using tensile stress in the structural elements as boundary functions for the up-crossing method are given in [Figure 7.48](#).

Figure 7.48 – Peak tensile stresses for beams V1, V2, V4 (up-crossing method).



Source: Author.

Final results show that, in the up-crossing method, full stiffness can be assumed for beams that had to be modelled with reduced effective stiffness due to cracked sections in the worst-case method. The only exception is V1, on the first underground level. This beam answers to the dynamic loads with a tensile strength slightly above the critical value for a 10-year return period and is the only one with such behaviour in the whole building. Therefore, a small reduction in its stiffness would not generate noticeable changes in the overall dynamic behaviour of the structure. On the other hand, for 50-year winds, the gap between tensile and critical stresses for this beam is more relevant. This confirms the previous statement that one model should be created for SLS purposes (1-year and 10-year return period), whilst another model with reduced effective stiffness for V1 should be made for ULS purposes (50-year return period).

As a final observation, the mode displacement superposition, which takes place in the core of the methodology used and developed in this thesis, relies on a superposition of linear responses. When non-linear physical effects such as cracked sections are modelled (mostly for ULS), a superposition of non-linear responses occur. Since the superposition of modal displacements depends on linear responses to occur, this validation serves to justify the linear analyses used in this thesis for SLS.

7.2.6 SUMMARY OF CRITERIA FOR BUILDING A

Taking into consideration the results of the extensive analysis carried out for building A, some conclusions can be drawn.

First, the modelling criteria are very relevant for comfort and for the SLS analysis. They represent a substantial increase in the building's natural frequencies (up to 19.66%). In addition, there were visible changes in mode deflection shapes, generating relevant deviations in the probabilistic wind climate analysis.

Time-domain analyses present several paybacks when compared to frequency domain analyses. The assessment of complex motion is one of them, where one can precisely calculate the exact vector acceleration at any floor location for all time steps. This feature allows for a precise modal combination (including higher modes) and peak responses without the need for any modal combination rule or statistical peak factors, and also allows for the assessment of the exact values

through the rms acceleration. In addition, time-domain analyses enable the correct assessment of the transient response, which leads to two developments:

- Accurate calculation of higher modal response, which presented important features of transient behaviour, instead of Gaussian values for the peak responses;
- Smaller results due to the precise assessment of transient response, instead of average Gaussian values with statistical peaks, especially for rms results.

Higher modes presented an important contribution to the final acceleration (up to 9.47%). This result goes in a different direction from the studied criteria. All criteria studied in this thesis tend to reduce responses by adding accuracy to the procedure. Part of this increase in the accuracy is given by higher modal truncation and tends to increase the response. However, this increase is largely compensated by a decrease in other criteria, as it can be observed in [Table 7.7](#).

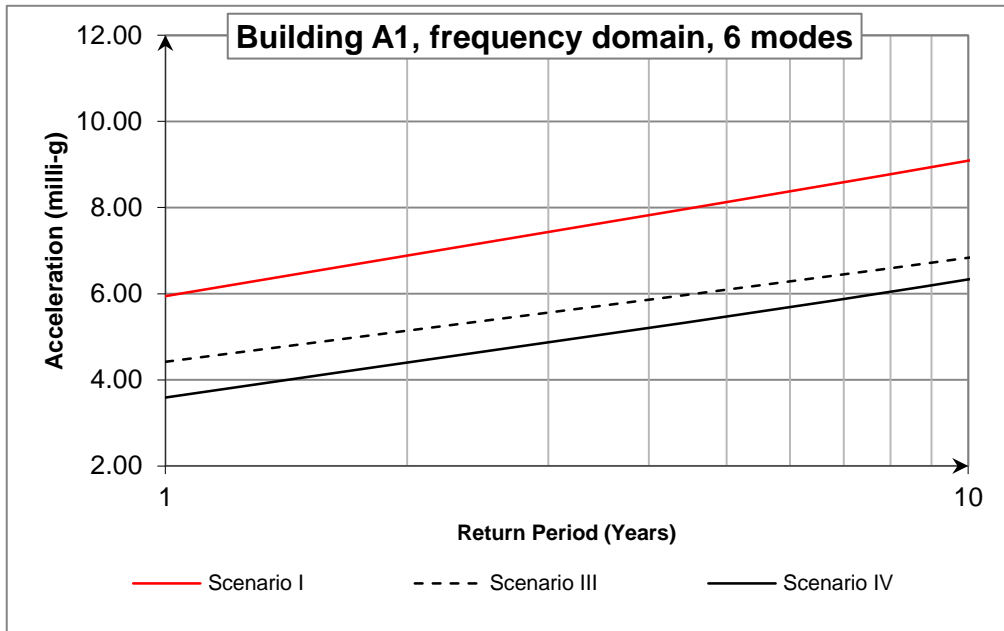
Moreover, higher modal contribution showed more relevance to cross-wind accelerations than along-wind accelerations, in discrepancy with some authors. A higher modal contribution will appear for the relative direction of the building motion (along-wind or cross-wind) for which the higher mode deflection shapes present better correlation to the wind-load distribution and precise turbulence features for the contribution to happen.

The wind climate criteria presented the most relevant impact in the final response, decreasing the overall response by nearly 37.1%. Furthermore, the up-crossing method brings a full probabilistic approach to the procedure when combined with the probabilistic approach for comfort evaluation. This is the next step required for the reliability examination to provide a full probabilistic approach to wind loads ULS, by assessing exact loads on key structural members.

[Figure 7.49](#) shows the application of the up-crossing method for scenarios (1), (3), and (4), as explained in [Chapter 4](#). The application was made without any changes to any other criteria, so as to provide a comparison with no interference. In this figure, one can observe that even in a non-directional wind climate, the sectors where the building response presents a lower contribution provide smaller responses than the worst-case method, represented in this figure by scenario (1). The up-crossing method for the directional wind climate and building response showed the

smaller results. This analysis is in agreement with previous research (BURTON, 2015) and leads to the conclusion that even with conservative criteria for the wind climate (non-directional), the directional behaviour of the building will always generate smaller results in the up-crossing method.

Figure 7.49 – Wind climate results comparison.



Source: Author.

Different mode shapes due to structural modelling criteria also contributed to the wind climate analyses, since these mode shapes changed the critical direction of the building.

Table 7.7 – Summary of results of each set of criteria for building A.

Structural modeling	Time vs. frequency domain	Higher modal contribution	Wind climate modeling	Comfort criteria	Total
-11.4%	-7.6%	6.4%	-39.8%	-36.9%	-62.6%

Source: Author.

Table 7.7 shows the summary of variation results for each set of criteria studied in this thesis for building A through an exhaustive analysis of Figure 7.35. This figure summarizes the full set of criteria investigated in this thesis: structural modelling, dynamic analysis (time domain vs. frequency domain and higher modal contribution), wind climate modelling, and comfort criteria.

Structural modelling criteria were evaluated by comparison of the results of buildings A1 and A3 in the frequency domain for six modes of vibration (worst-case method). The time vs. frequency domain variation was calculated cumulatively with structural modelling criteria by relating results from building A1 for three modes in the frequency domain to building A3 for three modes in the time domain (up-crossing method). Finally, higher modal contribution is evaluated by comparison of the results from building A3 for three and six modes in the time domain (up-crossing method).

Wind modelling criteria could be evaluated through the variation of the results of building A1 for the worst-case method and for the up-crossing method. The increase in the response of building A1 due to the higher modal contribution is negligible for this comparison.

The comfort criteria were evaluated using the ratios of the most precise result (A3, six modes, time domain, up-crossing method) and two thresholds of comfort: ISO 10137 (2007) and Sarkisian's (2012) for offices. These ratios were respectively: $3.53/8.20 = 0.43$ and $3.53/13.0 = 0.27$, and its variation was -36.9% .

The total variation was analysed for the ratio between the most conservative set of criteria (A1, six modes, frequency domain, worst case method and ISO 10137 standard) which is $5.96/8.20 = 0.73$. The comparison was made with the ratio of the most precise set of criteria with the highest comfort threshold ($3.53/13.0 = 0.27$), where the total variation was -62.6% .

This result means that the most precise set of criteria with certain comfort thresholds may represent only 37.4% of the magnitude of results obtained from a conservative analysis and a conservative threshold.

Reduced and more precise responses lead to more efficient designs, which, in turn, lead to reduced use of material, lower costs and lower embodied energy of the structure. In addition, the accurate comfort assessment allows for the design of a better performance of the building for the user, which is directly related to the social pillar of sustainable development. Along with the other two, economic (lower costs) and environmental (lower embodied energy), the use of criteria associated with these results may lead to more sustainable structures.

The comfort criteria still present the biggest discrepancy among all studied areas. Part of this discrepancy may still be justified by different acceptances to

motion in different countries and cultures. Nevertheless, the same building presented very satisfactory results, according to the criterion of NBCC (1990), and somewhat unsatisfactory results, according to NBR6123-1988 or to the probabilistic approach.

The results were calculated considering the worst peak value in the most severe location of the floor, which is consistent with a comfort evaluation based on perception, since the first users to perceive motion would probably alarm the others. However, if the comfort assessment has its target on criteria other than perception (compensatory behaviour, for example), the use of average floor values becomes imperative, as they lead to much smaller peaks and peak factors.

Section 7.2.5 shows that the effective stiffness for horizontal loads uses full sections of shear walls and floor slabs. For beams, the effect of the wind climate modelling and the return period is quite relevant.

When using the worst-case method, the effective stiffness of beams requires a noticeable reduction in both SLS and ULS. When using the up-crossing method, the effective stiffness of beams uses full sections for SLS and reduced sections for ULS in one case. With both methods, the wisest path is to create one structural model for SLS and another for ULS.

As the contribution of this study to the state of the art, these results consolidate and unify very different engineering and multidisciplinary areas of study (structures, reliability, wind, and comfort). Moreover, this study clarifies how the criteria from one area of study may strongly interfere with another and brings attention to the interactions of the links in Davenport's chain of wind loading. As a final result, this study closes the analysis with the validation of the overall building's stiffness after the application of the wind loads and their dynamic effects on the structure.

7.3 BUILDING B PRESENTATION

7.3.1 GENERAL INFORMATION

Building B is 178.00m high, with seven basement levels, which results in a structure with a height of 203.60m. The building has 35 typical floors, with a 4.00m – 5.00m floor-to-floor height, and four technical levels on the top, including a heliport. The whole extent of structural levels of this tall building is 51.

Figure 7.50 – Studied Building (renderization).



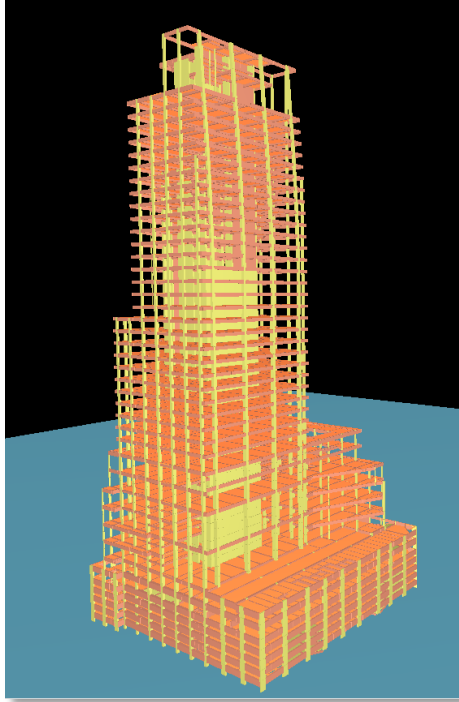
Source: courtesy of *Aflalo e Gasperini Architetas*.

This building structural design is quite similar to that of building A, based on gravity columns near its façade with a stiff concrete core in the centre. The main difference lies in the material used, which in this building is reinforced concrete, instead of the composite structure of building A.

The building could not be built according to the original design due to changes in the zoning limitations set by the city master plan for area uses. Because of these limitations, this building was actually built 14 floors lower than its initial design. However, this thesis will analyse the original design set-up with its respective wind loads and floor accelerations.

The structural modelling was made using the commercial software TQS, the same used for building A (see [Figure 7.51](#)).

Figure 7.51 – Structural model of the building using TQS software.



Source: Author.

7.3.2 BUILDING'S DYNAMICS AND MECHANICAL PROPERTIES

The mass distribution, natural frequencies, and mode shapes of Building B were calculated using the same modelling criteria used for building A. Its natural frequencies, angular frequencies, and periods of vibration are given in [Table 7.8](#).

Table 7.8 – Building B natural frequencies and periods of vibration.

Mode	$f_{(Hz)}$	$T_{(s)}$	$\omega_{(rad/s)}$
1	0.2060	4.855	1.294
2	0.2187	4.573	1.374
3	0.3012	3.320	1.893
4	0.5821	1.718	3.657
5	0.6812	1.468	4.280
6	0.7380	1.355	4.637
7	1.0581	0.945	6.648
8	1.2327	0.811	7.746
9	1.2737	0.785	8.003

Source: Author.

The building's inertial properties (floor mass, moment of inertia, and height) are given in *Appendix 4 – “Building B” mechanical properties* (see *Table A4.1*) – where the structure's mass is calculated with 30% of the live loads, resulting in a building's total mass of 178,000ton and an approximate building density of 390 kg/m³. When compared with that of building A, this higher density value is due to the fact that the structure of this building is made with reinforced concrete, which leads to a structure heavier than a composite/steel one.

The building's mode shapes for translations in the X and Y axes, and torsion, are also given in *Appendix 4 – “Building B” mechanical properties* (*Figure A4.1* and *Figure A4.2*). Like building A, this building model will be called building B1, whilst the subsequent application of the structural modelling previously described and applied to the previous case study will give origin to buildings B2 and B3, respectively. These mode shapes were also normalized to meet the terms of eq. **(1.21)**.

7.4 RESULTS FOR BUILDING B

7.4.1 STRUCTURAL MODELLING CRITERIA

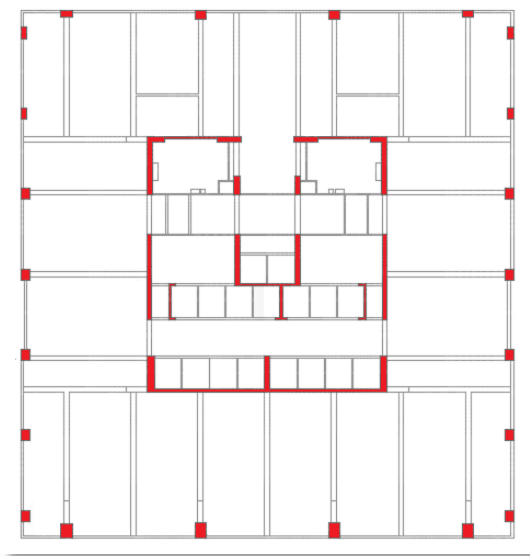
Different modelling criteria allowed for the assessment of natural frequencies for buildings B2 and B3 (see *Table 7.9*). The overall increase in the natural frequencies varied between 4% and 7%. The results for step one (using probable Young's modulus) to create building B2 are consistent with the results of Kim et al. (2009) for the equivalent modelling criterion. On the other hand, the second modelling step (floor slab modelling) showed results slightly reduced when compared with building A. This is due to two main factors: first, the building structural system is composed of moment frames in both orthogonal directions (see *Figure 7.52*); second, the stiffness increase in the mass ratio is considerably smaller for this building when compared with building A (as the average density is nearly 56% higher for building B).

Table 7.9 – Natural frequencies comparison for B1, B2 and B3 structural models.

Mode	f_n (Hz)						Type
	B1	i_{1-2}	B2	i_{2-3}	B3	i_{1-3}	
1	0.2060	+ 3.61%	0.2134	+ 3.40%	0.2207	+ 7.13%	Translational y dir.
2	0.2187	+ 2.98%	0.2252	+ 0.98%	0.2274	+ 3.99%	Translational x dir.
3	0.3012	+ 2.34%	0.3083	+ 3.35%	0.3186	+ 5.77%	Torsional
4	0.5821	+ 2.57%	0.5970	+ 1.70%	0.6072	+ 4.31%	Torsional
5	0.6812	+ 3.31%	0.7037	+ 2.30%	0.7199	+ 5.69%	Tors. with transl. in y dir.
6	0.7380	+ 3.75%	0.7657	+ 0.54%	0.7698	+ 4.31%	Tors. with transl. in x dir.
7	1.0581	+ 2.62%	1.0858	+ 1.04%	1.0971	+ 3.69%	Torsional
8	1.2327	+ 0.71%	1.2415	+ 1.07%	1.2547	+ 1.78%	Translational x dir.
9	1.2737	+ 2.67%	1.3077	+ 0.92%	1.3197	+ 3.61%	Tors. with transl. in y dir.

Source: Author.

Figure 7.52 – Building B floor plan.



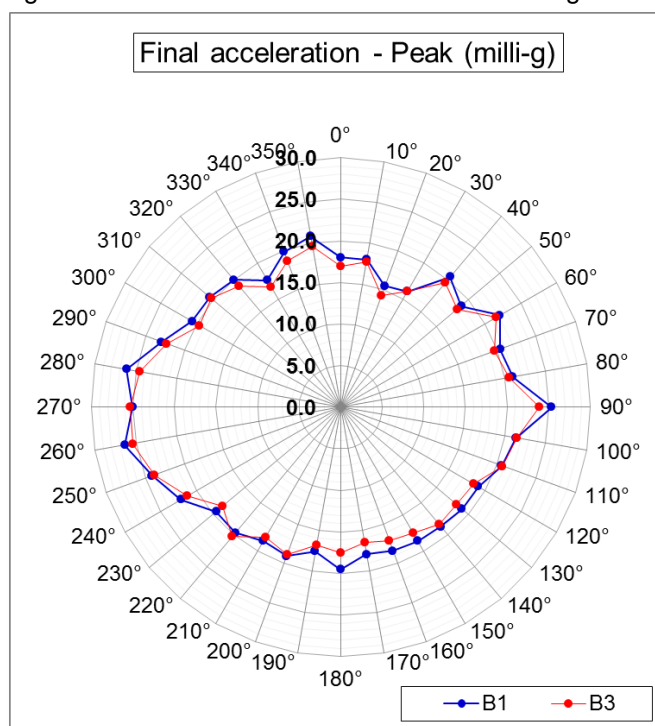
Source: Author.

Resultant accelerations using the same methodology used for building A were calculated using a 50-year return period (BLWT normalized wind pressures for 44m/s wind speed at 500m of altitude) and a total of seven modes of vibration. The modal truncation criteria for this building will be discussed in [section 7.4.3](#), using the PSD of the modal responses (validating the use of seven modes of vibration for a precise analysis), whilst the return period for the comfort analysis will be introduced later in the analysis of the wind climate criteria.

The “moment frame” and/or “coupled shear walls” structural systems in both directions lead to a reduced participation of the floor slab as a structural element, as previously discussed in building A’s case study and showed in the study of Kim et al.

(2009). Added to well-behaved mode deflection shapes in well-defined directions (translations in X and Y axes with little to no torsional components), this leads to no differences between these shapes for the three assessed models (B1, B2, and B3).

Figure 7.53 – Resultant accelerations for buildings B1 and B3.



Source: Author.

As previously observed in [Table 7.9](#), the structural modelling criteria play a reduced role in this building when compared with building A. Nevertheless, the pattern “B1>B3” is respected for all the azimuths with little exceptions in [Figure 7.53](#). Differently from building A, there is no change in the critical direction for building B, since there is no change in the mode deflection shapes due to different modelling criteria. The reduction in the resultant acceleration due to the structural modelling criteria is around 3.6%.

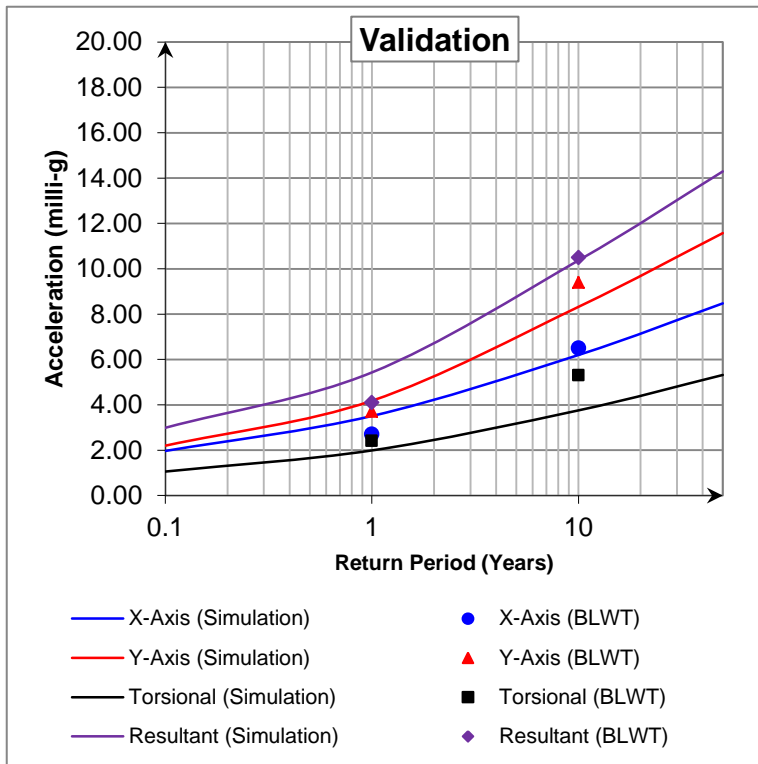
7.4.2 ANALYSIS VALIDATION WITH BLWT RESULTS

A validation was made for building B using the same modelling criteria used with building A. Model B1 (with the same criteria used in the BLWT dynamic analysis) was analysed in the frequency domain with the modal truncation limited to

three modes (one translation in each axis and the first torsional mode, similarly to the dynamic analysis performed by the BLWT).

The results were obtained using the up-crossing method to introduce the wind climate modelling to the examination. These results are presented in *Figure 7.54*, which shows nearly 20% to 30% variations for a one-year resultant acceleration and a ten-year torsional component, respectively. Nevertheless, close agreement is obtained between the dynamic analysis of the BLWT and the results obtained with the methodology proposed in this thesis.

Figure 7.54 – Up-crossing method validation with BLWT results for building B1.



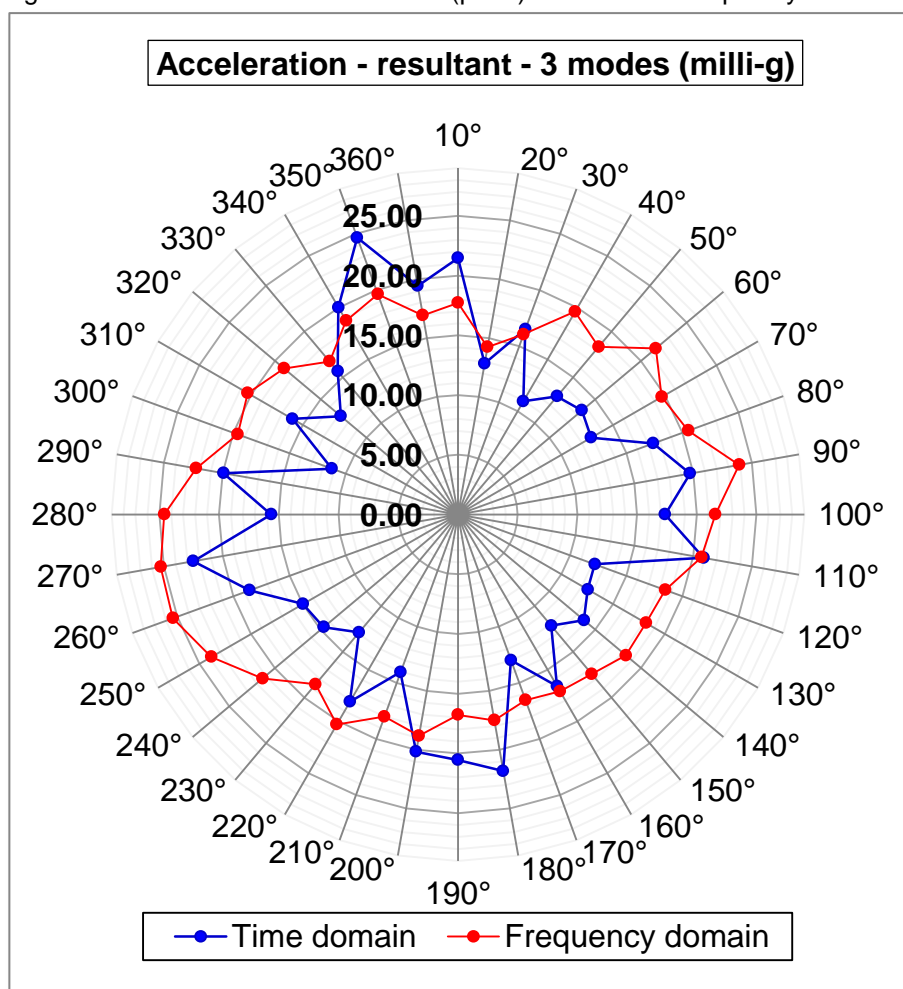
Source: Author.

Along with building A’s previous validations, *Figure 7.54* endorses even further the methodology used in this thesis. Moreover, the results are consistent for two different buildings (building A and building B) and two different BLWT’s, serving as point of departure for the further criteria experimentations in the next sections of this thesis.

7.4.3 DYNAMIC ANALYSIS CRITERIA

The first results presented for the dynamic analysis criteria are the time-domain and frequency-domain responses. The results for the resultant peak acceleration for three modes of vibration are presented in [Figure 7.55](#). As projected from building A's results and from previous studies (JEARY, 2003; WU ET AL., 2007), the time-domain response is lower than the frequency-domain response, with a few exceptions. These exceptions, as explained before, are due to sometimes higher peak factors in time-domain responses, when compared with the standard Gaussian peak factor assessment. The rms accelerations presented lower responses for all azimuths.

Figure 7.55 – Resultant accelerations (peak) for time and frequency domains (Building B3).

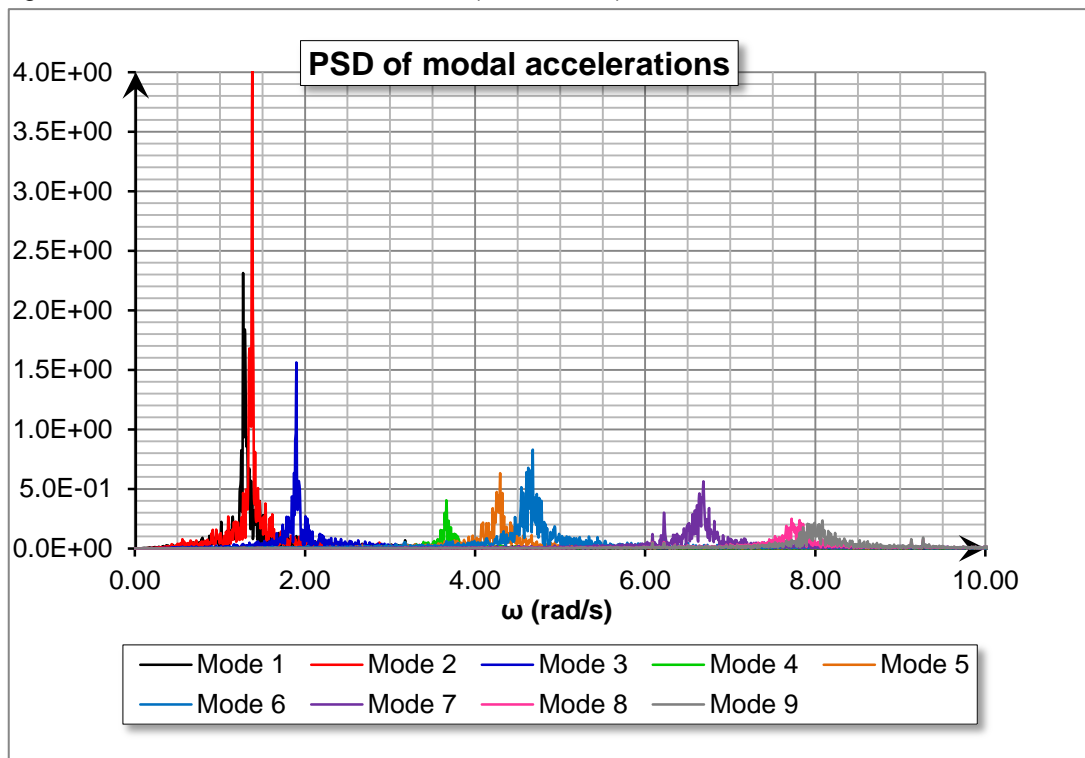


Source: Author.

A validation of the modal truncation at the seventh mode of vibration is provided in [Figure 7.56](#), which shows the relative importance of the last two modes

(eightieth and ninth) when compared with the first seven modes analysed. This figure shows that the first three modes of vibration clearly present important contribution to the final response, whilst modes 4 – 7 present similar magnitudes, and modes 8 – 9 present even lower magnitudes when compared with modes 4 – 7. The input of modes 8 – 9 to the final response was assessed and contributions below 1% were expected for these modes, leaving them out of the subsequent analyses.

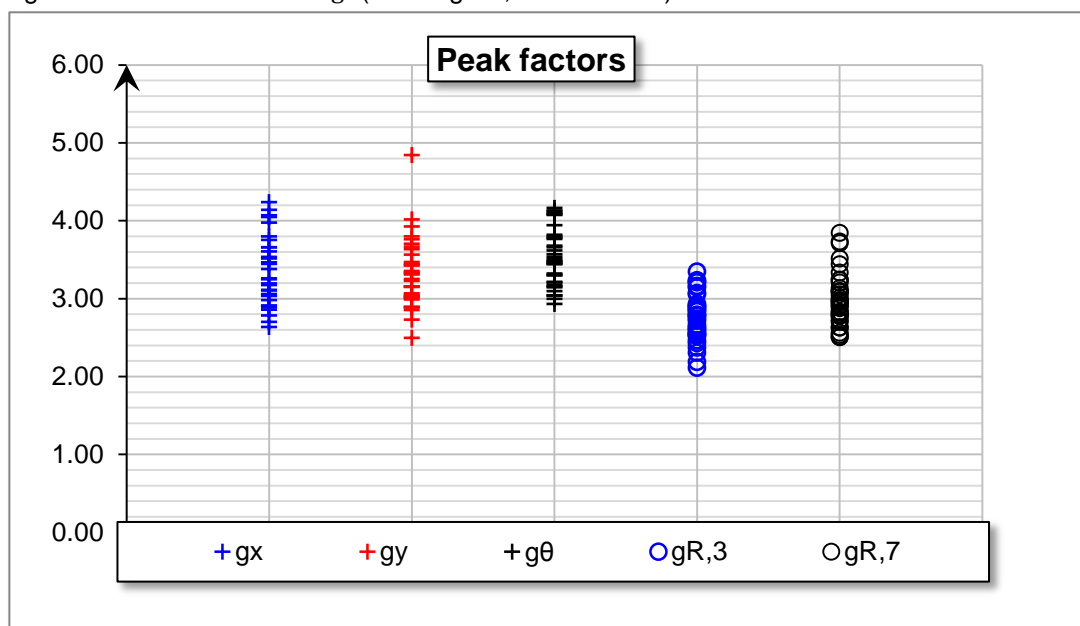
Figure 7.56 – Modal accelerations PSD (260° sector).



Source: Author.

Subsequent higher modal analyses take into consideration only seven modes (instead of nine). Peak and rms analyses of time-domain responses showed average peak factors of 2.76 and 3.02 for the three-mode resultant acceleration and the seven-mode resultant acceleration, respectively. Average lower peak factors are expected for this building when compared with building A, due to its lower natural frequencies. Peak factors “g” are provided in [Figure 7.57](#) for each acceleration component (x, y, and θ), using three modes of vibration, and resultant acceleration, using three and seven modes of vibration (“gR, 3” and “gR, 7,” respectively).

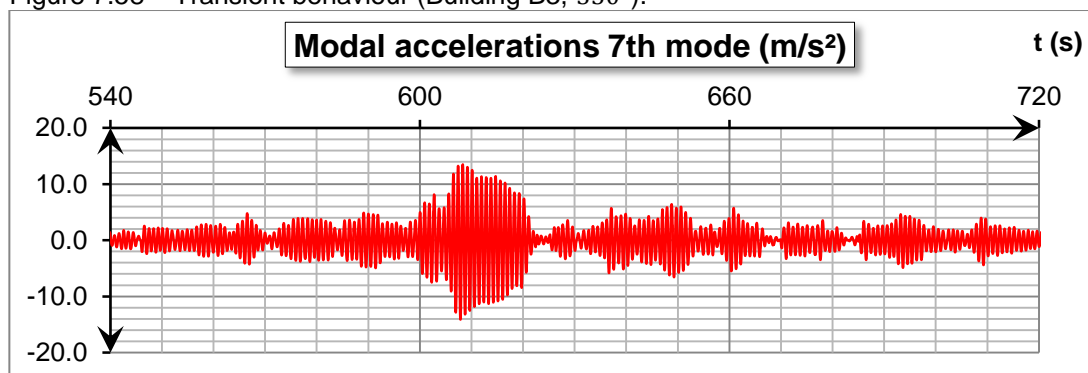
Figure 7.57 – Peak factors “g” (Building B3, time domain).



Source: Author.

The increase in the peak factors of the resultant acceleration with higher modal contribution (see [Figure 7.57](#)) corroborates the discussion presented in [section 7.2.2.2](#), where the transient behaviour of higher modes leads to lower rms acceleration and higher peak results. This transient behaviour is also observed in the seventh mode of vibration (see [Figure 7.61](#)).

Figure 7.58 – Transient behaviour (Building B3, 350°).

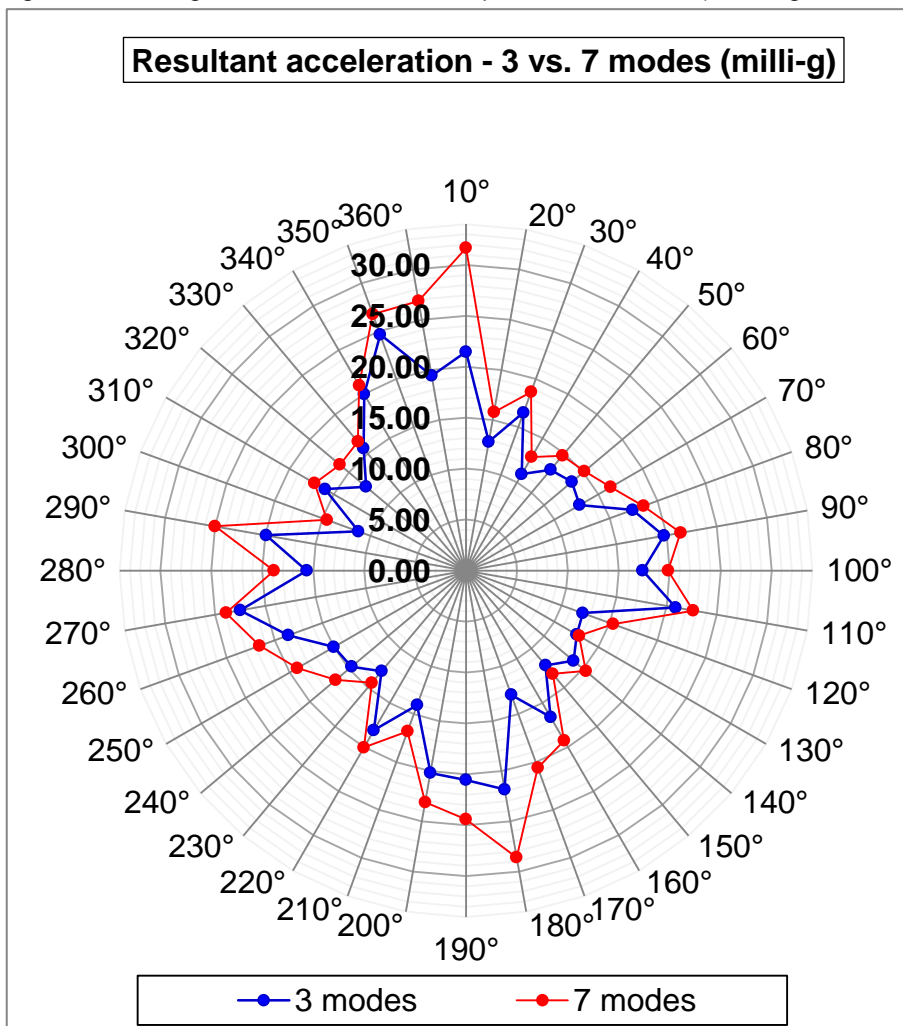


Source: Author.

Finally, higher modal contribution results are presented in [Figure 7.59](#), where a noticeable increase in the maximum peak resultant acceleration can be observed. The most perceptible increase of 47% is in the 10° sector. In that sector,

components x, y, and torsional presented results of 19%, 23%, and higher than 50%, respectively, due to the contribution of modes 4 – 7. In this case study, the contribution of higher modes was equally important for both along-wind and cross-wind loads, whilst the torsional component showed to be far more relevant than both translational components.

Figure 7.59 – Higher modal contribution, peak acceleration (Building B3, time domain).

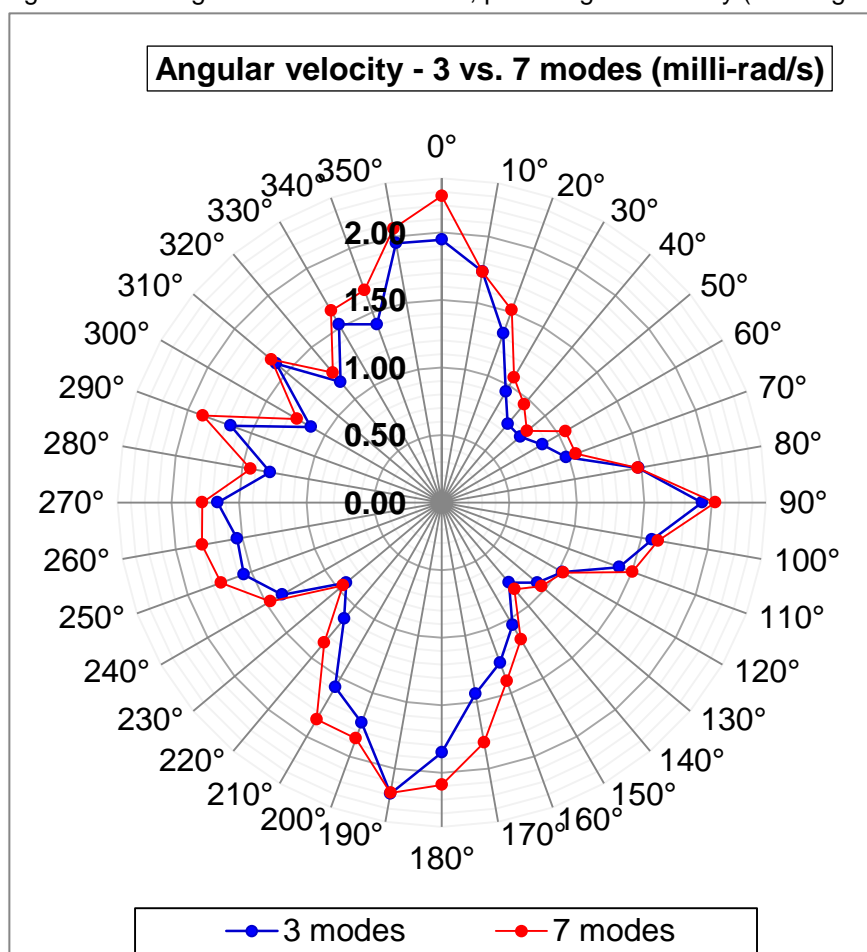


Source: Author.

The higher modal contribution to the peak angular velocity is presented in [Figure 7.60](#), where a noticeable increase can be observed in this response (up to 25%). The participation of higher modes in this response is fairly superior when compared with the responses of building A. This is due to the important torsional components in the mode deflection shapes of this building, also responsible for the

higher relevance of the torsional acceleration component, when compared with translational components, as previously discussed.

Figure 7.60 – Higher modal contribution, peak angular velocity (Building B3, time domain).



Source: Author.

The smaller contribution from higher modes to the angular velocity, when compared with accelerations (up to 47%), is consistent with the results from building A. The angular velocity has a smaller derivative with respect to time than acceleration, and therefore it presents a smaller contribution from higher modes to the final response.

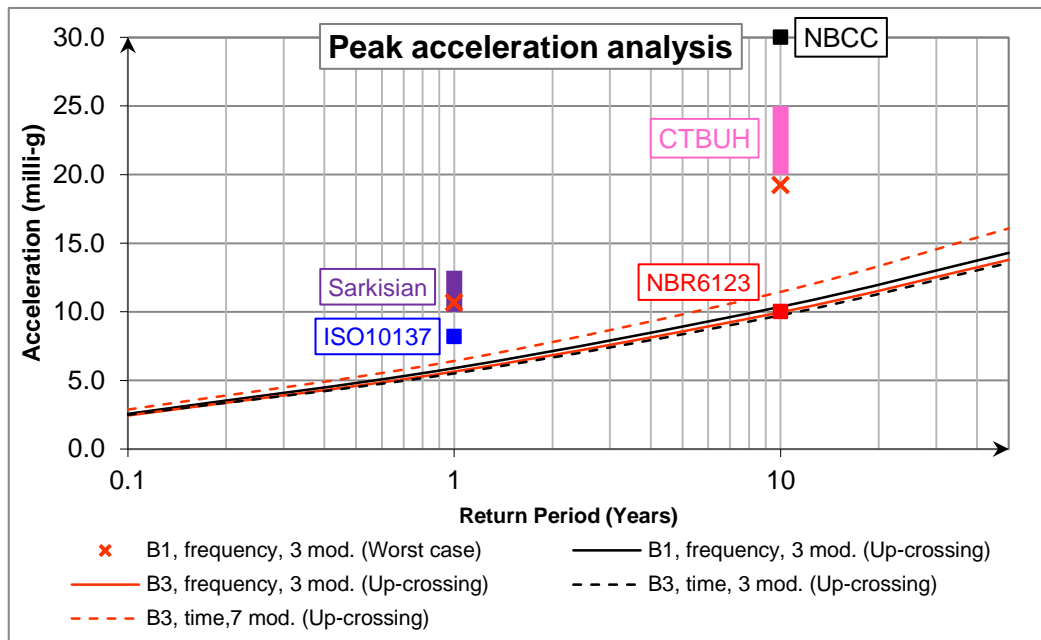
One last and important observation is about the difference in height between building B and building A. This height difference along with the higher density of building B lead to a greater number of natural frequencies below 1Hz, making this building more susceptible to present a noticeable, higher modal contribution when compared with building A.

7.4.4 WIND, COMFORT AND COMPLETE CRITERIA FOR BUILDING B

The acceleration assessment using the most representative group of criteria is presented in *Figure 7.61* including five main results:

- Building B1, frequency domain, worst-case method, three modes of vibration: standard criteria used by the wind code in Brazil;
- Building B1, frequency domain, up-crossing method, three modes of vibration: standard criteria used by the BLWT who performed the WTT;
- Building B3, frequency domain, up-crossing method, three modes of vibration: standard criteria used by the BLWT who performed the WTT with improved structural model;
- Building B3, time domain, up-crossing method, three modes of vibration: more precise dynamic analysis method with the most precise structural model;
- Building B3, time domain, up-crossing method, seven modes of vibration: most precise dynamic analysis method with the most precise structural model.

Figure 7.61 – Peak acceleration analysis (Building B3).



Source: Author.

The results show that the resultant acceleration using the first set of criteria (B1, frequency domain analysis, three modes of vibration, and worst-case method) does not meet the comfort criteria of ISO10137 (2007), but it meets Sarkisian's

(2012) critical accelerations standards for linear acceleration for a one-year return period. The same set of criteria for a ten-year return period significantly surpasses NBR6123 (1988) threshold of comfort, whilst it fairly meets Sarkisian's (2012) comfort criteria, and stands far below the NBCC (1990) threshold of comfort.

These disagreements illustrate once more the changeability issue between different normative codes. Taking into consideration the results from building A and the discussion carried out in [Chapter 5](#), the use of two different criteria in Brazilian projects: ISO10137 (2007) and/or Sarkisian's (2012) lower threshold for comfort. The implementation of such a directive to consider both standards would lead to the following thresholds:

- Residential use (one-year return period): curve two from [Figure 5.3](#) (ISO10137, 2007), or 5.0milli – g (SARKISIAN, 2012) from [Figure 1.21](#);
- Residential use (ten-year return period): 10.0milli – g (SARKISIAN, 2012) from [Figure 1.22](#);
- Office use (one-year return period): curve one from [Figure 5.3](#) (ISO10137, 2007), or 10.0milli – g (SARKISIAN, 2012) from [Figure 1.21](#);
- Office use (ten-year return period): 20.0milli – g (SARKISIAN, 2012) from [Figure 1.22](#).

The set of thresholds proposed here still leaves some variability and room for further discussion. However, it aims at the perception of movement whilst allowing some design margin for the comfort assessment using other indicators, such as compensatory behaviour or motion sickness, for example. This set allows for a more efficient and economic design, whilst it still has a design reserve from higher thresholds, which are better aligned with comfort using dizziness and other indicators, since Brazil has a new history with high-rise projects.

As for the comfort assessment for hotel designs, the literature contains other thresholds that are slightly higher than the residential ones and lower than office ones (CTBUH; SARKISIAN, 2012). This thesis recommends the use of these thresholds always validated by the owner of the project, for the following reasons:

- Hotels have lower a permanence rate of users than residences, allowing for higher thresholds for comfort assessment;

- Hotels are occupied by people from all parts of the world, which means that a hotel's comfort thresholds should follow international, concise standards, despite of the location where it is located;
- Hotels may present very different standards of comfort/quality, which means that the same structure may or may not afford certain levels of motion, leaving space for subjective design decisions about habitability during wind-induced motion;
- Despite of the subjectivity, these comfort levels should not be lower than the residential thresholds.

The dashed lines (black and orange) in *Figure 7.61* define the region of responses affected by dynamic analysis criteria and structural modelling criteria. In this case study, they play a smaller but important role in the final response. According to *Table 7.10*, structural modelling criteria, time and frequency-domain analyses and higher modal contribution represent, respectively, 4.3%, 2.4% and -16.5% of changes in the final response. Comfort criteria represented 36.9% and wind climate modelling criteria represented 44.7%.

Table 7.10 – Summary of results of each set of criteria for building B.

Wind climate modeling	Structural modeling	Time vs. frequency domain	Higher modal contribution	Comfort criteria	Total
-44.7%	-4.3%	-2.4%	16.5%	-36.9%	-62.0%

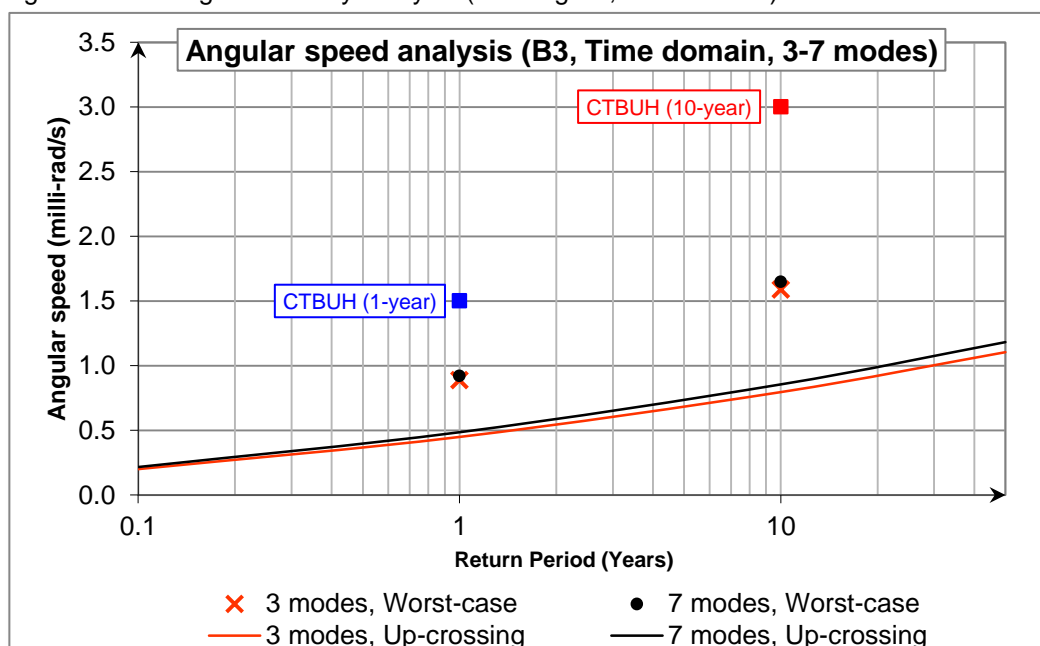
Source: Author.

These relative reductions (or increase, in the case of higher modal contribution) were calculated in the same fashion for building A, but this time starting with the wind climate modelling, and using the results for building B1 for three modes of vibration in the frequency domain in a comparison between the worst-case method and the up-crossing method. Then, for the structural modelling criteria, the results for buildings B1 and B3 were compared (both for three modes of vibration, frequency domain, and up-crossing method). Subsequently, the results from building B3 using the previous set of criteria were compared with the results from building B3 in the time domain. Later, building B3's results in the time domain and with the up-crossing method were compared with the three and for seven modes of vibration. Finally, the comfort criteria were evaluated using the ratios of the most precise result (B3, seven

modes, time domain, up-crossing method) and two thresholds of comfort: ISO 10137 (2007) and Sarkisian's (2012) for offices.

It is important to draw attention to the continuous orange line in [Figure 7.61](#) and to the dashed orange line in the same figure. Besides representing the boundaries in the structural modelling and dynamic analysis criteria, the first represents the structural set used in the WTT, whilst the second and last represents the most precise set of criteria presented in this thesis. In a comparison with the threshold for a ten-year return period from NBR6123 (1988), the set used by the BLWT meets the comfort criteria, whilst the second set doesn't. The 16.5% increase in the final acceleration is sufficient to fail the structure in the comfort assessment. However, the current threshold for comfort from NBR6123 (1988) is conservative and all sets of criteria analysed for building B meet the proposed comfort criteria in this section (20.0milli – g).

Figure 7.62 – Angular velocity analysis (Building B3, time domain).



Source: Author

The angular velocity analysis was performed in the time domain only and the results are shown in [Figure 7.62](#). The angular velocity is more relevant for building B than it is for building A (see [Figure 7.37](#)). This is due to the torsional feature of the mode deflection shapes of building B, along with the higher modal contribution

relevance for this building, which, on its turn, is due to the building height, primarily. Nevertheless, even for a 203.6m tall building structure, the angular velocity did not govern the design parameter. Therefore, it is accurate to affirm that higher structures will generate higher angular velocity responses and that the angular velocity will govern the design criterion for tall buildings much higher than 200m, or for tall buildings with severe torsional motion due to an unusual shape and/or structural elements distribution.

7.5 SYNTHESIS OF CASE STUDIES (BUILDINGS A AND B)

The outcome of the cases studies of buildings A and B regarding the structural modelling criteria can be summarized at:

- The modelling floor slab and probable Young's modulus for the concrete may reduce the overall building's responses and allow for more economical structural designs (always validating stiffness, see item below);
- Structural members may be modelled with full stiffness (EI, EA) for SLS. However, *tensile stresses and cracked sections must be validated*;
- Higher modal contribution needs be taken into consideration, necessarily, where the number of modes used can be assessed through the PSD analysis;
- Time-domain analyses should be used for more accurate and sometimes lower responses, allowing for an economical and precise structural design.

All responses (concrete stresses, accelerations, velocities, and displacements) for a 50-year return period take into consideration the linear behaviour of structural concrete (no cracking or plastification zones of the gross section). This also means a lower damping rate for the structure, reason why damping ratios of 1.25% (building A) and 1.00% (building B) from the SLS analyses were kept for the 50-year return period analysis. This hypothesis is valid for shear walls and floor slabs. However, they are not valid for concrete beams (see [section 7.2.5.3](#)) where cracking occurs for 50-year return period winds. Since the studied responses and validations of this thesis focus on the SLS (up to a ten-year return period), the responses for a 50-year return period will be kept as an evidence and as an illustration of the need for different validations for ULS analyses and for future research.

The wind climate modelling allows for a probabilistic approach that leads to an efficient structural design even in scenarios where there is no wind preferential directions (see [Figure 4.1](#) and [Figure 7.31](#)). The probabilistic approach to actions (building's responses using wind modelling criteria) combined with the probabilistic approach to comfort assessment (see [section 5.3.5](#)) allow for a full probabilistic approach applied to human comfort in tall buildings subjected to wind induced motion.

For SLS purposes, methods that take into consideration different wind statistical data for different sectors (like up-crossing method, sector-by-sector method, or storm passage method), also called directional methods, should be taken into consideration, since they might lead to more efficient design and allow for a full probabilistic approach.

8 CONCLUSIONS

Recalling the specific and general objectives of this thesis from [section 1.6](#), there were three main disciplines/lines of investigation: structural engineering, wind engineering, and comfort assessment. The results presented below are linked to the case studies from [Chapter 7](#).

To begin with, the structural engineering presented a noticeable influence on the final response. The structural modelling criteria were responsible for increases of up to 19.66% in building A's natural frequencies and up to 7.13% for building B (see [Table 7.2](#) and [Table 7.9](#)). Hence, significant changes were observed in the mode deflection shapes for building A. These changes in natural frequencies and mode deflection shapes were responsible for several singularities: changes in the critical sector of the building's response (see [Figure 7.32](#)); decreases of up to 11.4% in the overall resultant acceleration (see [Table 7.7](#)); secondary interferences combining both previous effects when the up-crossing method was applied (according to [section 7.2.3.2](#)).

Still in the structural engineering field, the time-domain vs. frequency-domain analyses and higher modal contributions were addressed. The time-domain analysis showed several benefits when compared with the frequency-domain analysis: precise assessment of acceleration components with no need for peak factors or joint action factors (see [section 7.2.2.2](#)); exact assessment of higher modal contribution with peak combinations (see [Figure 7.25](#)); accurate simulation of transient behaviour, especially for higher modes, leading to a reduction in the resultant acceleration response (up to 7.6%, according to [Table 7.7](#)). The higher modal contribution, on the other hand, showed increases in the overall acceleration of up to 16.5% (see [Table 7.10](#)). Subsequently, the stiffness of structural members was validated through verifications of cracked sections (see [section 7.2.5](#)), closing the Davenport's chain of wind loading and fortifying the link between "Dynamic Effects" and "Criteria" (see [Figure 1.24](#)). The discussions in [chapters 2](#) and [3](#) helped to bring familiarity to structural engineers with the dynamic analysis and to wind engineers with the structural modelling, respectively. The results discussed in [Chapter 7](#) corroborated the relevance of the structural modelling and the dynamic analysis criteria by proving a precision gain with the methodology discussed in [Chapter 6](#), and by providing a

benchmark of criteria for future projects (see [section 7.4.4](#)) with probable lower responses and more economical designs.

Second, the design wind speed and the wind climate modelling were discussed according to two main techniques: *worst-case* method and *up-crossing* methods. Directional methods, such as the up-crossing method, allow for the use of a full probabilistic approach to comfort assessment, which leads to efficient structural designs even in scenarios where there are no wind preferential sectors (see [section 7.2.3.1](#)). The discussion in [Chapter 4](#) and the bibliographic research may assist to enlighten structural engineers about wind engineering and wind climate modelling. The wind climate modelling showed to be the most relevant criterion, with reductions of up to 44.7% (according to [section 7.4.4](#)).

Third and last, the comfort evaluation, extensively discussed in [Chapter 5](#), brought about a complete overview of the discipline to both structural and wind engineers, raising significant facts from the early explorations from the 60's to the latest researches in the field. The consistency of different comfort thresholds was exposed and applied to real cases. The criteria related to this discipline showed to be the second most relevant, with reductions of up to 36.9% (see [Table 7.7](#) and [Table 7.10](#)).

Clearly, this field is the one that presents the greatest uncertainties among all the fields of study presented/discussed in this thesis, and probably the one with greater potential for discoveries. The biodynamic amplification (see [Figure 5.15](#)) seems to be a way to age modelling, sedentary behaviour, and other physiological factors to parametrize motion thresholds, since weaker muscles may indicate a less stiff body and smaller body damping to motion, leading to a higher amplification of the motion in the head (where the vestibular organs are located). Even with such parametrization, this field of study remains multidisciplinary, primarily due to inputs from psychology (expectancy of movement, cultural differences, fear, and alarm from other users). As an outcome of this thesis to improve this field of study in Brazilian projects, a set of comfort thresholds was proposed in [section 7.4.4](#), taking into consideration all of the discussion carried out in [Chapter 5](#) and the case studies in [Chapter 7](#).

The results achieved in this work consolidate the main engineering and multidisciplinary areas of study involved in WTT, clarifying the impact of the criteria from one field of studies on another, and strengthening the last links of the Davenport's chain through validation of the mechanical properties of a building using response amplitudes. The general purpose of this work is to provide more governability to each field of study involved in the WTT with the proposed methodology, and to increase the precision of procedures through the subsequently proposed criteria, so as to achieve a sustainable design.

BIBLIOGRAPHY

ALI, M. M.; MOON, K. S. **Structural Developments in Tall Buildings: Current Trends and Future Prospects.** *Architectural Science Review*. Vol 50.3, pp 205-223. 2007.

ALY, M. A. **Pressure integration technique for predicting wind-induced response in high-rise buildings.** *Alexandria Engineering Journal*. Vol 52, pp 717-731. 2013.

American Society of Civil Engineers (ASCE-88). **Minimum Design Loads for Buildings and Other Structures**, 1988.

American Society of Civil Engineers (ASCE), 2005. **Wind Tunnel Studies of Buildings and Structures**. No. 67.

Architectural Institute of Korea. **Korean building code-structural**, 2005.

ASCE/SEI 7-10. American Society of Civil Engineers. **Minimum Design Loads for Buildings and Other Structures**, 2010.

AIJ-Guidelines, 2004. **Guidelines for the evaluation of habitability to building vibration.** Architectural Institute of Japan, Maruzen, pp. 132.

BASHOR, R.; KIJEWski-CORREA, T.; KAREEM, A. **On the Wind-Induced Response of Tall Buildings: The Effect of Uncertainties in Dynamic Properties and Human Comfort Thresholds.** Proceedings of the 10th America's Conference on Wind Engineering, Baton Rouge, LA. 2005.

BEEDLE, L.; LYENGAR, H. (1982). **Selected Works of Fazlur R. Khan (1920-1982)**. IABSE Structure C-23/82.

BLESSMANN, J. (1988). **Introdução às ações dinâmicas do vento**. Universidade Federal do Rio Grande do Sul (UFRGS).

BOGGS, D. **Acceleration indexes for human comfort in tall buildings – Peak or RMS?** CTBUH Monograph Chapter 13: Motion Perception Tolerance and Mitigation. 1997.

BREEZE, G.; STOLOVAS, S. **The Practical Implementation of High Frequency Pressure Integration (HFPI) using Discrete Cosine Transforms (DCT)**. XIV International Conference on Wind Engineering (ICWE), Porto Alegre. 2015.

BURTON, M.; LI, Y. F.; CAMMELLI, S. **Wind Directionality Effects: Revisiting an Old Conundrum**. XIV International Conference on Wind Engineering (ICWE), Porto Alegre. 2015.

BURTON, M. D.; KWOK, K. C. S.; HITCHCOCK, P. A.; DENOON, R. O. **Frequency Dependence of Human Response to Wind-Induced Building Motion**. Journal of Structural Engineering, ASCE, v. 132 (2), p. 296-303. 2006.

CAVALERI, L.; PAPIA, M. **A new dynamic identification technique: application to the evaluation of the equivalent strut for infilled frames**. *Engineering Structures*, 25, p. 889-901. 2003.

CEB-FIP Model Code 1990. **Committee Euro-International du Béton**. Trowbridge, Wiltshire, UK: Redwood Books; 1990.

CHAN, C. M.; HUANG M. F.; KWOK, K.C.S. (2010). **Integrated wind load analysis and stiffness optimization of tall buildings with 3D modes.** *Journal of Wind Engineering and Industrial Aerodynamics*, 32, p. 1252-1261.

CHANG, F. K. **Human Response to Motions in Tall Buildings.** *Journal Structural Division, ASCE*, v. 99 (6), p. 1259-1272. 1973.

CHAPRA, S. C.; CANALE, R. P. **Métodos Numéricos para Engenharia.** 5th ed. McGraw-Hill Interamericana do Brasil. 2008.

CHEN, P. W.; ROBERTSON, L. E. (1972). **Human Perception Thresholds of Horizontal Motion.** *Journal Structural Division, ASCE*, v. 98 (8), p. 1681-1695. 1972.

CHOI, H. S.; GOMAN, H.; JOSEPH, L.; MATHIAS, N. **Outrigger Design for High-Rise Building: An output of the CTBUH Outrigger Working Group Council of Tall Buildings and Urban Habitat: Chicago.** 2012.

CHOPRA, A. K. **Dynamics of structures: Theory and applications to earthquake engineering.** 2nd ed. Prentice-Hall; 2000.

CLOUGH, R.; PENZIEN, J. **Dynamics of Structures,** 2nd ed., Berkeley: Computers and Structures. 2010.

CRANDALL, S. H; MARK, W. D. **Random Vibration.** *Academic Press.* New York, 1973.

DAVENPORT, A. G. (1975). **Tall Buildings – An Anatomy of Wind Risks.** Construction in South Africa.

DENOON, R. O.; ROBERTS, R. D.; LETCHFORD, C. W.; KWOK, K. C. S. **Field experiments to investigate occupant perception and tolerance of wind-induced building motion.** Research Rep. No. R803, Department of Civil Engineering, University of Sydney, Sydney, Australia, 2000. 999p.

DREW, C.; FERNANDEZ, K.; FANNING, K. **The Environmental Impact of Tall vs. Small: A comparative study.** Proceedings of Council of Tall buildings and Urban Habitat (CTBUH) – Future Cities. Towards Sustained Vertical Urbanism. Shanghai. p. 418-424. 2014.

FERRARETO, J. A.; FRANÇA, R. L. S.; MAZZILLI, C. E. N. **The Impact of Comfort Assessment Criteria on Building Design.** Proceedings of Council of Tall buildings and Urban Habitat (CTBUH) – Future Cities, Towards Sustained Vertical Urbanism. Shanghai, p. 722-730. 2014.

FERRARETO, J. A.; FRANÇA, R. L. S.; MAZZILLI, C. E. N. **Wind-induced motion on tall buildings: a comfort criteria overview.** *Journal of Wind Engineering and Industrial Aerodynamics*, 142 p. 26-42. 2015.

FERRARO, V.; PETER, A. I.; GARY, K. S. **Wind Induced Building Accelerations.** *Journal of Wind Engineering and Industrial Aerodynamics*, 36 p. 757-767. 1990.

GOTO, T. **Studies on wind-induced motion of tall buildings based on occupants' reactions.** *Journal of Wind Engineering and Industrial Aerodynamics*, 13, p. 241-252. 1983.

GOULD, P. L.; ABU-SITTA, S. H. **Dynamic Response of Structures to Wind and Earthquake Loading**, London: Pentech Press. 1980.

GRIFFIS, L. G. **Serviceability Limit States under Wind Load.** Engineering Journal AISC, 1st Qtr, p. 1-16. 1993.

HANSEN, R. J.; REED, J. W.; VANMARCKE, E. H. **Human Response to Wind-Induced Motion of Buildings.** Journal of Structural Division, ASCE, v. 99 (7), p. 1589-1605. 1973.

HOLMES, J. D.; BEKELE S. A. **Directionality and wind-induced response – calculation by sector methods.** XIV International Conference on Wind Engineering (ICWE), Porto Alegre. 2015.

HOLMES, J. D. **Wind Loading of Structures,** Taylor and Francis, New York, 2001.

HUANG, G., CHEN, X. **Wind load effects and equivalent static wind loads of tall buildings based on synchronous pressure measurements.** Engineering Structures, v. 29, p. 2641-2653. 2007.

IRWIN, A. W. **Human Response to Dynamic Motion of Structures.** The Structural Engineer, v. 56A (9), p. 237-244. 1978.

IRWIN, A. W. **Perception, comfort and performance criteria for human beings exposed to whole body pure yaw vibration and vibration containing yaw and translational components.** Journal of Sound and Vibration, v. 76 (4), p. 481-497. 1981.

IRWIN, P.; DENOON, R.; SCOTT, D. **Wind Tunnel Testing of High-Rise Buildings:** An output of the CTBUH Wind Engineering Working Group. Council of Tall Buildings and Urban Habitat: Chicago. 2013.

IRWIN, P.; GARBER, J.; HO, E. **Integration of Wind Tunnel Data with Full Scale Wind Climate.** Proceedings of the 10th Americas Conference on Wind Engineering. Baton Rouge, LA, 2005.

ISYUMOV, N.; HO, E.; CASE, P. **Influence of wind directionality on wind loads and responses.** *Journal of Wind Engineering and Industrial Aerodynamics*, 133, p. 169-180. 2014.

ISO6897. **Guidelines for the evaluation of the response of occupants of fixed structures, especially buildings and offshore structures, to low-frequency horizontal motion (0.063 to 1 Hz).** International Organization for Standardization, Geneva. 1984.

ISO10137. **Bases for design of structures – Serviceability of buildings and walkways against vibrations.** International Organization for Standardization, Geneva. 2007.

JEARY, A. P.; MORRIS, R. G.; TOMLINSON, R. W. (1988). **Perception of the vibration – Tests in tall buildings.** *Journal of Wind Engineering and Industrial Aerodynamics*, 29, p. 361-370.

JEARY, A. P. **The effect of time-constants on the response of very large structures.** In: Eleventh international conference on wind engineering, 2003.

KANDA, J.; TAMURA, Y.; NAKAMURA, O.; UESU, K. **Probabilistic criteria for serviceability limit of wind response.** Proceedings of an International Colloquium, Structural Serviceability of Buildings, Göteborg, Sweden. IABSE Reports, 1993, Vol. 69, pp. 59–66.

KARA, I. F.; DUNDAR, C. **Prediction of deflection of reinforced concrete shear walls.** *Advances in Engineering Software*, 40, 2009, p. 777-785.

KASPERSKY, M. **Design wind loads for a low-rise building taking into account directional effects.** *Journal of Wind Engineering and Industrial Aerodynamics*, 95, p. 1125-1144. 2007.

KIJEWSKI-CORREA, T.; PRINIA, J. D.; BASHOR, R.; KAREEM, A.; KILPATRICK, J.; YOUNG, B. **Full-scale performance evaluation of tall buildings under winds.** *Proceedings of international conference on wind engineering*, 12, 2007. p. 351-358.

KIM, Y. J.; YU, E.; KIM, Y. D.; KIM, S. **Calibration of analytical models to assess wind-induced acceleration responses of tall buildings in serviceability level.** *Engineering Structures*, 31, p. 2086-2096. 2009.

KWOK, K. C. S.; HITCHCOCK, P. A.; BURTON, M. D. **Perception of vibration and occupant comfort in wind-excited tall building.** *Journal of Wind Engineering and Industrial Aerodynamics*, v. 97, p. 368-380. 2009.

LAMB, S.; KWOK, K. C. S.; WALTON, D. **Occupant comfort in wind-excited tall buildings: Motion sickness, compensatory behaviors and complaint.** *Journal of Wind Engineering and Industrial Aerodynamics*, 119, p. 1-12. 2013.

LEE, B. E. **The perception of the wind-induced vibration of a tall building: a personal viewpoint.** *Journal of Wind Engineering and Industrial Aerodynamics*, 12, p. 379-384. 1983.

LEE, D. G.; KIM, H. S.; CHUN, M. H. **Efficient seismic analysis of high-rise building structures with the effect of floor slabs.** *Engineering Structures*, v. 24 (1), p. 613-623. 2002.

LENZEN, K. **Vibration of Steel Joist-Concrete Slab Floors.** Engineering Journal, American Institute of Steel Construction, AISC. 1966.

LETCHFORD, C. W.; MANS, C.; CHAY, M. T. **Thunderstorms – their importance in wind engineering (a case for the next generation wind tunnel).** *Journal of Wind Engineering and Industrial Aerodynamics*, 90, p. 1415-1433. 2002.

LOREDO-SOUZA, A. M.; DAVENPORT, A. G. **The effects of high winds on transmission lines.** *Journal of Wind Engineering and Industrial Aerodynamics*, 74-76, p. 987-994. 1998.

LOREDO-SOUZA, A. M.; SCHETTINI, E. B. C.; PALUCH, M. J. **Turbulência, Cap. 5: Simulação da Camada Limite Atmosférica em Túnel de Vento.** Edição de Sergio Viçosa Müller e de Jorge Hugo Silvestrini. Universidade Federal do Rio Grande do Sul (UFRGS). Vol. 4. 2004.

MELBOURNE, W. H.; PALMER, T. R. **Accelerations and comfort criteria for buildings undergoing complex motions.** *Journal of Wind Engineering and Industrial Aerodynamics*, p. 105-116. 1992.

MICHAELS, N. M.; KWOK, K. C. S; TUNG, Y. K. **Exploratory analyses and modelling of parameters influencing occupant behaviour due to low-frequency random building motion.** *Journal of Wind Engineering and Industrial Aerodynamics*, p. 82-92. 2013.

MOON, SK.; LEE, DG. **Effects of inplane floor slab flexibility on the seismic behavior of building structures.** *Engineering Structures*, v.16 (2), p. 129-144. 1994.

NBCC, National Building Code of Canada. Part 4 Structural Design, Chapter 4 Commentaries on Part 4 of the National Building Code. 1990.

NBR6118. Projeto de estruturas de concreto – Procedimento. Associação Brasileira de Normas Técnicas, Rio de Janeiro, Brasil. 2014.

NBR6123. Forças devidas ao vento em edificações. Associação Brasileira de Normas Técnicas, Rio de Janeiro, Brasil. 1988.

NBR8800. Projeto de estruturas de aço e de estruturas mistas de aço e concreto de edifícios. Associação Brasileira de Normas Técnicas, Rio de Janeiro, Brasil. 2007.

NSPRC, National Standard of the People's Republic of China. Load Code for the Design of Building Structures, GB50009 – China Architecture and Building Press, 2012.

ROSA, L.; TOMASINI, G.; ZASSO, A.; ALY, A. M. **Wind-induced dynamics and loads in a prismatic slender building: A modal approach based on unsteady pressure measurements.** *Journal of Wind Engineering and Industrial Aerodynamics*, 107-108, p. 118-130. 2012.

RWDI – Roman Williams Davies & Irwin Inc. **Technotes: Design-oriented wind engineering studies new China Central Television Headquarters.** Issue number 26. 4p.

SARKISIAN, M. P. Designing Tall Buildings Structure as Architecture, New York: Routledge. 2012.

SCHNEIDER, J. **Introduction to Safety and Reliability of Structures.** International Association for Bridge and Structural Engineering (IABSE). 2nd Ed. 2006.

SIMIU, M.; SCANLAN, R. H. **Wind Effects on Structures.** 3rd. ed. *John Wiley & Sons, Inc.*, 1996.

TAMURA, Y. **Application of damping Devices to suppress wind-induced responses of buildings.** *Journal of Wind Engineering and Industrial Aerodynamics*, 74-76 p. 49-72. 1998.

TAMURA, Y. **Design issues for tall buildings from accelerations to damping.** The 11st International Conference on Wind Engineering, Construction and Maintenance of Structures, Lubbock, Texas, June, 2003.

TAMURA, Y.; KAWANA, S.; NAKAMURA, O.; KANDA, J.; NAKADA, S. **Evaluation perception of wind-induced vibration in buildings.** Proceedings of Institution of Civil Engineers, Structures and Buildings, v. 159 (SB5), p. 283-293. 2006.

TAMURA, Y. (2007) **Wind resistant design of tall buildings in Japan.** 1st International Conference on Modern Design, Construction and Maintenance of Structures, Hanoi, Vietnam, December 2007.

TARANATH, B. S. (1998) **Steel, Concrete and Composite Design of Tall Buildings.** McGraw Hill: New York.

TARANATH, B. S. (2012) **Structural analysis and design of tall buildings: steel and composite construction.** 1st ed. Florida: CRC Press, 2012.

VAN DER HOVEN , I. **Power spectrum of horizontal wind speed in the frequency range from 0.0007 to 900 cycles per hour.** *Journal of Meteorology*, v.14, p. 160-164. 1957.

VILLAVERDE, R. **Simple method to estimate the seismic nonlinear response of nonstructural components in buildings.** *Engineering Structures*, v.28 (8), p. 1209-1221. 2006.

WISS, J. F.; PARMELEE, R. A. **Human Perception of Transient Vibrations.** *Journal of Structural Division, ASCE*, v. 100 (4), p. 773-787. 1974.

WU, J. R.; LIU, P. F.; LI, Q. S. **Effects of amplitude-dependent damping and time constant on wind-induced responses of super tall building.** *Computers and Structures*, v. 85, p. 1165-1176. 2007.

ZHANG X.; CHEN X. **Assessing Extreme Wind Load Effects for Various Mean Recurrence Intervals with Consideration of Directionality and Uncertainty.** XIV International Conference on Wind Engineering (ICWE), Porto Alegre. 2015.

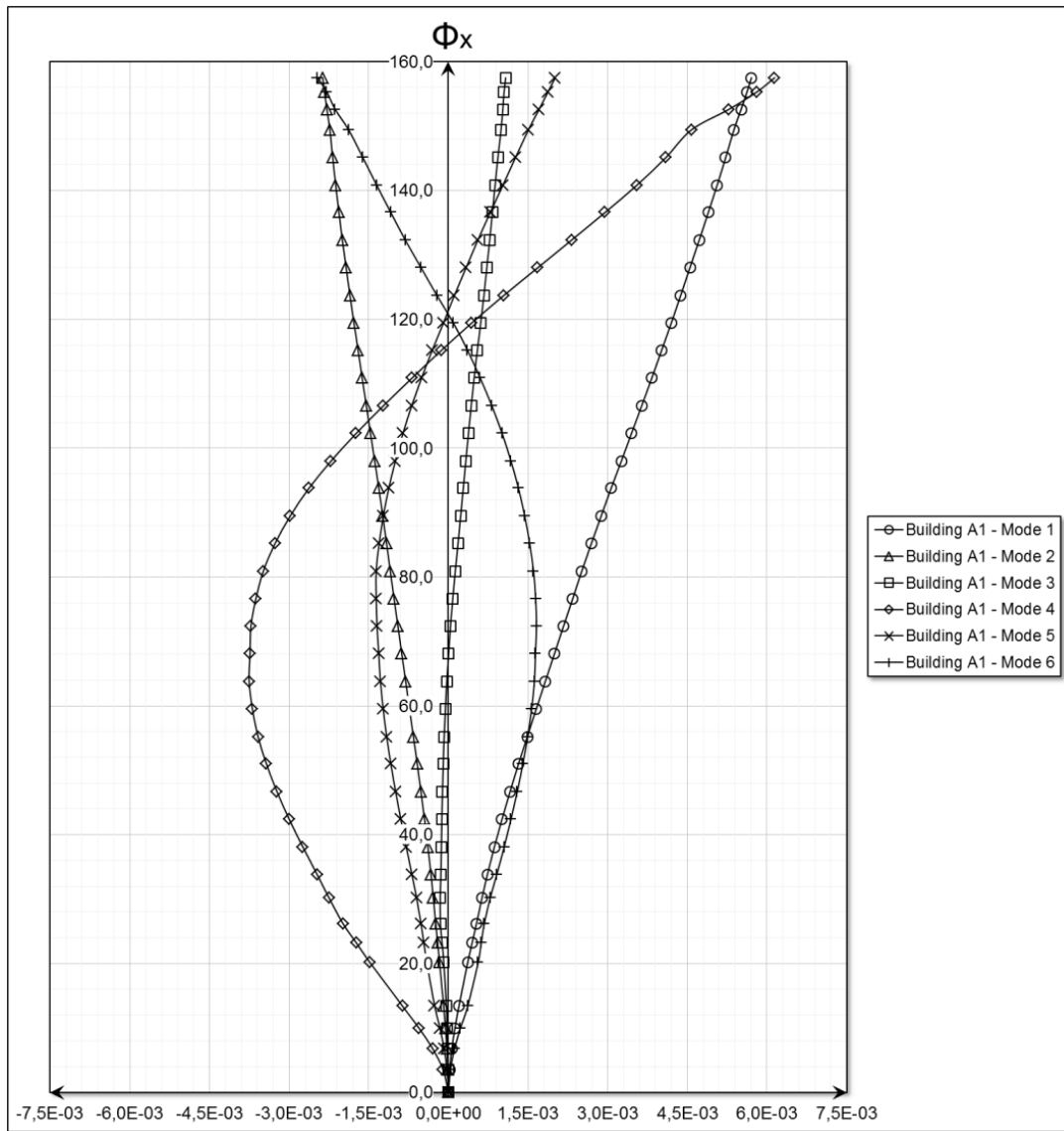
APPENDIX 1 – “BUILDING A” MECHANICAL PROPERTIES

Table A1.1 – Building A's inertial properties.

n	Floor	Level(m)	$m_{(t)}$	I_z (t.m ²)
1	5 th Basement	704.7	6.88E+02	8.49E+04
2	4 th Basement	708.2	3.53E+03	2.16E+06
3	3 rd Basement	711.5	3.42E+03	2.15E+06
4	2 nd Basement	714.7	3.51E+03	2.26E+06
5	1 st Basement	718.1	5.80E+03	4.03E+06
6	Ground Level	724.9	7.26E+03	5.68E+06
7	1 st Mezzanine	727.9	5.62E+02	1.69E+05
8	1 st	730.9	2.21E+03	8.68E+05
9	2 nd Mezzanine	734.9	1.20E+03	3.72E+05
10	2 nd	738.5	2.68E+03	1.05E+06
11	3 th	742.8	2.61E+03	1.06E+06
12	4 th	747.1	2.61E+03	1.07E+06
13	5 th	751.4	2.62E+03	1.07E+06
14	6 th	755.7	2.62E+03	1.08E+06
15	7 th	759.9	2.63E+03	1.09E+06
16	8 th	764.2	2.63E+03	1.09E+06
17	9 th	768.5	2.63E+03	1.09E+06
18	10 th	772.8	2.65E+03	1.09E+06
19	11 th	777.1	2.63E+03	1.09E+06
20	12 th	781.3	2.66E+03	1.09E+06
21	13 th	785.6	2.64E+03	1.07E+06
22	14 th	789.9	2.53E+03	1.03E+06
23	15 th	794.2	2.50E+03	1.02E+06
24	16 th	798.5	2.49E+03	1.01E+06
25	17 th	802.7	2.47E+03	9.90E+05
26	18 th	807	2.45E+03	9.68E+05
27	19 th	811.3	2.44E+03	9.51E+05
28	20 th	815.6	2.41E+03	9.27E+05
29	21 th	819.9	2.43E+03	9.09E+05
30	22 th	824.1	2.39E+03	8.71E+05
31	23 th	828.4	2.30E+03	8.32E+05
32	24 th	832.7	2.24E+03	7.86E+05
33	25 th	837	2.19E+03	7.48E+05
34	26 th	841.3	2.17E+03	7.19E+05
35	27 th	845.5	2.09E+03	6.63E+05
36	28 th	849.8	2.07E+03	6.37E+05
37	29 th	854.1	3.55E+03	1.20E+06
38	3 rd Mezzanine	857.3	3.27E+02	3.90E+04
39	Attic	860	4.71E+02	6.30E+04
40	Heliport	862.2	8.86E+02	1.28E+05

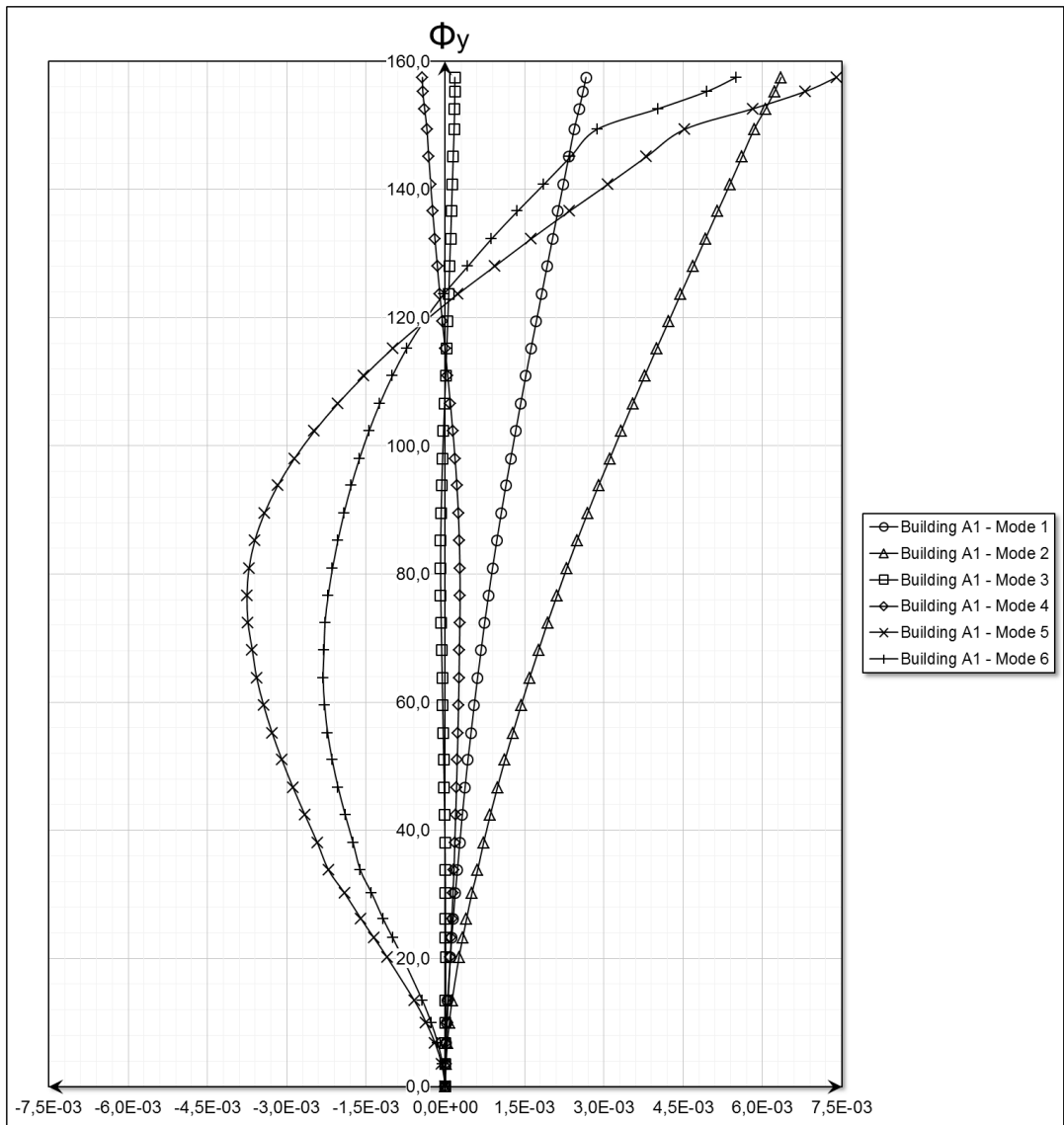
Source: Author.

Figure A1.1 – Mode shapes for A1 structural model (X axis components).



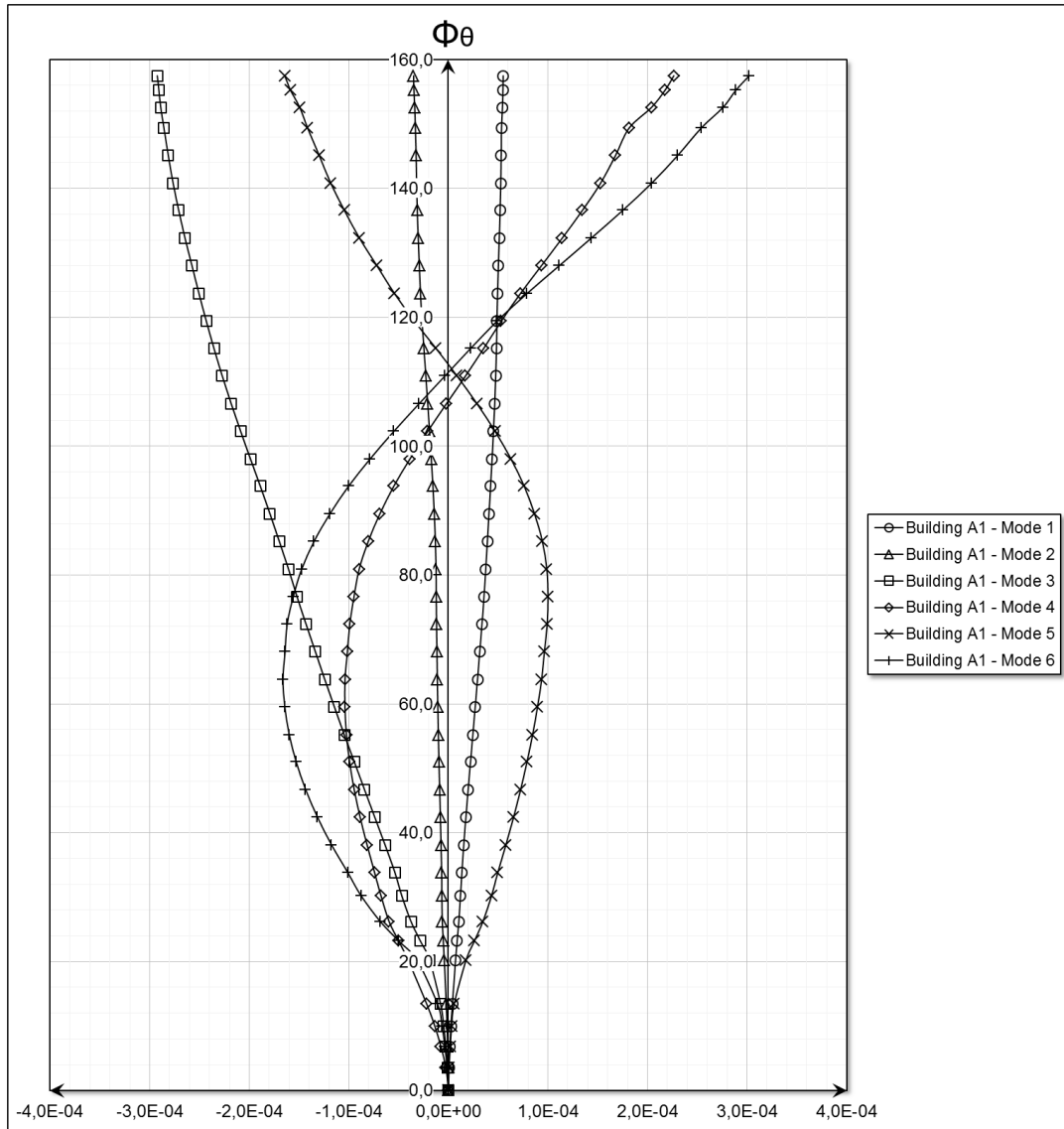
Source: Author.

Figure A1.2 – Mode shapes for A1 structural model (Y axis components).



Source: Author.

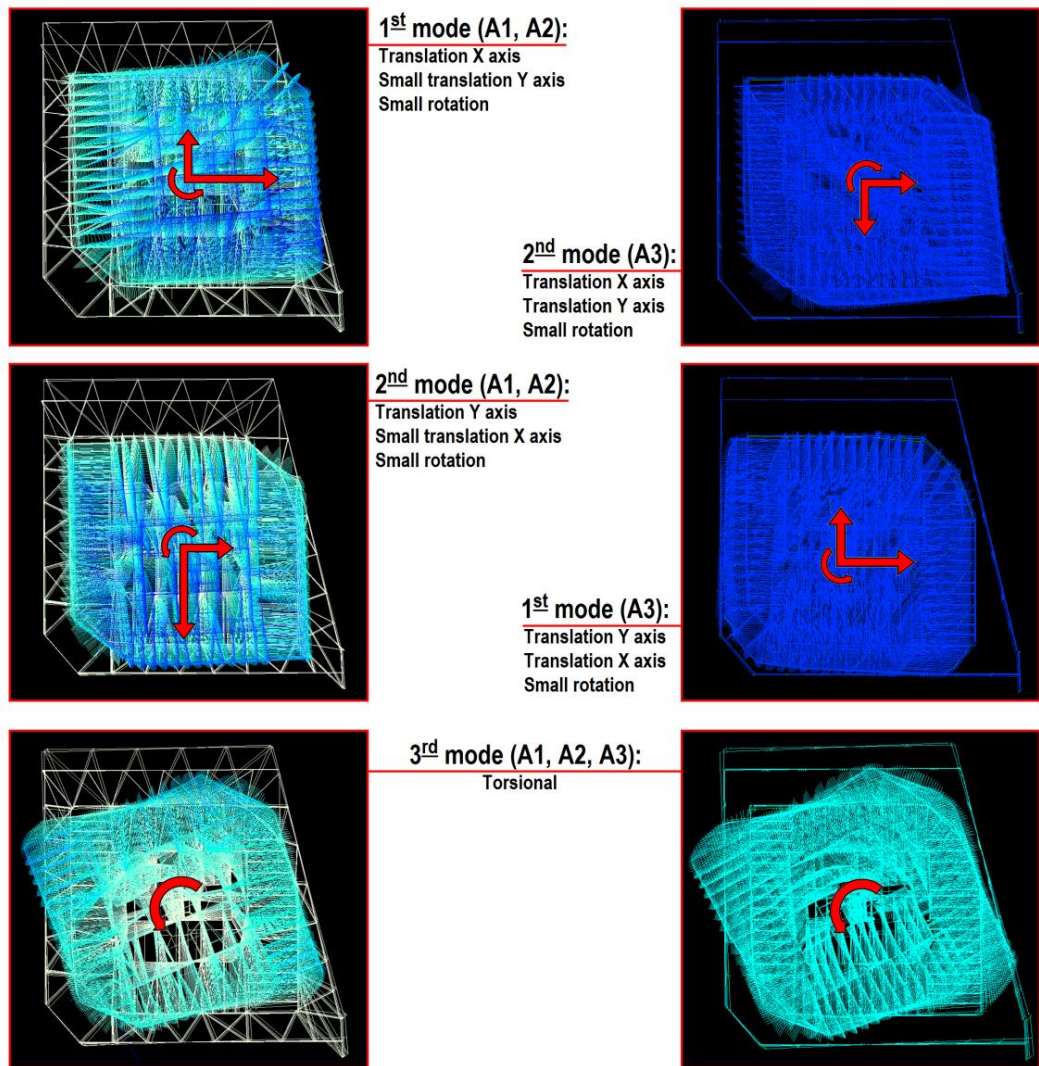
Figure A1.3 – Mode shapes for A1 structural model (torsional components).



Source: Author.

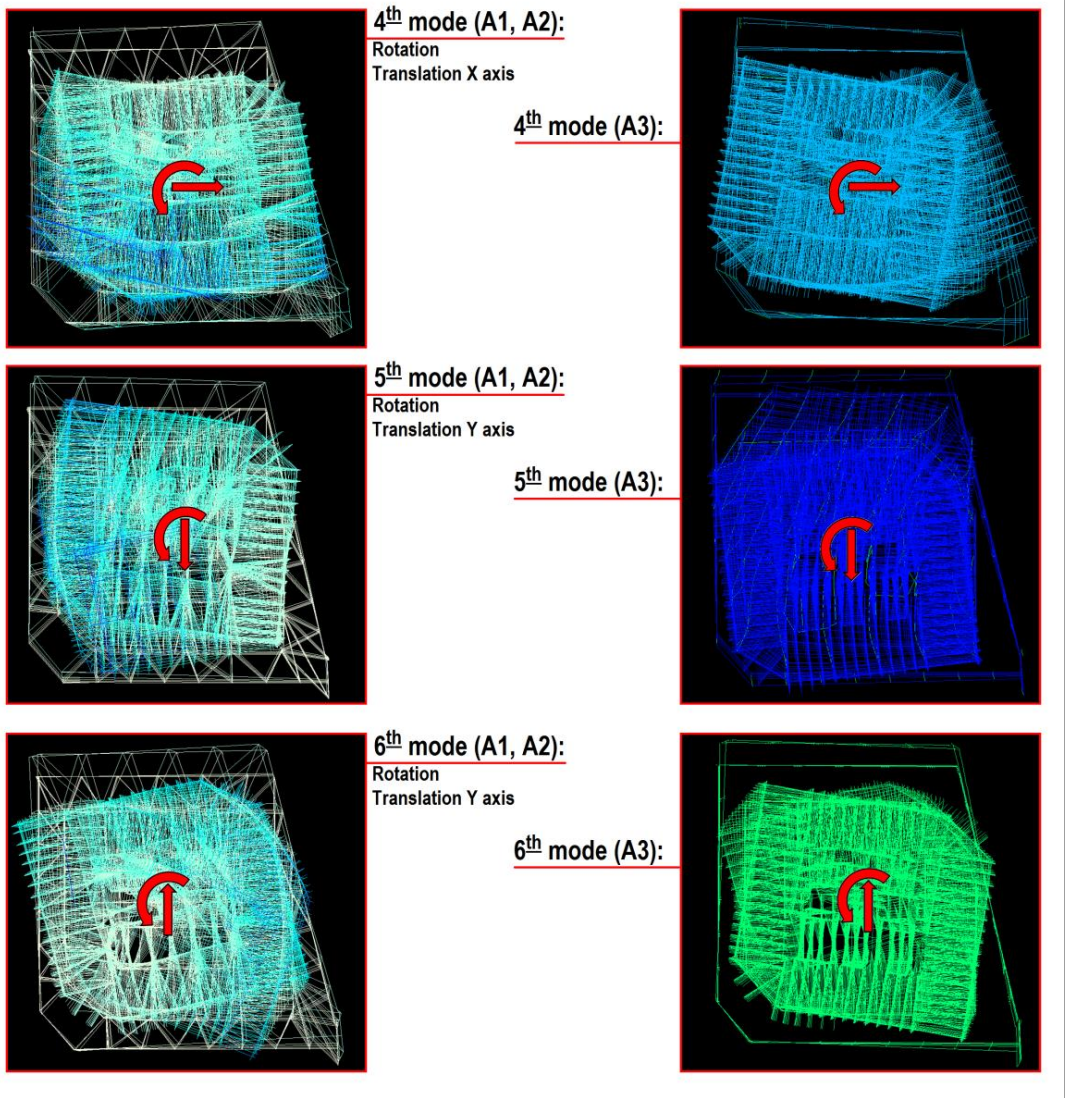
APPENDIX 2 – BUILDINGS A1, A2 AND A3 MODE SHAPES VIEW

Figure A2.1 – Mode shapes for A1, A2 and A3 buildings (1st, 2nd, and 3rd modes)



Source: Author.

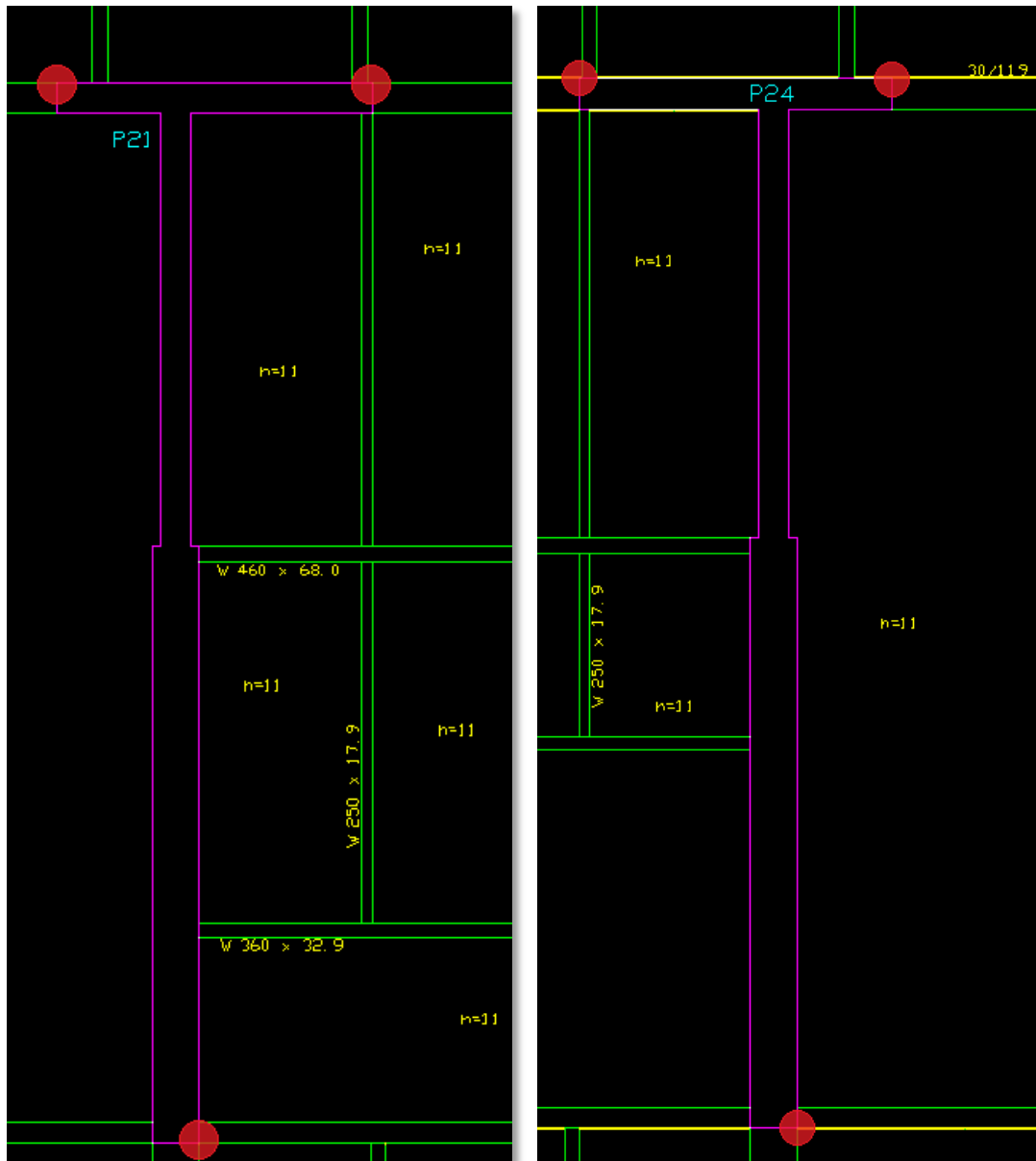
Figure A2.2 – Mode shapes for A1, A2 and A3 buildings (4th, 5th, and 6th modes)



Source: Author.

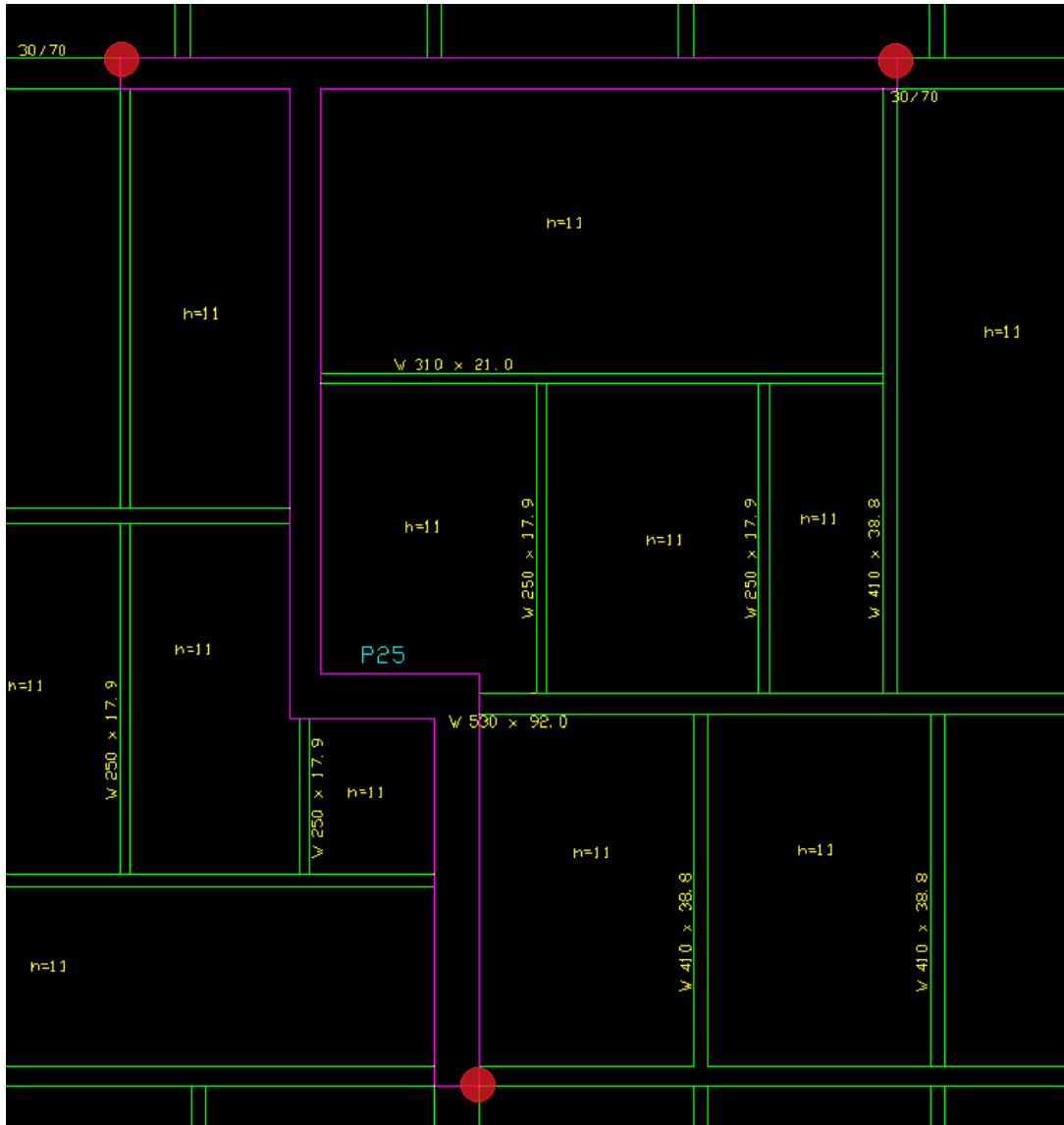
APPENDIX 3 – “BUILDING A” STUDIED SHEAR WALLS

Figure A3.1 – Shear walls “P21” (left) and “P24” (right).



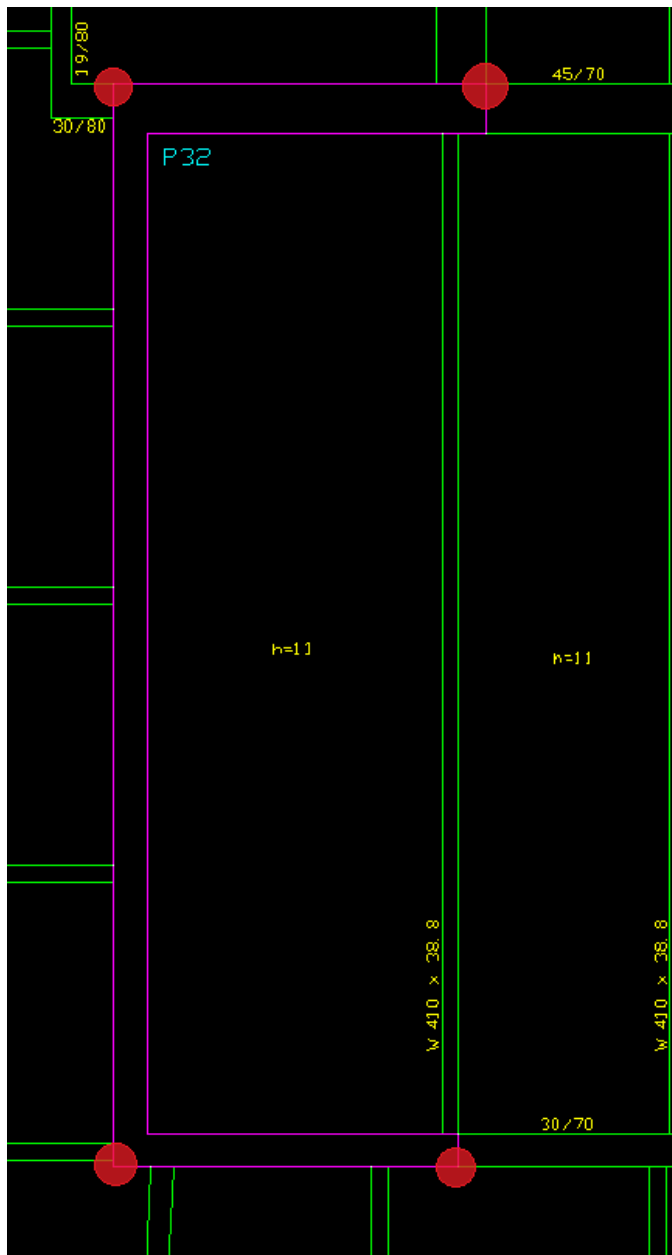
Source: Author.

Figure A3.2 – Shear wall “P25”.



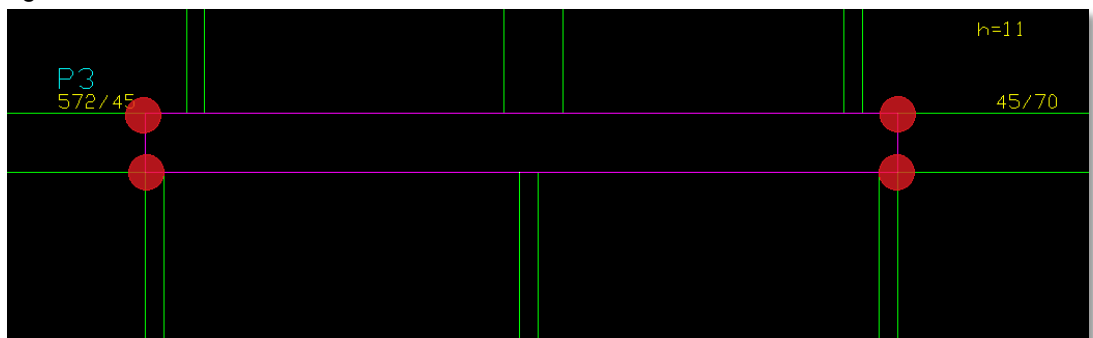
Source: Author.

Figure A3.3 – Shear wall “P32”.



Source: Author.

Figure A3.4 – Shear wall “P3”.



Source: Author.

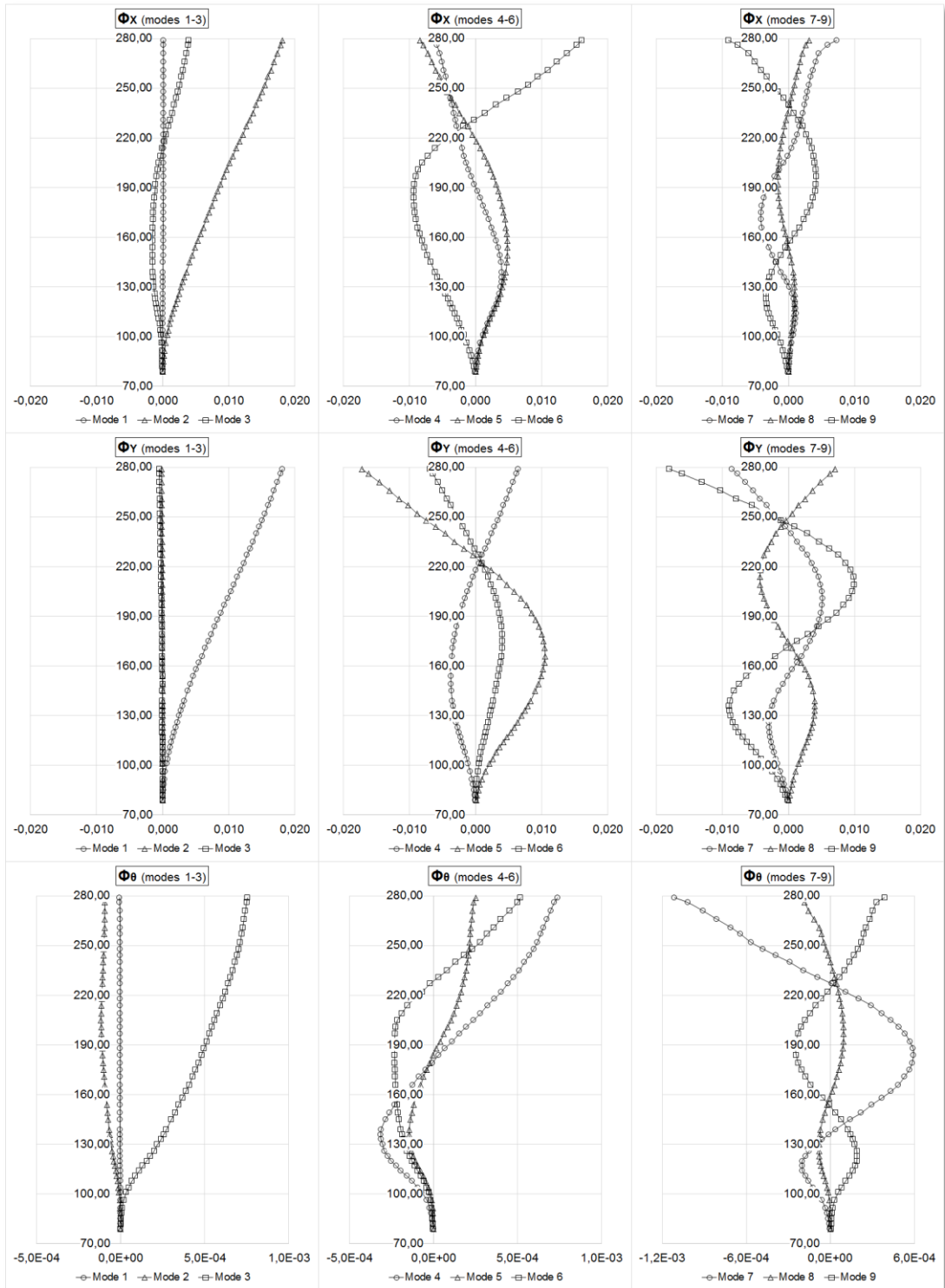
APPENDIX 4 – “BUILDING B” MECHANICAL PROPERTIES

Table A4.1 – Building B’s inertial properties.

n	Floor	Level _(m)	m _(t)	I _z (t.m ²)
0	7 th Basement	75.4	0.00E+00	0.00E+00
1	6 th Basement	78.9	6.59E+06	1.03E+10
2	5 th Basement	82.1	6.99E+06	1.11E+10
3	4 th Basement	85.3	8.21E+06	1.07E+10
4	3 rd Basement	88.5	6.47E+06	1.00E+10
5	2 nd Basement	91.7	7.06E+06	1.13E+10
6	1 st Basement	96.4	7.66E+06	1.02E+10
7	Ground Level	101.0	9.78E+06	1.52E+10
8	1 st Mezzanine	104.0	9.82E+05	4.62E+08
9	1 st	108.0	5.72E+06	7.21E+09
10	2 nd Mezzanine	111.0	1.00E+06	4.69E+08
11	2 nd	114.0	6.05E+06	7.35E+09
12	3 rd Mezzanine	117.0	1.02E+06	4.71E+08
13	3 th	120.0	6.28E+06	7.98E+09
14	4 th Mezzanine	123.0	1.16E+06	4.65E+08
15	4 th	126.0	7.33E+06	8.15E+09
16	5 th Mezzanine	130.0	1.01E+06	4.19E+08
17	5 th	133.0	4.52E+06	4.21E+09
18	6 th Mezzanine	136.0	2.13E+06	1.11E+09
19	6 th	139.0	9.32E+06	8.69E+09
20	7 th	145.0	2.97E+06	1.10E+09
21	8 th	149.0	2.87E+06	1.07E+09
22	9 th	154.0	2.87E+06	1.07E+09
23	10 th	158.0	2.87E+06	1.07E+09
24	11 th	162.0	2.87E+06	1.07E+09
25	12 th	166.0	2.87E+06	1.07E+09
26	14 th	171.0	2.87E+06	1.07E+09
27	15 th	175.0	2.87E+06	1.07E+09
28	16 th	179.0	2.87E+06	1.07E+09
29	17 th	184.0	2.87E+06	1.07E+09
30	18 th	188.0	2.82E+06	1.03E+09
31	19 th	192.0	2.41E+06	7.54E+08
32	20 th	197.0	2.41E+06	7.55E+08
33	21 st	201.0	2.42E+06	7.55E+08
34	22 nd	205.0	2.71E+06	7.75E+08
35	23 rd	209.0	2.53E+06	7.85E+08
36	24 th	214.0	2.41E+06	7.68E+08
37	25 th	218.0	2.41E+06	7.64E+08
38	26 th	222.0	2.40E+06	7.59E+08
39	27 th	227.0	2.40E+06	7.53E+08
40	28 th	231.0	2.39E+06	7.44E+08
41	29 th	235.0	2.38E+06	7.36E+08
42	30 th	240.0	2.36E+06	7.20E+08
43	31 st	244.0	2.35E+06	7.02E+08
44	32 nd	248.0	2.33E+06	6.93E+08
45	33 rd	252.0	2.32E+06	6.82E+08
46	34 th	257.0	2.34E+06	6.76E+08
47	35 th Technical	261.0	4.23E+06	1.32E+09
48	Technical	266.0	6.59E+05	1.08E+08
49	Technical	271.0	1.42E+06	2.25E+08
50	Attic	276.0	6.33E+05	1.01E+08
51	Heliport	279.0	1.22E+06	2.38E+08

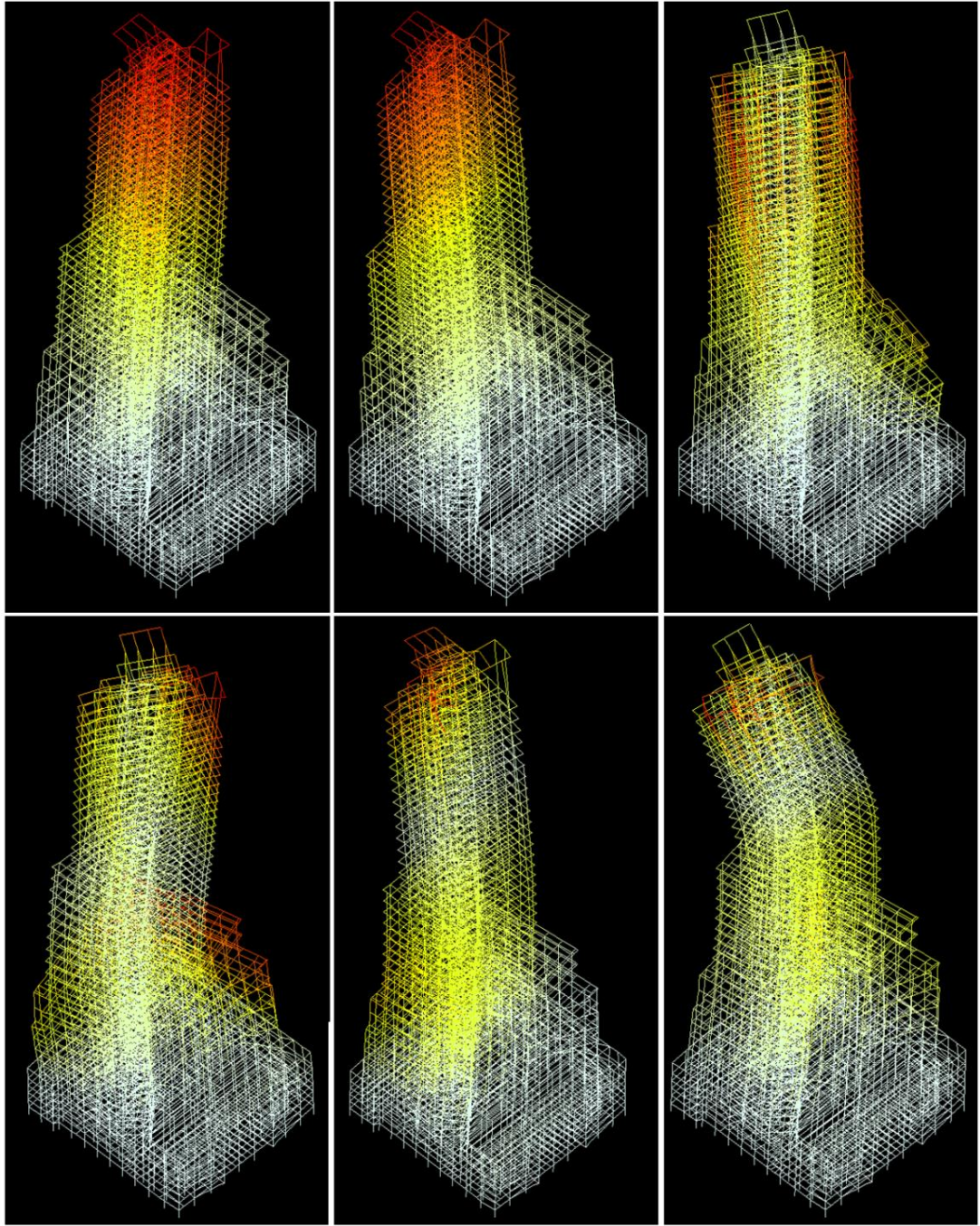
Source: Author.

Figure A4.1 – Building B mode deflection shapes.



Source: Author.

Figure A4.2 – Building B mode deflection shapes (modes 1 to 6).



Source: Author.

APPENDIX 5 – PROPOSAL FOR REVISION OF THE NBR6123 STANDARD: COMFORT CHAPTER (PORTUGUESE)

A proposta apresentada neste anexo é direcionada unicamente ao subitem referente ao cálculo de acelerações máximas para verificação de conforto, presente na revisão da ABNT/NBR6123-1988.

INTRODUÇÃO

A verificação do estado limite de serviço referente ao conforto de usuários é feita pela aceleração e pela velocidade angular de uma região específica de um piso do edifício (HANSEN ET AL., 1973; ISO6897, 1984; ISO10137, 2007; SARKISIAN, 2012; TARANATH, 2012; FERRARETO ET AL., 2015). Alguns autores, incluindo esta tese, discutiram os efeitos de deslocamentos, da velocidade, das acelerações angulares e da derivada da aceleração na avaliação de conforto (CHANG, 1973; HANSEN ET AL., 1973; IRWIN, 1981; BASHOR ET AL., 2005; KWOK ET AL., 2009; FERRARETO ET AL., 2015). No entanto, as variáveis cinemáticas recomendadas para verificação de conforto continuam sendo a aceleração e a velocidade angular em todos os códigos normativos ao redor do mundo (ISO6897, 1984; ISO10137, 2007; NBCC, 1990), inclusive nesta proposta de revisão.

Ainda assim, é necessário salientar a importância da avaliação dos deslocamentos diferenciais entre pisos, tanto para fins estruturais quanto para a integridade de vedações e de elevadores (GRIFFIS, 1993; FERRARETO ET AL., 2015). Os critérios propostos para os cálculos de acelerações são aplicáveis, com suas respectivas adaptações, aos cálculos de deslocamentos. Os limites aplicáveis para os deslocamentos diferenciais máximos variam para cada tipo de vedação, de material e de fixação utilizados e devem ser tratados em conjunto com o projeto específico para estes elementos, a mesma lógica se aplica a elevadores. Para fins estruturais, os deslocamentos diferenciais e de topo máximos são definidos por norma específica (NBR6118-2014; NBR8800-2007).

As acelerações e velocidades angulares máximas devem ser calculadas de acordo com o uso do edifício, sendo estas calculadas no piso mais elevado ocupado quando se tratam de pisos de escritórios (HANSEN ET AL., 1973; FERRARETO ET AL., 2015). Quando o projeto possui pisos com apartamentos residenciais ou com quartos de hotel, a verificação se faz no piso mais elevado de cada um destes usos,

mesmo quando este piso está a uma altitude inferior à do piso mais elevado ocupado por escritórios (FERRARETO ET AL., 2015).

CRITÉRIOS DE ANÁLISE DINÂMICA

Uma das maneiras de se realizar o cálculo dinâmico da estrutura é através de um modelo discreto com massas aglomeradas (NBR6123-1988; ROSA ET AL., 2012; BREEZE AND STOLOVAS, 2014), representado na *Figure 1.12*. Na escolha deste método, a resposta final do edifício é calculada pelo método de superposição modal (CLOUGH AND PENZIEN, 2010). Os cálculos de acelerações, velocidades angulares e deslocamentos devem incluir não apenas os três primeiros modos naturais de vibração, mas também a contribuição de modos de vibração mais elevados, quando possível. O uso de modos de vibração além dos três modos fundamentais aumenta a precisão do cálculo, sobretudo para contribuições de modos com torção do pavimento (ROSA ET AL., 2012; FERRARETO ET AL., 2014). Geralmente os modos com frequências naturais abaixo ou próximas a 1.0Hz são relevantes no cálculo, porém recomenda-se fazer uma análise da densidade espectral da resposta para validar a quantidade exata de modos de vibração relevantes.

O cálculo final pode ser realizado tanto no domínio do tempo quanto no da frequência (WU ET AL., 2007; CLOUGH AND PENZIEN, 2010; BREEZE AND STOLOVAS, 2014). Recomenda-se inicialmente realizar os cálculos no domínio da frequência, incluindo-se uma análise de densidade espectral da resposta, para validação dos modos a serem utilizados posteriormente nos cálculos no domínio do tempo.

Cálculos de movimentos complexos, em dois eixos e com componentes torcionais requerem tratamento vetorial e análise em cada passo de tempo, conforme *Figure 6.8*. Análises no domínio da frequência necessitam de ajustes empíricos para combinação de movimentos ortogonais e de diferentes modos de vibração, diminuindo a precisão dos resultados (MELBOURNE AND PALMER, 1992; BOGGS, 1997). Assim, análises no domínio do tempo com a contribuição de modos mais elevados são recomendadas para o cálculo da resposta final do edifício.

CRITÉRIOS DE ANÁLISE ESTRUTURAL

O conjunto de dados estruturais (frequências naturais e formas modais) obtidos na modelagem estrutural é de grande relevância na precisão das respostas dinâmicas de um edifício. Na obtenção destes dados, recomenda-se observar a influência na rigidez global da estrutura devido a: elementos estruturais secundários (flexão de lajes fora de seu plano); elementos não estruturais (alvenarias); ganho de rigidez do concreto após a cura em 28 dias (MOON AND LEE, 1994; LEE, KIM AND CHUN, 2002; CAVALERI AND PAPIA, 2003; VILLAVERDE, 2006; KIM ET AL. 2009; NBR6118-2014). A aplicabilidade de cada um dos itens listados no modelo estrutural é sujeita à validação para cada caso e o ganho de rigidez do concreto limitado somente para análises de conforto.

CRITÉRIOS DE MODELAGEM PARA A VELOCIDADE DE VENTO

A aplicação da mesma velocidade de projeto em todos os azimutes é sempre segura. Esta abordagem faz parte de um método não direcional conhecido como *Worst case method*, no qual se considera que a velocidade de vento mais alta atinge a estrutura em seu azimute mais crítico (HOLMES AND BEKELE, 2015).

No entanto, para análises de conforto e estados limites de serviço, métodos direcionais são aplicáveis sem perda de segurança para o edifício. O uso destes métodos possui a vantagem de alcançar resultados mais baixos quando comparados com os resultados de métodos ditos não direcionais. Uma série de técnicas está disponível para este tipo de análise, são elas: *Up-crossing method*; *Sector methods*; *Storm passage method* (IRWIN ET AL., 2005; HOLMES AND BEKELE, 2015; BURTON ET AL., 2015).

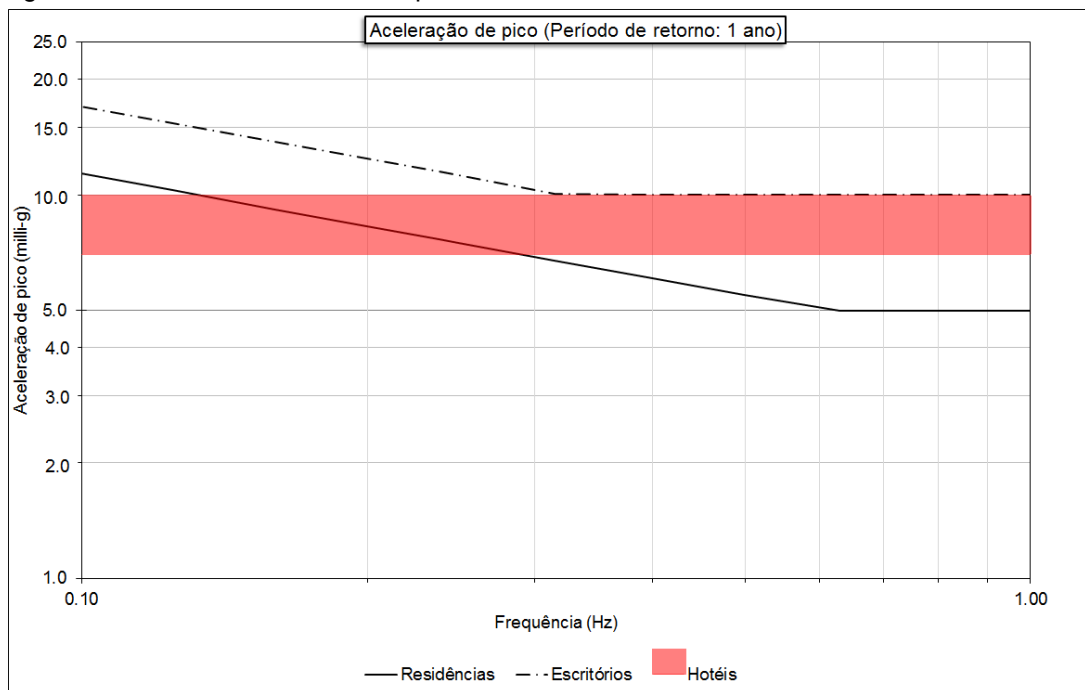
CRITÉRIOS DE CONFORTO

Critérios de conforto em edifícios sob a ação do vento se dividem dois tipos principais: critérios de percepção (AIJ-GEH-2004; ISO10137, 2007) e critérios de conforto propriamente dito, incluindo irritabilidade, perda de produtividade e comportamentos compensatórios (GOTO, 1983; NBCC, 1990; SARKISIAN 2012; LAMB, 2013). Alguns autores já discutiram a influencia de aspectos culturais sobre limiares de conforto (IRWIN, 1978; MICHAELS ET AL., 2013). De tal modo, pessoas que viveram em cidades com histórico de edifícios altos ou com outras fontes de vibração estrutural tendem a possuir uma maior aceitabilidade com relação à

movimentação de um edifício pela ação dinâmica do vento. Assim, nestas localidades, critérios de aceleração máxima apontam para limiares de conforto. Em contrapartida, em outras localidades critérios de aceleração máxima tendem a aproximar-se de critérios de percepção.

O Brasil possui um histórico relativamente recente sobre edifícios altos e, logicamente, deveria seguir limiares de percepção. No entanto, segundo o conceito da CTBUH para esta família de estruturas, sua vida útil deve ser mais extensa que a de uma construção comum. Assim, um edifício construído hoje, com limiares mais baixos de aceleração (percepção), no futuro, quando a população aceitar limiares mais altos (conforto), estará com margens excessivas de serviço. O resultado seria um conjunto inicial de estruturas oneradas por análises de conforto.

Figura A5.1 – Critérios de conforto para a revisão da NBR6123-1988.



Fonte: Autor

Seguindo o exemplo de Shanghai, que começou seu histórico de edifícios altos ao final da década de 1990 e hoje já aplica critérios de conforto em seus projetos de edifícios altos, a proposta para curvas de conforto da revisão da NBR6123-1988 segue limiares intermediários entre percepção e conforto (ver [Figura A5.1](#)). Outro exemplo relevante é o do Japão, que possui curvas de percepção em sua norma, porém as acelerações máximas de seus edifícios estão bastante acima

destes limiares e, ao mesmo tempo, são bem aceitas pela sociedade (AIJ-GEH-2004; TAMURA ET AL., 2006).

Estes limiares de conforto já foram previamente discutidos na [seção 7.4.4](#), onde também se encontra uma proposta para acelerações com período de retorno de 10 anos. Velocidades angulares máximas não devem ultrapassar 1.5milli – g para períodos de retorno de um ano.

As acelerações máximas para hotéis seguem com base em conforto e em normas internacionais, pois:

- Hotéis possuem menor ocupação (tempo) que residências, permitindo limiares mais altos (conforto);
- Hotéis são ocupados por pessoas de todas as partes do mundo, o que significa que seu dimensionamento deve buscar consistência com normas e critérios internacionais, independentemente de onde esteja localizado.